CORA Cork Open Research Archive
Cartlann Taighde Oscailte Chorcaí

Title	Electrochemical biosensor based on microfabricated electrode arrays for life sciences applications
Authors	Mohd Said, Nur Azura
Publication date	2014
Original Citation	Mohr Said, N. A. 2014. Electrochemical biosensor based on microfabricated electrode arrays for life sciences applications. PhD Thesis, University College Cork.
Type of publication	Doctoral thesis
Rights	© 2014, Nur Azura Mohd Said - http://creativecommons.org/licenses/by-nc-nd/3.0/
Download date	2026-11-07 01:41:55
Item downloaded from	https://hdl.handle.net/10468/1759



UCC
University College Cork, Ireland
Coláiste na hOllscoile Corcaigh

ELECTROCHEMICAL BIOSENSOR BASED ON MICROFABRICATED ELECTRODE ARRAYS FOR LIFE SCIENCES APPLICATIONS

NUR AZURA MOHD SAID, B.Sc. M.Sc.



A dissertation submitted for the degree of Doctor of Philosophy

National University of Ireland

April 2014



Supervisors

Dr. Vladimir I. Ogurtsov

Dr. Grégoire Herzog

Head of Chemistry Department

Prof. Martyn Pemble

DECLARATION

I hereby declare that this thesis is based on my own work otherwise stated. All research activities were carried out in Tyndall National Institute of University College Cork, Ireland between April 2010 and October 2013. Neither this thesis nor any part of it has been submitted for a degree at this or any other university.

ACKNOWLEDGEMENT

All praises to Allah the Lord Almighty for giving me the opportunity and strength in completing pursue of my PhD degree.

First and foremost, I would like to thank Dr. Grégoire Herzog for answering my enquiry e-mails four years back then; giving me the chance to study and doing research abroad in Cork, Ireland. I truly appreciate his kindness and continuous support. My immense gratitude also goes to Dr. Vladimir Ogurtsov for his guidance, patience and supervision. Without their help, this dissertation would not have been possible. My sincere appreciation also goes to Malaysian Agricultural Research and Development Institute (MARDI) for the scholarship and sponsorship.

To LSI team, especially Eileen Hurley the lab manager, thank you for ensuring that we are all safe and sound in the lab besides taking care of the chemicals purchase orders. To LSI lab beauty, Dr. Karen Twomey, thank you for the discussions and experiments that we had done together. I definitely would not forgot the good old memories from the previous batch of LSI members (Azrilawani, Waleed, Jon Ellis, Anna, Francesco, Eve, Jorg) as well as the new batch (Walter, Kon, Michelle Fitzgerald, Gerard, Patricia Vazquez) for keeping the lab alive. Special acknowledgement also goes to the interns whom I have enjoyed working with- Claire O'Connell, James Sheehan, and the French girls- Juliette and Florienne- *merci beaucoup*!

My deepest appreciation and love also to my beloved husband, Mior Haslem Mior Rashdi, for his continuous love, support and motivation throughout this journey. I could not thank him enough for single-handedly minding our children during my busy days in the lab and writing thesis. And for fetching and waiting for me in the darkness cold while I was running some overnight experiments. To my bestie, Monika Żygowska, I love you to bits. Thanks for the encouragement (*Yes, we can do this together*), gossiping time and I would surely miss your lemon-drizzle cake!

It would be fair as well to express my gratitude to Marina, Maryam and Aga helping out with the AFM instrumentation (and aligning the laser light!), Vince Lodge for the SEM images, Anushka for lending me microfabrication textbooks, Dan O'Connell and Aidan Daly for the fabrication discussion and Tyndall's IT Department for the IT support. I would like to take this opportunity to thank Microbiology Department, UCC and Queen's University Belfast for providing us with the protein and antibody for the experimental work.

A special thank you also for my mentor, Dr. Faridah Salam, for the immunology discussion/suggestions, Noor Azlina Masdor and her husband (Dr. Yunus Shukor)

for the assistance on the Graphpad Prism software, JC of Metrohm Malaysia for helping out with the GPES software, and my direct superiors in Malaysia for their support.

My endless love and gratitude for my beloved parents (Mama and Ayah) for raising me and providing me with good education (and funding as well) until I become as what I am now. For my sisters and brothers, I hope I make you all proud. This thesis also is dedicated to my in-laws (mak and Kak Jut) for their prayer and help throughout the time, and not forgetting my late father-in-law.

For my children, Maizara Zulaikha and Mior Nasrid (whom was born amidst my PhD struggle), I hope both of you will treasure the meaning, value and pride of having good knowledge. Ignorance is certainly not bliss in these modern challenging days, kids.

With that, I present to you this dissertation.

“Sometimes, the ocean floor is only a stop on the journey. And it is when you are at this lowest point, that you are faced with a choice. You can stay there at the bottom, until you drown. Or you can gather pearls and rise back up- stronger from the swim and richer from the jewels”

-Yasmin Mogahed, ***Reclaim Your Heart***

“The secret of life, though, is to fall seven times and to get up eight times”

-Paulo Coelho, ***The Alchemist***

“Success is not measured by what you accomplish, but by the opposition you have encountered, and the courage with which you have maintained the struggle against overwhelming odds”

-Orison Swett Marden

ABSTRACT

In developing a biosensor, the utmost important aspects that need to be emphasized are the specificity and selectivity of the transducer. These two vital prerequisites are of paramount in ensuring a robust and reliable biosensor. Improvements in electrochemical sensors can be achieved by using microelectrodes and to modify the electrode surface (using chemical or biological recognition layers to improve the sensitivity and selectivity). The fabrication and characterisations of silicon-based and glass-based gold microelectrode arrays with various geometries (band and disc) and dimension (ranging from 10 µm-100 nm) were reported. It was found that silicon-based transducers of 10 µm gold microelectrode array exhibited the most stable and reproducible electrochemical measurements hence this dimension was selected for further study. Chemical electrodeposition on both 10 µm microband and microdisc were found viable by electro-assisted self-assembled sol-gel silica film and nanoporous-gold electrodeposition respectively. The fabrication and characterisations of on-chip electrochemical cell was also reported with a fixed diameter/width dimension and interspacing variation. With this regard, the 10 µm microelectrode array with interspacing distance of 100 µm exhibited the best electrochemical response. Surface functionalisations on single chip of planar gold macroelectrodes were also studied for the immobilisation of histidine-tagged protein and antibody. Imaging techniques such as atomic force microscopy, fluorescent microscopy or scanning electron microscope were employed to complement the electrochemical characterisations. The long-chain thiol of self-assembled monolayer with NTA-metal ligand coordination was selected for the histidine-tagged protein while silanisation technique was selected for the antibody immobilisation. The final part of the thesis described the development of a T-2 labelless immunosensor using impedimetric approach. Good antibody calibration curve was obtained for both 10 µm microband and 10 µm microdisc array. For the establishment of the T-2/HT-2 toxin calibration curve, it was found that larger microdisc array dimension was required to produce better calibration curve. The calibration curves established in buffer solution show that the microelectrode arrays were sensitive and able to detect

levels of T-2/HT-2 toxin as low as 25 ppb (25 μg kg^{-1}) with a limit of quantitation of 4.89 ppb for a 10 μm microband array and 1.53 ppb for the 40 μm microdisc array.

TABLE OF CONTENTS

Declaration ……..i
Acknowledgement……...……...ii
Abstract…….……...v
TABLE OF CONTENTS……..vii
List of Abbreviations and Symbols……...xiv

CHAPTER 1
LITERATURE REVIEW: ELECTROCHEMICAL BIOSENSORS 1
1.1 Biosensor 2
1.1.1 Electrochemical Biosensors 5
1.1.2 Immobilisation of Biological Receptors 8
1.2 Electrochemical Techniques 10
1.2.1 Fundamental Concepts of Electrochemistry 11
Electrochemical Cells and Reaction 11
Faradaic and Non-Faradaic Processs 12
Electrode/Solution Interface 13
Mass Transport-Controlled Reactions 14
1.2.2 Amperometry and Voltammetry 16
Cyclic Voltammetry 17
1.2.3 Potentiometry 19
1.2.4 Conductometry 20
1.2.5 Electrochemical Impedance Spectroscopy 21
Nyquist Plot 22
Bode Plot 22
Equivalent Circuit Model 24
1.3 Microelectrode and Nanoelectrode Array in Biosensing 30
1.3.1 Microelectrode Definition 31
1.3.2 Advantages of Microelectrodes 31

1.3.3 Types of Microelectrodes and Their Electrochemical Behaviour 32
1.3.4 Microelectrode Arrays Designs and Difusion Profile 35
Microdisc Array 36
Microband Array 37
1.3.5 Fabrication of Micro- and Nanoelectrodes 38
1.3.6 Micro- and Nanoelectrode Application 39
1.4 Microfabrication Techniques for Biosensor 39
1.4.1 Substrate Materials 40
Silicon 40
Glass 41
Other Materials 41
1.4.2 Photolithography 43
1.4.3 Thin-Film Growth/Deposition 45
Dielectrics 45
Silicon 45
Metals 46
Polymers 46
Biomolecules 46
1.4.4 Etching 46
Wet Etching 47
Dry Etching 47
1.4.5 Electron Beam Lithography 49
1.5 Electrodes Biofunctionalisation 50
1.5.1 Self-Assembled Monolayers 51
Thiols Modified Electrodes 52
Silanes Modified Electrodes 54
1.5.2 Conducting Electroactive Polymers 55
1.5.3 Sol-gel Silica Films 58
1.5.4 Electrodes Functionalised with Carbon Materials 59
1.6 Conclusion and Objectives of The Study 60
1.7 References 62

CHAPTER 2

EXPERIMENTAL PROCEDURES 77

2.1 Chemicals and Biological Reagents 77

2.2 Instrumentations 79

2.3 Microelectrode Cleaning Using Plasma Cleaner 80

2.4 Electrochemical Measurements 82

2.4.1 Electrochemical Cell 82

Reference Electrode 83

Counter Electrode 83

Working Electrode 83

2.4.2 Microelectrode Array Fabrication 84

Photoresist Removal 85

2.4.3 Redox Solution Preparation 85

2.5 Sol-Gel Silica Film Electrodeposition on Gold Surface 86

2.5.1 Electrochemical Assited Self-Assembly Sol-Gel Silica Film Electrodeposition 86

2.6 Surface Biofunctionalisation for Histidine-tagged Protein Immobilisation 86

2.7 Surface Biofunctionalisation for Anti-T-2 Toxin Monoclonal Antibody Immobilisation 88

2.7.1 CM-Dextran Method 88

Electrode Surface Pretreatment 88

Surface Preparation 88

Antibody Immobilisation and Surface Blocking 89

10 mM Phosphate Buffer pH 6.5 Preparation 89

2.7.2 Silanisation Using GOPTS with PEG Linker 90

Electrode Surface Pretreatment 90

Silanisation 90

PEG LayerPreparation 90

Surface Activation (Cross-Linker Attachment) 90

Antibody Immobilisation 91

2.7.3 Silanisation Using APTES with PDITC Cross-Linker 91

Electrode Surface Pretreatment 92

Silanisation 92
Surface Activation (Cross-Linker Attachment) 92
Antibody Immobilisation 92
Testing the Immobilised Antibody with Optical Reading 92
0.1 M Sodium Borate Buffer pH9.3 Preparation 93
2.7.4 Silanisation Using APTES with EDC-NHS Amine Coupling 93
Antibody Immobilisation without Protein A 93
Antibody Immobilisation with Protein A 93
Optical Study of the Antibody Immobilisation 94
Antibody Immobilisation Calibration Curve Establishment 94
Antibody-Antigen Calibration Curve Establishment 94
2.8 References 95

CHAPTER 3

DEVELOPMENT OF MICRO- AND NANOELECTRODE ARRAYS 97

3.1 Introduction 97
3.2 Micro- and Nanoelectrode Array Fabrication 102
3.3 Optical Study for Visual Characterisation 104
3.4 Electrochemical Studies 108
3.4.1 Role of Passivation Layer 108
3.4.2 Cyclic Voltammetry Studies- Experimental vs. Theory 111
Microdisc Array 111
Microband Array 114
Limiting Current 117
3.4.3 Influence of the Scan Rate 123
3.4.4 Electrochemical Impedance Spectroscopy Study 127
Microdisc Array Impedance Spectra 128
Microdisc Array Impedance Spectra 132
EIS Comparison Between Silicon-Based and Glass-Based Microelectrode Array 134
3.4.5 Influence of Recess Depth on CV and EIS Experiments 135
3.4.6 Influence of the Nature of the Substrate 136

3.5 Chemically Modified Electrodes for Recessed Microelectrode Array 138
3.5.1 Electrochemically-Assisted Self-Assembly of Silica Film 139
EASA Silica Film on Gold Surface 141
EASA Silica Film on Recessed Microband Array 146
3.5.2 Nanoporous-Gold Modified Surface 154
3.6 Conclusion 161
3.7 References 163

CHAPTER 4
DEVELOPMENT OF AN ON-CHIP MICROELECTROCHEMICAL CELL……...174
4.1 Introduction 174
4.2 On-Chip Microelectrochemical Cell Fabrication 180
4.3 Optical Study for Visual Characterisation 181
4.4 Electrochemical Characterisation 185
4.4.1 Cyclic Voltammetry Studies 186
Characterisation of On-Chip Electrodes and Commercial Electrodes 186
Scan Rate Effect on Voltammogram for Different Centre-to-Centre Spacing 194
4.4.2 On-Chip RE Stability Study 200
4.4.3 Electrochemical Impedance Spectroscopy Study 202
4.5 Conclusion 206
4.6 References 207

CHAPTER 5
SURFACE BIOFUNCTIONALISATION FOR BIOMOLECULE IMMOBILISATION 211
5.1 Introduction 211
5.1.1 Plasma-Cleaning Effect for Surface Functionalisation 212
5.2 Histidine-Tagged Protein Immobilisation on Gold Surface 213
5.2.1 Atomic Force Microscopy 214

5.2.2 PduA Shell Protein 217
5.2.3 Gold Surface Modification 218
5.2.4 Results and Discussions 221
Evaluation of Immobilisation Procedure Using a Fluorescent Model 221
PduA Shell Protein Adsorption Study 222
Electrochemical Characterisation of Immobilised PduA Shell Protein 225
AFM Study of Immobilised PduA Shell Protein 229
5.3 Antibody Immobilisation on Gold Surface 233
5.3.1 Carboxymethyl Dextran 234
5.3.2 Surface Silanisation Using GOPTS and APTES 234
5.3.3 Results and Discussions 236
EIS Study on Different Surface Functionalisations for Antibody Immobilisation 237
Optical Inhibition Study for Immobilised Anti-T-2 Toxin Antibody on APTES-PDITC Functionalised Surface 241
5.4 Conclusion 244
5.5 References 245

CHAPTER 6

DEVELOPMENT OF T-2 TOXIN IMMUNOSENSOR 254

6.1 Introduction to Immunosensor 254
6.1.1 Antibodies 256
Antibody-Antigen Binding 257
6.2 T-2 Toxin 258
6.2.1 Conventional and Current Methods for T-2 Toxin Detection 260
Instrumentation Methods 260
Screening Methods 261
Biosensor for T-2/HT-2 Toxin Detection 262
6.3 Objectives of the Study 262

6.4 Results and Discussions 263
6.4.1 Silanisation Using APTES with PDITC Cross-Linker 264
6.4.2 Silanisation Using APTES with EDC-NHS Amine Coupling 270
Optical Study Using Fluorescent-Labelled Antigen 272
Covalent-Orientated Immobilisation Strategy Using Protein A 274
Covalent Attachment of Anti-T-2 Toxin Monoclonal Antibody Using EDC/NHS 276
Anti-T-2 Toxin Monoclonal Antibody Calibration Curve 277
T-2/HT-2 Toxin Calibration Curve 281
6.5 Conclusion and Suggestions for Future Work 284
6.6 References 285

CHAPTER 7
CONCLUSION AND SUGGESTIONS 293
7.1 Conclusion 293
7.1.1 Fabrication of Microelectrode Array 293
7.1.2 Surface Functionalisation on Microfabricated Silicon-Based Gold Electrode 296
7.2 Suggestions for Future Work 298

LIST OF CONFERENCES AND PUBLICATION 299

LIST OF ABBREVIATIONS AND SYMBOLS

Chemistry

APTES	(3-Aminopropyl) triethoxysilane
Ag	silver
Ag/AgCl	silver/silver chloride
Au	gold
CTAB	cetrimonium bromide (hexadecyltrimethyl ammonium bromide)
DAPEG	diamino poly(ethylene glycol)
DEA	diethanolamine
DMAP	dimethylaminopyridine
DMF	dimethylformamide
DSC	*N,N'*-disuccinimidyl carbonate
EDC	1-ethyl-3-(3-dimethylaminopropyl)carbodiimide
EtOH	ethanol
FITC	fluorescein isothiocyanate
FCA	ferrocenecarboxylic acid
FcMeOH	ferrocene methanol
GOPTS	(3-Glycidyloxypropyl)trimethoxysilane
HCl	hydrochloric acid
H_2O_2	hydrogen peroxide
H_2SO_4	sulfuric acid
IPA	isopropanol alcohol
KCl	potassium chloride
$K_3Fe(CN)_6$	potassium ferricyanide
$K_4Fe(CN)_6$	potassium ferrocyanide
MeOH	methanol
MPTMS	mercaptopropyltrimethoxysilane

11-MUA	11-mercaptoundecanoic acid
N_2	nitrogen
NaCl	sodium chloride
NaOH	sodium hydroxide
NHS	*N*-hydroxysuccinimide
PEG	poly(ethylene glycol)
PDITC	1,4-phenylene diisothiocyanate
Pt	platinum
Si_3N_4	silicon nitride (passivation layer)
Ti	titanium
TEOS	tetraethyl orthosilicate
TMOS	tetramethoxysilane

Acronyms

Ab	antibody
Ab-Ag	antibody-antigen binding
AFM	atomic force microscopy
BSA	bovine serum albumin
CV	cyclic voltammetry
DI	deionised (water)
EASA	electrochemically assisted self-assembly
EDX	energy dispersive x-ray microscopy
EIS	electrochemical impedance spectroscopy
HPLC	high performance liquid chromatography
HRP	horseradish peroxidase
Hz	hertz
Ig	immunoglobulins
IPA	intermittent pulse amperometry
KHz	kilo hertz
MAb	monoclonal antibody
MEA	microelectrode array
MEMS	micro-electro mechanical systems
OCP	open circuit potential

PBS	phosphate buffered saline
PEVCD	plasma-enhanced chemical vapor deposition
RT	room temperature
SAM	self-assembled monolayers
SEM	scanning electron microscopy
SPCE	screen-printed carbon electrode
TMB	tetramethylbenzemidine

Symbols

C	bulk concentration
C_{dl}	double layer capacitance (F)
d	centre-to-centre interspacing
D	diffusion coefficient
e-	electron
E	electrochemical potential (V)
$E_{1/2}$	half wave potential
F	Faraday constant
i	current
i_p	peak current
i_{ss}	steady state current (A)
l	recess depth
n	number of electrodes in an array
r	radius of the disk electrode
R	gas constant
R_{ct}	charge transfer resistance
R_s	solution resistance
t	time (s)
T	temperature
v	scan rate in a cyclic voltammetry experiment (V s^{-1})

Greek Symbols

ΔEp	peak-to-peak separation
ρ	roughness factor

CHAPTER 1

LITERATURE REVIEW: ELECTROCHEMICAL BIOSENSORS

1.1 Biosensor

The biosensor field has seen a phenomenal growth spurt in recent decades in terms of publications and market trend. The first developed biosensor system reported was a glucose biosensor employing an enzyme electrode described by Clarks & Lyons back in 1962 [1] and ever since that, the biosensor research has been booming. Table 1.1 shows the number of articles and reviews with the keyword "biosensor" and its associated keywords published between 2005 and 2013. As can been seen from the table, the glucose biosensor still dominates the biosensor area. In fact it is one of the success stories in biosensing owing to its enzyme stability, market demand for diabetic patients and low cost of the product itself. On the other hand, the trending research areas in biosensors include DNA biosensor, biofuels cells and biosensor with nanomaterials.

There is no standard or precise definition of 'biosensor' available from International Union of Pure and Applied Chemistry (IUPAC) [2]. However according to Collings & Caruso (1997) the consensus term of biosensor is *"an analytical device, which exploits a biological detection or recognition system for a target molecule or macromolecule, in conjunction with a physicochemical transducer, which converts the biological recognition event into a useable output signal"*[3]. The biological recognition element can be either integrated within or in close proximity with the transducer.

Table 1.1 Numbers of articles and reviews published in the biosensor research field of interest between 2005 and 2013 (Source: Web of Knowledge, Thomson Reuters). The fonts in *italic* represent biosensor work related with this thesis study.

Keywords (Topic)	**Numbers of articles published**	**Numbers of reviews published**
"Biosensor"	29,831	1,192
"Biosensor" and "amperometric"	4,958	169
"Biosensor" and "antibody"	4,022	181
"Biosensor" and "biochip"	206	21
"Biosensor" and "biofuel cell"	224	23
"Biosensor" and "conducting polymer"	596	53
"Biosensor" and "DNA"	5,320	310
"Biosensor" and "electrochemical"	8,690	363
"Biosensor" and "electrochemical impedance spectroscopy"	1,152	30
"Biosensor" and "glucose"	5,053	190
"Biosensor" and "glucose oxidase"	3,386	73
"Biosensor" and "histidine-tagged protein"	33	7
"Biosensor" and "microelectrode"	683	37
"Biosensor" and "microelectrode array"	252	17
"Biosensor" and "microfabrication"	80	12
"Biosensor" and "microfluidics"	279	34
"Biosensor" and "nano"	803	57
"Biosensor" and "nanobiosensor"	62	11
"Biosensor" and "nanoelectrode"	77	12
"Biosensor" and "nanomaterial"	121	44
"Biosensor" and "nanoporous gold"	78	3
"Biosensor" and "reagentless"	290	11
"Biosensor" and "self-assembled monolayer"	1,235	109
"Biosensor" and "silanization"	60	0

Table 1.1 *(continued)*

Keywords (Topic)	**Numbers of articles published**	**Numbers of reviews published**
"Biosensor" and "sol-gel"	749	37
"Biosensor" and "optical"	3,827	291
"Biosensor" and "protein chip"	690	41

A biosensor system is comprised of three essential components:

i) *Detector* - recognizes the biological element of interest (DNA, antibody, enzymes, cells, bacteria etc.)
ii) *Transducer* - converts one form of energy into another [4]. In biosensor, a transducer converts the biological element recognition to a signal; and
iii) *Output system* - involves amplification and display of the signal.

Depending on the biorecognition element, the biosensor detector can be categorized into several categories namely catalytic (enzymes, organelles, tissues), affinity (antibody-antigen) and hybrid receptors (DNA). A range of physical and chemical transducers has been used to monitor these biological recognition events. It can be broadly classified into electrochemical, optical and mechanical devices (Fig. 1.1). The operation principle of the mechanical transducers (e.g. piezoelectric and MEMS) in biosensors is based on the change of mechanical property of the thin layer adhering to the transducer surface due to biorecognition reaction. The most popular piezoelectric transducer is the quartz crystal microbalance (commonly abbreviated QCM) where QCM oscillation frequency varies due to changes in the thickness of thin layers adhering to a the crystal surface as a result of a biorecognition reaction. With regard to the optical transducer, the surface plasmon resonance (SPR), internal reflection spectroscopy including total internal reflection fluorescence (TIRF) and ellipsometry (TIRE) methods are among the most widely reported techniques [3]. Electrochemical transducers represent may be the most widely exploited in biosensing group of transducers. They are based on the use biomodified electrodes, pore, particles where signal is provided by application one of the electrochemical

techniques e.g. voltammetry, galvanometry, impedance spectroscopy. The latter technique will be described in details later on.

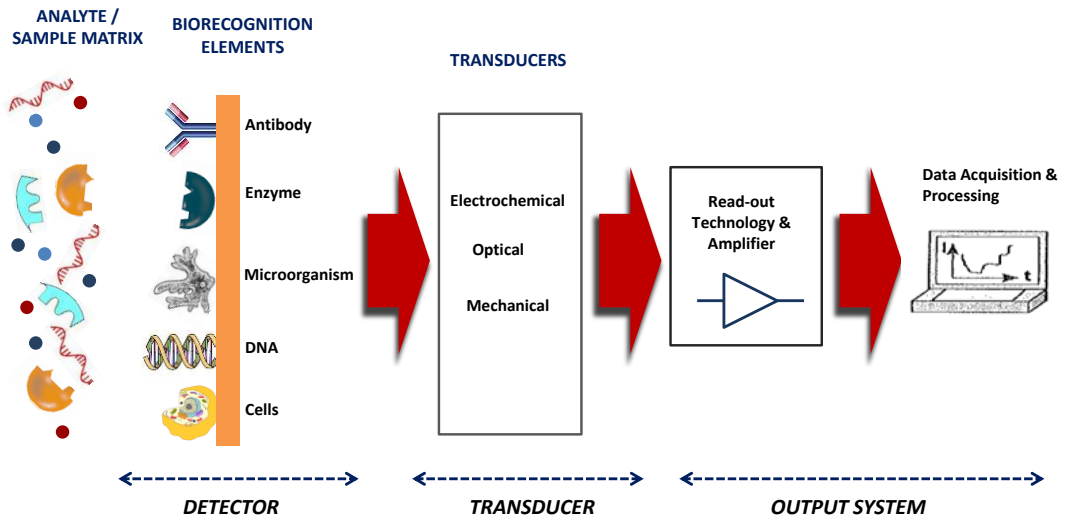


Figure 1.1: Schematic diagram of biosensor comprising three components: detector, transducer and output system.

In accordance with biosensor advancement over the last fifty years, the biosensors have been categorised into "first-generation", "second-generation" and "third-generation" biosensors [5].

(i) *"First-generation" biosensors* - the simplest approach of biosensor based on direct detection of either the increase of an enzymatically generated product (e.g. H_2O_2) or the decrease of a substrate (e.g. O_2) of the redox enzyme.

(ii) *"Second-generation" biosensors* - an artificial redox mediator is additionally introduced in the system (e.g. ferrocene) in order to achieve a biosensor operating at moderate redox potentials. The redox mediator should provide reversible electrochemistry, specificity for the selected electron transfer pathway, be stable in both oxidised and reduced forms; and produce no side reactions.

(iii) *"Third-generation" biosensors* - presenting a different approach in biosensor architecture involving immobilisation of a redox enzyme on electrode surface, allowing direct electron transfer between active site of enzyme and the transducer. The free-diffusing redox mediators are thus not necessary for these types of biosensors.

The critical features of the biosensor are the selectivity of the biodetector for the specific target analyte and the possibility to maintain this selectivity even in the presence of interfering species. The combination of these features together with miniaturization, low cost and essentially real-time measurements in a variety of applications has generated intense commercial interest. The major areas for biosensor applications include medical/clinical [6, 7], agriculture which include food pathogen and food safety testing [8-11], environment [12, 13] and defence [14], to name a few. The market potential for biosensor area is so vast that as reported in 2008 that $300 US million was spent on biosensor R&D per year [15] which generated market size of $563 million for food pathogen testing [16]. The miniaturization of the whole biosensor system that provides a portable and in-situ measurements for on-site applications is indeed of a current trend in the biosensing research/market [10, 17].

Despite the plethora of biosensor developments nowadays, it is also important to emphasize the characteristics and qualities that construct a good biosensor. This has been elaborated by Borgmann and co-workers [5] and Grieshaber et al. [18]. In short, among the criteria that need to be addressed are the sensor sensitivity and limit of detection, linear concentration range, the selectivity and reliability, sample throughput as well as the reproducibility and storage stability [19].

1.1.1 Electrochemical Biosensors

Electrochemical biosensors, a subclass of chemical sensors, are defined by the International Union of Pure and Applied Chemistry (IUPAC) as *"a self-contained integrated device, which is capable of providing specific quantitative or semi-quantitative analytical information using a biological recognition element*

(biochemical receptor) which is retained in direct spatial contact with an electrochemical transduction element" [20]. Generally, an electrochemical biosensor is a biosensor with an electrochemical transducer (Fig. 1.2) which is also considered as chemically modified electrode (CME).

Among the transducers used in biosensors, the electrochemical devices seem to dominate the research field and have attracted considerable attention [21, 22]. The transducer that is being used in electrochemical biosensor usually refers to an electrode (ion-selective electrode, metal electrode, glass electrode, interdigitated electrode- to name a few); it transfers the signal from the binding of the recognition system to an electrical signal that is proportional to the analyte concentration. This signal is ultimately collected, amplified, filtered from noise, processed and displayed by the corresponding microelectronic hardware. The detection modes of electrochemical transduction are divided into several techniques.

The electrochemical reaction can either generate a measurable current (amperometric), a measurable potential or charge accumulation (potentiometric) or measurably alter the conductive properties of a medium (conductometric) between electrodes. The use of electrochemical impedance spectroscopy by monitoring both resistance and reactance in the biosensor is also becoming more popular [22].

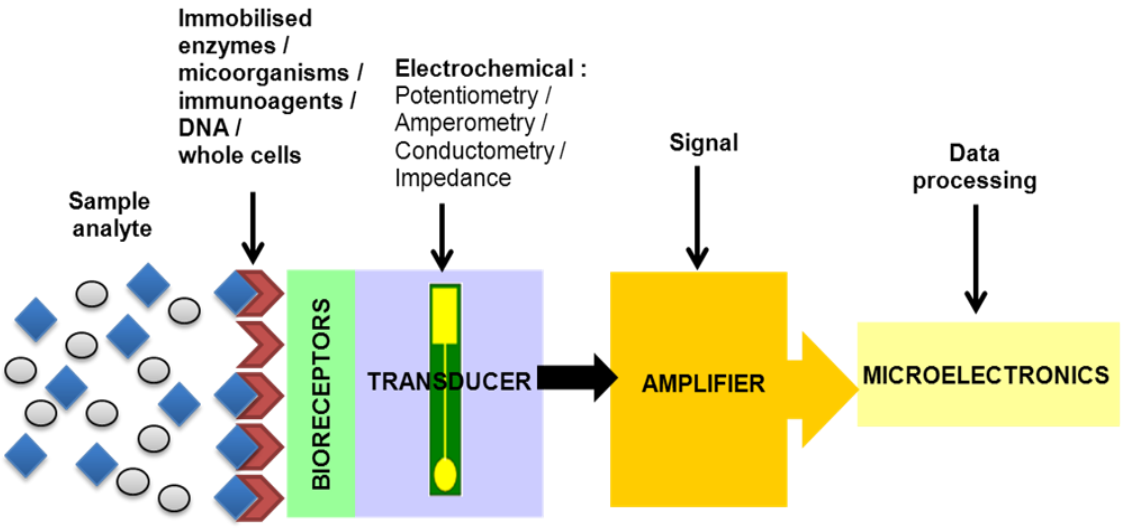


Figure 1.2: A schematic biosensor with electrochemical transducer (electrode).

Electrochemical detection for the transducer is the most favourable because of the low cost, ease of use, portability and simplicity of construction [23]. The high sensitivity, selectivity and ability of electrochemical biosensor to detect biomolecule interactions at low detection limits have resulted in vast application of this type of biosensors in various fields. These applications include medicine, food industry, environmental monitoring, food safety and agriculture which contain rapid detection of toxins, heavy metals, pesticides, insecticides, herbicides, antibiotics residues; besides having potential market for protein or DNA analysis of genetically modified (GM) food testing [8].

Electrochemical biosensors can be divided into two main categories based on the nature of the biological recognition process, namely biocatalytic sensors and affinity sensors [20, 23, 24].

Biocatalytic sensors: Biocatalytic sensors incorporate enzymes, whole cells or tissue slices that recognize the target analyte and produce electroactive species or some other detectable outcome. Among these three, enzyme is the most common and well-developed recognition system.

Affinity sensors: Affinity sensors use the selective and strong binding of biomolecules such as antibodies (Ab), membrane receptors or oligonucleotides, with a target analyte to produce a measurable electrical signal. The molecular recognition in affinity sensors is mainly determined by the complementary size and shape of the binding site to the analyte of interest. Due to the lack of electron transfer generated in affinity sensors' biomolecules, detection of electrochemical immunosensors is generally rely on the use of electroactive labels, usually based on enzyme labelling and amplification techniques.

In electrochemical biosensor, the transducer (electrode) size has advanced from macro dimensions (>100 μm) towards micrometer (<100 μm) and nanometer (<1 μm) size. Instead of using a single working active surface on the electrode, an array of electrode is produced on the working electrode. By utilising micro- and nanoelectrode arrays, voltammetric responses with higher current densities and considerably less background and capacitive currents is attainable [25]. It explains the heightened interest in using these transducers for biosensing in recent years. This

area of biosensing is novel and on the rise in recent decades due to the progress in microfabrication technology in producing micro- and nano- transducers [26].

1.1.2 Immobilisation of Biological Receptors

After selecting the desired transducer in a biosensor system, the next crucial part is to establish a biocompatible layer for the recognition of the analyte of interest. The interaction can also happen in a free solution system but normally the immobilisation of the biological receptors at the transducer is preferred. Immobilisation of biological elements on the transducer surface is important in designing the biorecognition part of the biosensor. This aspect is a key factor in developing efficient biosensors with good operability, high sensitivity and selectivity, short response time and high reproducibility. The immobilised biomolecules have to be able to maintain their structure, their function and their biological activity after immobilisation and not to be easily desorbed (leached out) during the use of the biosensor.

The principal methods of immobilization include physical or chemical adsorption at a solid surface, covalent binding to a surface, entrapment within a membrane (e.g. polymer, sol-gel) and cross-linking between molecules [3, 18]. The immobilisation method employed will depend on a number of factors, but in general it needs to be compatible with the biomolecule being immobilised, the sensor surface or matrix on which immobilisation is to take place, and, ultimately, the end use of the sensor. Table 1.2 presents various immobilisation strategies with both their advantages and drawbacks.

Table 1.2 Immobilisation methods descriptions with their advantages and disadvantages (*B*=biomolecules). Taken and adapted from Ref. [3, 27].

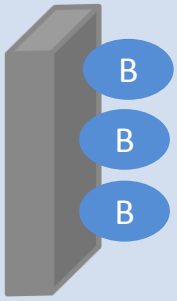
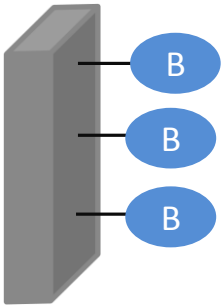
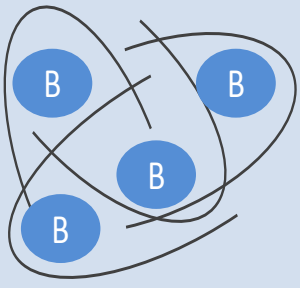
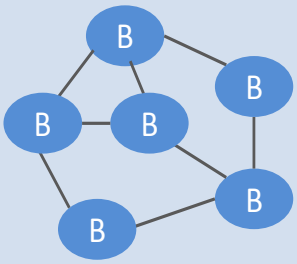
Immobilisation methods	Descriptions
Adsorption 	*Binding nature* : Weak bonds *Advantages*: • Simple and easy (can be performed in mild conditions) *Disadvantages*: • Desorption (poor stability)
Covalent binding 	*Binding nature:* Chemical binding between functional groups of the biomolecules and on the support *Advantages*: • No diffusion barrier, stable and short response time *Disadvantages*: • Matrix not regenerable, produce random and non-uniform protein orientation
Entrapment 	*Binding nature*: Incorporation of biomolecules within a gel or polymer *Advantages*: • Straightforward process and several types of biomolecules can be immobilised within the same polymer *Disadvantages*: • Diffusion barrier, biomolecules leakage and high concentrations of monomer and biomolecules needed for electropolymerization

Table 1.2 *(continued)*

Immobilisation methods	Descriptions
Cross-linking 	*Binding nature*: Bond between biomolecules /cross-linker (e.g. glutaraldehyde)/ inert molecule (e.g. bovine serum albumin) *Advantages*: • Strong and enhanced stability of the biomolecules *Disadvantages*: • Difficult to control the reaction, large diffusional barrier and decrease in activity of the biomolecules

In addition to these conventional methods, more recently the methods of Langmuir–Blodgett (LB) deposition, sol–gel entrapment [28] and electropolymerisation [29] have all been extensively used to immobilise biological components. The two latter techniques, together with other few, will be discussed further in Section 1.5.

Despite the aforementioned biomolecules immobilisation methods, their adaptation with different electrode materials alongside with the biorecognition elements for specific target is still a challenge particularly when dealing with micro- and nanoelectrodes in which their fabrication features (small size, recess, etc.) can create additional problems.

1.2 Electrochemical Techniques

Electrochemistry is the science that investigates chemical reactions and adsorption phenomena at an electrode-solution interface. Since electrochemistry is a surface technique, it offers certain advantages for detection in biosensors. For instance, the measurement does not depend strongly on the reaction volume whereby very small sample quantities can be used for its analysis [30]. Based on their operating principle, the electrochemical biosensors can employ potentiometric, amperometric

and impedimetric transducers converting the chemical information into a measurable signal [31]. Before discussing on the electrochemical techniques that can be employed in electrochemical biosensor, we first look into the fundamental concepts of electrochemistry.

1.2.1 Fundamental Concepts of Electrochemistry

Electrochemical Cells and Reaction

In electrochemical systems, the transport of charge occurs across the interface between an electronic conductor (an *electrode)* and an ionic conductor (an *electrolyte).* Charge is transported through the electrode by the movement of electrons. Typical electrode materials include solid metals (e.g., Pt, Au), liquid metals (Hg, amalgams), carbon (graphite), and semiconductors (indium-tin oxide, Si). In the electrolyte phase, charge is carried by the movement of ions. The most frequently used electrolytes are liquid solutions containing ionic species, such as, H^+, Na^+, Cl^-, in either water or a nonaqueous solvent [32].

Electrochemical cells can be divided into galvanic and electrolytic cells [32, 33] (Fig. 1.3). A galvanic cell produces electrical energy while electrolytic cell consumes electricity from an external source. The fuel cell is one of the examples of the commercial importance of galvanic cells. Electrolytic cells are frequently employed to carry out desired chemical reactions and its industrial applications include electrolytic syntheses, electrorefining and electroplating [32].

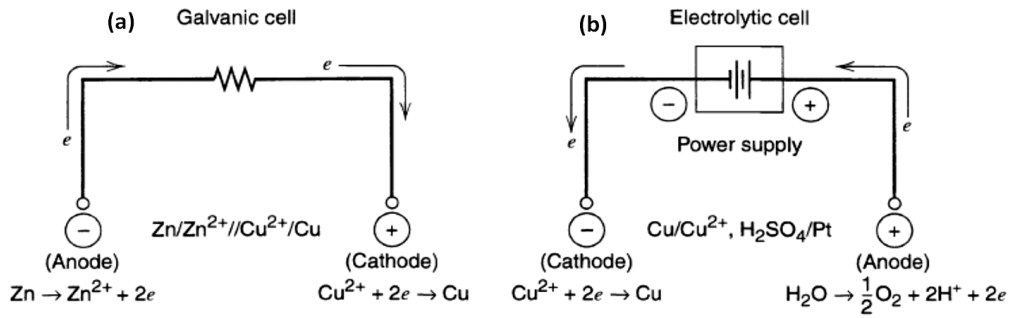


Figure 1.3: (a) Galvanic and (b) electrolytic cells. Taken from Ref [32].

An electrochemical reaction involves a transfer of charge via an electron or ion [32, 33]. A redox reaction implies the transfer of at least one electron from a chemical species to another one and induces the change of oxidation stage of the species. This reaction can occur through the application of an external voltage or through the natural release of chemical energy. Redox reaction involves oxidation, where the species loses electrons, and reduction, where it gains electrons:

Reduction: Oxidant + e^- ⟶ Product

Oxidation: Reductant ⟶ Product + e-

In electrochemical cells, the electrode at which reductions occur is referred as the *cathode*, and the electrode at which oxidations occur is the *anode.* A current in which electrons cross the interface from the electrode to a species in solution is a *cathodic current,* while electrons flow from a solution species into the electrode is an *anodic current.* In an electrolytic cell, the cathode is negative with respect to the anode; but in a galvanic cell, the cathode is positive with respect to the anode.

Faradaic and Non-Faradaic Process

In an electrochemical cell, two types of processes can occur at the electrodes. If the process involves an electron transfer at the electrode-solution interface as mentioned earlier, it is referred as faradaic process. This redox reaction obeys Faraday's law (Eq. 1.1) which states that the quantity of reacted species is directly proportional to the quantity of electricity (electrical charge) passing through the cell.

$$Q = nNF \qquad \dots (Eq.\ 1.1)$$

where Q is the charge (in Coulombs, C), n is the number of electrons involved in the reaction, N is the number of moles (in mol) and F is the Faraday's constant (F=96485 C). Electrodes at which Faradaic process takes place are sometimes called charge-transfer electrodes.

Adsorption and desorption can also occur at the electrode-solution interface, known as non-faradaic processes. In this case, although charge does not cross the interface, external currents can flow when the potential, electrode area or solution composition changes. The electrode-solution interface acts as a capacitor when a non-faradaic

process occurs in an electrochemical cell, (Fig. 1.3). When a potential is applied to a capacitor, charges accumulate at the metal plates according to Eq. 1.2:

$$\frac{Q}{E} = C \qquad \ldots (Eq.\ 1.2)$$

where Q is the charge stored in the capacitor (in Coulombs, C), E is the potential across the capacitor (in volts, V) and C is the capacitance (in Farads, F). A current, called charging current, flows during this charging process.

Electrode/Solution Interface

The strong interactions between the molecules in solution and the electrode surface result in the formation of the electrical double layer [33, 34] and is characterised by a double layer capacitance [32]. The model of the double layer is shown in Fig. 1.4. The double layer model is thought to be made of several "layers" where the layer closest to the electrode, called the inner layer, contains solvent molecules and species that are specifically adsorbed. This inner layer is also called the compact, Helmholtz or Stern layer.

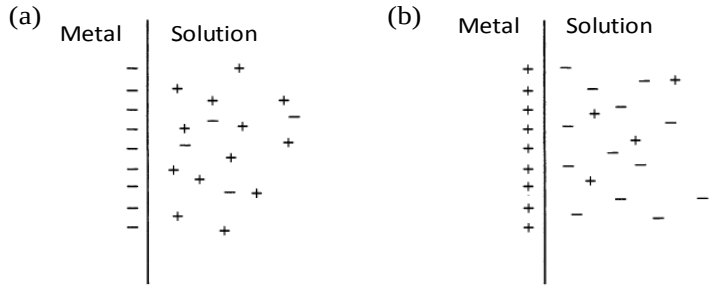


Figure 1.4: The metal-solution interface acts as a capacitor with a charge on the metal, (a) negative and (b) positive. Taken from Ref. [32].

The inner or Helmholtz layer itself is then divided into the Inner Helmholtz Plane (IHP) and the Outer Helmholtz Plane (OHP) as shown in Fig.1.5. Centres of the specifically adsorbed ions are in the IHP while solvated ions closest to the electrode

plane are in the OHP. The non-specifically adsorbed ions are spread in a diffuse layer, which is located between OHP and the bulk solution.

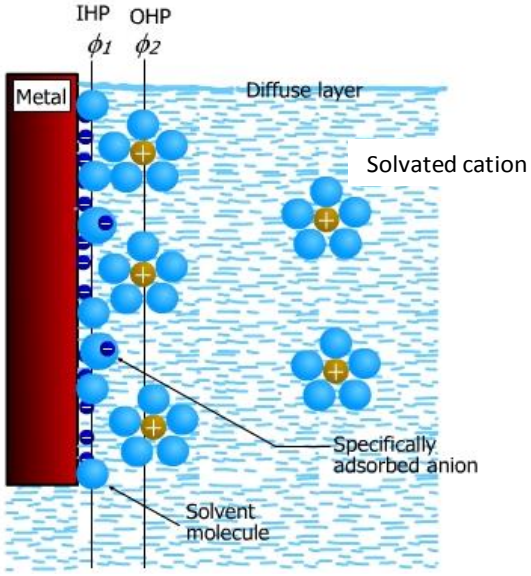


Figure 1.5: Electrical double layer model under conditions where anions are specifically adsorbed. Adapted from Ref. [32].

The thickness of the diffuse layer depends on the total ionic concentration in the solution. In most cases, the charging current generated by the double layer is negligible compared to the current generated by faradaic processes. However, at low concentrations of electroactive species, the charging current can be much larger than the faradaic current for the reduction or oxidation reaction.

Mass Transport-Controlled Reactions

Mass transfer is the movement of material from one location in solution to another. There are three modes of mass transport:

i) Diffusion

Diffusion can be defined as a spontaneous movement that is influenced by the concentration gradient, from high concentration regions to lower concentration regions [33, 34]. The rate of diffusion

is directly proportional to the slope of concentration gradient, as described by Fick's First Law (Equation 1.3):

$$j = -D\frac{\partial c}{\partial x} \qquad \ldots (Eq.1.3)$$

where j is the flux/mol $cm^{-2}s^{-1}$ corresponding to the number of moles passing through unit area in unit time, $\frac{\partial c}{\partial x}$ is the local concentration gradient at point x and D is the diffusion coefficient ($cm^2\ s^{-1}$), typically the magnitude of D lies in the range 10^{-6} -10^{-5} $cm^2\ s^{-1}$. As a rule of thumb, the bigger the molecule, the smaller the diffusion coefficient.

ii) Migration

Migration is the movement of the charged species along an electrical field. When a potential is applied to the electrodes, the interface becomes charged and any charged species near the interface will be attracted or repelled from it by electrostatic force [34].

iii) Convection

There are two forms of convection i.e. natural and forced. Natural convection occurs as a result of density gradients in solution causing a flow of material from the denser to the less dense region. Density gradients are also caused by localised thermal variations. Natural convection is generally irreproducible and undesirable in electrochemical experiments. Forced convection, on the other hand, is the deliberate stirring or agitation of the solution by mechanical means. It is often designed to be part of the experiment so as to dominate the mass transport in the system. Hydrodynamic voltammetry is one example based on controlled convective mass transport [35].

Taking the three modes of mass transport into account, the rate of mass transport is described by the Nernst-Planck equation (Eq. 1.4):

$$J(x) = \underbrace{-D\frac{\partial C(x)}{\partial x}}_{\text{diffusion}} \underbrace{-\frac{zF}{RT}DC\frac{\partial \phi(x)}{\partial x}}_{\text{migration}} + \underbrace{C\,v(x)}_{\text{convection}} \quad \ldots (Eq.\,1.4)$$

where $J(x)$ is the flux of species (mol s^{-1} cm^{-2}), D is the diffusion coefficient (cm^2 s^{-1}), $\partial C(x)/\partial x$ is the concentration gradient, z, F and C are the charge of the species, Faraday constant (96485 C) and concentration (mol cm^{-3}) respectively, R is the ideal gas constant (8.314 J K^{-1} mol^{-1}), T is the temperature (K), $\partial\phi(x)/\partial x$ is the potential gradient and $v(x)$ is the velocity (cm s^{-1}).

The three terms on the right-hand side represent the contributions of diffusion, migration, and convection to the flux respectively [32]. The equation becomes complex especially when all the three processes happen simultaneously. To simplify the situation during electroanalysis, a strong supporting electrolyte is added to the media and the solution remains unstirred so that the migration and convection processes can be considered negligible in comparison with the diffusion effect.

1.2.2 Amperometry and Voltammetry

Voltammetric and amperometric techniques are characterised by applying a potential to a working electrode versus a reference electrode and measuring the current. If current is measured at a constant potential as a function of time, it is referred to as *amperometry*. However, if the current is measured during controlled variations of the potential, then this is referred to as *voltammetry* [36]. Voltammetric methods include linear sweep voltammetry, cyclic voltammetry, hydrodynamic voltammetry, differential pulse voltammetry, square-wave voltammetry, ac voltammetry, polarography and stripping voltammetry. These methods provide a wide dynamic range, and are useful for low level quantification [23]. Of all these techniques, cyclic

voltammetry (commonly abbreviated as CV) is one of the most widely used method in providing information regarding the redox potential and electrochemical reaction rates of analyte solutions.

Voltammetry and amperometry techniques are usually performed with a Pt-, Au- or C- based working electrode or an array of electrodes with respect to a reference electrode, which may also serve as the auxiliary electrode, if currents are low (10^{-9} to 10^{-6} A). The resulting current is directly correlated to the bulk concentration of the electroactive species [20]. Amperometric detection is commonly used with biocatalaytic and affinity sensors because of its simplicity and low limit of detection. Although not all protein analytes in these classes of biosensors are intrinsically capable to serve as redox partners in electrochemical reactions and thus require mediators for the electrochemical reaction, amperometric devices is still favoured and their sensitivity is often superior in comparison to potentiometric devices [24, 36].

Cyclic Voltammetry

Cyclic voltammetry (CV) is the most widely used technique to investigate an electrochemical system. Besides indicating the degree of reversibility of an electrochemical process, it also provides information about kinetics of a reaction. The CV experiment involves applying a potential to the working electrode which changes with time as shown in Fig. 1.6. The experiment records the current flowing through the working electrode (WE) as a function of the applied potential and a plot of current versus potential is constructed, which is known as a 'voltammogram'. The potential of the working electrode starts at a value, E_1, and then swept in a linear manner to voltage, E_2. In this point, the direction of scan is reversed and the working electrode potential returned usually to its original value.

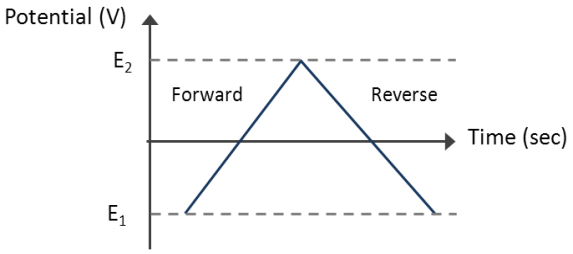


Figure 1.6: The potential waveform applied to the working electrode in the cyclic voltammetry experiment.

A typical cyclic voltammogram is shown in Fig. 1.7 exhibiting two asymmetric peaks (cathodic and anodic) with typical reversible electrochemical reaction. Information obtained and extracted from the CV i.e. the potential interval ($\Delta E_p = E_{pc} - E_{pa}$) and current peak ratio (i_{pc}/i_{pa}) could provide information regarding the reversibility of the redox model system [37] (Table 1.3).

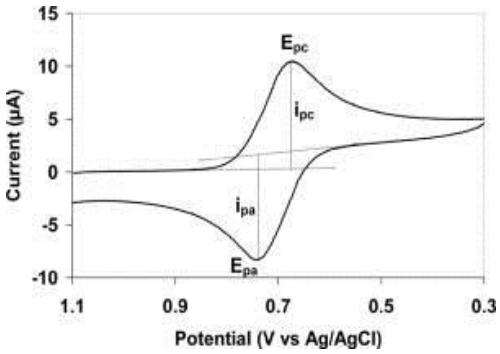


Figure 1.7: Typical cyclic voltammogram with peaks of reduction (E_{pc}), peaks of oxidation (E_{pa}), reduction current (i_{pc}) and oxidation current (i_{pa}).

The peak current can be plotted against the square-root of the scan rates. The Randles-Ševčík equation predicts that the peak current should be proportional to the square root of the scan rate (Eq. 1.5).

The Randles-Ševčík equation:

$$I_p = 2.69 \times 10^5 \times n^{3/2} \times A \cdot C \cdot D^{1/2} \cdot v^{\frac{1}{2}} \qquad \ldots (Eq. 1.5)$$

where n is the number of electrons involved in the reaction, A is the electrode surface area (cm^2), C is the bulk concentration (mol cm^{-3}), D is the diffusion coefficient ($cm^2\ s^{-1}$) and υ is the sweep rate ($V\ s^{-1}$).

The reversibility of the system is indicated by the ratio of i_{pa}/i_{pc} (a result of 1 indicates a reversible reaction) and the difference between peak potentials (ΔE_p). In a one-electron transfer redox reaction, the ΔE_p (in V) should be 0.059 at 25°C as follows from Eq. 1.6:

$$\Delta E_p = \frac{0.059}{n} \qquad \ldots (Eq.\ 1.6)$$

where n is the number of electron involved in the reaction. To sum up, Table 1.3 below gives the parameters for both reversible and quasi-reversible system. For a non-reversible system on the other hand, no peak is observed in the reverse scan.

Table 1.3 CV parameters for reversible and quasi-reversible systems

Parameters	Reversible	Quasi-reversible
$\boldsymbol{\Delta E_p}$	(59/n) mV independent of v	>(59/n) mV increases with v
$\boldsymbol{i_p}$	Proportional to $v^{1/2}$	Not proportional to $v^{1/2}$
$\boldsymbol{i_{pa}/i_{pc}}$	1	1

i_{pa}=current for anodic peak, i_{pc}=current for cathodic peak

1.2.3 Potentiometry

Potentiometry provides information about the ion activity in an electrochemical reaction [38] with no current flowing [18]. Common examples of potentiometry devices are the ion-selective electrode (ISE) and pH electrodes for ions such as K^+, Ca^{2+}, Na^+ and Cl^- [20, 22, 23]. Two reference electrodes are used to measure the potential across a membrane that selectively reacts with the charged ion of interest. This type of chemical sensors can be turned to biosensors by coating them with a biological element such as an enzyme that catalyzes a reaction which forms the ion that the underlying electrode is designed to sense [23].

For potentiometric measurements, the relationship between the concentration and the potential is governed by the Nernst equation (Eq. 1.7), where E_{cell} represents the observed cell potential at zero current. This is sometimes also referred to as the electromotive force or EMF. According to this equation, potential changes are logarithmically proportional to the specific ion activity.

$$EMF\ or\ E_{cell} = E^0_{cell} - \frac{RT}{nF} ln\, Q \qquad ....(Eq.1.7)$$

where E^0_{cell} is a constant potential contribution to the cell, *R* the universal gas constant, *T* the absolute temperature (in degrees Kelvin), n is the charge number of the electrode reaction, *F* is the Faraday constant and *Q* is the ratio of ion concentration at the anode to ion concentration at the cathode.

1.2.4 Conductometry

Conductometric detection monitors changes in the electrical conductivity of the sample solution/analyte (electrolyte solutions) or a medium (e.g. nanowires), as the composition of the medium changes during chemical reaction [23]. Conductometric can be considered as a subset of impedimetric devices [18]. The capacitance changes are measured using metal electrodes (mostly Au or Pt) [39] and in some cases, interdigitated microelectrodes are also employed [40, 41]. Conductometric biosensors is said to pose advantages over other types of transducers as they can be produced through inexpensive thin film standard technology, no reference electrode is needed and differential mode measurements allow cancellation of a lot of interferences [37]. This technique has been used as the detection mode in biosensors for environmental monitoring [42], clinical analysis and to detect foodborne pathogens [23]. The drawback of this technique however is that the high ionic strength of biological matrices makes it difficult to record the relatively small net conductivity changes caused by the signalling reaction [39].

1.2.5 Electrochemical Impedance Spectroscopy

Electrochemical Impedance Spectroscopy (EIS) that was initially used for the determination of the double layer is gaining interest and attention in recent years as a complementary technique for the characterisation of electrode processes at complex interfaces. It is becoming a powerful tool in electroanalysis as EIS analysis is able to provide information regarding electrode interface, its structure and the reactions taking place.

EIS is an alternating current method that describes the response of an electrochemical cell to a small amplitude sinusoidal voltage signal as a function of frequency. The resulting current sine wave differs in time (phase shift, φ) (Fig. 1.8) with respect to the perturbing (voltage) wave, and the ratio between the voltage and current is defined as the impedance (Z) [43]. EIS demonstrates the ability of a circuit to resist flow of electrical current and to store electrical energy, represented by the "real impedance" and "imaginary terms respectively" [44]. The most popular formats for evaluating electrochemical impedance data are the Nyquist and Bode plots.

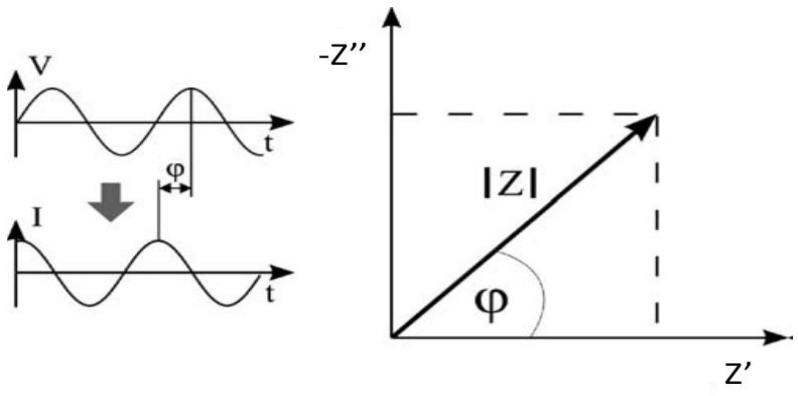


Figure 1.8: Impedance experiment: sinusoidal voltage input (*V*) at a single frequency (*f*) and current response (*I*). It can be expressed as the modulus |Z| and the phase angle φ, or it can be represented by the real (*Z*') and the imaginary (*Z*'') part. Taken from Ref. [45].

Nyquist Plot

In Nyquist plot, the impedance is usually expressed as a complex number, where the ohmic resistance is the real component (x-axis, Z') and the capacitive reaction (y-axis, $-Z''$) is the imaginary one. The shape of the Nyquist plot yields insights into possible conduction mechanisms or kinetic governing phenomena. For example, if the plot displays a perfect semicircle, the impedance response corresponds to a single activation-energy-controlled (or charge-transfer) process. A depressed semicircle indicates a more detailed model is required whilst multiple loops indicate that more than one time constant is required to describe a process [44]. The shape of the typical Nyquist plot may also include a semicircle followed by a straight line (Fig. 1.9a). The linear part observed at low frequency implies a mass-transfer limited process [46] whilst the semi-circle observed at high frequency indicates a charge-transfer limited process. The advantage of Nyquist plot representation is that it gives a quick overview of the data and a qualitative interpretation can be made from the plot. While plotting data in Nyquist format the real axis must be equal to the imaginary axis so as not to distort the shape of the curve. The shape of the curve is important in making qualitative interpretations of the data. However, the disadvantage of the Nyquist plot is that the frequency dimension of the data is not stated in the plot. This can be overcome by labelling the frequencies on the curve [47]. The Nyquist plot also makes the determination of low impedance values observed at very high frequencies very difficult.

Bode Plot

Another form of EIS data presentation is the Bode plot, which shows the phase angle (denote by φ) and the logarithm of the impedance magnitude as a function of the logarithm of frequency, *f*. Unlike Nyquist plots, Bode plots show frequency information and reveal an important low impedance behaviour seen at high frequencies. The slope of transition between low and high frequency asymptotes provide useful information regarding the nature of the impedance response. The popularity of the Bode plot representation is based on its utility in circuit analysis.

Phase-angle plots are sensitive to system parameters and therefore provide a good means of comparing the model to the experimental results.

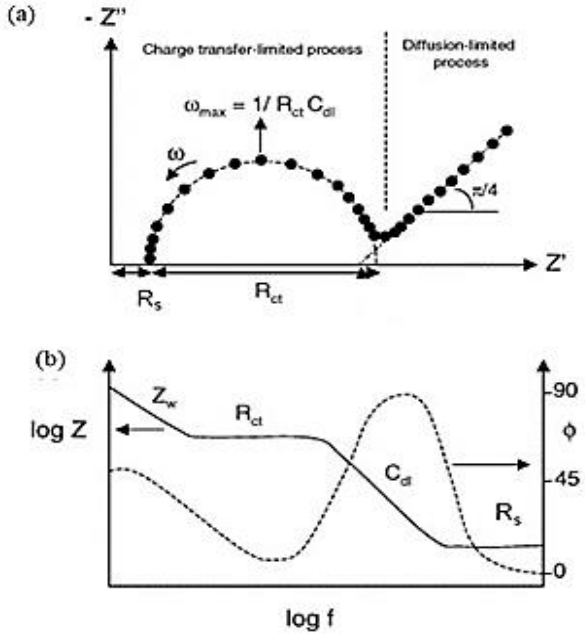


Figure 1.9: (a) Nyquist plot and (b) Bode plot; $\omega=2\pi f$ is angular frequency, R_s is solution resistance, R_{ct} is charge-transfer resistance, C_{dl} is double-layer capacitance and Z_w is infinite diffusion.

EIS technique is routinely used in the characterisation of coatings, batteries [48], fuel cells and corrosion phenomena. However, due to its ability to study any intrinsic material property or specific processes that could influence the conductivity, resistivity or capacitivity of an electrochemical system, this technique is gaining popularity in immunosensor as it offers label-free detection for antibody-antigen binding recognition [49, 50]. Several publications also have reported application of EIS in label-free DNA detection [51, 52]. In addition, EIS has found widespread applications in the field of characterisation of materials in the recent years. It has also been used extensively as a tool for investigating mechanisms in electro-deposition, electrodissolution, passivity, investigation of ion diffusion across membranes and in the study of semiconductor interfaces.

Equivalent Circuit Model

Impedance data is commonly analyzed by fitting it to an equivalent circuit model. Equivalent circuit models have long been used to simulate the interface impedance. This concept was first introduced by Warburg in 1899; he proposed that the electrode-liquid interface could be represented by a polarization resistance in series with a polarization capacitor [53]. Later, experimental findings revealed that the polarization capacitance exhibited a frequency dependency [54] which were simulated by a constant phase angle impedance of the interface capacitance. The equivalent circuit theory evolution continues until Randles came up with his renowned Randles model in 1947 [55].

The rule of thumb in developing an equivalent circuit model is that it should always be selected on the basis of understanding the electrochemical system and does not contain arbitrarily chosen circuit elements [56]. Producing the best fit between the model and experimental data does not necessarily mean that the developed equivalent circuit model has physical meaning.

As a basis, an equivalent circuit model is an integration of *passive elements* such as resistors (*R*), capacitors (*C*) and inductors (*L*) and *distributed elements* such as constant phase element (CPE) and Warburg impedance (Z_w). These elements can be combined in series and parallel to give complex equivalent circuits. Table 1.4 lists the common circuit elements, the equation for their current-voltage relationship and impedance.

Table 1.4 Ideal circuit elements used in the models

Component	Equivalent element	Current vs. Voltage	Impedance
Resistor	R (ohm)	$V = IR$	$Z_R = R$
	Notes: • Impedance of resistor is independent of frequency • No imaginary component		
Capacitor	C (F or ohm^{-1} s)	$I = C\, dV/dt$	$Z_C = \frac{1}{j\omega C}$
	Notes: • Impedance of capacitor decreases as the frequency raises • Has only imaginary component • Current through capacitor is phase-shifter -90° with respect to voltage • e.g. double layer capacitance (C_{dl}) and coating capacitance (C_c)		
Inductor	L (H, or ohm s)	$V = L\, dI/dt$	$Z_L = j\omega L$
	Notes: • Impedance of inductor increases with frequency • Has only imaginary component • Current through an inductor is phase-shifted +90° with respect to the voltage • Inductor gives a physical meaning of adsorption of reactants on surface which appears at low frequency and artefact that appears at high frequency		

Table 1.4 *(continued)*

Component	Equivalent element	Current vs. Voltage	Impedance
Infinite diffusion	Z_w (ohm)		$Z_{w=\frac{R_W}{\sqrt{j\omega}}}$
	Notes: • Warburg impedance was developed to model the diffusion of ionic species at the interface in electrochemical systems and also can be used to model semi-infinite linear diffusion • Characterized with a straight line with a slope of 45° in the Nyquist plot and phase angle of -45° in the Bode plot		
Constant Phase element (CPE)	Q (ohm^{-1} s$^{\alpha}$)		$Z_Q = \frac{1}{Q(j\omega)^{\propto \leq 1}}$
	Notes: • CPE exists when there is a lack of homogeneity involve (e.g. electrode's roughness) • For ideal electrodes equation reduces to infinite diffusion equation with α=0.5 thus Q is equal to $1/R_W$ • The double layer capacitance (C_{dl}) and coating capacitance (C_c) are also very often modelled with a CPE • Characterized with a straight line with a slope of between 0 and 90° in the Nyquist plot and phase angle of between 0 and -90° in the Bode plot		

The inverse value of resistance is called conductance and for this reason some investigators name such systems as conductometric [31]. Here, several simple electrical circuits are presented.

i) Series R-C circuit

A series of R-C circuit model (Fig. 1.10) is usually modelled an ideally polarizable electrode (i.e. ideal capacitor) where no charge transfer (faradaic current) occurs across the solution-electrode boundary. This model is considered as an ideal behaviour circuit and the examples are the mercury electrode - supporting electrolyte solution and also can be used to model a metal with an undamaged high impedance coating [57].



Figure 1.10: Series R-C circuit.

ii) Parallel R-C circuit

The parallel RC circuit (Fig. 1.11) is generally of less interest compared to the series circuit. This is because the output voltage is equal to the input voltage and thus this circuit does not act as a filter on the input signal unless fed by a current source.

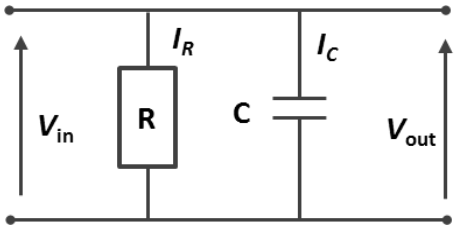


Figure 1.11: Parallel R-C circuit.

iii) RLC circuit

When an inductance element is added in the R-C series, this is then known as the RLC circuit (Fig. 1.12). The L element is represented by a loop symbol in a circuit as the inductors are usually constructed from coils of wire. This circuit is being used in

many different types of oscillator circuits. Another of its importance also is for tuning, such as in radio receivers or television sets, where they are used to select a narrow range of frequencies from the ambient radio waves. The circuit model with series of RLC also can be used to model the response of a supercapacitor.

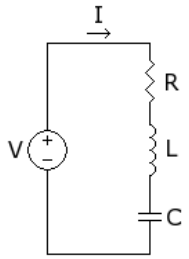


Figure 1.12: An RLS series circuit.

iv) Resistance serial with capacitance and resistance in parallel

This circuit includes a solution resistance, a double layer capacitor or a CPE and polarization resistance, also known as the 'three component' model (Fig. 1.13). It is used to model corrosion processes [58] and is often the starting point for other more complex models. The studies in electrode-electrolyte interface indicate that the respective model only valid in the absence of faradaic current where no diffusion prevails.

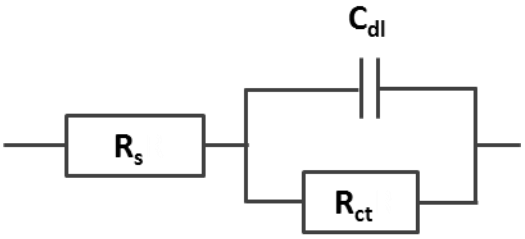


Figure 1.13: Series of R_s with parallel connection of R-C circuit.

v) Randles circuit (Mixed kinetic and diffusion control)

A Randles circuit is an equivalent electrical circuit that consists of an active electrolyte resistance, R_S, in series with the parallel combination of the double-layer capacitance, C_{dl}, and a faradaic reaction consists of an active charge transfer

resistance, *Rct*, and a specific electrochemical element of diffusion known as Warburg element, *W* (Fig. 1.14). Warburg impedance (Z_w) accounts for the diffusion of ions from bulk electrolyte to the electrode interface.

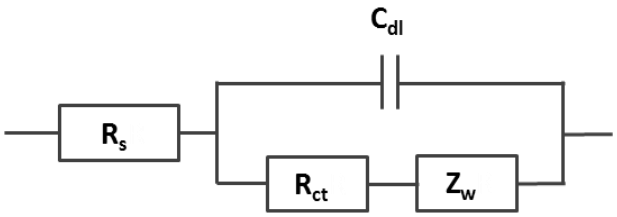


Figure 1.14: Randles circuit model.

This model can be used to describe electrode processes when both kinetics and diffusion are important. This circuit was initially proposed by Randles for modeling of interfacial electrochemical reactions in presence of semi-infinite linear diffusion of electroactive particles to flat electrodes. The Randles equivalent circuit is one of the simplest possible models describing processes at the electrochemical interface.

In real electrochemical systems, impedance spectra are usually more complex and some deviation from ideal behaviour can be observed. Under these circumstances, the Randles circuit may not give appropriate results. A two Randles circuits in series can be used for instance, to model the response of batteries as shown by Rodrigues and co-workers [48]. In the process of heterogeneous electron transfer, the nonuniformity of rough electrode surfaces (inhomogeneity, roughness, edge orientation and porosity) is frequently responsible for nonideality and frequency dispersions and resulting in the CPE behaviour. More detailed information regarding the EIS and equivalent circuit models can be found elsewhere [44, 59].

vi) Modified Randles circuit for microelectrode

The main difference between macro and micro electrodes relates to their different diffusion behaviour: macroelectrodes are associated with plane 1-D diffusion whereas microelectrodes are associated with cylindrical (2-D) and spherical (2-D) diffusions. The first can be modelled with Warburg impedance; the second required

more complex models. An analytical solution was found for diffusion impedance of microdisc electrode as well it was suggested modification of the Randles circuit to account these changes in the diffusion behaviour.

Gabrielli et al. (2006) proposed the following equivalent circuit model (Fig. 1.15) for a microelectrode in a thin-layer cell [60]. It was suggested that microelectrode in a thin-layer cell has two different types of diffusion profile at high and low frequency. Here, the Warburg impedance in the previous Randles circuit is replaced by Z_m that accounts for spherical diffusion at high frequency and Z_w that accounts for low-frequency contribution.

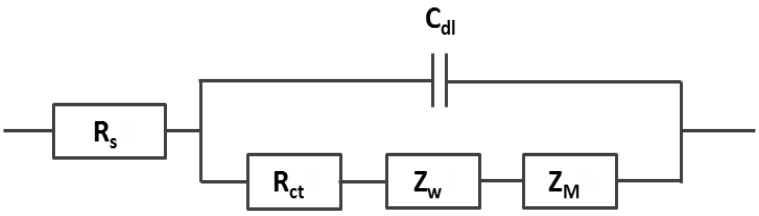


Figure 1.15: Equivalent circuit suggested for microelectrode.

1.3 Microelectrode and Nanoelectrode Array in Biosensing

Microelectrode arrays are gaining popularity in recent decades, particularly in electroanalytical chemistry. This comes from the fact that integration of micro- and nanoelectrodes into arrays allow retention of the microelectrode advantages which will be described below together with an increase of the total signal and signal to noise ratio. Historically, the greatest drive towards the early development of solid microelectrodes arose in the 1940s and 1950s when the need to measure oxygen concentrations in living biological organisms became of paramount importance [61] with the first tungsten microelectrode fabricated over 50 years ago by the 1981's Nobel Laureate David H. Hubel [62].

1.3.1 Microelectrode Definition

There are many definitions of dimensions for microelectrodes available, but IUPAC has generally outlined that a microelectrode has dimensions of tens of micrometers or less, down to submicrometer range [63] whilst nanoelectrode is defined as an electrode having dimensions on the order of a few tens of nanometers [64]. In comparison with these, the conventional 'macroelectrodes' electrodes have dimensions greater than 100 μm and commonly their dimensions are of the order of millimetres. There are also terms ultramictroelectrodes or abbreviated as UMEs which is also widely used in publications. The UMEs is referred to electrodes with length less than 20 μm [65]. However for this study, the terms micro- and nanoelectrodes are chosen and used to discuss the following topics.

1.3.2 Advantages of Microelectrodes

Among the characteristics/behaviours that distinguish microelectrodes from macroelectrodes are the following keys:

- *Non-planar diffusion* - Microelectrodes have faster rates of mass transport than macroelectrodes, facilitating the measurement of faster kinetics
- *Reduced capacitance* - The capacitance of the double layer is directly proportional to the area of the electrode

Due to their small sizes, microelectrodes offer a series of advantages compared with the conventional macroelectrodes. A major feature of microelectrode voltammetry is the ready access to near steady-state conditions (radial diffusion) where the influence of the ohmic (*iR*) drop is considerably reduced relative to that associated with the transient response (linear diffusion) [66]. As electrodes decrease in size, radial diffusion becomes dominant and results in faster mass transport. This high rate of mass transport (diffusion) at small electrodes enables measurement of kinetics by steady-state experiments rather than transient techniques. Microelectrodes provide an attractive alternative over macroelectrodes because they can produce a voltammetric response of similar magnitude to those macro counterparts, but with considerably less background and capacitive current [67].

The best known property of microelectrodes is their ability to generate steady-state current/voltage curves in quiescent solutions compared to macroelectrodes producing peak shapes voltammograms. Fletcher & Horne (1999) has compared the peak obtained from their random assemblies microdiscs (RAM™) with a 3 mm carbon macrodisc in a 10^{-3} M solution if potassium ferricyanide/ferrocyanide in 0.1 M potassium nitride [67]. It can be seen that the random assembly electrode produced a steady-state voltammogram whereas the carbon macrodisc produced a peak-shaped voltammogram (Fig. 1.16).

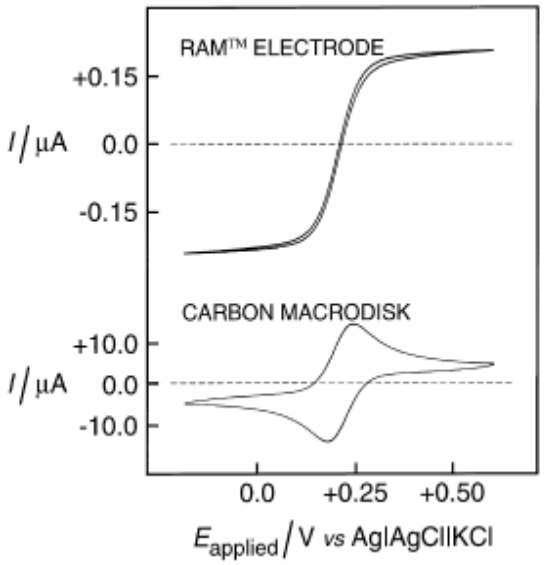


Figure 1.16: CV comparison for random assembly microelectrodes (RAM™) and carbon monodisc in 10^{-3} M $K_4Fe(CN)_6/K_3Fe(CN)_6$ in 0.1 M KNO_3. Scan rate 20 mV s^{-1}. Taken from [67].

1.3.3 Types of Microelectrodes and Their Electrochemical Behaviour

Various types of array electrodes have been made, and among the most common ones are planar (also known as *in-laid* electrode) or recessed microdisc electrode arrays, microband electrode arrays, interdigited microelectrode arrays (planar and vertical) and linear microelectrode arrays. The basic types of microelectrodes and their arrays as outlined by IUPAC [63] are shown in Fig. 1.17. According to Arrigan (2004), if collections of these electrodes are arranged in an ordered manner with a

controlled inter-electrode spacing, they are referred to as *arrays*; and if the collections are not so ordered and there is no specific control over the inter-electrode spacing, then they are referred to as *ensembles* [25].

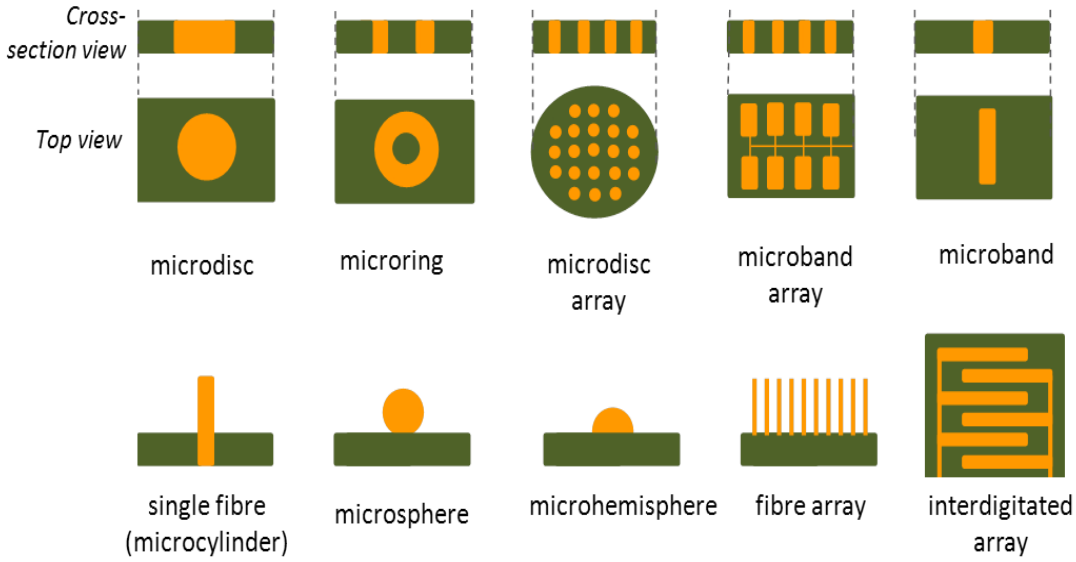


Figure 1.17: Most important geometries of microelectrodes and microelectrode array.

Of all these electrode geometries, Bond et al. [61] reported that microband electrodes and cylindrical symmetry electrodes do not attain true steady states. On the other hand, only three microelectrode geometries that attain true steady states- namely hemispheres, inlaid discs and rings.

Recessed electrodes, in comparison with inlaid electrodes are not flat electrodes. Recessed electrodes are electrodes that are located in a recess or gap (Fig. 1.18b) that can affect the diffusion of the species according to some theories, or not affect it according to other theories. Alden & Compton [68, 69] has focused on four types of non-ideal microelectrodes in their studies, namely:

- Elevated microelectrode (with conductive supporting sides)
- Recessed microelectrode (with insulating pit walls)
- A platform microelectrode (with insulating supporting sides); and
- Line microelectrode (Inlaid electrode)

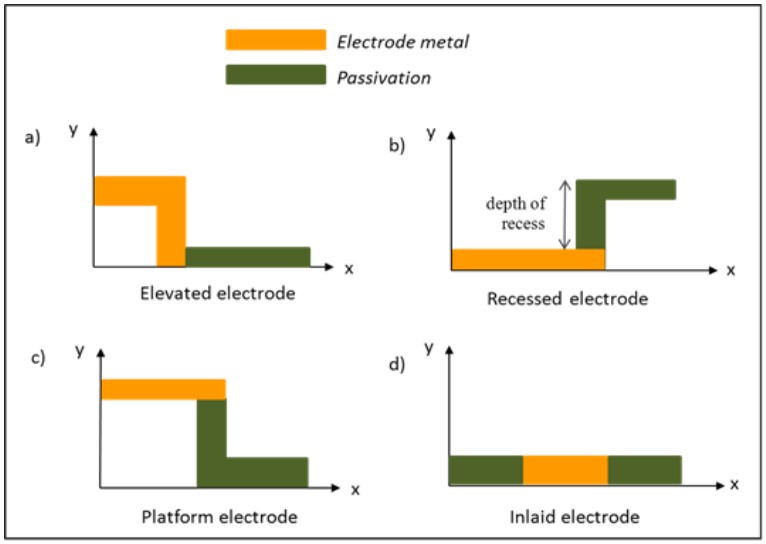


Figure 1.18: The geometries of the four non-ideal electrodes studied by Alden & Compton [69]: (a) elevated electrode; (b) recessed electrode; (c) platform electrode; and (d) line/inlaid electrode.

The electrochemical behavior of microelectrodes depends largely on its design. Depending on the aforementioned geometries, each microelectrode has their own diffusion patterns thus affecting the type of voltammetric response, and each has different limiting current equations (Fig. 1.19) [25].

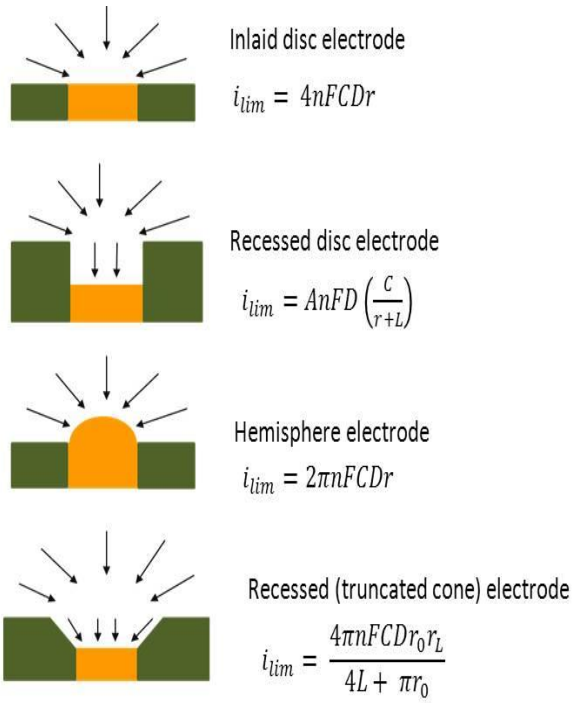


Figure 1.19: Diffusion modes and the equations of the micro- and nanoelectrodes for the corresponding steady-state current; where *n* is the number of electrons involved in the reaction, *F* is Faraday constant (96,485 C mol^{-1}), *C* is the bulk concentration of the redox-active species, *D* is diffusion coefficient, *r* is the disc radius (cm) and *L* is recess depth (cm).

1.3.4 Microelectrode Arrays Designs and Diffusion Profiles

It is interesting to note that single microelectrodes, in comparison with microelectrode arrays, have low current output which are more susceptible to interference [67, 70]. These, however, can be overcome by the fabrication of high-density arrays or ensembles.

The challenge in microelectrodes array design is to put maximum number of electrodes in an array on an available surface to reach maximum current. This task has to be done prudently as the spacing between each of the electrodes or the number density in the array is a crucial factor to ensure independent diffusion regimes to each of the electrodes in the array (Fig. 1.20). If this number of density is exceeded, capacitive, resistive and diffusive interferences may occur and there is a possibility

that the diffuse parts of their electrical double layers might overlap thus the whole assembly may behave as a single large electrode. The most widely reported designs of microelectrode arrays are either microdisc array or microband array.

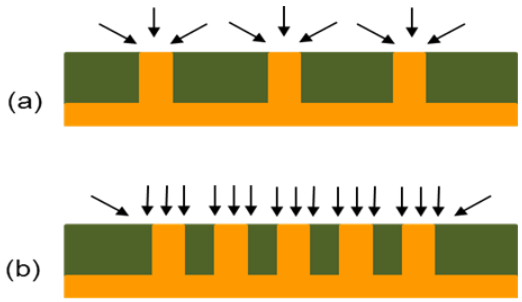


Figure 1.20: Diffusion profile for micro- and nanoelectrode arrays or ensembles. (a) individual diffusion regimes to each electrode of the array; (b) overlapping diffusion regimes

Microdisc Array

Microdisc electrode arrays retain all the advantages of individual microelectrodes, such as low capacitive currents and steady-state current [71]. The disc arrays are usually arranged in either hexagonal or a cubic manner (Fig. 1.21). Of this two, the hexagonal closed packed arrangement is favoured because of its high packing density of microdiscs within a given area [72].

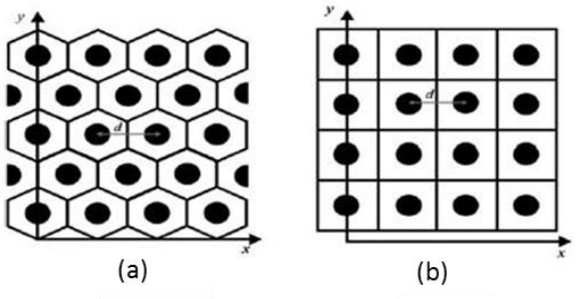


Figure 1.21: Regular arrangement of microdisc electrode array: (a) hexagonal; and (b) cubic. *d* is inter electrode distance.

Microband Array

Microband array also has becoming an interest in microelectrode array sensing application as its current responses are similar to the microhemicylinder electrodes and the currents at microband electrodes scale directly with the length [73]. The interdigitated microband arrays for instance, are often used in redox cycling experiments [74].

Based on the size and geometry of the microelectrodes array, Davies & Compton had outlined four categories of diffusion profiles [72], as illustrated in Fig. 1.22, and Table 1.5 summarizes the cyclic and linear sweep voltammetric characteristics associated with each category.

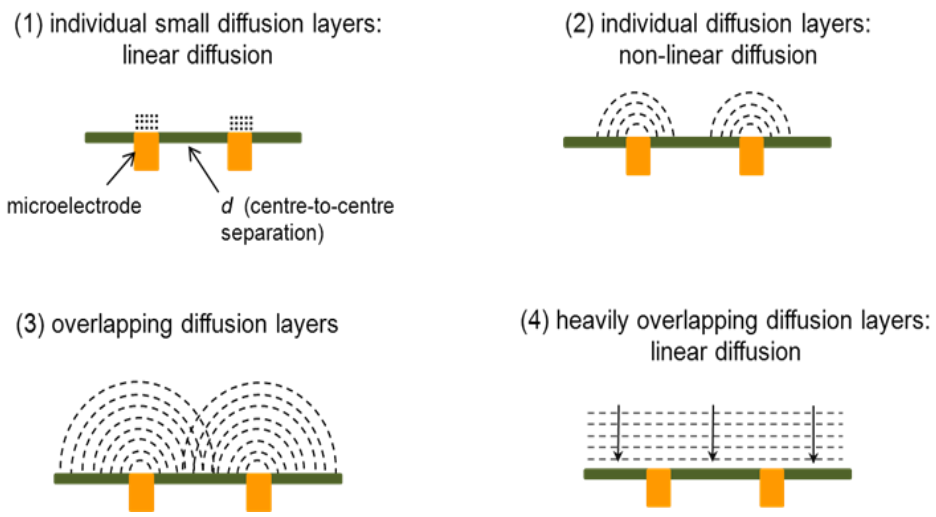


Figure 1.22: Schematic diagram of the four categories a diffusion profile may belong to for an array of microelectrodes.

Table 1.5 Linear sweep and cyclic voltammetry characteristics associated with the four categories in Fig. 1.22, where δ is the size of the diffusion zone, R_b is the microdisc radius, d is the centre-to-centre separation, I_p is the peak current, I_{lim} is the limiting current and v is the scan rate.

Property	**Category**			
	1	2	3	4
δ vs. R_b	$\delta < R_b$	$\delta > R_b$	$\delta > R_b$	$\delta > R_b$
δ vs. d	$\delta < d$	$\delta < d$	$\delta > d$	$\delta >> d$
Type of response	Clear peak, I_p	Steady state, I_{lim}	Slight peak to clear peak, I_p	Clear peak, I_p
Scan rate dependence	Yes	No	Yes	Yes
Current dependence	$I_p \propto v^{0.5}$	$I_{lim} \propto R_b$	-	$I_p \propto v^{0.5}$

1.3.5 Fabrication of Micro- and Nanoelectrodes

In terms of microelectrode arrays fabrication techniques, Huang et al. (2009) [75] has described mainly five techniques which include: i) assembly techniques (e.g. random assemblies of micro-wires [67]); ii) photolithography (thin film fabrication by the deposition of metallic film, namely Ag, Pt, Au and Ir, on Si_3N_4 or silicon oxides layer [76-78]); iii) screen-printing technique (for mass production and cheaper regular disc arrays [71]); iv) direct electrodeposition; and v) modification of the microelectrode array (molecular modification on the array surface, hydrophobic block, patterned electrodeposition, and pattern-based carbon nanotube/nanofiber microarrays). Apart from that, other techniques reported are the focused ion beam

milling for the fabrication of recessed nanoband electrodes [70] and nanopore array electrodes [79], reactive-ion etching [80] and CMOS [81].

Among all the techniques, the photolithographic techniques are a very convenient method to produce microdisc arrays with well-defined electrode dimensions and spacings and are a common approach to the fabrication of microdisc array [82, 83]. Besides that, they also are able for mass fabrication production at reasonable cost. Photolithography technique is described in detail in Section 1.4. Unfortunately photolithographic fabrication techniques generally produce arrays of microelectrodes which are recessed rather than inlaid and this ultimately leads to a slight reduction in the observed steady state current [82].

1.3.6 Micro- and Nanoelectrode Applications

Due to their small sizes and superior behaviors, microelectrodes have lend themselves well in *in vivo* measurements applications where only small sample volumes required and low depletion of target molecules [64]. Microelectrode arrays has created an opportunity for the integration of living, biological systems into lab-on-chip devices which are very important for both *in vitro* and *in vivo* biological applications such as enzyme-linked assays [84] and the detection of many other biomolecules. For instance, Parker et al. have investigated the application of gold microelectrode array based immunosensor for detecting aflatoxin M_1 in milk [11] and Moujahid et al. use microelectrode array to detect pollutants in seawater [85]. A nanoarray membrane sensor has been developed by a group of Singaporean researcher for sensing of water pollutants [86]. Another application of microelectrodes that have attracted researchers' interest is their ability to be used in resistive (organic solvent) media [66, 87-95] or in a two-electrode system, rather than the conventional three-electrode system configuration.

1.4 Microfabrication Techniques for Biosensor

Microfabrication of micro and nanoelectrode transducers refer to the fabrication of devices with at least some of their dimensions in the micrometer range [26]. These

terms are also occasionally referred as micromachining and micromanufacturing. Using tools originally developed for the silicon integrated circuit (IC) industry, people are now fabricating miniaturized transducers from silicon and other materials [4] to be used in various biosensor application such as environmental monitoring [96, 97], food safety [98]and medical [99]. The substrates used in microfabrication for biosensor application varied from silicon, glass, polymer and ceramics.

1.4.1 Substrate Materials

Silicon

Silicon is the most common material in microfabrication. It comes in a single-crystal wafer form (Fig. 1.23), with typical diameters of 75–200 mm and thicknesses of 0.25–1.0 mm. In addition to its excellent electrical properties, silicon also has outstanding mechanical properties, enabling the design of micromechanical structures [100]. It is also the most common substrate material for microfabricated chemical and biosensors. However for biological or medical microsystems, silicon may not be the material of choice as it is not optically transparent hence preventing the use of transmission microscopy besides the large cost for disposable devices purposes [101].

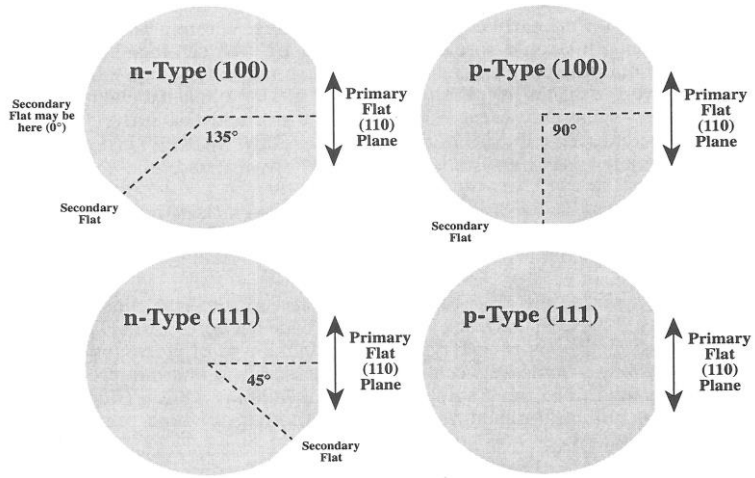


Figure 1.23: Types of silicon wafer. Wafers are typically marked with "flats" to indicate the orientation of certain crystal planes. Taken from Ref. [4].

Glass

The use of glass is less extensive compared to silicon in microfabrication, nevertheless glass exhibit attractive electrical and optical properties. Particularly glass has very high resistivity that decreases parasitic capacitance of the device. Since glass is transparent for visible light, it is particularly suited for devices with optical detection. Like silicon, glass is also supplied in wafer form and is available in different compositions (e.g., quartz, fused silica and borosilicate glass wafers). Another interesting features regarding glass substrate is that glasses are chemically inert and suitable for high-temperature applications. However the fragility of the glass may be posed difficulties in handling and dicing the wafers.

Other Materials

Apart from silicon and glass, polymers and ceramics are also employed as substrates in micromachining. Polymers particularly, are cheap and relatively easy to process. Disposable devices, such as microfluidic arrays or microstructured immuno or DNA assays, are often based on polymers (e.g. poly(dimethylsolixane) or PDMS) owing to its low cost production [102]. The PDMS use together with the SU8 resist is well-established materials for the microfluidics fabrication with soft lithography approach (e.g. micro-contact printing) [103, 104].Ceramics (e.g. alumina, Al_2O_3) also have been used extensively as substrate for hybrid microelectronics and are common in microelectronics packaging [105]. Unfortunately electrochemical transducers on polymer substrate still cannot be compared with those produced on silicon and glass. Ceramic transducers for instance are expensive, thus this type of the transducers are not widely used in biosensing.

This miniaturisation technology in fabricating electrochemical transducer (electrode) has advantages such as increasing the sensor performance and reliability with a reduced cost as devices are normally fabricated in large batches [4, 101, 105]. In the biosensor area particularly, microfabrication lends itself well as it produces small size devices that are suitable for biosensor system miniaturisation besides having high surface-area-to-volume ratios that are compatible for integration with electronics, high throughput, small sample volume needed and geometrical control of the devices. The disadvantages are on the other hand, is that the whole fabrication

process may consume long time, depending on the complexity of the system [101]. Table 1.6 below shows several examples of the microfabrication processes and how the techniques could be applied in the fabrication of the microchemical biosensors' components.

Table 1.6 Table of example processes used in microfabrication and their application in biosensor's component fabrication. Taken and adapted from Ref. [4] and [97].

Process Type	**Example**	**Application to biosensor's components**
Lithography	Photolithography, screen printing, electron-beam lithography, x-ray lithography	Electrode pattern, electrode layer pattern
Thin-Film Deposition	Chemical vapor deposition (CVD), plasma-enhanced chemical vapor deposition (PECVD), sputtering, evaporation, spin-on application, plasma spraying etc.	Insulation
Etching	Plasma etching, reactive-ion enhanced (RIE) etching, deep reactive ion etching (DRIE), wet chemical etching, electrochemical etching etc.	Container, flow cell, liquid junction, needle structure

The other two major types of processing terms are *subtractive* and *additive*. Subtractive process refers to processes such as etching, laser machining, mechanical milling etc.; while additive refers to deposition of dielectrics, metals etc. Basic microfabrication techniques used in IC fabrication is shown in Fig. 1.24. A thin layer, such as an insulating silicon dioxide film, is deposited on a substrate. A light-sensitive photoresist layer is then deposited on top and patterned using photolithography. Finally, the pattern is transferred from the photoresist layer to the

silicon dioxide layer by an etching process. After removing the remaining photoresist, the next layer is deposited and structured. Doping of a semiconductor material by ion implantation can be done directly after photolithography or after patterning an implantation mask (e.g., a patterned (sacrificial) silicon dioxide layer).

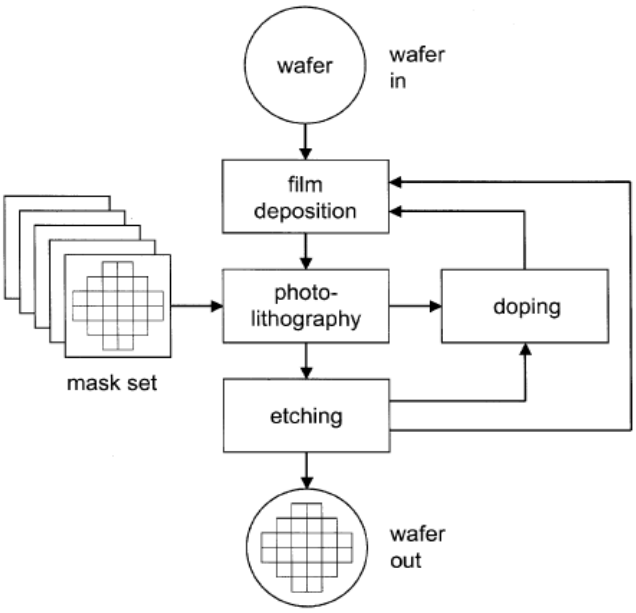


Figure 1.24: Flow diagram of an IC fabrication process using the four basic microfabrication techniques: deposition, photolithography, etching and doping. Taken from Ref. [105].

1.4.2 Photolithography

The most widely used form of lithography is photolithography. This is the most common technique in fabricating microelectrodes. Photolithographic techniques have made possible the fabrication of microelectrodes with controlled dimensions.

In photolithography, a pattern is transferred to a photosensitive polymer (a photoresist) by exposure to a light source (UV light) through an optical mask. The optical mask usually consists of opaque patterns (usually chrome or iron oxide) on a transparent support (usually quartz) used to define features on a wafer [103]. The photoresist can have either a positive or negative polarity (Fig. 1.25) and commonly applied to the substrate by spin coating. The photoresist thickness depends on the

photoresist's viscosity, the speed and time duration of the spin. Longer time duration will produce thinner photoresist layer. A common step before spinning on a resist with Si as a substrate is to grow a thin layer of oxide on the wafer surface by heating it between 900-1150°C in steam or in a humidified oxygen stream. Dry oxygen also can be employed but wet oxygen and steam produce faster results. The oxide can serve as a mask for a subsequent wet etch or boron implant [26].

The UV light exposure changes the photoresist's chemical resistance to the developer solution. The photoresist is developed in wet chemicals in order to remove the soluble parts to form the desired pattern and then baked to drive off the excess solvent. The pattern in the photoresist is then transferred to the underlying substrate by subtractive (etching) or additive (deposition) techniques.

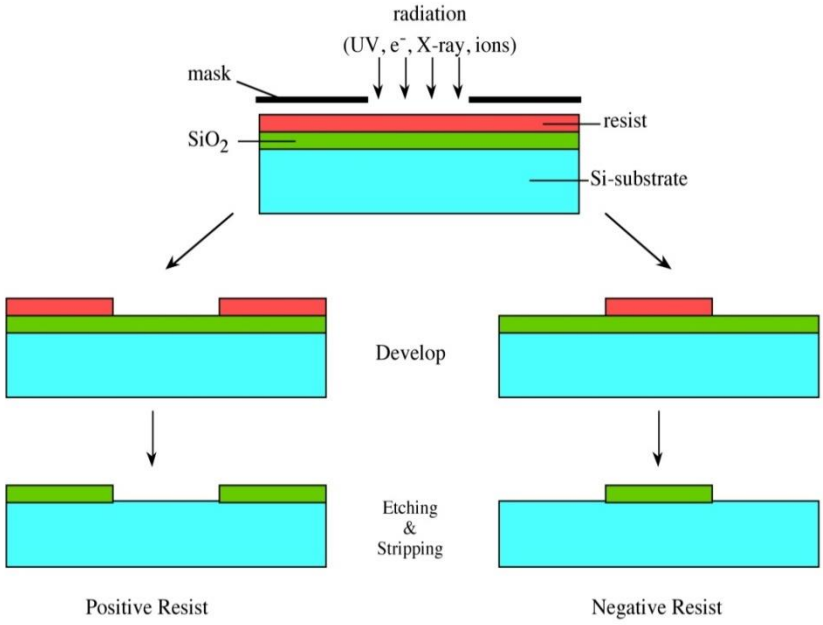


Figure 1.25: The photolithography process with negative and positive photoresist.

A good quality pattern requires careful control of the UV exposure and development conditions. If there is insufficient light energy reaching the photoresist, the chemical reaction is incomplete and thus the photoresist is not completely soluble or fully polymerised. In this case, called *under exposure*, the pattern is only partially developed and the corners and edges, which receive slightly less light than the centre of the pattern, are poorly defined at the end of the process. On the opposite, when too

much light energy reaches the photoresist and the chemical reaction spreads outside the bounds of the exposed area, *over exposure* could take place. This is partially due to chemical transport within the photoresist, but is mostly caused by stray light reaching the masked area. This effect results in poor definition of the pattern formed in subsequent processing. The effects of developing solution also should be considered whereby *underdeveloping* can lead to residual photoresist in an exposed area. Other parameters such as baking time and length of UV exposure also should be considered in order to have a well-defined pattern and accurate thickness [104].

1.4.3 Thin-Film Growth/Deposition

Thin films are used for a variety of different purposes in microstructures, such as for masking materials, structural materials, sacrificial materials or as electrical devices [101]. The most common films are outlined below:

Dielectrics

Dielectric layers, predominantly silicon dioxide (SiO_2) and silicon nitride (Si_3N_4), are used as insulating material, as mask material and for passivation. Thermal silicon dioxide is grown by placing a silicon substrate in a high-temperature (900–1200°C) oxidation furnace. Oxide growth by this approach is limited to ~1 μm because thicker layers take prohibitively long to grow. Thicker films (10–20 μm) can be obtained by chemical vapour deposition (CVD), however, they are not as robust as thermally grown oxide films. Silicon nitride layers, which are commonly used for device passivation, are deposited by CVD.

Silicon

Polycrystalline and amorphous silicon thin films, deposited by chemical-reaction-driven processes, are frequently used as structural materials in microsystems. Highly doped polycrystalline silicon (polysilicon) is used as gate material for MOSFETs, as electrode and resistor material, for piezoresistive sensing structures, as thermoelectric material and for thermistors. Polysilicon microstructures released by sacrificial layer etching are also widely used in sensor applications. Polysilicon is

usually deposited in a low pressure CVD (LPCVD) process using silane (SiH) as gaseous precursor.

Metals

Metal layers are used for electrical interconnects, as electrode material, for resistive temperature sensors (thermistors), or as mirror surfaces. It can also be a surface for self-assembled monolayers for biological application [102]. Metals, such as aluminum, titanium, and tungsten, are routinely deposited by sputtering or by electron-beam evaporation. Depending on the application, a large number of other metals, including gold, palladium, platinum, silver, or alloys, can be deposited with physical vapour deposition (PVD) methods.

Polymers

Polymers (e.g. plastic) can be used as compliant mechanical structures, as thick structural layers for molding, or as chemically sensitive films. Polyimides and photoresist are commonly deposited by spin- or spray-coating.

Biomolecules

Deposition and patterning of biomolecules, most commonly proteins, are rather important in biological applications of microfabrication. Three methods to accomplish this have been reported i.e. protein adsorption, biomolecular patterning via photochemistryand self-assembly monolayers [101].

1.4.4 Etching

Etching consists of removing material away from the defined patterns. Etching is categorised as a subtractive process; and can be divided into wet or dry etching. Either method can lead to isotropic or anisotropic etching. Isotropic etching etches in all directions equally; leading to mask undercutting and a rounded etch profile (Fig. 1.26). Anisotropic etching is one-directional and etching hits straight down to bottom. Dry etching is often anisotropic, resulting in a better pattern transfer.

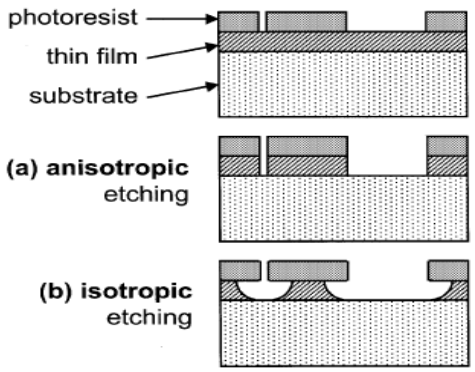


Figure 1.26: Schematic of anisotropic and isotropic thin-film etching. Taken from Ref. [105].

Wet Etching

Wet etching requires immersion of substrate in a solution containing chemicals which react with the material that it is not protected. The main advantages of wet etching are the low cost and high etching rate that provides better selectivity for the materials to be etched. The disadvantages of wet etching are the liquid chemical waste handling and contamination. Wet etching can be divided into three types:

i) Oxide etching - oxide is etched with hydrofluoric acid (HF) solution. HF dip is selective towards photoresist, nitride and silicon. It produces isotropic etching

ii) Nitride etching - phosphoric acid (H_3PO_4) is used in nitride etching. This is selective towards silicon and oxide; and produces isotropic etching

iii) Silicon etching - potassium hydroxide (KOH) is used. KOH is selective towards oxide and nitride with etching characteristics being dependent on silicon's crystal orientation.

Dry Etching

As the name implies, dry etching does not involve any wet chemical and instead it relies on glow discharge and ion beam. Fig. 1.27 is presented to give a clear layout on the dry etching techniques.

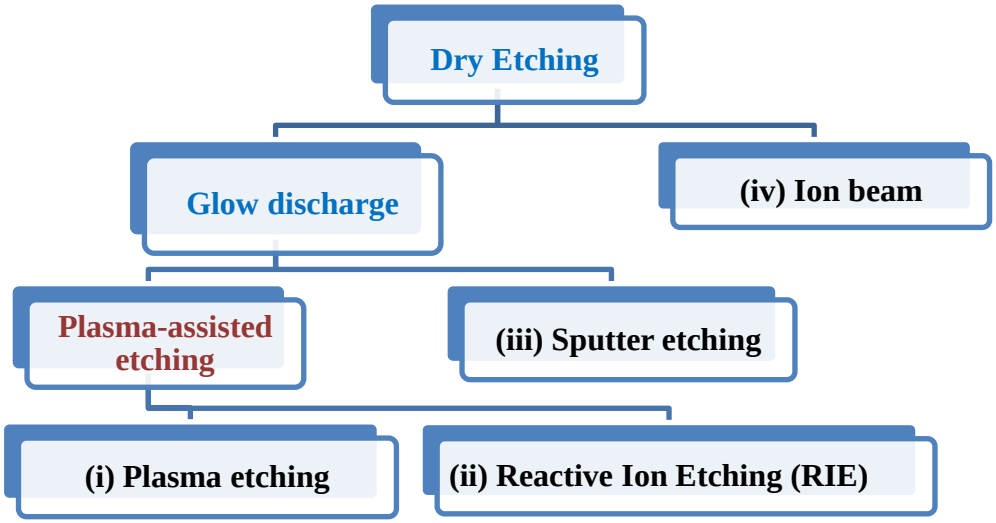


Figure 1.27: Dry etching techniques based on glow discharge (plasma) and ion beam.

i) Plasma etching – involves chemical reaction where reactive gas, fluorine (F) is used. Si will be removed and SiF_4 reaction product which is volatile will desorb from the surface. This chemical etching occurs in all directions and isotropic behaviours.

ii) Reactive ion etching (RIE) - consists of chemical and physical process. In an RIE system, reactive ions generated in plasma are accelerated toward the surface to be etched, thus providing directional etching (anisotropic) characteristics.

iii) Sputter etching - only physical action without any chemical reaction involved where an inert gas with high energy (Ar) is used. Ions being accelerated physically break atoms loose from the surface. Ions hit in straight direction and do not impact on the sidewalls hence exhibiting anisotropic characteristics.

iv) Ion beam - the ion beam etching (IBE) is a physical dry etch process. Ar ions are radiated onto the surface as an ion beam. The etching is anisotropic however the selectivity is low because there is no differentiation of the individual layers. Almost every material can be etched with this method. Due to the low selectivity and the low etch rate, this process is less favoured.

The comparison of the both wet and dry etching processes are summarized in Table 1.7. Based on the comparison, RIE exhibits the most superior etching results.

Table 1.7 Comparison between wet etching and dry etching (plasma etching, physical sputter and RIE)

	Wet etching	**Plasma etching**	**Physical sputter**	**RIE**
Critical dimension control	Not good (isotropic)	Not good (isotropic)	Good (aniosotropic)	Good (anisotropic)
Selectivity (etch rate)	Good	Good	Not good	Good
Throughput (amount of wafers processed in a given time)	Good	Good	Not good	Good

1.4.5 Electron-Beam Lithography

Electron-beam lithography (EBL) or commonly addressed as 'e-beam' is a lithography based on charged-particle beams. Another lithography technique in this class is the ion-beam lithography. In e-beam, the mask fabrication process is significantly simpler as it employs a *direct write system* or a software mask. In direct write systems, the computer-stored pattern is directly converted to address the writing particle beam, enabling the pattern to be exposed sequentially, point by point, over the whole wafer. E-beam lithography involves high current density in narrow electron beams whereby the smaller the beam sizes, the better the resolution but more time will be needed to write the pattern [26].

E-beam lithography is usually applied in the nanoscale lithography as it is a high-resolution patterning technique. In comparison with photolithography technique that

has line-widths of 2-3 μm visible photons, e-beam's line-widths are 0.1 μm. E-beam also exhibits several interesting and attractive features as opposed to photolithography, which include:

i) precise control of the energy and dose
ii) imaging of electrons to form a small point of <100 Å (photolithography produces spot of 5000 Å)
iii) no physical mask needed
iv) able to register accurately over small areas of a wafer
v) lower defect densities

In spite of such precision, among the disadvantages of e-beam lithography are:

i) fast electron scattering thus limiting the practical resolution to dimension greater than 10 nm
ii) involve apparatus that is more complex than photolithography as the charged particles (electrons) need to be held in vacuum instead
iii) slow exposure speed as an electron beam need to be scanned across entire wafer (e.g. 4 inch wafer requires approximately 1 hour for scanning)
iv) high system cost

Due to such limitations, e-beam technique is used only for specialised applications with small batches of customs ICs. Similar in photolithography, writing an e-beam also can be additive or subtractive.

More comprehensive reading and information on the microfabrication processes could be found in several textbooks [4, 26, 106].

1.5 Electrodes Biofunctionalisation

After selecting the desired transducer with the suitable electrochemical technique in biosensor system, the next crucial part is to establish a biocompatible layer responsible for the recognition of the analyte of interest. The interaction can also happen in a free solution system but normally the immobilisation of the biological

receptors at the transducer is preferred as this provide a more robust, stable and reproducible detection with lower detection limit. The principal methods of immobilisation mentioned previously in Section 1.1.2 could be employed but these conventional procedures have low reproducibility and poor spatially controlled deposition [107].

By deliberately attaching or treating the chemical reagent on an electrode surface, the surface would take on the chemical properties of the attached reagents hence providing a higher selectivity to the analyte of interest [108]. Electrodes biofunctionalisation can be achieved by monolayer adsorption (e.g. self-assembled monoloyer), covalent modification (e.g. functionalising the metal oxide surfaces with amine group and organosilanes [109]), polymer modification (e.g. redox/ conducting/ electroactive polymers coating) and composite formation [110].

The challenge of these biofunctionalised/modified electrodes is that they have to be durable enough and able to retain the activity of the biological receptors so that they do not denature easily and impair the chemical reaction activity. The successful applications of biofunctionalised electrodes in biosensor have been reported in various applications such as in environmental i.e. detection of formaldehyde [111], phenol [112] and pesticides [113, 114], to name a few.

1.5.1 Self-Assembled Monolayers

Self-assembled monolayer (SAMs) is one of the most widely employed and reported technique for surface biofunctionalisation. It has been used in electroanalytical chemistry for almost 20 years now as the basis of electrochemical sensors [115]. Self-assembly monolayers are monomolecular layers that could be formed spontaneously by immersing a solid substrate into a solution containing adsorbate of interest in the solution (Fig. 1.28). The most common studied SAMs are alkanethiols for metal surfaces and silanes to modify silica surface.

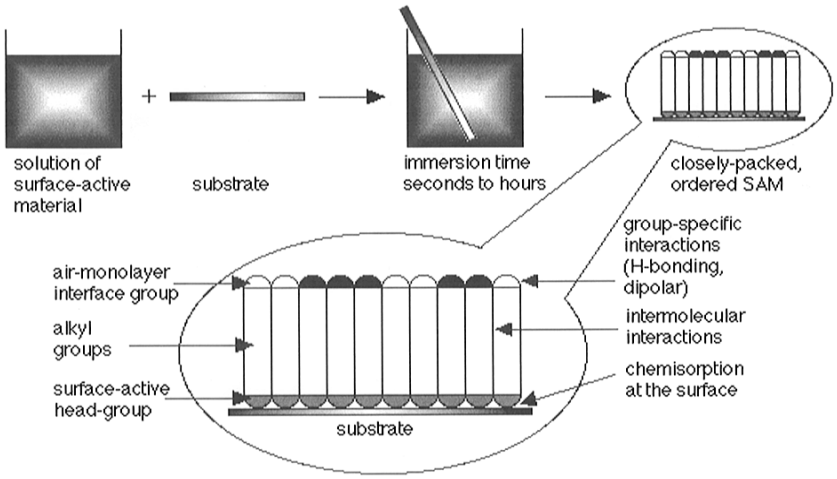


Figure 1.28: SAMs formation on a substrate by simple immersion into a solution containing surface-active material. Taken from Ref. [116].

Thiols Modified Electrodes

Thiols adsorb on electrode metal surfaces due to the high affinity between sulphur in the –SH terminal and the metal atom so forming a monolayer. The adsorption process is a fast one, involving cleavage of the S-H bond whereby it was implied that the sulfur atom of the thiols donates electron to the metal surface. This transfer of charge induces the proton of the SH group to hydrogen (Fig. 1.29). Such a mechanism has been confirmed by open-circuit potential (OCP) studies [117, 118]. It was found that thiol adsorption results in a drop of the OCP indicating that a negative charge is transferred from the thiol to the electrode surface.

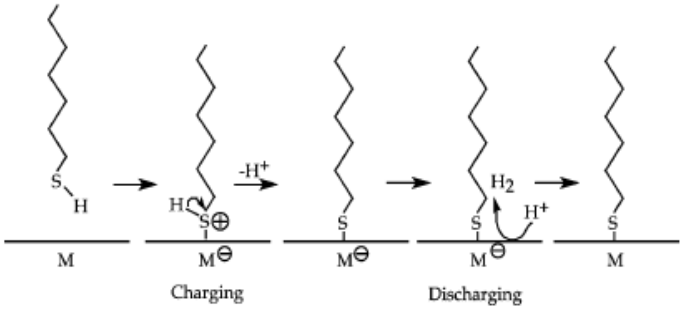


Figure 1.29: Proposed mechanism for the adsorption of thiols onto a metal surface. Taken from Ref. [117]

Thiols SAMs on electrodes are formed with a long alkyl chain (usually more than 8 CH_2 groups). When being left at longer hours, they are able to produce a highly ordered, orientated and packed structure. Long-chain alkanethiols has proven to form a very well ordered surface coverage with less defect and a higher electron transfer resistance [115, 119, 120]. The concentration of alkanethiols being used in SAMs formation normally vary from 1-10 mM, however SAM formation using a dilute solution gives ordered monolayers whereas a high concentration and longer time incubation (up to 6 days) favor multilayer formation [121]. A better formation of the SAMs could be formed by submerging the cleaned electrodes overnight in deaerated (N_2 purging) thiol solutions [122]. The use of mixed SAMs also has been reported, particularly in microelectrodes. For instance, Ionescu and co-workers (2011) have formed a mixed monolayer from 11-mercaptoundecanoic acid (11-MUA) and 2-mercaptoethanol (2-ME) with a ratio 1:5 on gold interdigitated electrodes as the use of 11-MUA alone leads to a dense monolayer. Thus by adding 2-ME, the short thiols act as spacers in monolayers and improve charge transfer at the working electrode [123].

In electrochemical biosensor detection, different functionalisations techniques are used to couple biological recognition elements. For example, carboxyl groups often serve for antibody immobilization; esters form amine couplings and biotin coupling can be used to bind streptavidin and further biotin functionalized biomolecules [124]. In electrochemical applications it is essential that the SAM allows electron or analyte diffusion. Although the most widely used electrode metals for thiol-based SAMs measurements are gold and silver, the formation of SAMs on other metals such as nickel, copper, palladium, mercury, platinum and ITO also have been investigated [125]. In fact, SAMs on palladium surface have been proven to work better for microcontact printing [126-128].

Electrodes biofunctionalisation for enzymes immobilisation (hence *enzyme elecrodes*) with SAMs techniques as models for glucose biosensor detection have been demonstrated by numerous researchers such as Creager & Olsen (1995) [129], Riklin & Willner (1995) [130], Jiang & co-workers (1995) [131] and Rubin & co-workers (1996) [132]. The application of SAMs for the immobilisation of

cytochrome C [133], DNA [134-136] and antibodies [122, 137] were also reported successful.

The simplest and effective method to monitor the structure and composition of monolayer is contact angle measurement [138]. In order to assess the rate of electron transfer of redox-activated SAMs on the other hand, various electrochemical methods are employed namely cyclic voltammetry, AC voltammetry, chronoamperometry [125] and recently the electrochemical impedance spectroscopy technique are the most favorable [139].

Silanes Modified Electrodes

Another approach of SAM in hydroxyl-terminated surfaces (e.g. glass and oxidized silicon wafers) is the organosilane. The most profound organosilane used in surface modification is the (aminopropy1)-triethoxysilane (abbreviated as APTES) (Fig. 1.30). Its diverse applications include the field of organic chemistry (silica surfaces treated with this aminosilane are used as catalysts), analytical chemistry area (HPLC separation) [140] and biological chemistry. With regard to the latter, silica/metallic/polymeric substrates treated with APTES have been utilized for the immobilization of biomolecules such as enzymes, antibodies and DNA [140, 141] for the development of microarray and lab-on-chip [142].

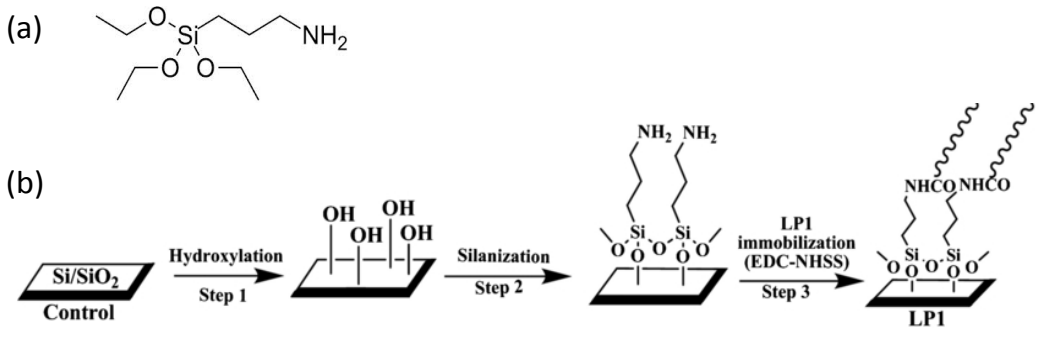


Figure 1.30: (a) Chemical structure of APTES (b) A schematic representation of the functionalization of silicon surfaces and immobilisation of peptides (LP1) using APTES with the aid of EDC-NHS cross-linker. Taken from [143].

Although initially intended on silica surface, the use of APTES has been ventured on gold electrode surface in biosensor application and proven successful in immobilizing antibodies [98, 144].

1.5.2 Conducting Electroactive Polymers

Various types of polymers have been employed in immobilization procedures which include hydrogel polymers comprising acrylate or poly (ethylene glycol) films [145-147] and electrogenerated polymer (also known as conducting electroactive polymers) [29, 148]. The major advantage of the latter polymer film is that electrochemical deposition allows precise and controllable formation of the polymer coating over the electrode surface. Unlike SAM, which is bounded only to gold electrode surface, the electrochemical formation of both conducting and non-conducting polymers can be performed over a wider range of electrode materials (platinum, gold, glassy carbon, ITO, etc.) and the electrogenerated polymers are stable in organic solvents. Due to the low cost and its easy production, electrogenerated polymer films are favourable for the modification of the transduction part in the electrochemical biosensors and biochips design.

Polyaniline, polypyrrole, polythiophene, polyphenol and polyacetylene are among the conducting polymers used in biosensor for biomolecule immobilisation (Fig. 1.31). Polypyrroles are formed under mildly oxidatives conditions from aqueous media. The mild conditions used for polymerisations are thus ideal for the immobilisation most of the biological elements from enzymes to whole living cells. Polyanilines can be formed under similar conditions require the addition of acid whereas polythiophenes require a more extensive oxidation potential while the monomers are not soluble in water.

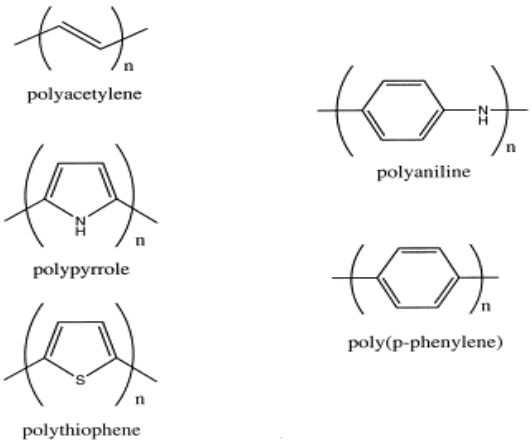


Figure 1.31: Structures of electrogenerated polymer films used for biomolecule immobilisation.

The most widely reported immobilisation procedure for the biological elements on the conducting polymers is via the entrapment or attachment to the electrochemically polymerized films [107]. The polymer formation is carried out by controlled potential electrolysis of an aqueous solution containing monomers and biomolecules. In this particular procedure, polypyrrole is the most favourable polymer film owing to its applications' versatility and stability. Biomolecules entrapment in polypyrrole also has been applied to a single microelectrode [149, 150]. Various enzymes [107, 151, 152], coenzymes [150], antibodies [153-155] and cells [156] have been successfully entrapped on conducting polymers. Several efforts also have been reported in improving the biocompatibility property of the electrogenerated polymers in order to preserve the structure of the immobilised protein thus retaining its biological activity. As the nature of the organic polymers is hydrophobic, hydrophilic additives can be added or by introducing functional groups within these films to preserve the hydration layer of proteins into the polymer chains.

Biomolecules also can be immobilised on the electrogenerated polymers via chemical linkage. This is achieved by electropolymerisation of functionalised biomolecules or chemical grafting of biomolecules on the film. This particular method would suit the DNA or oligonucleotides immobilisation the most as this approach provide a better access to the immobilized biomolecules and facilitates macromolecular interactions. The immobilisation of anti-West Nile Virus antibody

also has been successfully reported by photochemical grafting the bacteriophage on the copolymer [157].

For biomolecules that require specific orientation, a regioselective grafting of the biomolecule attachment by affinity interactions with functionalized polymers films can be conducted. The protein affinity binding at functionalized polymeric films can be achieved by employing transition metal (namely Ni, Cu) and nitrilotriacetic acid (NTA) ligand complex prior immobilising the histidine-tagged enzymes or proteins for biosensor detection (Fig. 1.32) [158]. The biotinylated polymer films using avidin-biotin linkage strategy also presents a variety of specific advantages over other immobilization techniques. The avidin-biotin immobilisation method able to maintain biomolecule activity more successfully than other regularly used methods due to the specific and high-affinity interaction. The drawback of both chemical grafting or by affinity of the biomolecule at the functional group, however is that the amount of immobilized biomolecules is restricted to a monolayer at the interface polymer-solution. Such limitation hence hindered its further application in micro- and nanoelectrodes. Another major drawback from the conducting electroactive polymers approach on microfabricated electrode array as highlighted by Wallace and co-workers (1995) is that it induces the lifting of the insulating photoresist layer hence destructing the metal layer of the working electrode [148].

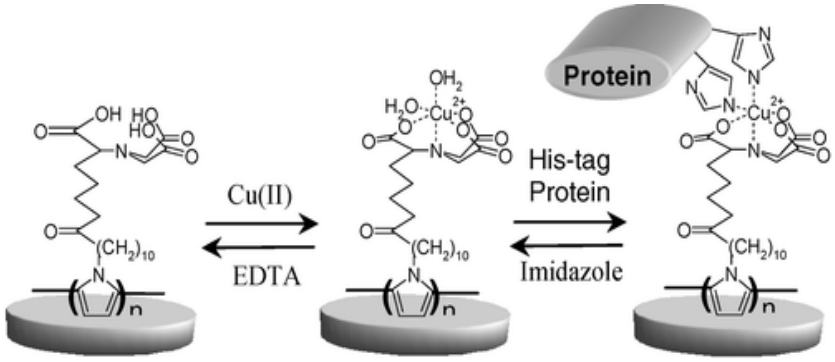


Figure 1.32: Schematic representation of the reversible immobilization of histidine-tagged biomolecules to an electrogenerated poly(pyrrole)-NTA film on a 5 mm Pt electrode as carried out by Cosnier and co-workers [158].

1.5.3 Sol-gel Silica Films

Among any other chemically modified electrodes, silica-modified electrodes, particularly sol-gel are gaining increasing attention. The reasons behind this include the compatibility of the precursors to be activated at room temperature and the ability of sol-gel to encapsulate or immobilise enzymes of interest without impairing their activities [28]. Braun et al. were the first ones to report about successful enzyme entrapment in a sol-gel matrix [159]. Since then, sol-gel encapsulation has opened up a new way to immobilize an array of biological materials including catalytic antibodies, DNA, RNA, antigens, live bacterial, fungal, plant and animal cells and even whole protozoa [160] and been widely reported in biosensor [161-164]

Sol-gel material is formed via partial or complete hydrolysis of a suitable precursor, usually silanes, mixed with biomolecules, followed by the gelation and aging steps. Aging strengthens the network and the drying process simultaneously leads to shrinkage. The strategies to confine the nonconductive silica-based materials on electrode surfaces were mostly directed to either the preparation of bulk composite carbon electrodes (powdered materials dispersed in carbon paste or sol-gel derived ceramic-carbon composites) or their deposition as thin films on solid electrode substrates. The latter approach is a straightforward film formation, achieved by spin-coating or dip-coating and produced film thickness varying between 100 nm to a few microns. However the disadvantage of this technique is that it can be applied to a flat surface and the films are deposited unselectively on both conducting and insulating parts of the substrate/electrode [165].

Under this circumstance, the novel sol-gel electrodeposition approach lends itself well in forming the sol-gel film selectively on the desired surface (working electrode) without smearing the edges or insulating parts. In comparison with the conventional dip-coat sol-gel fabrication technique, electrodeposited or electro-assisted self-assembled (EASA) of sol-gels offers more tunable and controlled sol-gel deposition on an electrode surface. By applying galvanostatic conditions and varying the deposition time, thickness of the films can be accurately controlled and problems with overpotential can be eliminated [166].

1.5.4 Electrodes Functionalised with Carbon Materials

Carbon nanomaterials have attracted considerable attention in electrochemical biosensors owing to their outstanding physical properties and remarkable conductivities [167]. Carbon nanotube modified electrodes (CNTs) for instance, have advantages in terms of their high surface area, mechanical strength, excellent electrical conductivity and good chemical stability. They are especially interesting because enzymes can be entrapped in the inner cavity. Single-walled carbon nanotubes (SWCNT) functionalised with biotin for the immobilisation of glucose oxidase has been carried out on microelectrode array on a silicon chip [168].

When mentioning CNT and carbon allotropes, it would be fair as well to include graphene (Fig. 1.33). Since the graphene breakthrough by a group of Manchester researcher headed by Andre Geim back in 2004 [169], there has been a booming interest in graphene research area. These include graphene synthesis and the challenge to produce them in large quantity scale with nanosheets diameter size. Graphene is favoured over carbon nanotubes as it can be obtained easily by chemical conversion of the inexpensive graphite and for its outstanding electrical and mechanical properties [170]. This unique nanostructure material has high surface area, excellent electrical conductivity and carbon mobility at room temperature, robust mechanical properties and flexibility. Its vast application includes optoelectronic devices, supercapacitors, gas sensors, pH sensors, chemical sensors, biosensors and nanocomposites.

In electrochemical biosensors, graphene modified electrodes (mostly with glassy carbon electrodes) have been successfully applied to sense some biological and organic molecules such as DNA [172, 173], glucose oxidase [174, 175], IgG [176, 177], NADH, hydrogen peroxide, paracetamol [178], dopamine [179], ascorbic acid and serotonin hormone, to name a few.

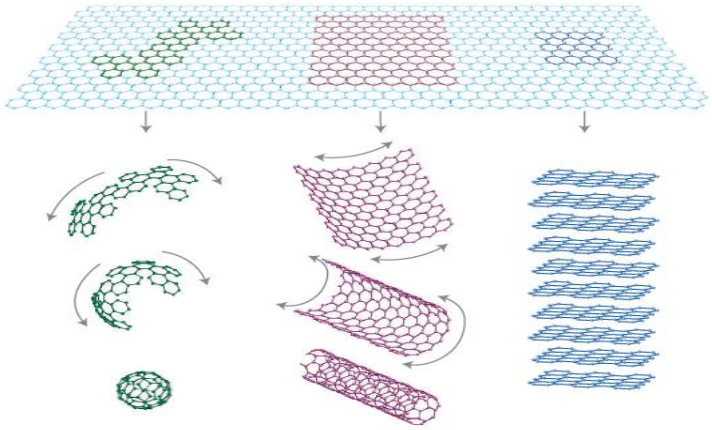


Figure 1.33: Graphene is a 2D building block for carbon-based materials. It can be wrapped up into 0D buckyballs, rolled into 1D nanotubes or stacked into 3D graphite. Taken from Ref [171].

1.6 Conclusion and Objectives of The Study

From this literature review on electrochemical biosensor, microelectrode fabrication process and the electrode surface functionalisation for biosensing, we learnt that:

i. The biosensors have significant interest in research and market related to highly commercial applications in clinical diagnostics, food, environmental and security fields.
ii. Electrochemically based biosensors transducers in comparison with other types of biosensors have the virtue of compatibility with modern microfabrication technologies. The simplicity of electrochemical instrumentation, low fabrication cost of the electrodes, the ability to achieve low detection limit besides maintaining consistency with label free detection approach are among the advantages that make this technique very attractive for practical and commercial life-sciences applications.
iii. Cutting-edge electrochemical transducers with electrode dimension advancing from macro to micro and nano scale, in combination of the electrodes assembled in an array, allow improvement of the biosensors parameter in terms of sensitivity and detection limit. With this regard, only a small volume of a sample will be required for sensing purpose.

iv. Additional improvements of transducer electrochemical performance can be achieved by additional modification or treatment of the electrode surface i.e. deposition of additional films as graphene, conducting polymers etc. and endow the surface structure with additional roughness. Both of these approaches also have interest from the biosensing applications as they provide additional sites for biomolecule attachment in the process of biomodification

v. Plane/flat micro and nanoelectrodes have certain advantages over other electrodes dimension (e.g. nanowire, microfibre). They are easier to fabricate and their surface biofunctionalisation is more feasible to conduct in reproducible manner.

vi. Surface functionalisation enables researchers to enhance both sensitivity and selectivity of the electrode surface in biosensing. Biofunctionalisation at microelectrode array is still at its infancy stage and requires detailed study as not all the immobilisation at macro dimension will suit the microelectrodes since microelectrodes are more susceptible to noise and organic chemical traces.

vii. Surface biofunctionalisation on microelectrode array could be achieved by electrodeposition technique that is selective to the metal/surface of interest without smearing the passivation tracks/area in comparison with the conventional dip-coating method.

Based on these outcomes, the objectives for this thesis study can be formulated as follows:

i. To design, fabricate and characterise microelectrode arrays with different substrates (silicon and glass), geometries (disc and band), dimensions (spanning from micro to nano) that can be used in biosensor.

ii. To investigate different chemical modifications techniques enhancing electrochemical activity that can be conducted on the microelectrode array for further biological applications.

iii. To design, fabricate and characterise an on-chip electrochemical cell with different geometries (disc and band) and parameters (number of electrodes

and disc interspacing distance) that can be used as a transducer platform for biosensing application.

iv. To study surface biofunctionalisation on gold substrate for the immobilisation of biological elements namely Histidine-tagged protein and antibody.

v. To apply the obtained results on development on gold microelectrode array transducers and surface biofunctionalisation methods to the development of mycotoxin T-2 toxin biosensor

1.7 References

1. Clark, L.C. and C. Lyons, *Electrode systems for continuous monitoring in cardiovascular surgery.* Annals of the New York Academy of Sciences, 1962. **102**(1): p. 29-45.
2. Turner, A.P., *Current trends in biosensor research and development.* Sensors and Actuators, 1989. **17**(3): p. 433-450.
3. Collings, A. and F. Caruso, *Biosensors: recent advances.* Reports on Progress in Physics, 1997. **60**(11): p. 1397.
4. Kovacs, G.T., *Micromachined transducers sourcebook*1998: WCB/McGraw-Hill New York.
5. Borgmann, S., et al., *Amperometric biosensors.* Advances in Electrochemical Science and Engineering,, WILEY-VCH Verlag GmbH & Co. KGaA, Weinheim, 2011.
6. Meadows, D., *Recent developments with biosensing technology and applications in the pharmaceutical industry.* Advanced Drug Delivery Reviews, 1996. **21**(3): p. 179-189.
7. Jamal, M., et al., *Sensor and biosensor to detect vascular graft infection: diagnosis and challenges.* Analytical Methods, 2012. **4**(7): p. 1865-1875.
8. Tothill, I.E., *Biosensors developments and potential applications in the agricultural diagnosis sector.* Computers and Electronics in Agriculture, 2001. **30**(1-3): p. 205-218.
9. Ngundi, M.M., et al., *Multiplexed detection of mycotoxins in foods with a regenerable array.* Journal of Food Protection, 2006. **69**(12): p. 3047-3051.

10. Carlson, M.A., et al., *An automated, handheld biosensor for aflatoxin.* Biosensors and Bioelectronics, 2000. **14**(10–11): p. 841-848.
11. Parker, C.O., et al., *Electrochemical Immunochip Sensor for Aflatoxin M-1 Detection.* Analytical Chemistry, 2009. **81**(13): p. 5291-5298.
12. Ahmad, A. and E.J. Moore, *Comparison of Cell-Based Biosensors with Traditional Analytical Techniques for Cytotoxicity Monitoring and Screening of Polycyclic Aromatic Hydrocarbons in the Environment.* Analytical Letters, 2009. **42**(1): p. 1-28.
13. Rawson, D.M., A.J. Willmer, and A.P.P. Turner, *Whole-cell biosensors for environmental monitoring.* Biosensors, 1989. **4**(5): p. 299-311.
14. Viveros, L., et al., *A fluorescence-based biosensor for the detection of organophosphate pesticides and chemical warfare agents.* Sensors and Actuators B: Chemical, 2006. **115**(1): p. 150-157.
15. Luong, J.H.T., K.B. Male, and J.D. Glennon, *Biosensor technology: Technology push versus market pull.* Biotechnology Advances, 2008. **26**(5): p. 492-500.
16. Alocilja, E.C. and S.M. Radke, *Market analysis of biosensors for food safety.* Biosensors and Bioelectronics, 2003. **18**(5–6): p. 841-846.
17. Herranz, S., M.D. Marazuela, and M.C. Moreno-Bondi, *Automated portable array biosensor for multisample microcystin analysis in freshwater samples.* Biosensors and Bioelectronics, 2012. **33**(1): p. 50-55.
18. Grieshaber, D., et al., *Electrochemical biosensors-Sensor principles and architectures.* Sensors, 2008. **8**(3): p. 1400-1458.
19. Thevenot, D.R., et al., *Electrochemical biosensors: recommended definitions and classification.* Pure and applied Chemistry, 1999. **71**(12): p. 2333-2348.
20. Thévenot, D.R., et al., *Electrochemical biosensors: recommended definitions and classification.* Biosensors and Bioelectronics, 2001. **16**(1-2): p. 121-131.
21. Scheller, F.W., et al., *Biosensors: trends and commercialization.* Biosensors, 1985. **1**(2): p. 135-160.
22. Pejcic, B. and R. De Marco, *Impedance spectroscopy: Over 35 years of electrochemical sensor optimization.* Electrochimica Acta, 2006. **51**(28): p. 6217-6229.

23. Ronkainen, N.J., H.B. Halsall, and W.R. Heineman, *Electrochemical biosensors.* Chemical Society Reviews, 2010. **39**(5): p. 1747-1763.
24. Luppa, P.B., L.J. Sokoll, and D.W. Chan, *Immunosensors--principles and applications to clinical chemistry.* Clinica Chimica Acta, 2001. **314**(1-2): p. 1-26.
25. Arrigan, D.W.M., *Nanoelectrodes, nanoelectrode arrays and their applications.* Analyst, 2004. **129**(12): p. 1157-1165.
26. Madou, M., *Fundamentals of microfabrication: the science of miniaturization*2002: CRC press.
27. Sassolas, A., L.J. Blum, and B.D. Leca-Bouvier, *Immobilization strategies to develop enzymatic biosensors.* Biotechnology Advances, 2012. **30**(3): p. 489-511.
28. Walcarius, A., *Electroanalysis with Pure, Chemically Modified and Sol-Gel-Derived Silica-Based Materials.* Electroanalysis, 2001. **13**(8-9): p. 701-718.
29. Cosnier, S., *Biosensors based on electropolymerized films: new trends.* Analytical and bioanalytical chemistry, 2003. **377**(3): p. 507-520.
30. Ronkainen-Matsuno, N.J., et al., *Electrochemical immunoassay moving into the fast lane.* TrAC Trends in Analytical Chemistry, 2002. **21**(4): p. 213-225.
31. Pohanka, M. and P. Skladal, *Electrochemical biosensors–principles and applications.* J Appl Biomed, 2008. **6**(2): p. 57-64.
32. Bard, A.J. and L.R. Faulkner, *Electrochemical methods: fundamentals and applications*. Vol. 2. 1980: Wiley New York.
33. Wang, J., *Analytical electrochemistry*2006: Wiley. com.
34. Bond, A.A.M. and F. Scholz, *Electroanalytical methods: guide to experiments and applications*2010: Springer.
35. Compton, R.G. and C.E. Banks, *Understanding voltammetry*2007: World Scientific.
36. Grieshaber, D., et al., *Electrochemical Biosensors - Sensor Principles and Architectures.* Sensors, 2008. **8**(3): p. 1400-1458.
37. Richard G Compton, C.E.B., *Understanding Voltammetry*. Vol. 2. 2011, London: Imperial College Press. 429.
38. Bakker, E. and E. Pretsch, *Potentiometric sensors for trace-level analysis.* TrAC Trends in Analytical Chemistry, 2005. **24**(3): p. 199-207.

39. Luppa, P.B., L.J. Sokoll, and D.W. Chan, *Immunosensors—principles and applications to clinical chemistry.* Clinica Chimica Acta, 2001. **314**(1): p. 1-26.
40. Chouteau, C., et al., *Development of novel conductometric biosensors based on immobilised whole cell Chlorella vulgaris microalgae.* Biosensors and Bioelectronics, 2004. **19**(9): p. 1089-1096.
41. Cullen, D.C., R.S. Sethi, and C.R. Lowe, *Multi-analyte miniature conductance biosensor.* Analytica Chimica Acta, 1990. **231**: p. 33-40.
42. Jaffrezic-Renault, N. and S.V. Dzyadevych, *Conductometric microbiosensors for environmental monitoring.* Sensors, 2008. **8**(4): p. 2569-2588.
43. Prodromidis, M.I., *Impedimetric immunosensors--A review.* Electrochimica Acta, 2010. **55**(14): p. 4227-4233.
44. Lvovich, V.F., *Impedance spectroscopy: applications to electrochemical and dielectric phenomena*2012: John Wiley & Sons.
45. Lisdat, F. and D. Schäfer, *The use of electrochemical impedance spectroscopy for biosensing.* Analytical and bioanalytical chemistry, 2008. **391**(5): p. 1555-1567.
46. Berggren, C., B. Bjarnason, and G. Johansson, *Capacitive biosensors.* Electroanalysis, 2001. **13**(3): p. 173-180.
47. Zhou, L.J., F. Yin, and Y. Zhou, *Fabrication of Hydrogen Peroxide Biosensors Based on Microelectrode Array of Silicon Dioxide Cavities.* Chinese Journal of Analytical Chemistry, 2011. **39**(9): p. 1313-1317.
48. Rodrigues, S., N. Munichandraiah, and A.K. Shukla, *A review of state-of-charge indication of batteries by means of a.c. impedance measurements.* Journal of Power Sources, 2000. **87**(1–2): p. 12-20.
49. Ionescu, R.E., et al., *Label-free impedimetric immunosensor for sensitive detection of atrazine.* Electrochimica Acta, 2010. **55**(21): p. 6228-6232.
50. Wang, M., et al., *Application of impedance spectroscopy for monitoring colloid Au-enhanced antibody immobilization and antibody-antigen reactions.* Biosensors and Bioelectronics, 2004. **19**(6): p. 575-582.
51. Keighley, S.D., et al., *Optimization of label-free DNA detection with electrochemical impedance spectroscopy using PNA probes.* Biosensors and Bioelectronics, 2008. **24**(4): p. 906-911.

52. Kafka, J., et al., *A label-free DNA sensor based on impedance spectroscopy.* Electrochimica Acta, 2008. **53**(25): p. 7467-7474.
53. Warburg, E., *Ueber das Verhalten sogenannter unpolarisirbarer Elektroden gegen Wechselstrom.* Annalen der Physik, 2006. **303**(3): p. 493-499.
54. Fricke, H., *XXXIII. The theory of electrolytic polarization.* The London, Edinburgh, and Dublin Philosophical Magazine and Journal of Science, 1932. **14**(90): p. 310-318.
55. Franks, W., et al., *Impedance characterization and modeling of electrodes for biomedical applications.* Biomedical Engineering, IEEE Transactions on, 2005. **52**(7): p. 1295-1302.
56. Krause, S. and A. Bard, *Encyclopedia of Electrochemistry, Vol. 3: Impedance Methods*, 2001, Wiley-VCH, Weinheim, Germany.
57. *Electrochemical Impedance Spectroscopy (EIS) Part 4- Equivalent Circuit Models*. Autolab Application Note EIS04 2011 1 July 2011; Available from: http://www.ecochemie.nl/export/Homepages/Autolab/download/Applicationnotes/Autolab_Application_Note_EIS04.pdf.
58. Pardo, A., et al., *Influence of microstructure and composition on the corrosion behaviour of Mg/Al alloys in chloride media.* Electrochimica Acta, 2008. **53**(27): p. 7890-7902.
59. Lasia, A., *Electrochemical impedance spectroscopy and its applications*, in *Modern aspects of electrochemistry*2002, Springer. p. 143-248.
60. Gabrielli, C., et al., *Electrochemical impedance spectroscopy investigations of a microelectrode behavior in a thin-layer cell: Experimental and theoretical studies.* The Journal of Physical Chemistry B, 2006. **110**(41): p. 20478-20485.
61. Bond, A.M., K.B. Oldham, and C.G. Zoski, *Steady-state voltammetry.* Analytica Chimica Acta, 1989. **216**: p. 177-230.
62. Hubel, D.H., *Specifity of responses of cells in the visual cortex.* Journal of Psychiatric Research, 1971. **8**(3-4): p. 301-307.
63. Štulík, K., et al., *Microelectrodes. Definitions, Characterization, and Application* Pure Appl. Chem., 2000. **72**(8): p. 1483-1492.
64. Compton, R.G., et al., *Design, fabrication, characterisation and application of nanoelectrode arrays.* Chemical Physics Letters, 2008. **459**(1-6): p. 1-17.

65. Aoki, K., *Theory of ultramicroelectrodes.* Electroanalysis, 1993. **5**(8): p. 627-639.
66. Bond, A.M., Past, present and future contributions of microelectrodes to analytical studies employing voltammetric detection - A Review. Analyst, 1994. **119**(11): p. R1-R21.
67. Fletcher, S. and M.D. Horne, *Random assemblies of microelectrodes (RAM(TM) electrodes) for electrochemical studies.* Electrochemistry Communications, 1999. **1**(10): p. 502-512.
68. Alden, J.A., et al., *Diffusional mass transport to microband electrodes of practical geometries: A simulation study using the strongly implicit procedure.* Journal of Electroanalytical Chemistry, 1995. **389**(1-2): p. 45-54.
69. Alden, J.A. and R.G. Compton, *Microband electrodes of ideal and nonideal geometries: AC impedance spectroscopy.* Electroanalysis, 1996. **8**(1): p. 30-33.
70. Lanyon, Y.H. and D.W.M. Arrigan, *Recessed nanoband electrodes fabricated by focused ion beam milling.* Sensors and Actuators B: Chemical, 2007. **121**(1): p. 341-347.
71. Ordeig, O., et al., *Electroanalysis utilizing amperometric microdisk electrode arrays.* Electroanalysis, 2007. **19**: p. 1973-1986.
72. Davies, T.J. and R.G. Compton, *The cyclic and linear sweep voltammetry of regular and random arrays of microdisc electrodes: Theory.* Journal of Electroanalytical Chemistry, 2005. **585**(1): p. 63-82.
73. Amatore, C. and B. Fosset, *Equivalence between Microelectrodes of Different Shapes: Between Myth and Reality.* Analytical Chemistry, 1996. **68**(24): p. 4377-4388.
74. Streeter, I., et al., *Voltammetry at Regular Microband Electrode Arrays: Theory and Experiment.* The Journal of Physical Chemistry C, 2007. **111**(32): p. 12058-12066.
75. Huang, X.J., A.M. O'Mahony, and R.G. Compton, *Microelectrode Arrays for Electrochemistry: Approaches to Fabrication.* Small, 2009. **5**(7): p. 776-788.
76. Beni, V. and D.W.M. Arrigan, *Microelectrode arrays and microfabricated devices in electrochemical stripping analysis.* Current Analytical Chemistry, 2008. **4**(3): p. 229-241.

77. Berduque, A., et al., *Voltammetric characterisation of silicon-based microelectrode arrays and their application to mercury-free stripping voltammetry of copper ions.* Talanta, 2007. **71**(3): p. 1022-1030.
78. Godino, N., et al., *Mass Transport to Nanoelectrode Arrays and Limitations of the Diffusion Domain Approach: Theory and Experiment.* Journal of Physical Chemistry C, 2009. **113**(25): p. 11119-11125.
79. Lanyon, Y.H., et al., *Fabrication of nanopore array electrodes by focused ion beam milling.* Analytical Chemistry, 2007. **79**(8): p. 3048-3055.
80. Sandison, M.E., et al., *Optimization of the geometry and porosity of microelectrode arrays for sensor design.* Analytical Chemistry, 2002. **74**(22): p. 5717-5725.
81. Lenigk, R., et al., *Recessed microelectrode array for a micro flow-through system allowing on-line multianalyte determination in vivo.* Fresenius' Journal of Analytical Chemistry, 1999. **364**(1-2): p. 66-71.
82. Bartlett, P.N. and S.L. Taylor, *An accurate microdisc simulation model for recessed microdisc electrodes.* Journal of Electroanalytical Chemistry, 1998. **453**(1–2): p. 49-60.
83. Kounaves, S.P., et al., *Iridium-based ultramicroelectrode array fabricated by microlithography.* Analytical Chemistry, 1994. **66**(3): p. 418-423.
84. Dill, K., et al., *Immunoassays based on electrochemical detection using microelectrode arrays.* Biosensors and Bioelectronics, 2004. **20**(4): p. 736-742.
85. Moujahid, W., et al., *Microelectrochemical Systems on Silicon Chips for the Detection of Pollutants in Seawater.* Electroanalysis, 2011. **23**(1): p. 147-155.
86. Zhuo, L., et al., *Nanoarray Membrane Sensor Based on a Multilayer Design For Sensing of Water Pollutants.* Analytical Chemistry, 2010. **82**(11): p. 4329-4332.
87. Bond, A.M. and P.A. Lay, *Cyclic voltammetry at microelectrodes in the absence of added electrolyte using a platinum quasi-reference electrode.* Journal of Electroanalytical Chemistry and Interfacial Electrochemistry, 1986. **199**(2): p. 285-295.

88. Bond, A.M., M. Fleischmann, and J. Robinson, *Electrochemistry in organic solvents without supporting electrolyte using platinum microelectrodes.* Journal of Electroanalytical Chemistry and Interfacial Electrochemistry, 1984. **168**(1-2): p. 299-312.
89. Daschbach, J., et al., *Electrochemistry of ferrocene in acetonitrile: Evidence for irreversible kinetic behavior due to passive film formation.* Journal of Electroanalytical Chemistry and Interfacial Electrochemistry, 1987. **237**(2): p. 269-273.
90. Drew, S.M., R.M. Wightman, and C.A. Amatore, *Voltammetry of ferrocene in low electrolyte solutions.* Journal of Electroanalytical Chemistry and Interfacial Electrochemistry, 1991. **317**(1-2): p. 117-124.
91. Andrieux, C.P., et al., *Electrochemistry in hydrophobic Nafion gels: Part 1. Electrochemical behaviour of electrodes modified by hydrophobic Nafion gels loaded with ferrocenes.* Journal of Electroanalytical Chemistry and Interfacial Electrochemistry, 1990. **296**(1): p. 117-128.
92. Oldham, K.B., *Theory of microelectrode voltammetry with little electrolyte.* Journal of Electroanalytical Chemistry and Interfacial Electrochemistry, 1988. **250**(1): p. 1-21.
93. Jager, E.W.H., E. Smela, and O. Inganäs, *On-chip microelectrodes for electrochemistry with moveable PPy bilayer actuators as working electrodes.* Sensors and Actuators B: Chemical, 1999. **56**(1-2): p. 73-78.
94. Bond, A.M. and T.F. Mann, *Voltammetric measurements without ohmic and other forms of distortion in aromatic hydrocarbon solvents.* Electrochimica Acta, 1987. **32**(6): p. 863-870.
95. Buzzeo, M.C., C. Hardacre, and R.G. Compton, *Extended electrochemical windows made accessible by room temperature ionic liquid/organic solvent electrolyte systems.* Chemphyschem, 2006. **7**(1): p. 176-180.
96. Moujahid, W., et al., *Microelectrochemical Systems on Silicon Chips for the Detection of Pollutants in Seawater*. Electroanalysis, 2011. **23**(1): p. 147-155.
97. Suzuki, H., *Microfabrication of chemical sensors and biosensors for environmental monitoring.* Materials Science and Engineering: C, 2000. **12**(1–2): p. 55-61.

98. Parker, C.O., et al., *Electrochemical Immunochip Sensor for Aflatoxin M1 Detection.* Analytical Chemistry, 2009. **81**(13): p. 5291-5298.
99. Lauks, I.R., *Microfabricated biosensors and microanalytical systems for blood analysis.* Accounts of Chemical Research, 1998. **31**(5): p. 317-324.
100. Petersen, K.E., *Silicon as a mechanical material.* Proceedings of the IEEE, 1982. **70**(5): p. 420-457.
101. Voldman, J., M.L. Gray, and M.A. Schmidt, *Microfabrication in biology and medicine.* Annual review of biomedical engineering, 1999. **1**(1): p. 401-425.
102. Xia, Y. and G.M. Whitesides, *Soft lithography.* Annual review of materials science, 1998. **28**(1): p. 153-184.
103. Zaouk, R., B.Y. Park, and M.J. Madou, *Introduction to microfabrication techniques*, in *Microfluidic Techniques*2006, Springer. p. 5-15.
104. Delcourt-Lancon, A., *Electrochemical analysis supported by macro and microelectrode array*, 2011, Durham University.
105. Hierlemann, A., et al., *Microfabrication techniques for chemical/biosensors.* Proceedings of the IEEE, 2003. **91**(6): p. 839-863.
106. Brodie, I. and J. Muray, *The physics of microfabrication. 1982*, New York, Plenum Press.
107. Cosnier, S., *Biomolecule immobilization on electrode surfaces by entrapment or attachment to electrochemically polymerized films. A review.* Biosensors and Bioelectronics, 1999. **14**(5): p. 443-456.
108. Murray, R.W., A.G. Ewing, and R.A. Durst, *Chemically modified electrodes. Molecular design for electroanalysis.* Analytical Chemistry, 1987. **59**(5): p. 379A-390A.
109. Murray, R.W., *Chemically modified electrodes.* Accounts of Chemical Research, 1980. **13**(5): p. 135-141.
110. Arrigan, D.W.M., *Tutorial review. Voltammetric determination of trace metals and organics after accumulation at modified electrodes.* Analyst, 1994. **119**(9): p. 1953-1966.
111. Herschkovitz, Y., et al., *An electrochemical biosensor for formaldehyde.* Journal of Electroanalytical Chemistry, 2000. **491**(1–2): p. 182-187.
112. Skládal, P., N.O. Morozova, and A.N. Reshetilov, *Amperometric biosensors for detection of phenol using chemically modified electrodes containing*

immobilized bacteria. Biosensors and Bioelectronics, 2002. **17**(10): p. 867-873.

113. Skládal, P., *Detection of organophosphate and carbamate pesticides using disposable biosensors based on chemically modified electrodes and immobilized cholinesterase.* Analytica Chimica Acta, 1992. **269**(2): p. 281-287.

114. Nunes, G.S., et al., *Evaluation of a highly sensitive amperometric biosensor with low cholinesterase charge immobilized on a chemically modified carbon paste electrode for trace determination of carbamates in fruit, vegetable and water samples.* Analytica Chimica Acta, 1999. **399**(1–2): p. 37-49.

115. Gooding, J.J., et al., *Self-Assembled Monolayers into the 21st Century: Recent Advances and Applications.* Electroanalysis, 2003. **15**(2): p. 81-96.

116. Ulman, A., *Formation and structure of self-assembled monolayers.* Chemical Reviews, 1996. **96**(4): p. 1533-1554.

117. Cohen-Atiya, M. and D. Mandler, *Studying thiol adsorption on Au, Ag and Hg surfaces by potentiometric measurements.* Journal of Electroanalytical Chemistry, 2003. **550**: p. 267-276.

118. Zhong, C.-J., et al., *Formation of thiol-based monolayers on gold: implications from open circuit potential measurements.* Electrochemistry Communications, 1999. **1**(1): p. 17-21.

119. Campuzano, S., et al., *Characterization of alkanethiol-self-assembled monolayers-modified gold electrodes by electrochemical impedance spectroscopy.* Journal of Electroanalytical Chemistry, 2006. **586**(1): p. 112-121.

120. Anandan, V., R. Gangadharan, and G. Zhang, *Role of SAM chain length in enhancing the sensitivity of nanopillar modified electrodes for glucose detection.* Sensors, 2009. **9**(3): p. 1295-1305.

121. Kim, Y.T., R.L. McCarley, and A.J. Bard, *Observation of N-octadecanethiol multilayer formation from solution onto gold*. Langmuir, 1993. **9**(8): p. 1941-1944.

122. Susmel, S., G.G. Guilbault, and C.K. O'Sullivan, *Demonstration of labeless detection of food pathogens using electrochemical redox probe and screen*

printed gold electrodes. Biosensors and Bioelectronics, 2003. **18**(7): p. 881-889.

123. Chiriacò, M.S., et al., *EIS microfluidic chips for flow immunoassay and ultrasensitive cholera toxin detection.* Lab on a Chip, 2011. **11**(4): p. 658-663.

124. Pei, R., et al., *Amplification of antigen–antibody interactions based on biotin labeled protein–streptavidin network complex using impedance spectroscopy.* Biosensors and Bioelectronics, 2001. **16**(6): p. 355-361.

125. Eckermann, A.L., et al., *Electrochemistry of redox-active self-assembled monolayers.* Coordination Chemistry Reviews, 2010. **254**(15-16): p. 1769-1802.

126. Wolfe, D.B., et al., *Fabrication of palladium-based microelectronic devices by microcontact printing.* Applied Physics Letters, 2002. **80**(12): p. 2222-2224.

127. Love, J.C., et al., *Self-assembled monolayers of alkanethiolates on palladium are good etch resists.* Journal of the American Chemical Society, 2002. **124**(8): p. 1576-1577.

128. Love, J.C., et al., *Formation and Structure of Self-Assembled Monolayers of Alkanethiolates on Palladium.* Journal of the American Chemical Society, 2003. **125**(9): p. 2597-2609.

129. Creager, S.E. and K.G. Olsen, *Self-assembled monolayers and enzyme electrodes: Progress, problems and prospects.* Analytica Chimica Acta, 1995. **307**(2–3): p. 277-289.

130. Riklin, A. and I. Willner, *Glucose and Acetylcholine Sensing Multilayer Enzyme Electrodes of Controlled Enzyme Layer Thickness.* Analytical Chemistry, 1995. **67**(22): p. 4118-4126.

131. Jiang, L., C.J. McNeil, and J.M. Cooper, *Direct electron-transfer reactions of glucose-oxidase immobilized at a self-assembled monolayer.* Journal of the Chemical Society-Chemical Communications, 1995(12): p. 1293-1295.

132. Rubin, S., et al., *Electrical Communication between Components of Self-Assembled Mixed Monolayers.* Langmuir, 1996. **12**(2): p. 363-370.

133. Collinson, M., E.F. Bowden, and M.J. Tarlov, *Voltammetry of covalently immobilized Cytochrome-C on self-assembled monolayer electrodes.* Langmuir, 1992. **8**(5): p. 1247-1250.

134. Ihara, T., et al., *Gene sensor using ferrocenyl oligonucleotide.* Chemical Communications, 1997(17): p. 1609-1610.

135. Bardea, A., et al., *Sensing and amplification of oligonucleotide-DNA interactions by means of impedance spectroscopy: a route to a Tay-Sachs sensor.* Chemical Communications, 1999(1): p. 21-22.

136. Steel, A.B., T.M. Herne, and M.J. Tarlov, *Electrochemical Quantitation of DNA Immobilized on Gold.* Analytical Chemistry, 1998. **70**(22): p. 4670-4677.

137. Baldrich, E., et al., *Gold immuno-functionalisation via self-assembled monolayers: Study of critical parameters and comparative performance for protein and bacteria detection.* Journal of immunological methods, 2008. **336**(2): p. 203-212.

138. Samanta, D. and A. Sarkar, *Immobilization of bio-macromolecules on self-assembled monolayers: methods and sensor applications.* Chemical Society Reviews, 2011. **40**(5): p. 2567-2592.

139. Tlili, C., et al., *A new method of immobilization of proteins on activated ester terminated alkanethiol monolayers towards the label free impedancemetric detection.* Materials Science & Engineering C-Biomimetic and Supramolecular Systems, 2008. **28**(5-6): p. 861-868.

140. Kallury, K.M., P.M. Macdonald, and M. Thompson, *Effect of surface water and base catalysis on the silanization of silica by (aminopropyl) alkoxysilanes studied by X-ray photoelectron spectroscopy and 13C cross-polarization/magic angle spinning nuclear magnetic resonance.* Langmuir, 1994. **10**(2): p. 492-499.

141. Flink, S., F.C. van Veggel, and D.N. Reinhoudt, *Functionalization of self-assembled monolayers on glass and oxidized silicon wafers by surface reactions.* Journal of Physical Organic Chemistry, 2001. **14**(7): p. 407-415.

142. Kusnezow, W., et al., *Antibody microarrays: an evaluation of production parameters.* Proteomics, 2003. **3**(3): p. 254-264.

143. Thakurta, S.G., R. Miller, and A. Subramanian, *Adherence of platelets to in situ albumin-binding surfaces under flow conditions: role of surface-adsorbed albumin.* Biomedical Materials, 2012. **7**(4): p. 045007.
144. Vashist, S.K., et al., *Effect of antibody immobilization strategies on the analytical performance of a surface plasmon resonance-based immunoassay.* Analyst, 2011. **136**(21): p. 4431-4436.
145. Lin, D.M. and J.F. Che, *Hydrogel-Modified Bio-Electrodes.* Progress in Chemistry, 2010. **22**(6): p. 1195-1202.
146. Yan, J., et al., *Immobilizing Enzymes onto Electrode Arrays by Hydrogel Photolithography to Fabricate Multi-Analyte Electrochemical Biosensors.* Acs Applied Materials & Interfaces, 2010. **2**(3): p. 748-755.
147. Pelaez, L., et al., *Electrochemical characterization of hydrogels for biomimetic applications.* Polymers for Advanced Technologies, 2011. **22**(9): p. 1381-1388.
148. Wallace, G.G., M. Smyth, and H. Zhao, *Conducting electroactive polymer-based biosensors.* TrAC Trends in Analytical Chemistry, 1999. **18**(4): p. 245-251.
149. Llaudet, E., et al., *A three-enzyme microelectrode sensor for detecting purine release from central nervous system.* Biosensors and Bioelectronics, 2003. **18**(1): p. 43-52.
150. Pereira, A.C., et al., *Reagentless biosensor for isocitrate using one step modified Pt-Ir microelectrode.* Talanta, 2001. **53**(4): p. 801-806.
151. Razola, S.S., et al., *Hydrogen peroxide sensitive amperometric biosensor based on horseradish peroxidase entrapped in a polypyrrole electrode.* Biosensors and Bioelectronics, 2002. **17**(11–12): p. 921-928.
152. Uang, Y.-M. and T.-C. Chou, *Criteria for Designing a Polypyrrole Glucose Biosensor by Galvanostatic Electropolymerization.* Electroanalysis, 2002. **14**(22): p. 1564-1570.
153. Liu, Y.-C., et al., *Evaluation and application of conducting polymer entrapment on quartz crystal microbalance in flow injection immunoassay.* Biosensors and Bioelectronics, 2003. **18**(7): p. 937-942.

154. Ouerghi, C., et al., *Electrodeposited biotinylated polypyrrole as an immobilization method for impedimetric immunosensors.* Ieee Sensors Journal, 2004. **4**(5): p. 559-567.
155. Fredj, H.B., et al., *Polyaniline Based Immunosensor for Atrazine Sensing.* Sensor Letters, 2009. **7**(5): p. 661-666.
156. Jha, S.K., et al., *Entrapment of live microbial cells in electropolymerized polyaniline and their use as urea biosensor.* Biosensors and Bioelectronics, 2009. **24**(8): p. 2637-2642.
157. Ionescu, R.E., et al., *Amperometric immunosensor for the detection of anti-West Nile virus IgG using a photoactive copolymer.* Enzyme and Microbial Technology, 2007. **40**(3): p. 403-408.
158. Haddour, N., S. Cosnier, and C. Gondran, *Electrogeneration of a poly(pyrrole)-NTA chelator film for a reversible oriented immobilization of histidine-tagged proteins.* Journal of the American Chemical Society, 2005. **127**(16): p. 5752-5753.
159. Braun, S., et al., *Biochemically active sol-gel glasses: the trapping of enzymes.* Materials Letters, 1990. **10**(1–2): p. 1-5.
160. Gill, I. and A. Ballesteros, *Bioencapsulation within synthetic polymers (Part 1): sol–gel encapsulated biologicals.* Trends in biotechnology, 2000. **18**(7): p. 282-296.
161. Dave, B.C., et al., *Sol-gel encapsulation methods for biosensors.* Analytical Chemistry, 1994. **66**(22): p. 1120A-1127A.
162. Wang, J., *Sol–gel materials for electrochemical biosensors.* Analytica Chimica Acta, 1999. **399**(1): p. 21-27.
163. Walcarius, A., et al., *Exciting new directions in the intersection of functionalized sol–gel materials with electrochemistry.* Journal of Materials Chemistry, 2005. **15**(35-36): p. 3663-3689.
164. Jena, B.K. and C.R. Raj, *Electrochemical biosensor based on integrated assembly of dehydrogenase enzymes and gold nanoparticles.* Analytical Chemistry, 2006. **78**(18): p. 6332-6339.
165. Sibottier, E., et al., *Factors Affecting the Preparation and Properties of Electrodeposited Silica Thin Films Functionalized with Amine or Thiol Groups.* Langmuir, 2006. **22**(20): p. 8366-8373.

166. Goux, A., et al., *Oriented mesoporous silica films Obtained by electro-assisted self-assembly (EASA).* Chemistry of Materials, 2009. **21**(4): p. 731-741.
167. McCreery, R.L., *Advanced carbon electrode materials for molecular electrochemistry.* Chem. Rev, 2008. **108**(7): p. 2646-2687.
168. Haddad, R., et al., *Non-covalent biofunctionalization of single-walled carbon nanotubes via biotin attachment by π-stacking interactions and pyrrole polymerization.* Analyst, 2009. **134**(12): p. 2412-2418.
169. Van Noorden, R., *The graphene challenge.* Chemistry World, 2008. **5**(4): p. 56-59.
170. Xu, C., X. Wang, and J. Zhu, *Graphene−Metal Particle Nanocomposites.* The Journal of Physical Chemistry C, 2008. **112**(50): p. 19841-19845.
171. Geim, A.K. and K.S. Novoselov, *The rise of graphene.* Nature Materials, 2007. **6**(3): p. 183-191.

CHAPTER 2

EXPERIMENTAL PROCEDURES

2.1 Chemicals and Biological Reagents

All reagents used in this thesis are listed below (Table 2.1) in alphabetical order and of analytical grade (95% at least). They were used without further purification. All solutions were prepared using nano pure water with a resistivity of 18.2 MΩ cm from ELGA Ltd. System Maxima UltraPure Water (UK).

Table 2.1 Chemical/ biological reagents and suppliers

Chemical/Biological Reagent	Supplier	CAS number
Acetate buffer solution pH 4.6	Fluka	-
Acetone	Sigma-Aldrich	67-64-1
Albumin, from bovine serum (BSA)	Sigma	9048-46-8
(3-Aminopropyl)triethoxysilane (APTES)	Sigma-Aldrich	919-30-2
Anti-Mouse IgG-FITC	Sigma	-
Boric acid	Sigma	10043-35-3
Bromoacetic acid reagent grade, 97%	Aldrich	79-08-3
Copper acetate	Aldrich	142-71-2
Dextran 500 (technical grade)	SERVA Electrophoresis GmbH	9004-54-0
1,2-Dichloroethane (DCE)	Sigma-Aldrich	107-06-2
Diethanolamine	Aldrich	111-42-2
Diethylene glycol dimethyl ether anhydrous (Diglyme)	Sigma-Aldrich	111-96-6

Table 2.1 *(continued)*

Chemical/Biological Reagent	Supplier	CAS number
N-(3-Dimethylaminopropyl)-*N'*-ethylcarbodiimide hydrochloride (EDC)	Sigma-Aldrich	25952-53-8
4-(Dimethylamino)pyridine	Aldrich	1122-58-3
Dimethylformamide (DMF)	Acros	68-12-2
N,N'-Disuccinimidyl carbonate ≥95% (DSC)	Aldrich	74124-79-1
(±)-Epichlorohydrin purum, ≥99% (GC)	Fluka	106-89-8
Ethanol	Sigma-Aldrich	64-17-5
Ethanolamine chloride (≥99.0%)	Sigma-Aldrich	2002-24-6
Ferrocenecarboxylic acid (FCA)	Fluka	1271-42-7
Ferrocenemethanol	Aldrich	1273-86-5
(3-Glycidyloxypropyl)trimethoxysilane (GOPTS)	Aldrich	2530-83-8
Hexadecyltrimethyl ammonium bromide (Cetrimonium bromide, CTAB)	Sigma	57-09-0
Hydrochloric acid (37%)	Sigma-Aldrich	7647-01-0
Hydrogen peroxide solution (≥30%)	Sigma-Aldrich	7722-84-1
N-Hydroxy-succinimide (NHS)	Aldrich	6066-82-6
IgG from mouse serum	Sigma	-
Isopropyl alcohol	VLSI	67-63-0
16-Mercaptodexadecan-1-ol	InoChem	114896-32-1
(3-Mercaptopropyl)trimethoxysilane	Aldrich	4420-74-0
11-Mercaptoundecanoic acid	Aldrich	71310-21-9
Methanol	Sigma-Aldrich	67-56-1
Nα,Nα-Bis(carboxymethyl)-L-lysine hydrate (N-(5-amino-1-carboxypentyl) iminodiacetic acid) (NTA)	Aldrich	113231-05-3
Penta-His™ Alexa Fluor® 488 Conjugate	Qiagen GmbH	-
1,4-Phenylene diisothiocyanate (PDITC)	Aldrich	4044-65-9

Table 2.1 *(continued)*

Chemical/Biological Reagent	Supplier	CAS number
Phosphate buffered saline (PBS) tablet	Sigma-Aldrich	-
Phosphate buffer solution 50mM	Fluka	-
Poly(ethylene glycol) bis(amine)	Aldrich	24991-53-5
Potassium chloride	Fisher Scientific	7447-40-7
Protein A (from *Staphylococcus aureus*)	Sigma	-
Pyridine	Sigma-Aldrich	110-86-1
Sodium chloride	Sigma-Aldrich	7647-14-5
Sodium hydroxide	Sigma-Aldrich	1310-73-2
Sodium phosphate dibasic	Sigma-Aldrich	7558-79-4
Sodium phosphate monobasic	Sigma-Aldrich	7558-80-7
Sulfuric acid	Sigma-Aldrich	7664-93-9
Tetraethyl orthosilicate (TEOS)	Aldrich	78-10-4
Triethylamine ≥99%	Sigma-Aldrich	121-44-8
Veratox® T-2/HT-2 Toxin Quantitative Test Kit	Neogen	-

2.2 Instrumentations

A CH Instrument Potentiostat (CHI660B or CHI620B, IJ Cambria, Burry Port, Wales, UK) or an Autolab Potentiostat (PGSTAT302N, Metrohm, Switzerland) was either used to perform cyclic voltammetry experiment. Electrochemical impedance spectroscopy measurements were performed by the Autolab using Frequency Response Analyser (FRA) software. For cleaning the microelectrodes, a plasma cleaner (Harrick Plasma, New York, USA) was used. A high-resolution optical microscope (Olympus America Inc.) and scanning electron microscope (Quanta 650 FEG, FEI, Oregon USA) were used for visual characterisation study. Atomic force microscopy (AFM) measurements were carried out with a Veeco MultiMode Atomic Force Microscopy (NY) using either a Pointprobe-PLUS® Silicon-SPM-Sensor tip or SuperSharpSilicon™-SPM-Sensor (Nanosensors™, Switzerland). Contact angle measurement was performed using DataPhysics Contact Angle System OCA Instruments (Germany). Sonicator was from UltraWave, UK.

2.3 Microelectrode Cleaning Using Plasma Cleaner

Prior carrying out any electrochemical measurements, it is a prerequisite to clean the microelectrodes in order to attain a clean surface and to remove any contaminants that may exist on the surface. The most widely employed methods for cleaning microelectrodes are the renowned piranha solution or electrochemical cleaning using sulfuric acid. Plasma cleaning method is an emerging alternative for cleaning silicon-based microelectrodes. The following notes on the difference between cleaning macro and nanoelectrode should be taken into account.

Standard recommendation for cleaning gold electrodes of macroscopic dimension includes two consecutive steps. The first step is a mechanical polishing using diamond paste or alumina powder in water suspension. The second step is an electrochemical cleaning by applying to the electrode potentiadynamic cycling over potential range 0 to +1.5 V (vs Ag/AgCl) in 0.1-0.5 M H_2SO_4 until repeatable voltammograms are obtained (usually 100-200 cycles). In the case of a microelectrode representing a thin film of gold on the substrate surface (usually silicon-based), mechanical polishing is not advisable as each polishing removes a few atoms layers of metal film which could lead to electrode damage. Electrochemical cleaning by applying potentiodynamic cycling can be used but in our experience, this treatment significantly reduces the lifetime of the electrodes.

Under these circumstances, plasma cleaning offers a more feasible and furthermore practical way in cleaning microfabricated microelectrode. The oxygen plasma eliminates natural and technical oils; and grease at the nano-scale and reduces contamination better when compared with traditional wet cleaning methods (Table 2.2). Plasma cleaning enhances wettability or hydrophilicity property of a surface hence produces hydroxylated surface that are ready for bonding or further surface modification/functionalisation.

Ultra-violet light generated in the plasma is very effective in breaking the organic bonds of surface contaminants (Fig. 2.1). This is followed by energetic oxygen species created in the plasma which react with organic contaminants to form water and carbon dioxide. Both wastes were removed from the chamber by continuous pumping.

Table 2.2 Comparison of plasma cleaning and wet chemical cleaning

Plasma Cleaning	Wet Chemical (solvent/aqueous) Cleaning
Processes are precisely controllable through power, pressure, gas type and duration of time	Processes are very sensitive to processing time and chemical concentrations
No organic residues remain	Organic residues may exist which may require further processing steps
Wastes are harmless and always in gaseous form	High volume of liquid waste that requires expensive treatment and subjected to regulations
Most of the gases used have no toxicity	Most of the solvents and acids used are extremely hazardous

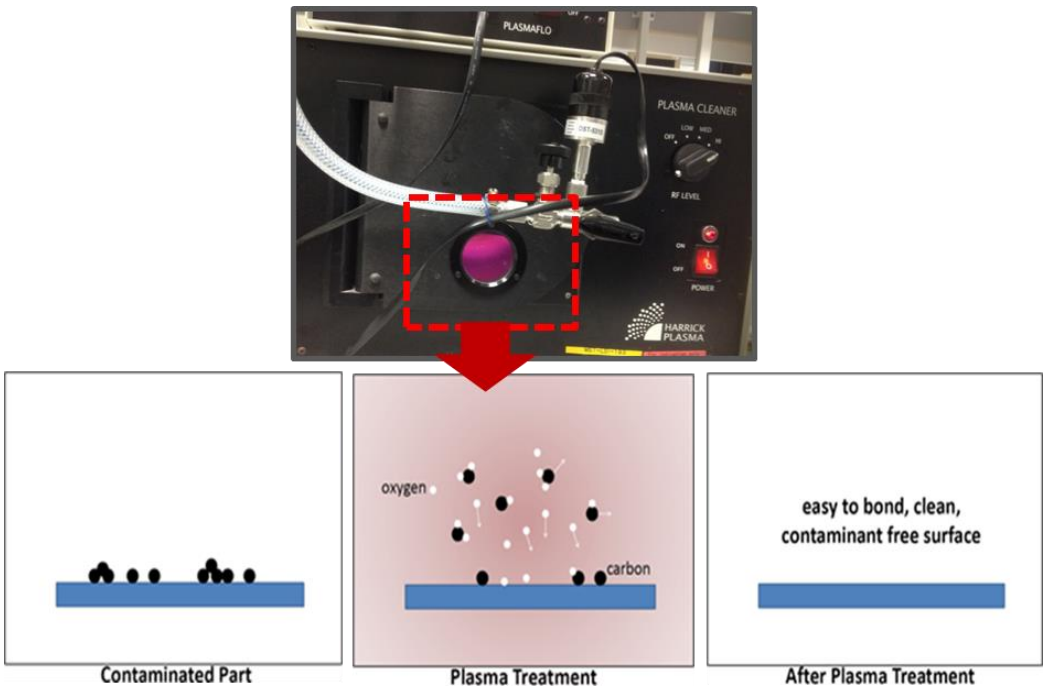


Figure 2.1: Schematic diagram on how plasma cleaning works. Adapted from [1].

2.4 Electrochemical Measurements

To conduct an electrochemical experiment, an electrochemical cell in which the electrochemical reactions take place, is required. The cell is then connected to a potentiostat, an electrochemical analyser that run the electroanalytical experiment, and placed in a Faraday cage. The Faraday cage usage is particularly important for microelectrode measurements as it helps to reduce electromagnetic noise that may interfere with the electrochemical measurement. The instrumentation system is connected to the computer via external interface.

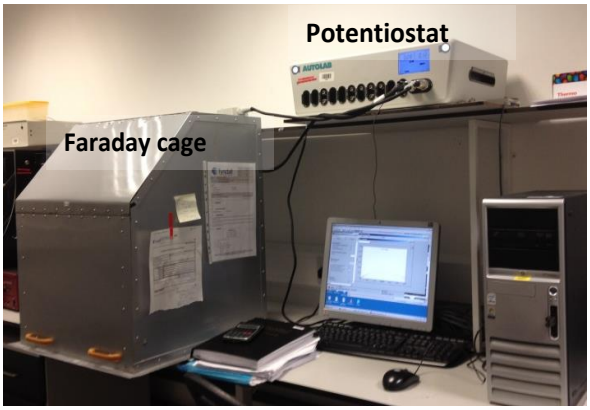


Figure 2.2: Experimental set-up for electrochemical experiment involving potentiostat and the Faraday cage.

2.4.1 Electrochemical Cell

In electrochemical experiments, the electrodes are the probes that come in immediate contact with the electrolyte. Electrochemical sensing usually requires a reference electrode (RE), a counter or auxiliary electrode (CE or AE) and a working electrode (WE), also known as the sensing or redox electrode. Depending on the electrochemical set-up and the type of electrodes, a three-electrode or two-electrode systems can be required. In the case of two-electrode system, the CE is merged with the RE and this configuration is often used when dealing with measurement of small currents [2, 3]. All the electrodes are immersed in a 20 mL beaker containing electrolyte (sample solution). All of the RE, CE and WE electrodes should be both

conductive and chemically stable. Therefore, platinum, gold, carbon (e.g. graphite) and silicon are commonly used as electrode materials [4].

Reference Electrode

The internationally accepted primary reference is the standard hydrogen electrode (SHE) or normal hydrogen electrode (NHE) but the most common and widely used is the saturated calomel electrode (SCE) and silver-silver chloride (Ag/AgCl) electrode. Potentials are often measured and quoted with respect to the reference electrode other than the NHE. For this study, the RE selected was the Ag|AgCl|KCl, 3M KCl (CH Instruments, IJ Cambria, Burry Port, Wales, UK).

Counter Electrode

In order to minimize errors from the cell resistance when controlling the potential of the working electrode, the CE is used. This electrode is made of a chemically inert conducting material with a surface area significantly greater than the surface area of the working electrode. Platinum wire is the most commonly used counter electrode in voltammetry study. The counter electrode used in this study was a Pt wire, also from CH Instruments (IJ Cambria, Burry Port, Wales, UK).

Working Electrode

The working electrode serves as the transduction element in the biochemical reaction. Common working electrodes can be made of inert metals such as gold, silver or platinum, or inert carbon such as glassy carbon and mercury drop and film electrodes [5]. In recent decades, the WE size for electroanalysis has evolved from a commercial one (rod/probe-shaped like) with macro size to an in-house fabricated electrodes (screen printed, photolithography etc.) with micro- and nano dimensions (Fig. 2.3). The commercial WEs however are still relevant for standard procedure and measurement as they are very stable and reproducible.

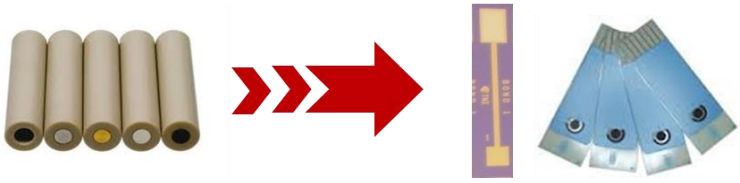


Figure 2.3: Revolution of probe-shaped WE to a chip-liked WE.

An example of the electrochemical set-up in this study is shown in Fig. 2.4.

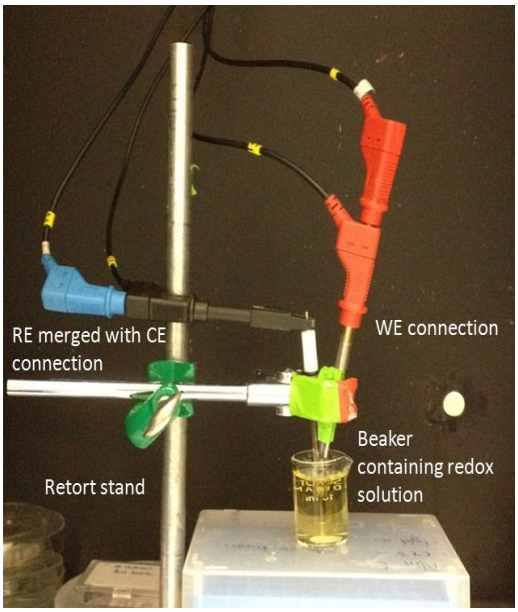


Figure 2.4: An example of electrochemical cell set-up in the study for the Autolab potentiostat.

2.4.2 Microelectrode Array Fabrication

The microelectrode array fabricated in this study is described accordingly as in Chapter 3 and 4. All microelectrode arrays were fabricated in-house by Tyndall National Institute's Central Fabrication Facilities (CFF) (Fig. 2.5) by Mr. Dan O'Connell.

Tyndall's CFF consists of three distinct cleanroom spaces, 250m^2 of class 1,000 and class 10 for silicon fabrication, 750m^2 of class 10,000 and class 100 for MEMS and

compound semiconductor fabrication and 40m^2 of class 1000 for e-beam lithography [6].



Figure 2.5: Picture of Tyndall's CFF (left) and CFF Wafer processing personnel with protective cleaning room clothing (right). Taken from [6].

Photoresist Removal

Once the wafers with diced microelectrodes were received from the fabrication lab, the microelectrodes were first treated to wash away the photoresist layer residues. This was done by immersing the electrodes in hot acetone (boiling point 56-57°C) for 5 minutes, rinsed with deionized water and followed by 2 minutes immersion in hot isopropyl alcohol (boiling point 82.5°C) for 2 minutes. The electrodes were washed with copious amount of deionised (DI) water and dried with nitrogen (N_2) flow.

2.4.3 Redox Solution Preparation

A 1 mM solution of ferrocenecarboxylic acid (FCA) in supporting electrolyte 0.01 M phosphate buffer saline (PBS) solution, pH 7.4 was used for electrochemical characterisation. Phosphate buffered saline (PBS) solution was prepared by dissolving one PBS tablet in 200 mL DI water yielding 0.01 M phosphate buffer, 0.0027 M KCl and 0.137 M NaCl, pH 7.4, at 25 °C. To prepare 1mM of FCA in PBS in 20 mL PBS, 0.046 g of FCA was weighed out and dissolved in 20 mL of PBS.

The solution was left in the sonicator for approximately 20 minutes to let the FCA completely dissolved. Electrochemical characterisation for the modified electrodes with electrochemical assisted self-assembly (EASA) sol-gel on the other hand, was carried out in a 5 mM ferrocenemethanol redox solution in 0.1 M NaCl.

2.5 Sol-Gel Silica Film Electrodeposition on Gold Surface

The electrodeposition of organosilica films was carried out at the ratio of hexadecyltrimethyl ammonium bromide (CTAB) to tetraethyl orthosilicate (TEOS) at 0.32 in 20 mL ethanol and 20 mL 0.1 M NaCl at pH 3 (or near) as described by Goux et al. [7]. The sol solution was left stir for 1 hour. The electrodeposition was achieved by galvanostatic method whereby the current applied to the corresponding surface area is -0.74 mA cm^{-2} for 8 seconds with sample time of 0.05 sec. All electrodes were plasma-cleaned beforehand. The deposited silica was dried and left aging overnight at 135°C. The surfactant or template removal was carried out by immersing the electrode in ethanolic solution of 0.1 M HCl. The cyclic voltammetry (CV) characterisation was carried out in 5mM ferrocenemethanol in 0.1 M NaCl prior electrodepostion for unmodified gold electrode and after each of modification steps, i.e. after sol-gel deposition, after overnight aging and after the sol-gel-surfactant template removal.

2.5.1 Electrochemical Assisted Self-Assembly Sol-Gel Silica Film Electrodeposition

Following plasma-cleaning, the gold electrode surface was first pretreated with (3-Mercaptopropyl)trimethoxysilane (MPTMS) monolayer by dropping an aliquot of 20 mM of MPTMS in ethanol for 20 minutes [8]. After rinsing in a 50:50 water/ethanol mixture, the electrode was transferred into the starting sol of CTAB/TEOS with MPTMS precursors in 90:10 ratio and left hydrolysed for 2.5 hours at pH 3. The current applied in galvanostatic electrodeposition was -0.74 mA cm^{-2} for the macroelectrode and -7.4 mA cm^{-2} for recessed microelectrode array; both used a deposition time of 8 seconds with a sample time of 0.05 sec. The

functionalised silica film was rinsed with distilled water and dried at 135°C in the oven or over the bench at RT for overnight. The surfactant or template removal was carried out by immersing the electrode in ethanolic solution of 0.1 M HCl. The CV and EIS characterisations were both carried out in 5mM ferrocenemethanol in 0.1 M NaCl prior electrodeposition for unmodified gold electrode and after each of modification steps, i.e. after sol-gel deposition, after overnight aging and after the sol-gel-surfactant template removal.

2.6 Surface Biofunctionalisation for Histidine-tagged Protein Immobilisation

The method employed for histidine-tagged protein immobilization in this study was taken and modified from Cass et al. [9]. For an initial study, Alexa Fluor® 488, a Penta-His fluorophore dye, was employed as a model of the histidine-tagged protein. Histidine-tagged PduA protein from *L.reuteri* was obtained from Microbiology Department, UCC.

All modification steps in this part were carried out at room temperature (RT). The electrodes were first plasma cleaned for 10 minutes and immersed in 2 mM 11-mercaptoundecanoic acid ethanolic solution for 20 hours. Prior to use, the ethanol was degassed for 30 minutes with nitrogen air. After rinsing alternately with ethanol and DI water, the electrodes with SAM formation were incubated in freshly prepared 0.1 M EDC and 0.1 M NHS in DI water for 30 minutes. The surfaces were then washed with PBS and then incubated for 1 hour in a solution of N_{α}, N_{α}-Bis(carboxymethyl)-$_{L}$-lysine (NTA) (1 mg mL^{-1} in 10 mM sodium carbonate, pH 8.0). After this coupling step of NTA derivative to the carboxyl terminal group of the SAM, the surfaces were further washed with PBS and incubated in 0.5 M diethanolamine solution, pH 8.5 for 30 minutes in order to block unreacted activated carboxyl groups. The surfaces were then incubated with 20 mM copper acetate in acetate buffer buffer (pH 4.5) for 30 minutes. Next, 3 µL of Alexa Fluor or 0.2 mg mL^{-1} PduA protein diluted in acetate buffer (pH 4.5) were subsequently dropped on the electrode surface and left for 2 hours. After washing the surfaces with PBS, the surfaces were then analysed by fluorescence microscopy or AFM. CV and EIS studies were carried out using Autolab potentiostat in 1 mM FCA in PBS.

2.7 Surface Biofunctionalisation for Anti-T-2 Toxin Monoclonal Antibody Immobilisation

Three different surface biofunctionalisation methods were first studied for antibody immobilisation at gold macroelectrode. The selected methods were carboxymethyl dextran (CM-Dextran), and surface silanisation using (3-Glycidyloxypropyl) trimethoxysilane (GOPTS) and (3-Aminopropyl)triethoxysilane (APTES) with different linkers such as poly(ethylene glycol) (PEG) and 1,4-Phenylene diisothiocyanate (PDITC). These biofunctionalisation techniques were chosen due to their reported successful applications for antibody immobilisation in biosensor [10-14].

2.7.1 CM-Dextran Method

This protocol requires several days for the surface modification. The first day involves the cleaning of the glassware and the three subsequent days for surface functionalisation. Six glass bottles in total were required to prepare the solutions/chemicals and to immerse the electrodes.

Day 1: All glassware were cleaned in piranha solution of H_2SO_4:30% H_2O_2 (7:3) for 1 hour at 90°C. The glassware were then rinsed with water followed by ethanol and dried in the oven. Prior to use, all glassware were cleaned via plasma-cleaner for 20 minutes and cleaned using ethanol and dried with N_2 flow.

Surface Preparation

Day 2: The electrodes were first washed with ethanol and dried under the stream of N_2 flow. In a first glass bottle, 1.4 mg of 16-mercaptohexadecan-1-ol was weighed and added to 1 mL ethanol/water (v/v: 80:20). The mixture was vortexed well and wrapped in aluminium foil. The electrodes were left immersed in the solution for overnight on rotamax.

The electrodes were taken out on the following day and dried with N_2 flow to remove excess solution. The electrodes were then transferred into second glass bottle

containing 56 μL 0.6 M epichlorohydrin in 0.4 M NaOH and Diglyme (v/v: 1:1) at 25^{o}C for 4 hours. Meanwhile, 0.3 g of dextran was dissolved in 1 mL of 0.1 M NaOH in the third glass bottle. The dextran may require some time to dissolve hence heating in the oven of 25°C is required. Following the epichlorohydrin reaction, the electrodes were taken out and washed alternately with water and ethanol. The electrodes were placed in the dextran solution and left 20 hours at 25°C.

Day 3: In the fourth glass bottle, bromoacetic acid was prepared by weighing 0.14 g of bromoacetic acid and added in 1 ml of 2 M NaOH. The electrodes were taken out from dextran solution and rinsed with water to remove excess. They were dried under the N_2 flow and left overnight in the bromoacetic acid.

Day 4: A mixture of 500 μL EDC (750 mg of EDC in 10 mL of DI water) and 500 μL NHS (115 mg NHS in DI water) was prepared in the fifth glass bottle. The electrodes from previous night was taken out, washed, dried under N_2 and left into the EDC-NHS solution for 30 minutes. The anti-T-2 toxin antibody dilution was prepared in 10 mM phosphate buffer pH 6 in eppendorf tubes.

Antibody Immobilisation and Surface Blocking

The electrodes from the EDC-NHS mixture were taken out and transferred into eppendorf tubes containing diluted anti-T-2 toxin antibody. The tubes need to be wrapped in aluminium foil. After incubation of 2 hours, the electrodes were straight transferred into blocking solution of 1ml of 1M ethanolamine (sixth glass bottle) for 30 minutes. The electrodes were then rinsed with DI water and dried with N_2, and ready for testing.

10 mM Phosphate Buffer pH 6.5 Preparation

Stock solutions of 250 mL of sodium phosphate monobasic 0.2 M (Solution A) and 250 mL of sodium phosphate dibasic 0.2 M (Solution B) were first prepared. These solutions are stable for six months at RT. 4.385 mL from Solution A and 0.615 mL from Solution B were taken and mixed together. A 5 mL of DI water was added to the mixed solution, giving 10 mL of 100 mM buffer at pH 6. A 1:10 dilution was then performed in order to get concentration of 10 mM. pH was then adjusted to pH 6.5 using 2 M NaOH.

2.7.2 Silanisation Using GOPTS with PEG Linker

The method described here for the surface modification using both GOPTS and PEG is as similar as reported by Wolter et al. (2008) [15]. In this work, *N,N'*-disuccinimidyl carbonate (DSC) was used as the cross-linker for Ab attachment.

Electrode Surface Pretreatment

All electrodes and glassware were first oxygen plasma-cleaned for 20 minutes at high setting. Following the plasma-cleaning, electrodes were immersed in HCl:MeOH (1:1, v/v) solution for 15 min and 32% sulfuric acid for a further 15 minutes. The activated electrode surfaces were then washed with copious amounts of DI water, dried under N_2 stream and stored at 70^{o}C for 15 minutes.

Silanisation

The pretreated electrodes were directly silanised in 1 mL of GOPTS in a clean glass bottle for 30 minutes at RT on the rotamax with 50 rpm speed. They were then sonicated sequentially in 10 mL of ethanol, methanol and ethanol for 15 minutes each and dried under the N_2 stream. The silanised electrodes were cured at 70°C for 15 minutes.

PEG Layer Preparation

The diamino poly(ethylene glycol) (DAPEG) was melted at 105°C. The melted DAPEG was dribbled at the middle of the electrode and then covered with another electrode on top before baking the electrodes at 105°C for overnight. The baked sandwiched electrodes were taken out from the oven the following day and were slid apart to separate. They were then sonicated in DI water for 15 minutes before drying under N_2 stream. The electrodes were further cured at 70^{o}C for 15 minutes.

Surface Activation (Cross-Linker Attachment)

80 mg of DSC* and 4 mg of dimethylaminopyridine (DMAP) were dissolved in 1.6 mL of DMF and 125 μL of triethylamine. The electrodes were immersed in the

* DSC is air-sensitive thus it needs to be wrapped with parafilm when storing

mixture (300 μL for each electrode) for 4 hours at RT, wrapped in aluminium foil and left shaking on the rotamax with 50 rpm. Following the incubation, the electrodes were sonicated in MeOH for 15 minutes and then dried under N_2.

Antibody Immobilisation

Antibody dilutions in 10 mM phosphate buffer pH 6.5 were carried out in large eppendorfs tubes. The electrodes were immersed in 100 μL of anti-T-2 toxin antibody solution with different concentrations of 0.1 and 1.0 mg mL^{-1} and left for 2 hours at RT, wrapped in aluminium foil. After the antibody immobilisation, the electrodes were removed, rinsed with DI water and dried with N_2. The electrodes can be stored in PBS.

2.7.3 Silanisation Using APTES with PDITC Cross-Linker

Unlike the two previous methods, this procedure is more straight-forward and do not require any overnight incubation. For the biofunctionalisation surface using APTES silanisation described here and following section (2.7.4), modification steps were carried out in microinsert tubes. Both microinsert tubes and bottle stand were supplied by Supelco (Sigma Aldrich) (Fig. 2.6).



Figure 2.6: Experimental set-up for surface biofunctionalisation using APTES silanisation methods for antibody immobilisation (left). A microinsert was used to accommodate the surface functionalisation on the working surface electrode (right).

Electrode Surface Pretreatment

The electrodes were first plasma-cleaned for 10 minutes and then immersed in HCl:MeOH (1:1, v/v) solution for 15 minutes. The electrodes were then sonicated in acetone and isopropyl alcohol for 5 minutes each; and rinsed with copious amounts of DI water and dry under a stream of N_2.

Silanisation

Silanisation for the electrode surfaces was carried out in 3% APTES in MeOH:DI water (19:1) solution for 30 minutes at RT. The electrodes were then rinsed sequentially with MeOH and DI water before left cure in the oven (dust free) for 15 minutes at 120°C.

Surface Activation (Cross-Linker Attachment)

Following the curing steps, the silanised electrodes were immediately immersed in 18 mL of DMF solution containing 2 mL of 10% pyridine and 0.098 g 1,4-phenylene diisothiocyanate (PDITC) (produces 25mM PDITC) for 2 hours. The electrodes were washed sequentially with DMF and DCE and dry under N_2.

Antibody Immobilisation

For this modification, anti-T-2 toxin antibody was diluted in in 0.1 M sodium borate pH 9.3. The electrodes were immersed in 100 µL of diluted antibody solution for 2 hours at RT, wrapped in aluminium foil. The electrodes were removed, rinsed with DI water and dried with N_2.

Testing the Immobilised Antibody with Optical Reading

50 µL of T-2/HT-2 conjugate and 50 µl of T-2/HT-2 standard solutions were mixed. Two standard solutions were being used, 0 and 250 ng mL^{-1} ml as negative and positive control respectively. The electrodes with immobilised anti-T-2 toxin antibody were placed in the mixtures and left incubated for 5 minutes at RT. The electrodes were then washed with copious amount of DI water, dried with N_2 and placed in 100 µL of substrates for 10 minutes at RT. 100 µL of stop solution was then added and solution was optically read at 650nm. All of the conjugate, standard solutions, substrates and stop solution used here were from the Veratox® kit.

0.1 M Sodium Borate Buffer pH 9.3 Preparation

0.31 g of boric acid was added to 35 mL of DI water. pH was adjusted to pH 9.3 with 1 M NaOH and solution was made up 50 mL with DI water.

2.7.4 Silanisation Using APTES with EDC-NHS Amine Coupling

The methods described here are adapted from the work on biofunctionalisation on Au SPR chip [16, 17]. All steps described here were carried out at RT. After 10 minutes of plasma cleaning, the electrodes were treated with piranha solution (60 μL of H_2SO_4:30 μL of H_2O_2 30%) for 3 minutes followed by extensive washing. The electrodes were then incubated in 2% APTES in DI water for 1 hour under the fume hood followed by five washes with DI water. Following this, different immobilisation strategies were applied.

Antibody Immobilisation without Protein A

A 495 μL of anti-T-2 toxin antibody from various concentrations (diluted in either borate buffer pH 8.3 or PBS pH 7.4) was pre-incubated with 5 μL of EDC (4 mg mL^{-1}) and NHS mixture (11 mg mL^{-1}) in DI water for 15 minutes. This led to the activation of carboxyl groups on the T-2 toxin antibody with EDC. The electrodes from APTES step was then immersed in this Ab solution and left 1 hour before tested.

Antibody Immobilisation with Protein A

For the antibody attachment with the aid of Protein A, 495 μL of Protein A (1 mg mL^{-1} in phosphate buffer 50 mM) was pre-incubated with 5 μL of EDC (4 mg mL^{-1}) and NHS mixture (11 mg mL^{-1}) in DI water for 15 minutes. The electrodes with APTES-functionalised surface were transferred in this mixture for 1 hour and rinsed with PBS for five times. The electrode surface was then blocked with 1% (w/v) BSA for 30 minutes. After washing the electrodes with PBS for five times, the electrodes were then incubated in antibody solution of various concentration, each concentration for 30 minutes.

Optical Study of the Antibody Immobilisation

To verify the success of the immobilisation procedures, mouse IgG was used as the substitute for anti-T-2 toxin antibody. The biofunctionalisation steps were similar as described earlier with piranha solution treatment, silanisation with APTES and EDC/NHS activation. Following the attachment of the Mouse IgG, the electrodes were transferred in microinsert tubes containing 1 mg mL^{-1} anti-mouse IgG-FITC labelled for 15 minutes to 1 hour. The electrodes were then analysed using fluorescence microscope with FITC filter.

Antibody Immobilisation Calibration Curve Establishment

A 495 µL of anti-T-2 toxin antibody from various concentrations (0.1, 0.25, 0.5, 0.75 mg mL-1 in PBS pH 7.4) was pre-incubated with 5 µL of EDC (4 mg mL^{-1}) and NHS mixture (11 mg mL^{-1}) in DI water for 15 minutes. The APTES-activated electrodes were then incubated in the antibody dilutions for 1 hour. The electrodes were washed with DI water and dried with N_2. Electrochemical measurements for CV and EIS were performed accordingly. For the control of 0 ppb antibody concentration, the PBS diluent was mixed with the EDC/NHS.

Antibody-Antigen Calibration Curve Establishment

Following the attachment of the anti-T-2 toxin antibody, the electrodes were transferred in the micro inserts with different T-2/HT-2 toxin concentrations[!] (0, 25, 50, 100 and 250 ppb) for 15-30 minutes incubation under the fume hood. The electrodes were washed with DI water and dried with N_2 and ready for the electrochemical measurements.

[!] Due to the toxicity of T-2/HT-2 toxin, all of the T-2/HT-2 toxin wastes, wash wastes and pipette tips used to dispense the toxin were collected in Schott glass bottle. 70% sodium hypochlorite was added to the waste bottle to deactivate the toxin. The electrochemical redox solution for T-2/HT-2 measurements was also disposed in the same manner.

2.8 References

1. *Plasma Surface Treatment*. Available from: http://www.plasmatreatment.co.uk/index.php/plasma-technology-overview?start=3.
2. Bard, A.J., Faulkner, L.R, *Electrochemical Methods, Fundamentals and Applications.* 2001.
3. Bond, A.M., T.L. Henderson, and W. Thormann, *Theory and experimental characterization of linear gold microelectrodes with submicrometer thickness.* The Journal of Physical Chemistry, 1986. **90**(13): p. 2911-2917.
4. Grieshaber, D., et al., *Electrochemical biosensors-Sensor principles and architectures.* Sensors, 2008. **8**(3): p. 1400-1458.
5. Xia, Y. and G.M. Whitesides, *Soft lithography.* Annual review of materials science, 1998. **28**(1): p. 153-184.
6. [cited 2013 20 September 2013]; Wafer Fabrication]. Available from: https://www.tyndall.ie/content/wafer-fabrication.
7. Goux, A., et al., *Oriented mesoporous silica films Obtained by electro-assisted self-assembly (EASA).* Chemistry of Materials, 2009. **21**(4): p. 731-741.
8. Sibottier, E., et al., *Factors Affecting the Preparation and Properties of Electrodeposited Silica Thin Films Functionalized with Amine or Thiol Groups.* Langmuir, 2006. **22**(20): p. 8366-8373.
9. Le, T.T., et al., *A simple method for controlled immobilization of proteins on modified SAMs.* Physical Chemistry Chemical Physics, 2011. **13**(12): p. 5271-5278.
10. Haasnoot, W., M. Bienenmann-Ploum, and F. Kohen, *Biosensor immunoassay for the detection of eight sulfonamides in chicken serum.* Analytica Chimica Acta, 2003. **483**(1): p. 171-180.
11. Howell, S., et al., *High-density immobilization of an antibody fragment to a carboxymethylated dextran-linked biosensor surface.* Journal of Molecular Recognition, 1998. **11**(1-6): p. 200-203.
12. Situ, C., et al., *Reduction of severe bovine serum associated matrix effects on carboxymethylated dextran coated biosensor surfaces.* Talanta, 2008. **76**(4): p. 832-836.

13. Mehne, J., et al., *Characterisation of morphology of self-assembled PEG monolayers: a comparison of mixed and pure coatings optimised for biosensor applications.* Analytical and bioanalytical chemistry, 2008. **391**(5): p. 1783-1791.
14. Parker, C.O., et al., *Electrochemical Immunochip Sensor for Aflatoxin M1 Detection.* Analytical Chemistry, 2009. **81**(13): p. 5291-5298.
15. Wolter, A., R. Niessner, and M. Seidel, *Preparation and Characterization of Functional Poly(ethylene glycol) Surfaces for the Use of Antibody Microarrays.* Analytical Chemistry, 2007. **79**(12): p. 4529-4537.
16. Vashist, S.K., *Comparison of 1-Ethyl-3-(3-Dimethylaminopropyl) Carbodiimide Based Strategies to Crosslink Antibodies on Amine-Functionalized Platforms for Immunodiagnostic Applications.* Diagnostics, 2012. **2**(3): p. 23-33.
17. Vashist, S.K., et al., *Effect of antibody immobilization strategies on the analytical performance of a surface plasmon resonance-based immunoassay.* Analyst, 2011. **136**(21): p. 4431-4436.

CHAPTER 3

DEVELOPMENT OF MICRO- AND NANOELECTRODE ARRAYS

3.1 Introduction

The transducer is a key component of any biosensor. To develop a robust biosensor system, the sensitivity and stability of the transducer are the main issues that need to be addressed. In electrochemical biosensor, the sensitivity of the transducer (electrode) can be improved by using microelectrode [1]. The use of a single microelectrode, however, leads to produce low current output and is more susceptible to interference [2, 3]. These drawbacks can be overcome with microelectrode arrays. One of the most important goals in using microelectrode arrays is to increase the current levels while maintaining the special features of a single microelectrode, such as steady-state current, low ohmic potential drop and a low time constant [4].

As described earlier in Chapter 1 (Section 1.3.5), there are many ways to fabricate microelectrode array. In this particular study, silicon-based microelectrode arrays were fabricated by combination of UV photolithography and electron-beam lithography. Silicon-based microelectrode array fabricated by either these means have been reported before by numerous groups [5-10]. It has long known also that the geometry, dimension, surface structure and choice of substrates of the electrode have profound effects on the electrochemical response [11]. Therefore this study will investigate the effect of the aforementioned factors towards the diffusion profile and its associated electrochemical characterisation of a microelectrode.

Firstly, two types of geometry, band and disc array; with three critical dimensions (100 nm, 1 μm and 10 μm) chosen for the microelectrode design were carefully

examined. The selected critical dimensions span size ranging from nano to micro; allowing us to compare the performance of a nanoelectrode array with a microelectrode array. Consideration of the two type of geometry (disc and band) on the other hand, would be able to assist us to gain insight regarding the diffusion profile associated with hemispherical (3D) and hemicylindrical (2D) diffusions.

The other parameter of interest in silicon-based microelectrode array was the thicknesses of passivation layer, which is an essential component of the electrode array responsible for an electrode recess. Recessed microelectrodes are the most common in the photolithography technique due to the nature of the fabrication process (e.g. etching). Thus, three different silicon nitride (Si_3N_4) layer thicknesses of 200, 300 and 500 nm (Fig. 3.1) were considered. The thicker silicon nitride layer, the less parasitic capacitance associated with the passivated part of the transducer surface. At the same time, the thicker the passivation layer, the deeper electrode recess and therefore the more it affects the electrochemical performance of the individual electrode in the array.

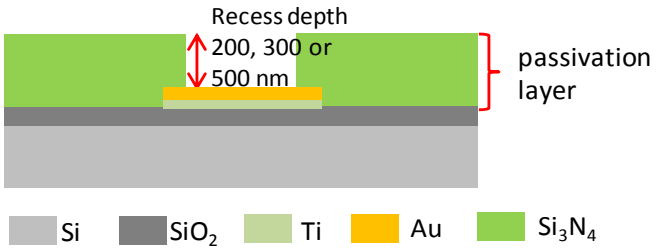


Figure 3.1: Schematic diagram of Si_3N_4 passivation layer on silicon substrate/SiO_2 layer and the recess depth with regard to the working microelectrode surface (Au layer) (not to scale).

At the same, in biosensor application, the recessed microelectrodes offer advantages of protecting immobilised biomolecule within the recess [12]. From another practical point of view, the recess protects the electrode surface from contamination and handling damage (scratch etc.) [13].

Finally, besides silicon, the microelectrode array was also fabricated on a glass substrate. The choice of these two substrates is interesting due to the difference of their physical property such as conductivity that can result in less parasitic capacitance for glass-based microelectrode vis-à-vis silicon-based microelectrode.

The fabrication of the microelectrode array is described in next section. The individual diced microelectrode array chip had dimension of 2.54 mm (*w*) x 15 mm (*l*) as shown in Fig. 3.2. This dimension has been selected to provide easy chip handling for characterisation experiments and future practical implementation. The chip length 15 mm will allow immersion of the transducer area in the solution without the risk of wetting the connection pad, represented by a rectangular (2 mm x 3mm) gold pad opening in the passivation layer. The microelectrode array surface is also represented by an open gold layer which is connected to the connection pad via a gold track isolated from the surrounding medium by silicon nitride. The layout of the underlying metal pattern on this end varies, depending on the design and dimension of the microelectrode.

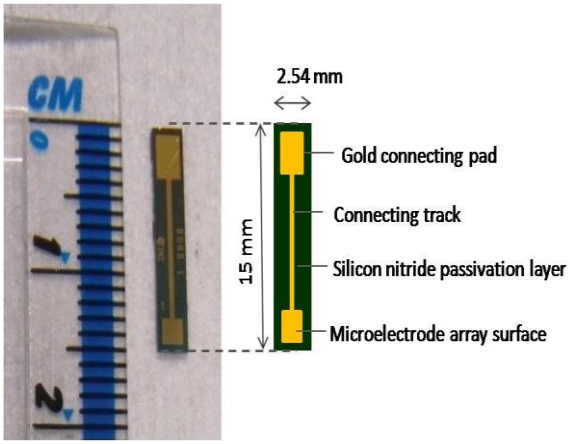


Figure 3.2: Single chip of microfabricated silicon-based microelectrode array.

Following the design and fabrication of the microelectrode array, the characterisation and optimisation of microelectrode array performance was carried out. The summary of the designs studied in terms of their geometry and sizes are presented in Table 3.1. Microelectrode characterisation studies are important for verification of the

microelectrode design and also as a viability indication of the whole fabrication process. The characterisations included microscopic and spectroscopic examinations of the fabricated microelectrode array to check the quality of array fabrication and also electrochemical characterisations which consisted of cyclic voltammetry (CV) and electrochemical impedance spectroscopy (EIS) techniques. The best working electrode dimension and geometry found from these characterisation studies were used for the subsequent on-chip microelectrochemical cell development as will be discussed in Chapter 4.

Table 3.1 Summary of the five different types of microelectrode array

Design	**Geometry**	**Width/diameter**	**Length**	***N* electrodes**	***Surface area/cm^2**
d1	Disc	10 μm	-	314	2.466 x 10^{-4}
d2	Disc	1 μm	-	75	5.89 x 10^{-4}
b1	Band	10 μm	500 μm	17	8.5 x 10^{-4}
b2	Band	1 μm	50 μm	9	4.5 x 10^{-6}
b3	Band	100 nm	5 μm	75	3.75 x 10^{-7}

*Surface area, *A*, is calculated using the following equations:

1. $A = N\pi\frac{d^2}{4}$ for disc electrodes

2. $A = Nwl$ for band electrodes

The terms were defined as: *N*=number of electrodes in the array, *d*=disc diameter, *w*=width of the bands and *l*=length of the bands.

All the disc arrays of d1 and d2 were arranged in a hexagonal manner so that the optimum number of electrodes in the array could be achieved. The microelectrodes were arranged in an array with centre-to-centre spacing (*d*) of 10 times more than the critical dimension in the case of 10 μm, and of 20 times more than the critical dimension for 1 μm. The five designs of d1, d2, b1, b2 and b3 are shown in Fig. 3.3.

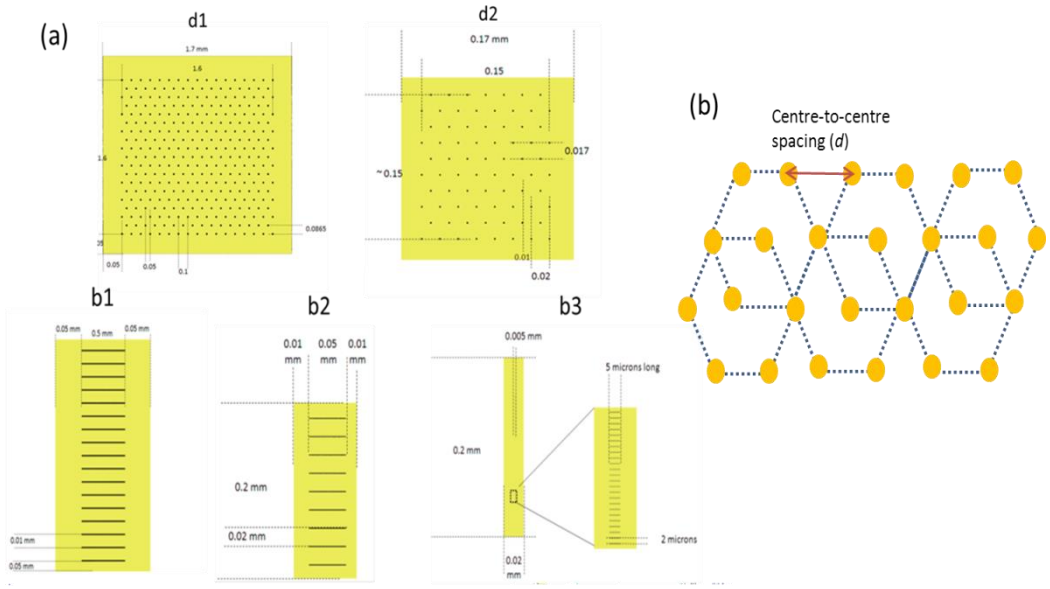


Figure 3.3: (a) Microelectrode arrangement for microdisc array (d1 and d2) and single array of microband electrodes (b1, b2 and b3); (b) disc arrangement in hexagonal manner (discs represented by yellow dots) with centre-to-centre distance (denote by *d*) (not to scale).

In the second part of this chapter, results for the microelectrodes which were undergone chemical modification to alter/modify the surface properties i.e. to increase surface roughness will be presented. The chemical modification was achieved via sol-gel and nanoporous gold; both via electrodeposition. This additional study allowed us to investigate the possibility of carrying out chemical modification on the recessed microelectrode array, thus demonstrating the future prospect on chemical modification for further biological application.

The objectives of this chapter are summarised as follow:

1. To design a number of gold microelectrode arrays with different geometries (disk and band) and dimensions
2. To fabricate and investigate the influence of geometry, dimensions and passivation layer thickness of the silicon-based microelectrode array on its electrochemical performance and diffusion profile
3. To fabricate and characterise the microelectrode array on glass substrate

4. To select the best design and geometry of microelectrode array for subsequent on-chip microelectrochemical cell development
5. To demonstrate the possibility of chemically modifying the recessed microelectrode array surface by electrochemical deposition of sol-gel and nanoporous gold

3.2 Micro- and Nanoelectrode Array Fabrication

The fabrication of microelectrode array was carried out in Tyndall National Institute's Central Fabrication Facilities (CFF)[*]. A combination of UV photolithographic and e-beam lithographic methods were used to pattern electrodes with critical dimensions of 10 μm, 1 μm and 100 nm. The fabrication process includes five stages: (i) preparation of the wafers, (ii) metal deposition, (iii) silicon nitride deposition, (iv) e-beam patterning and (v) silicon nitride plasma etching (Fig. 3.4).

A silicon wafer (N-Type<111>-orientation) with 525 μm thickness was used as the substrate. A silicon oxide layer with 1 μm thickness was thermally grown on the substrate and alignment marks for both photolithography and e-beam lithography was patterned on the wafer. Next, photoresist (a bi-level resist system with Micro-chem LOR3A and Shipley S1813) was spin-coated on the wafer. This resist was exposed using a mask aligner. Resist was then developed with Microposit MF319 Developer. For the fabrication of the metal electrodes, gold was deposited by evaporation. Titanium was used as the adhesion layer to ensure appropriate adhesion of the gold on the substrate in the proportion of 20:150 for Ti:Au. The remaining resist was then removed with excess metal by lift-off process using Microposit R1165 resist stripper. On the following stage, silicon nitride passivation layer with three different thicknesses (200, 300 and 500 nm) were deposited by plasma-enhanced chemical vapour deposition (PEVCD). For the 500 nm thick silicon nitride layer, a silicon oxide hard mask of 125 nm was deposited to improve accuracy of the subsequent etching.

[*] Microelectrode array fabrication was done by Mr. Dan O'Connell of Tyndall's CFF

This is followed by e-beam patterning for the opening electrodes with smallest dimensions of 100 nm and 1 μm. E-beam photoresist with 200 nm was spin-coated and e-beam lithography was carried out. Finally, the openings in the e-beam resist were transferred to the silicon nitride via inductively couple plasma (ICP) reactive-ion etching (RIE). The S1813 resist was used as the positive photoresist for the passivation. The opening of the largest features of 10 μm and the connecting pad was carried out by photolithography followed by plasma etching. Following fabrication, the wafers were diced into individual microelectrode array chips and no further packaging was required.

For the glass-based microelectrode array, glass substrate was used and fabrication was carried out with one silicon nitride thickness only (200 nm).

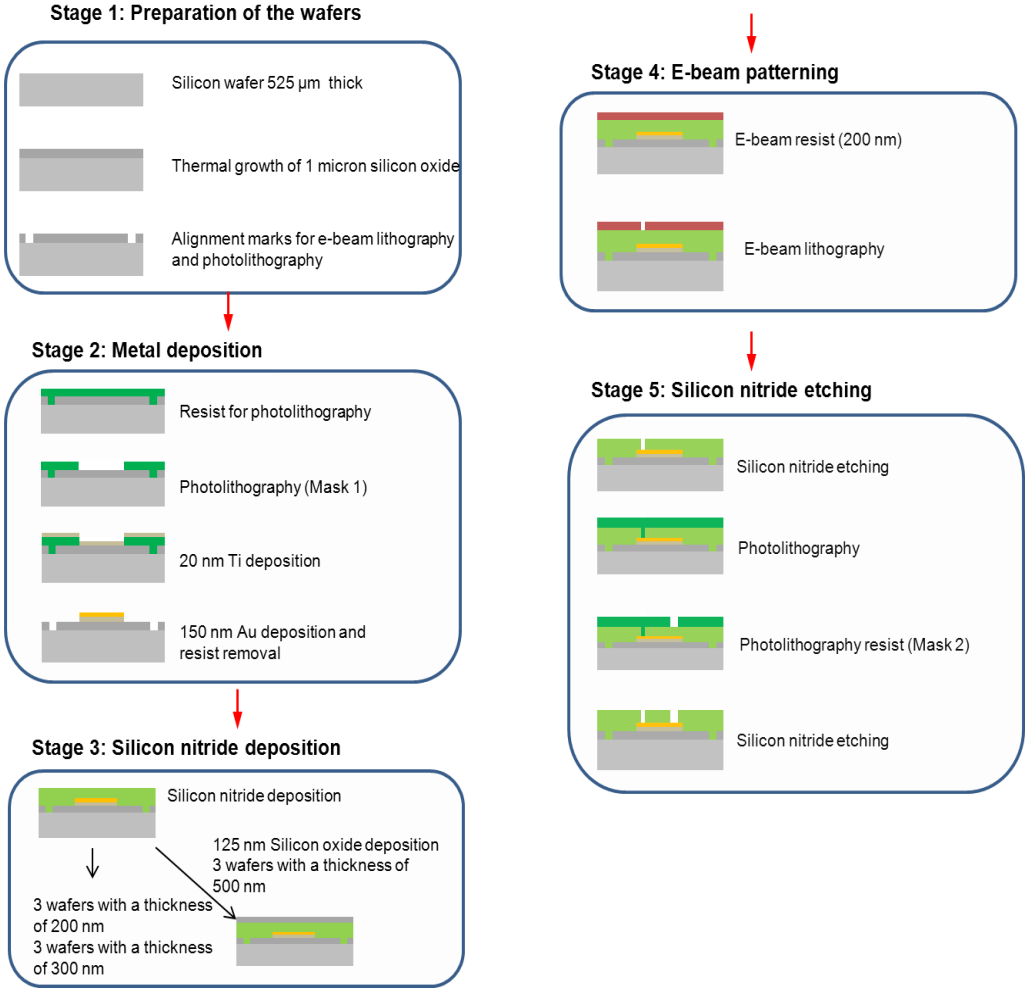


Figure 3.4: Detailed stages of microelectrode array microfabrication process (not to scale).

3.3 Optical Study for Visual Characterisation

The fabricated microelectrode arrays were inspected using scanning electron microscopy (SEM) and optical microscopy to confirm correspondence between the fabricated dimensions and the expected ones. An energy-dispersive X-ray spectroscopy (EDX) was performed as well to detect the chemical composition on the surface of the different components of the fabricated electrode. Although at first 100 nm nanodisc array were aimed to design, nevertheless due to fabrication problem related to the software bugs, this design was omitted in the study.

The SEM images[*] for all the studied designs were carried out but only images for microdisc array with 1 μm critical dimension, d2, (300 nm recess depth) and microband array with 1 μm (b2) and 100 nm (b3) (200 nm recess depth) were presented here (Fig. 3.5). The expected and the achieved critical dimensions for all of the microelectrode array's designs for the three thicknesses, however, are summarised in Table 3.2.

The larger feature dimensions (d1 and b1) that were realised corresponded to the expected dimensions with 10% accuracy regardless of the silicon nitride thickness. However, for the smallest features (d2, b2 and b3), the dimensions achieved varied greatly with the thickness. For silicon nitride thicknesses of 200 and 300 nm, there was no silicon oxide layer between the silicon nitride and the e-beam resist. As a result, the dimensions achieved for the 500 nm thick silicon nitride wafers were much closer to the expected dimensions compared to the wafers with thinner silicon nitride layers. The reason for the widening of the opening was due to the lack of selectivity of the etching process for silicon nitride over the e-beam resist. Therefore, in order to improve the selectivity for the development of future microelectrodes, a silicon oxide layer can be introduced on the silicon nitride layer (triplex layers of $SiO_2/Si_3N_4/SiO_2$) to ensure that the correct dimensions are realised [14].

[*] All SEM images in this chapter were captured by Mr. Vince Lodge from Central Fabrication Lab, Tyndall National Institute

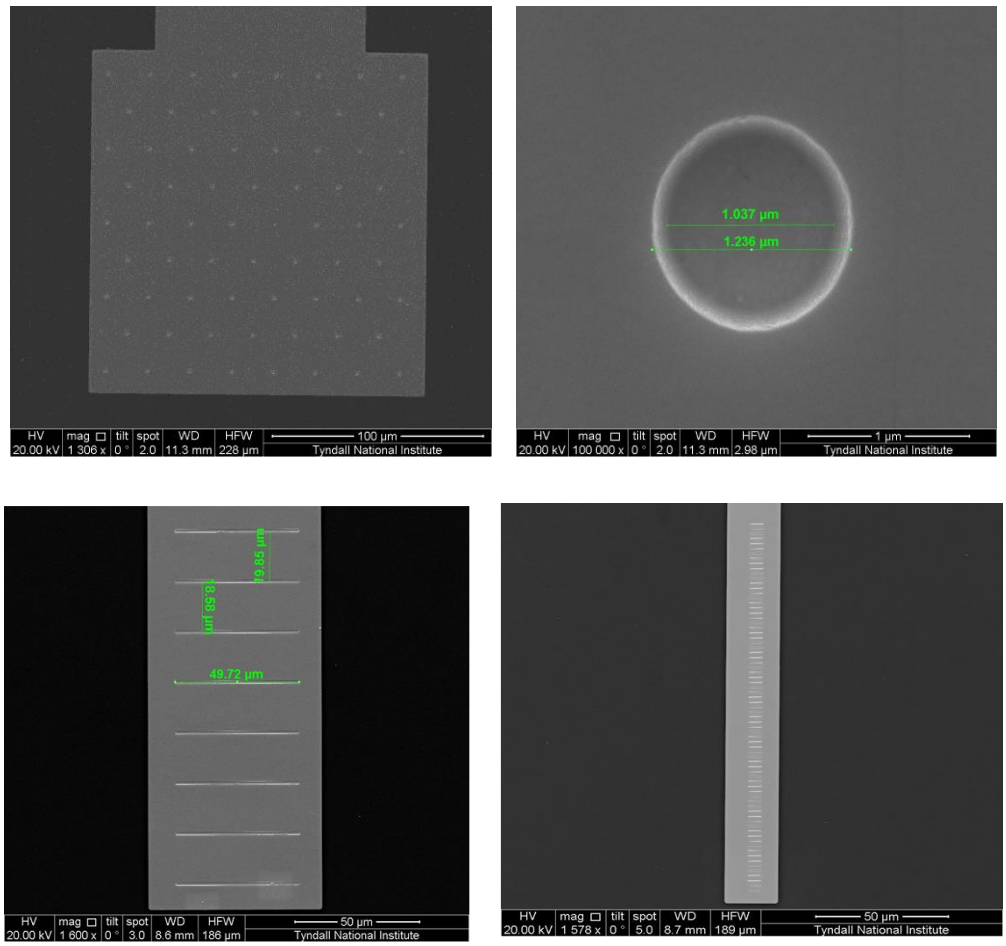


Figure 3.5: Top row: SEM images of 1 µm microdisc array, d2 (300 nm recess depth). *Bottom row*: SEM images of 1 µm microband, b2 (left) and 100 nm microband, b3 (right); both with 200 nm recess depth.

The presence of Au at the bottom of the trenches was confirmed by EDX analysis* (Figure 3.6) that confirmed the accuracy of the nitride plasma etching process step. Two spectra were recorded: the first one was taken at the silicon nitride passivation layer, and the second one was within the recess. These experiments prove that there is gold present in the band, although there is no visual difference on the SEM images between Si_3N_4 and gold.

* All EDX analysis were carried out by Mr. Vince Lodge from Central Fabrication Lab, Tyndall National Institute

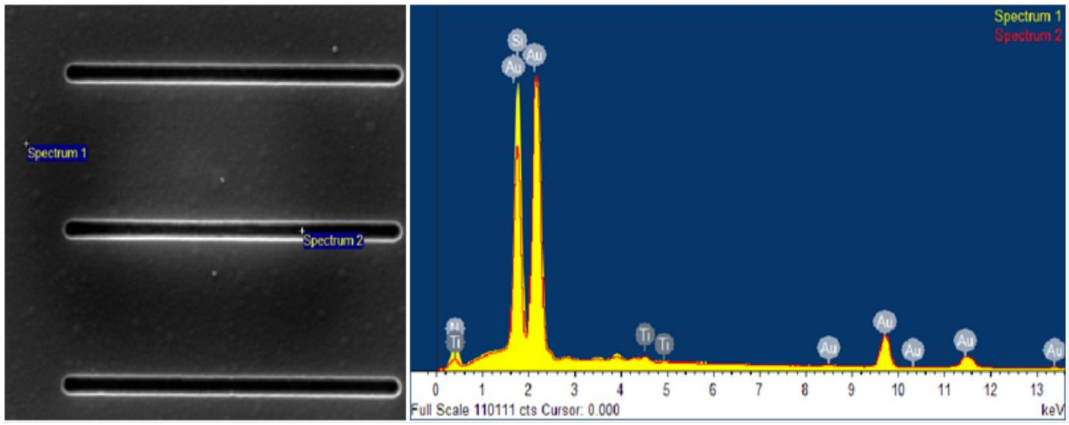


Figure 3.6: SEM image of design b3 of 200 nm recess depth (microband with 100 nm critical dimension) (left) and EDX analysis for the same microelectrode (right).

The SEM also was conducted on the glass-based microelectrode array. For the microelectrode array with 10 µm critical dimension, the designs were successfully patterned on the surface (Fig. 3.7).

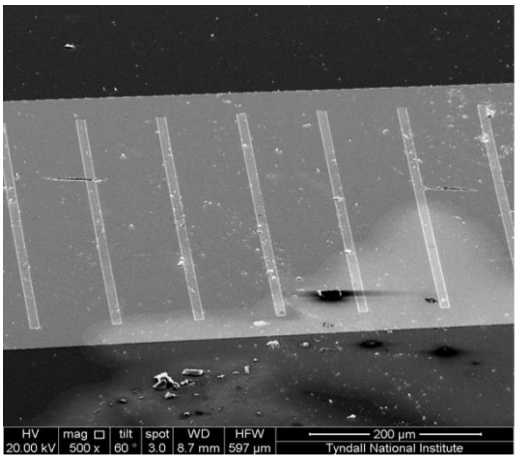


Figure 3.7: SEM image of glass-based microelectrode array for 10 µm microband array.

Table 3.2 Expected and achieved critical dimensions for microelectrode array on silicon substrate

		200 nm		300 nm		500 nm	
Design	Critical dimension, µm	Dimensions achieved, µm	Relative error	Dimensions achieved, µm	Relative error	Dimensions achieved, µm	Relative error
d1	10	9.31	-0.07	8.89	-0.11	8.89	-0.11
d2	1	1.17	0.17	1.23	0.24	0.97	-0.04
b1	10	9.52	-0.05	10.26	0.03	10.58	0.06
b2	1	1.20	0.19	1.30	0.30	1.03	0.03
b3	0.1	0.25	2.50	0.28	2.79	0.08	-0.16

3.4 Electrochemical Studies

The electrochemical analysis procedure described here has been established and successfully used in Tyndall National Institute for many years. The characterisation protocol has been published in a number of papers [2, 5, 14]. Prior their use, the microelectrode array chips were treated for 3-5 minutes in plasma-cleaner at 100 W, 600 mTorr to remove residual organic matter that may remain after the fabrication process. The electrodes were then rinsed with nanopure water and dried with nitrogen flow. The justification on cleaning the silicon-based microelectrode array has been described earlier in Chapter 2 (Section 2.3). The electrochemistry study was carried out in 1 mM solution of ferrocenecarboxylic acid (hereafter abbreviated as FCA) in PBS (0.01 M, pH 7.4). In this particular study, the fabricated microelectrode array chip was connected to the potentiostat using a custom made connector kindly provided by Uniscan Limited (Buxton, UK).

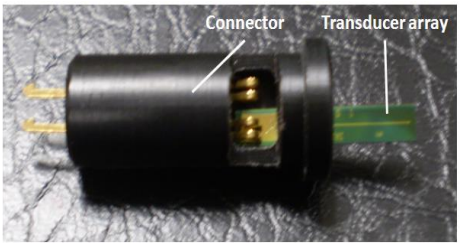


Figure 3.8: Picture of the custom made connector with the fabricated microelectrode array

3.4.1 Role of Passivation Layer

Passivation layers can be either organic or inorganic in nature. The example of organic passivation layer is the polyimides, and generally applied to the substrate by spin-coating process. Inorganic passivation layers, on the other hand, include silicon dioxide (SiO_2), silicon nitride (Si_3N_4), silicon oxinitrite ($Si_xO_yN_z$) and silicon carbide (SiC). Inorganic passivation layer can be applied as monolayers, duplex layers (e.g. SiO_2/Si_3N_4) or triplex layers (e.g. $SiO_2/Si_3N_4/SiO_2$, abbreviated by ONO). These layers are generally prepared by PEVCD via decomposition of appropriate gas

mixtures [15]. The optimisation of the passivation layer for silicon-based microelectrode array using buried conducting track with duplex (SiO_2/Si_3N_4) or triplex ($SiO_2/Si_3N_4/SiO_2$) layers has been studied in 2000 by Faβbender et al. [16].

In our study, using a duplex layers, silicon nitride layer was deposited on top of SiO_2. This passivation layer allows the contact of the solution only with the electrodes. In order to verify the efficiency of the Si_3N_4 layer in preventing diffusion and reaction at the underlying gold layer with the ferrocenecarboxylic acid, a cyclic voltammetry (CV) was carried out in the redox solution using microelectrodes with no opening in the silicon nitride layer.

Figure 3.9 shows the CV responses from an array of 1 μm microdisc (d2 design) to 1 mM FCA in PBS, at 5 mV s^{-1}; and the response from a passivated electrode with no microdisc patterning. Both d2 design and the control design with no opening had similar gold metal layout of 0.16 mm x 0.16 mm (surface area 2.56 x 10^{-4} cm^2). No faradaic current was recorded when there was no opening in the silicon nitride on the control designs, even for the thinnest passivation layer.

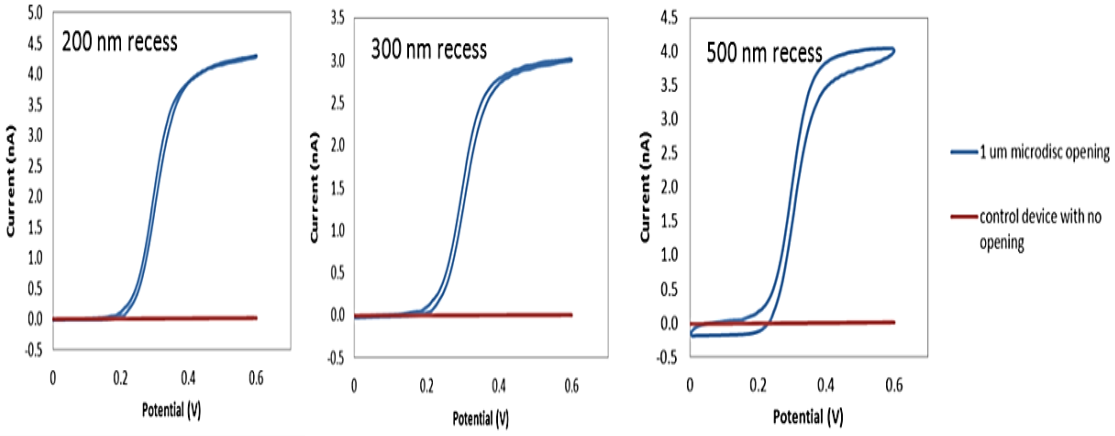


Figure 3.9: CV of 1 μm microdisc (d2) (red curve) and a control microelectrode with no opening in the Si_3N_4 (blue curve) in 1 mM FCA in PBS. Scan rate 5 mV s^{-1}.

The capacitance of the electrodes was estimated from CV experiments using the control design in 1 mM FCA in PBS (Fig. 3.10). Under these circumstances, no

faradaic current was present. The capacitance values were determined from the charging currents measured at +0.1 V at variety of sweep rates.

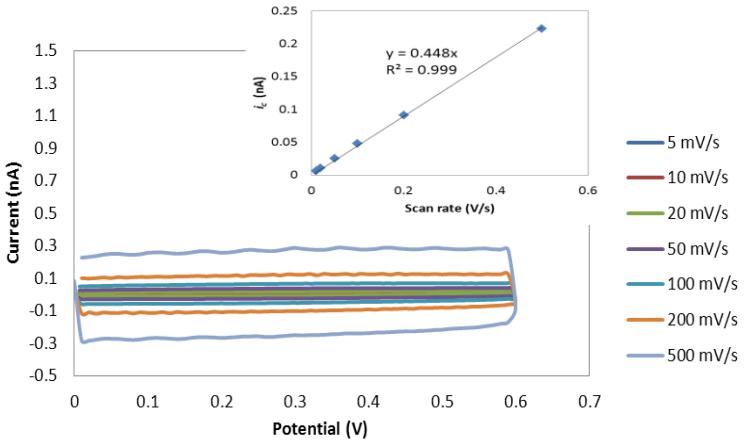


Figure 3.10: Microelectrode with no opening on the Si_3N_4 layer response in 1 mM FCA in PBS with Si_3N_4 thickness of 200 nm at charging current +0.1 V. *Inset*: Linear dependence of capacitive current, i_c, on the scan rate for the control microelectrode.

It was observed that the charging current, i_c, increased linearly with the scan rate, v (Fig. 3.10 inset). From this linear relationship, the capacitance contribution can be quantified from the slope ($2AC_{dl}$) of the following equation [17-19]:

$$i_c = 2AC_{dl}v \qquad \ldots . (Eq. 3.1)$$

The capacitance for the control microelectrode with no opening were found 0.83 ± 0.04, 0.82 ± 0.04 and 0.81 ± 0.03 µF for silicon nitride thicknesses of 200, 300 and 500 nm respectively. All these values were equal within measurement accuracies. Thus, the increment of the passivation layer thicknesses did not resulted in a significant decrease of the parasitic capacitance.

Although passivation layer provides protection to the electrode surface from scratch and particle contamination during the fabrication process [15], studies have shown that passivation layer has resulted in a slight reduction of the observed steady state current around 10% or more depending on the recess depth [20] and also a sensitivity drop of 13% of bio-impedance measurements [21, 22].

3.4.2 Cyclic Voltammetry Studies- Experimental vs. Theory

Cyclic voltammetry is a powerful electroanalytical method, often the first choice to characterise a new electrochemical system. Voltammetric studies with a model electroactive species are frequently used to determine nanoelectrode dimensions where imaging is not possible and to investigate the diffusion characteristics of the probe species to the electrode surface [2].

Microdisc Array

In cyclic voltammetric studies with microdisc electrode arrays, steady-state responses are expected if the hemispherical diffusion layers on the individual microelectrodes are not perturbed by the diffusion layers of the neighbouring microelectrodes. However, once the adjacent diffusion layers overlap, peak-shaped CVs with smaller current densities are observed, which is known as "shielding effect" [23].

CV curves for disc arrays of d1 (10 μm disc diameter) and d2 (1 μm disc diameter) (Fig. 3.11) obtained exhibited steady state shape peak at 100 mV s^{-1} for all wafer thicknesses of 200, 300 and 500 nm. Each electrode design was measured using 3 different electrodes (denoted as chip 1, 2 and 3) and an average of each reading was taken from 3 measurements (n=3) to study the repeatability and stability of the electrodes responses.

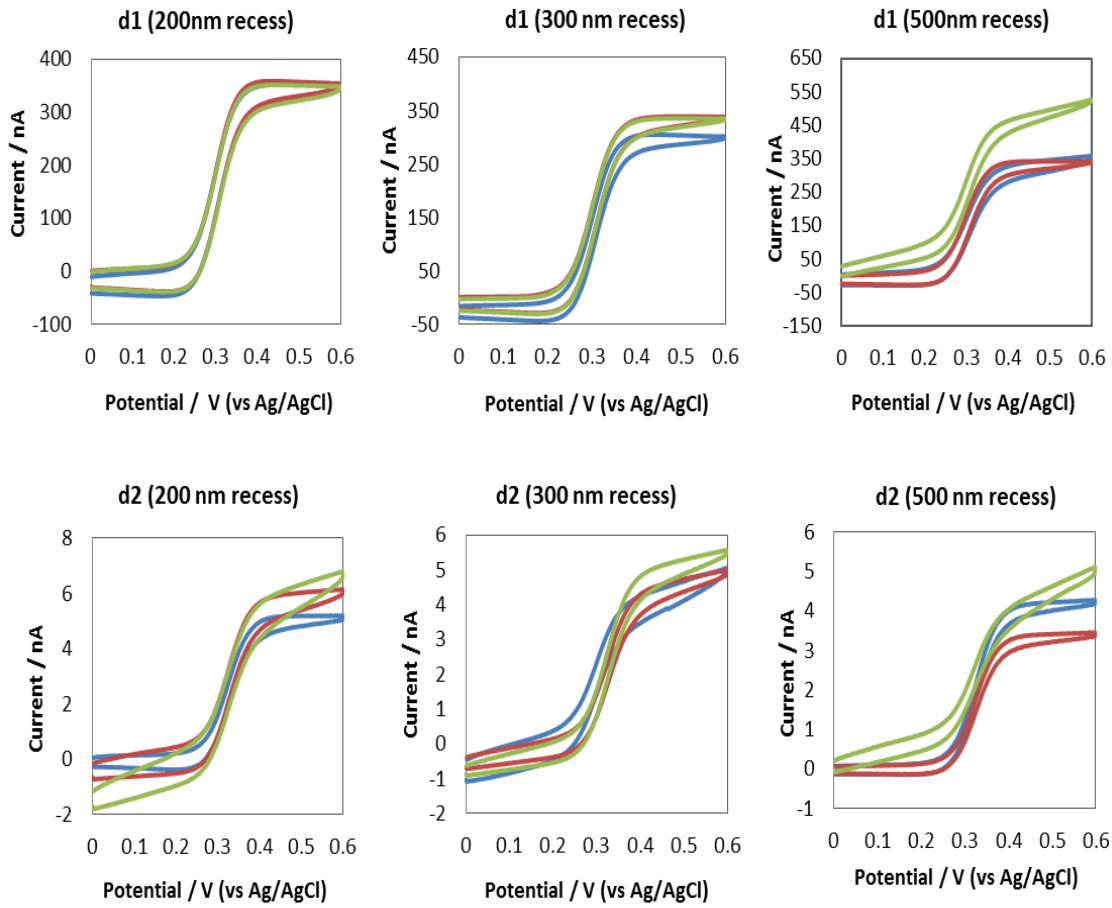


Figure 3.11: CV for disc array of d1 (10 µm disc diameter) and d2 (1 µm disc diameter) for all recess depths. Measurements were made using 3 different chips, scan rate 100mV s^{-1} in 1 mM FCA in PBS.

Comparing the steady-state voltammogram obtained from the disc arrays of d1 and d2 with the voltammograms from five categories of diffusion zones on disc microelectrode array as outlined by Guo and Lindner [23] (Fig. 3.12), the diffusion mode of the studied microdisc arrays can be assigned to category III. In this category, the diffusion zone resembles a hemispherical (also known as non-linear) diffusion layers on individual microdisc and no overlapping of diffusion zones is observed. This particular condition is referred as diffusional independence [24] and this ideal characteristic is aimed/favoured in a microelectrode array design and fabrication. Davies & Compton, described such voltammetry pattern as category 2 voltammetry (inset Fig. 3.12); where the diffusion layer thickness, δ, is larger than the microdisc radius ($\delta > a$) but smaller than its centre-to-centre spacing ($\delta < d$) [25].

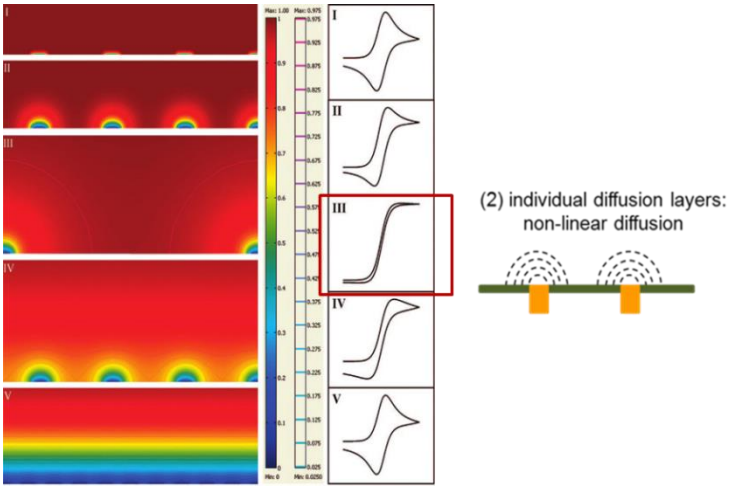


Figure 3.12: Simulated concentration profiles with isoconcentration contour lines over a microelectrode array representing the five main categories of diffusion modes with the related CVs of each category according to Guo and Lindner (2008) [23]. *Inset*: Diffusion profile of Category 2 suggested by Davies & Compton (2005).

The diffusion domain radius, R_{max}, for a microdisc array arranged in a hexagonal manner (Fig. 3.13) can be found from the cylindrical radial coordinate, r, using the following equation [24] (The expression R is used as the radial coordinate parameter in the numerical simulation):

$$\frac{\sqrt{3}}{2}d^2 = \pi r_{max}^2 \qquad \dots (Eq. 3.2)$$

where d= centre-to-centre spacing and r=radius of the disc.

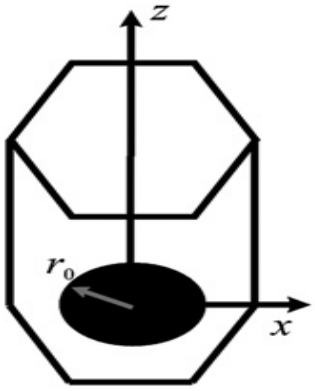


Figure 3.13: Unit cell in Cartesian coordinate hexagonal array.

Taking into account the diffusion layer thickness, δ, is similar to the diffusion domain radius, R_{max}, we can then find the δ value. The δ for both d1 and d2 calculated are 52.5 μm and 10.5 μm respectively. These values are within the range as outlined by Davies & Compton (2005) for Category 2 diffusion profile, i.e. $\delta > r$ and $\delta < d$ (d1: r=5 μm, d=100 μm; d2: r=0.5 μm, d= 20 μm).

A direct and easy calculation to verify the steady-state response for a microdisc electrode was suggested earlier by Fletcher and Horne in 1999 [3]:

$$d \geq 20r \quad \ldots (Eq. 3.3)$$

where d= centre-to-centre spacing and r=radius of the disc.

Similar to this, another given assumption that no overlapping diffusion layer occurred for microdisc array is calculated by the ratio of centre-to-centre spacing (r_d) and the radius (r_r). The large ratio of r_d/r_r minimises the overlaps between diffusion zones formed at adjacent interfaces [26]; no overlap occurs between micro-interfaces for ratios r_d/r_r of 20 and more [27]. In this study, the ratio for r_d/r_r for d1 and d2 microdiscs were both found 20 and 40 respectively hence suggesting no overlapping of diffusion layer should take place in this case.

Microband Array

For the microband electrodes of b1 on the other hand, the CVs tended towards slightly peak-shaped voltammograms for b1 and a steady-shape voltammogram for b2 was observed at scan rate of 100 mV s^{-1} (Fig. 3.13). The fact that microbands do not attain steady-shape voltammetry has been highlighted by Bond et al. in 1989 [28]. It was earlier deduced that only linear diffusion is possible for the recessed microband electrode geometry [29]. According to Nagale & Fritsch (1989), the band electrodes exhibit sigmoidal-shaped voltammograms at lower scan rates and are scan rate dependant [30]. At higher scan rates, cyclic voltammograms became more peak shaped due to an increasing contribution from linear diffusion [31]. As the categories of diffusion layers on microdisc arrays are also valid for discussing microband arrays [32], this type of CV can be concluded as Category IV from the previous Fig. 3.12. The type of diffusion suggested is a mixed diffusion layers of individual and little

overlapping of the individual diffusion layers. The size of the diffusion layer over the microband electrodes can be controlled by varying the scan rate. Changes in scan rate are able to induce transitions between Davies & Compton's categories on a fixed array dimension [32].

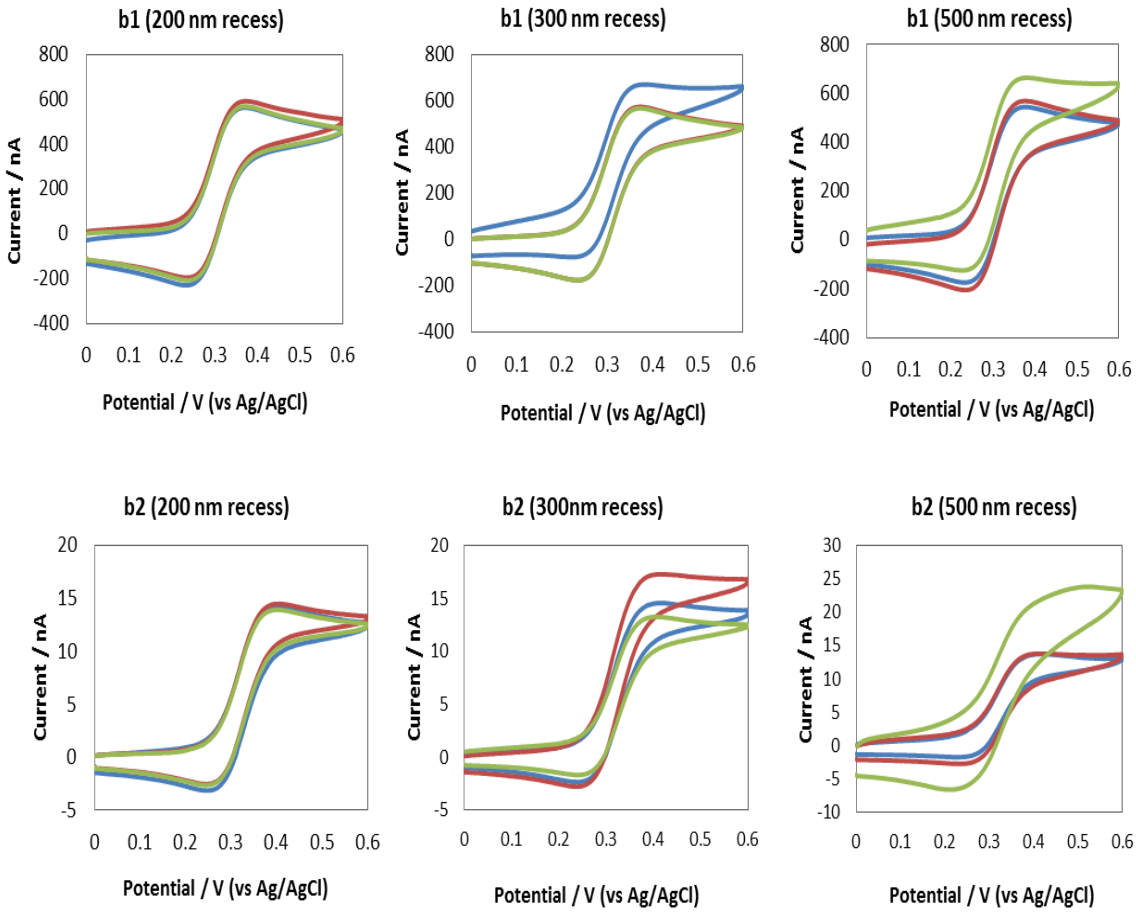


Figure 3.14: CV for microband array of b1 (10 µm band array) and b2 (1 µm band array) for all recess depths. Measurements were made using 3 different chips, scan rate 100mV s^{-1} in 1 mM FCA in PBS.

However for the b3 design, it was found that the CV varied from one recess depth to another. For 200 nm recess, the CV exhibited peak shape even at lower scan rate of 10 mV s^{-1} indicative of capacitive background that may suggest 'leaky' band electrodes due to delamination defects during fabrication [15, 31, 33]. The CVs for 300 and 500 nm recess depth at 10 mV s^{-1} scan rate on the other hand, were in

resemblance with steady-state shape voltammogram although capacitance effect still can be seen.

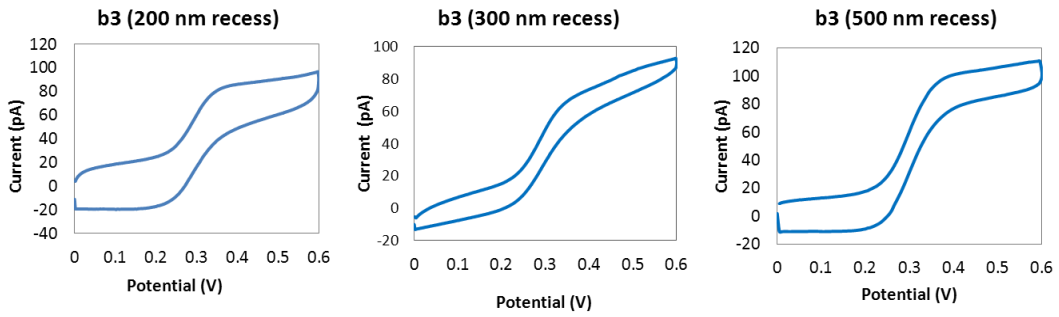


Figure 3.15: CV for band array of b3 of all recess depths. Scan rate 10 mV s^{-1} in 1 mM FCA in PBS.

The CV for the glass-based microelectrode array for both 10 µm microdisc and microband that were successfully fabricated were compared to those of silicon-based microelectrode array at 200 nm recess depth (Fig. 3.16). It was found that the CV for both substrates at the same dimension were within the same range and did not shift greatly hence suggesting the diffusion profile similar to described previously.

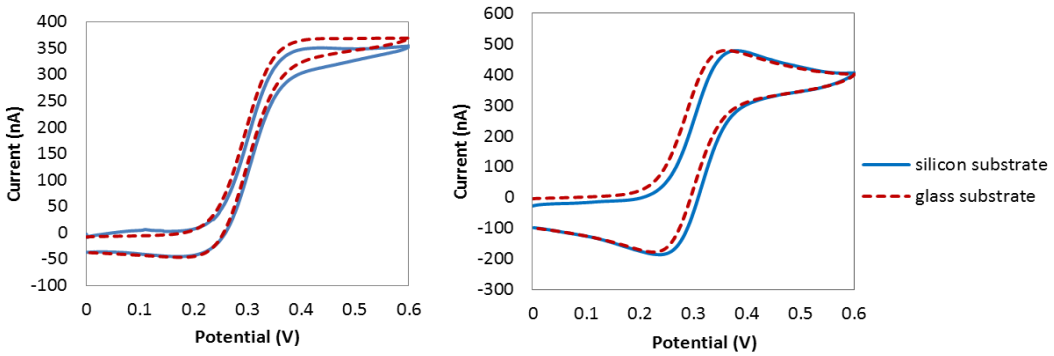


Figure 3.16: CV comparison for glass-based (red dotted line) and silicon-based microelectrode array (blue line) for 10 µm microdisc (right) and 10 µm microband (left) at 200 nm recess depth. Scan rate 100 mV s^{-1} in 1 mM FCA in PBS.

Limiting Current

The ideal voltammetric response for a steady-state response of an individual diffusion layer is the response of an individual microelectrode multiplied by the total number of electrodes in the array. This microelectrode response is characterized by the limiting current, which represents a swing of its CV characteristic and depends on electrode geometry.

For a recessed microdisc electrode array, the limiting current is defined by Eq. 3.4 [34] :

$$i_{lim} = \left(\frac{4\pi nFCDr^2}{4L + \pi r}\right)N \qquad \ldots (Eq. 3.4)$$

where n is the number of electrons involved in the reaction, F is Faraday constant (96,485 C mol^{-1}), C is the bulk concentration of ferrocene carboxylic acid (mol cm^{-3}), D is diffusion coefficient (5.7×10^{-6} cm^2 s^{-1}), r is the disc radius (cm), L is the silicon nitride thickness (recess depth) (cm) and N is the number of electrodes in an array.

For the microband electrode array, Eq. 3.5 was employed without taking into account the recess depth [2, 35]:

$$i_{lim} = \left(\frac{2n\pi FCDl}{\ln(64\ Dt/w^2)}\right)\ N \qquad \ldots (Eq. 3.5)$$

where l is the band electrode length (cm), w is the band electrode width (cm), t is the time of experiments and is equal to RT/Fv, where R is the gas constant (8.314 J mol^{-1} K^{-1}), T is the temperature (Kelvin), v is the scan rate (V s^{-1}), The other parameters are as described above.

Later, Guerette et al. [31] gave the following approximate expression for the diffusion-limited current for nanoband electrode as a function of recess depth (L):

$$i_{lim} = \left(\frac{nFDCl}{(\frac{1}{2\pi}\ln\left(\frac{64Dt}{w^2}\right) + \frac{L}{w}} \right) N \qquad \ldots (Eq. 3.6)$$

The limiting current comparison between theoretical and experimental for both microdisc and microband arrays are presented in Table 3.3. Theoretically, the diffusion limited current (i_{lim}) will decrease quickly as the depth of recess increased.

Table 3.3 Comparison between theoretical current and experimental current for microelectrode array of all recess depths*

Design	Recess depth/nm	Equation	Theoretical current/nA	Experimental current/nA
Microdisc	200		329	344±5
d1	300	**Eq. 3.4**	321	328±5
	500		306	318±12
	200		5.47	4.9±0.3
d2	300	**Eq. 3.4**	4.68	3.9±0.6
	500		3.63	3.3±0.7
Microband	200			529±7
b1	300	**Eq. 3.5**	649	510±28
	500			517±16
	200		632	529±7
b1	300	**Eq. 3.6**	624	510±28
	500		607	517±16
	200			13±0.3
b2	300	**Eq. 3.5**	17	13±2
	500			14±5
	200		15.0	13±0.3
b2	300	**Eq. 3.6**	14.1	13±2
	500		12.7	14±5

* The recess depths used in the calculation were taken from the estimation of the fabrication aspect, i.e. not determined/measured from the SEM.

Table 3.3 (continued)

Design	Recess depth/nm	Equation	Theoretical current/nA	Experimental current/nA
Microband	200			0.06±0.002
b3	300	**Eq. 3.5**	9.4	0.06±0.003
	500			0.07±0.001
	200		4.53	0.06±0.002
b3	300	**Eq. 3.6**	3.71	0.06±0.003
	500		2.73	0.07±0.001

A good agreement between experimental and theoretical data with acceptable standard error was found for microdisc array of d1 and d2. For the microband array, the discrepancy of theoretical limiting current calculation without and with considering the recess depth (Eq. 3.5 and Eq. 3.6 respectively) varied from 2-7% for 200 nm recess depth, 11-25% for 300 nm recess depth and greatly affected the 500 nm recess depth with 50-71% difference. It is thus prudent to take into account the recess depth when calculating the limiting current especially when dealing with large recess depth. Using Eq. 3.6 that considers the recess depth for the microband design, both b1 and b2 have the experimental limiting current within the close vicinity to the theoretical ones.

However, the current measured for the b3 is 100 times lower than expected. Such negative and large deviations for smaller width dimension of nanoband have been observed and reported before by several other groups [2, 30, 33]. The decrease of the current might due to the overlapping of the diffusion layers of neighboring microelectrodes in an array hence the behaviour of the array becomes that of a macroelectrode and the voltammograms tail off due to planar diffusion [25, 36]. The correlation graph of the experimental current and theoretical current obtained for all the silicon-based microelectrode array designs is presented in Fig. 3.17.

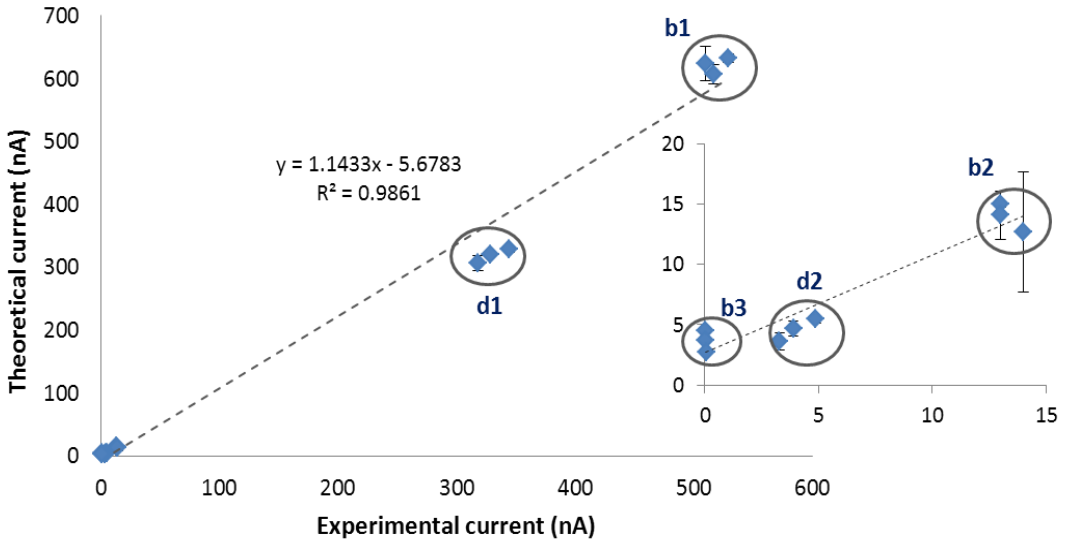


Figure 3.17: Correlation between experimental current and theoretical current for all the microelectrode designs and recess depth thicknesses. *Inset*: Correlation graph for 1 μm microdisc (d2), 1 μm microband (b2) and 100 nm microband (b3) arrays.

The limiting current can be plotted as a function of the geometrical parameters (i.e. radius and recess) to study the relationship and correlation of both. For a recessed interface, a linear dependence can be observed if the limiting currents are plotted against the term $\pi r^2/(4L+\pi r)$ for microdisc and $1/\ln (64Dt/w^2)/2\pi)+L/w$ for microband. For microdisc, the experimental limiting current obtained did not deviate greatly from the theoretical ones (Fig. 3.18A) with excellent R^2 value equal to 0.9997. This indicates that there were no overlapping of diffusion current as it was proved by the steady-state voltammogram. Hence the spacing between the microdisc in the array is sufficient to allow each individual electrode to have an independent hemispherical diffusion profile.

For microband electrode array, the experimental currents obtained for b1 are 14-18% less compared to the theoretical limiting current. Such negative deviation may suggest that overlapping diffusion profile has taken place for b1, hence reducing the effect of individual diffusion profile/current. Together with the inclined peak-shaped voltammogram, these may be related to the closer spacing between the bands [2]. On the other hand, the b2 experimental limiting current are in close agreement with the

theoretical values. Overall the R^2 found for the microband experimental current (Fig.3.18B) is still excellent.

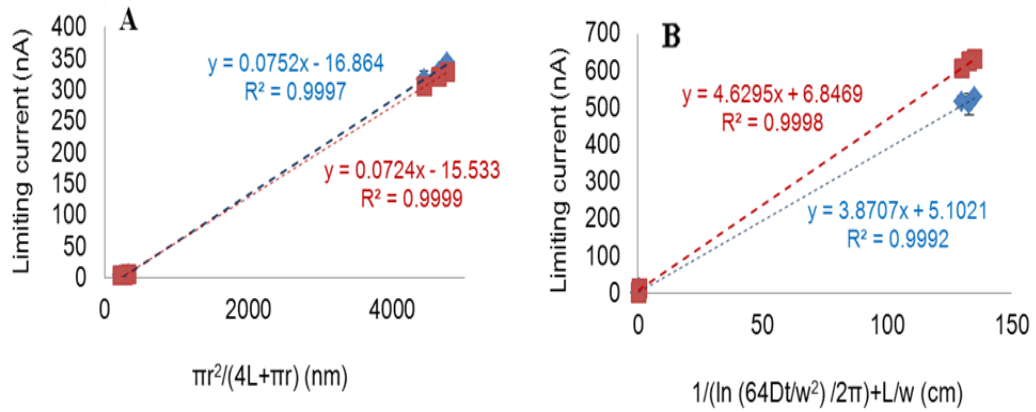


Figure 3.18: The theoretical limiting current (red line) and experimental limiting current (blue line) as a function of the electrode geometrical and dimension for (A) microdisc and (B) microband array.

In the case of microband array, the recess depth (L) to the width (w) ratio also had impact on the limiting current [5, 37]. For band electrodes with L/w ratio ≤ 0.5 (b1 and b2) the observed limiting currents were in good agreement with the calculated ones. However, as the L/w exceeded 1 (b3), the experimental current obtained progressively deviated from the theoretical current with distorted CV. Similar results whereby the experimental currents observed were greatly less that the calculated values for nanoband array with approximately 100 nm bandwidth also have been reported before [2]; and several groups also seconded that as the width/dimension of electrode becomes smaller, the deviation becomes greater [30, 33] and the voltammetric wave-shape worsen [27, 31].

It is interesting to note that the deviation is not specific to the type of material used for nanoband electrode [33], instead the deviation is attributed more to the shielding effect or electrode surface roughness from excess overhanging metal, cracks, recesses or delamination which add uncertainty to the actual exposed surface area [31].

The comparison for limiting current between silicon-based and glass-based microelectrode array at 200 nm recess depth is given in the table below. The limiting current for microband was calculated using Eq. 3.6 that considered the recess depth (L) measurement.

Table 3.4 Comparison between experimental current obtained for silicon-based and glass-based microelectrode array at 200 nm recess depth

Design	**Theoretical current (nA)**	**Experimental current (nA)**	
		Silicon-based microelectrode array	*Glass-based microelectrode array*
d1	329	344±5	339±46
b1	632	529±7	449±12

The experimental limiting current for 10 μm disc glass-based microelectrode array was closed as obtained for the silicon-based, and in excellent agreement with the theoretical current. Two chips of glass-based microelectrode were used for the measurement hence explaining the large standard deviation. For the band array, the current observed for glass-based microelectrode array was 15% less compared to the silicon-based and 29% less from the theoretical current. The decrease in current for the glass-based band array could be attributed to the scratch on the bands as seen from the previous SEM image (Fig. 3.7) thus affecting the active gold layer surface. Furthermore only one chip was available for the measurement. The reading of the limiting current could be achieved better if we had more than one chip of glass-based band microelectrode for the measurements. By having more than single chip also will allow us to verify the fabrication consistency from one chip to another.

3.4.3 Influence of the Scan Rate

Apart from the disc-to-disc distance (*d*) and the radius of the microdiscs (*r*) that influenced the diffusion profile of a microelectrode array, the scan rate (*v*) factor also is of importance. The scan rate (*v*) gives an insight of time dependence for the diffusion of electroactive species to the microarray.

The summary of the limiting current with various scan rates (5 mV s^{-1} to 500 mV s^{-1}) for designs d1, d2, b2 and b3 of all recess depth is presented in Fig. 3.19. The d1 design was strongly independent of the scan rate regardless of the recess depth whilst limiting current for d2 depended on the recess depth. Although various theoretical studies have been made to find the centre-to-centre spacing, *d*, value to exclude the possibility of shielding effect, it was reported that regardless of the *d* size, there will still be diffusion overlapping at certain scan rates [38]. The diffusion layer at disc electrodes continued to enlarge with the square root of time hence at higher scan rate, the diffusion control dominated leading to the higher current.

In the case of d2, it was seen that the linear dependence of the current in accordance with the scan rates deteriorated as the disc recess depth increased. According to Bartlett & Taylor (1988), at short times (high scan rate), when linear diffusion dominates, all of the curves converge to the Cottrell expression. At long times (low scan rate), radial diffusion becomes important and the currents tend to a steady state value. This steady state value decreased as the depth of the recess increased. The time when the current response changed over from cottrellian behaviour to steady state behaviour increased as the depth of the recess increases. This is expected because this change will occur for the deeper recesses when the concentration polarisation reaches the mouth of the recess [39]. Furthermore, as the recess depth becomes deeper, the hemispherical diffusion (non-linear) becomes less dominate and only linear diffusion prevails within the recess aperture.

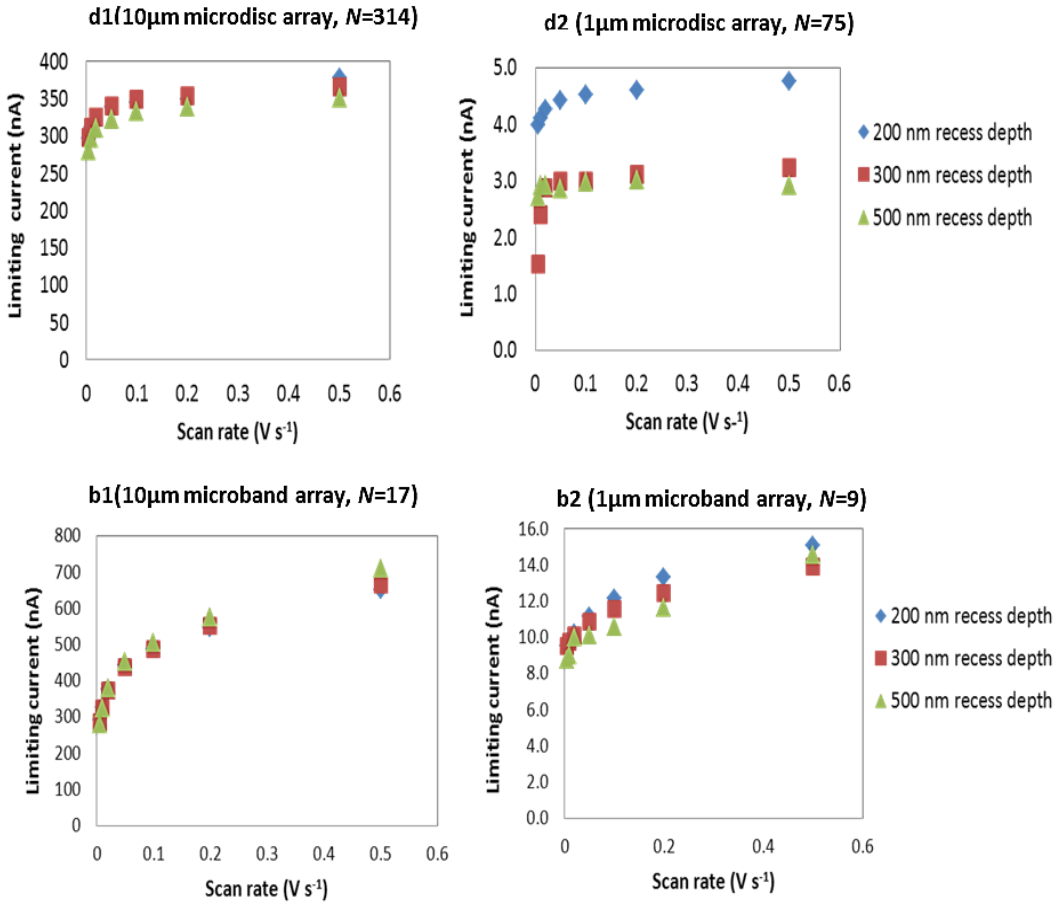


Figure 3.19: Influence of scan rate towards limiting current for microdisc array (*top row*) and microband array (*bottom row*) with critical dimensions of 10 µm and 1 µm. Scan rate study was conducted in 1 mM FCA in PBS.

The microband design of b1 and b2 on the other hand were both scan-rate dependent. For b2 particularly (1 µm microband), passivation layer thickness did affect the limiting current where it was observed that as the recess depth increased, the limiting current was reduced. In opposition to the quasi-steady-state regime usually expected at microband electrode, Amatore et al. reported that microband did reach a steady-state at longer times even in the presence of natural convection [40]. This derived from the microband design itself that can serve both as microscopic dimension (the width) or but macroscopic (the length) thereby resulting in larger currents [41].

Therefore, mass transport at microband is able to shift from linear to radial diffusion in accordance with the timescale of the experiments.

The experimental results for b2 were confirmed with COMSOL simulation* for a single 1 µm band. Overlapping diffusion zones is thus not considered in this case. In the simulation, three types of surface were studied i.e. co-planar (inlaid surface), and surface with recess depth of 100 and 200 nm. As one can see, the forward scan of the CV exhibited sigmoidal shape for the lower scan rate of 10 mV s^{-1} (Fig. 3.20a) and peak-shaped forward scan CV at higher scan rate (500 mV s^{-1}) (Fig. 3.20b).

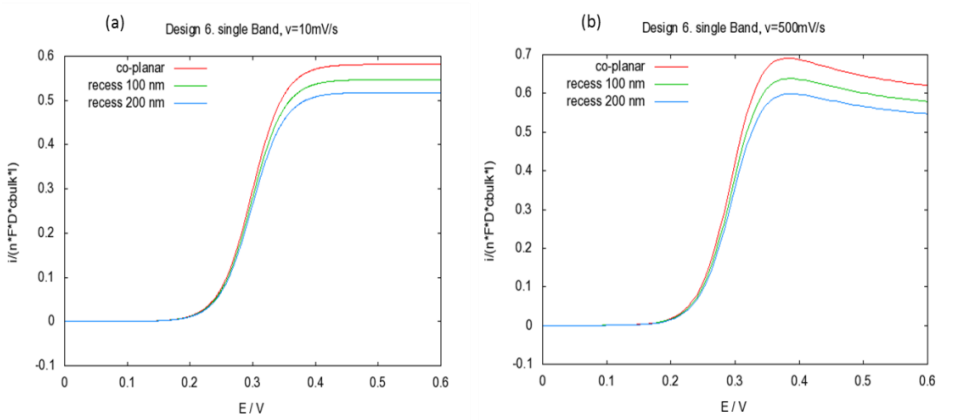


Figure 3.20: Simulations made for b2 microelectrode design with different recess depth for (a) lower scan rate (10 mV s-^{1}); and (b) higher scan rate (500 mV s^{-1}).

These simulation patterns were in agreement with the experimental curves obtained for the b2 microelectrode design at 200 nm depth recess (Fig. 3.21) and are in accordance as suggested by Nagale & Fritsch [30]. However, in Arrigan & co-worker's study that employed a single nanoband and array of five nanobands, there was no increase in faradaic current or change in wave shape observed for either nanoelectrode design within the potential sweep range 5-100 mV s^{-1} [2] which is contrary with our finding. The type of behaviour attained by Arrigan's group can be attributed to the sufficiently large interelectrode distances [34].

*CV simulation was carried out by Dr. Jorg Strutwolf, Tyndall National Institute, in November 2011

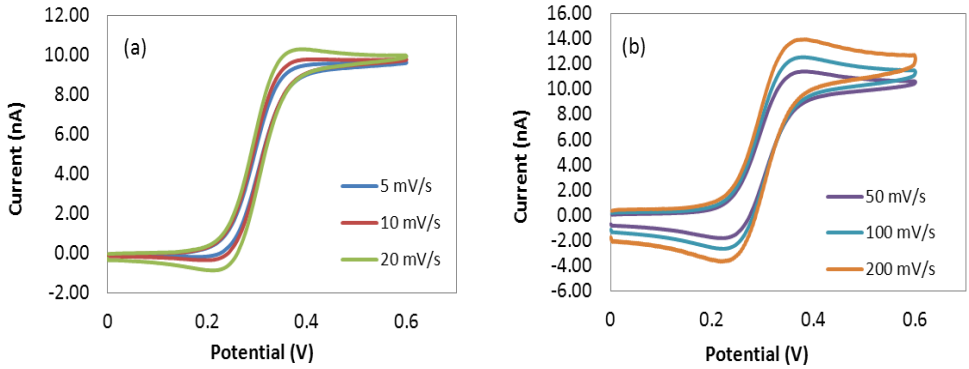


Figure 3.21: CV obtained for b2 microelectrode array for recess depth of 200 nm for (a) lower scan rates; and (b) higher scan rates in 1 mM FCA in PBS. It was observed that sigmoidal CV took place at the low scan rate and as the scan rate increased, the CV shifted to peak-shaped voltammogram.

Similar to the b2 design, b3 also is scan rate-dependent and exhibited peak-shaped CV at higher scan rate (Fig. 3.22). However as discussed earlier, CV for b3 (100 nm disc array) exhibited large capacitive background at higher scan rate more than 50 mV s^{-1} that could be addressed to the 'leaky' nanoband electrodes. The high capacitance effect of the edge band electrodes of 71.2 nm width at higher scan rate also have been reported before, indicative the defect of the silicon nitride passivation layer [30].

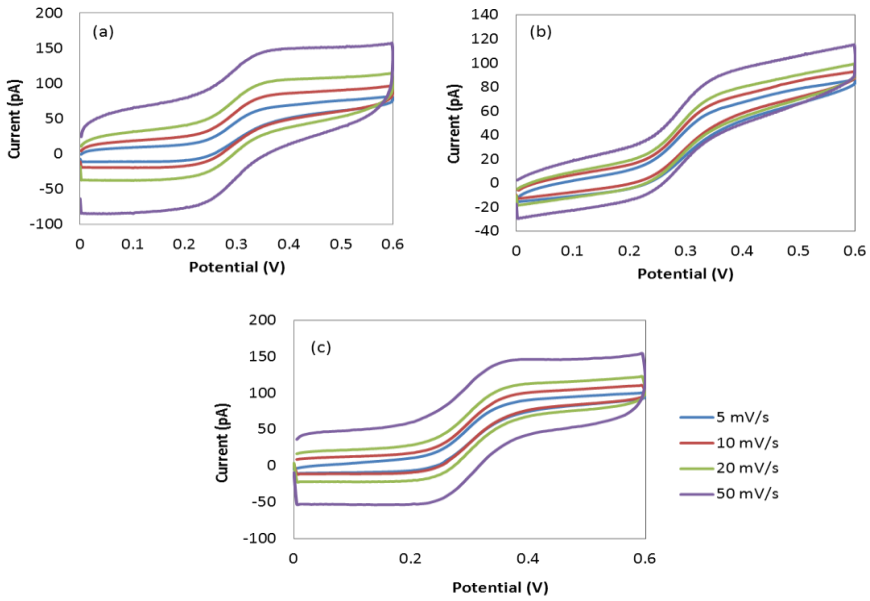


Figure 3.22: CVs for b3 microband array at different scan rates for Si_3N_4 thickness of (a) 200 nm; (b) 300 nm; and (c) 500 nm in 1 mM FCA in PBS. The capacitance CV starts trending from scan rate of 50 mV s^{-1}.

3.4.4 Electrochemical Impedance Spectroscopy Study

Despite the gaining attention and applications of the electrochemical impedance spectroscopy (EIS) technique, there is still lack of papers published in relation with EIS and microelectrodes, particularly microelectrode array and specifically recessed microelectrode array. Most of the publications available to date merely dedicated to theoretical work and simulation on planar microelectrodes [42, 43] due to the software limitation involving recessed boundaries [44].

Herein, we reported EIS experimental work carried out on the disc and band microelectrode array. The equivalent circuit models for both designs were then deduced based on the appropriate references. Due to the aging factor* of the silicon-based microelectrode array of and 1 µm and 100 nm disc, only EIS results of 10 µm critical dimension will be presented here.

* To be discussed in detail in Section 3.4.6

Microdisc Array Impedance Spectra

The EIS spectrum of the 10 µm microdisc (d1) with the three different recess depth (*L*) is first presented (Fig. 3.23). The curves for the microdisc array appeared as flattened semi-circles and this correlates well with simulation work for a recessed disc microelectrode reported by Ferrigno & Girault (2000) [44].

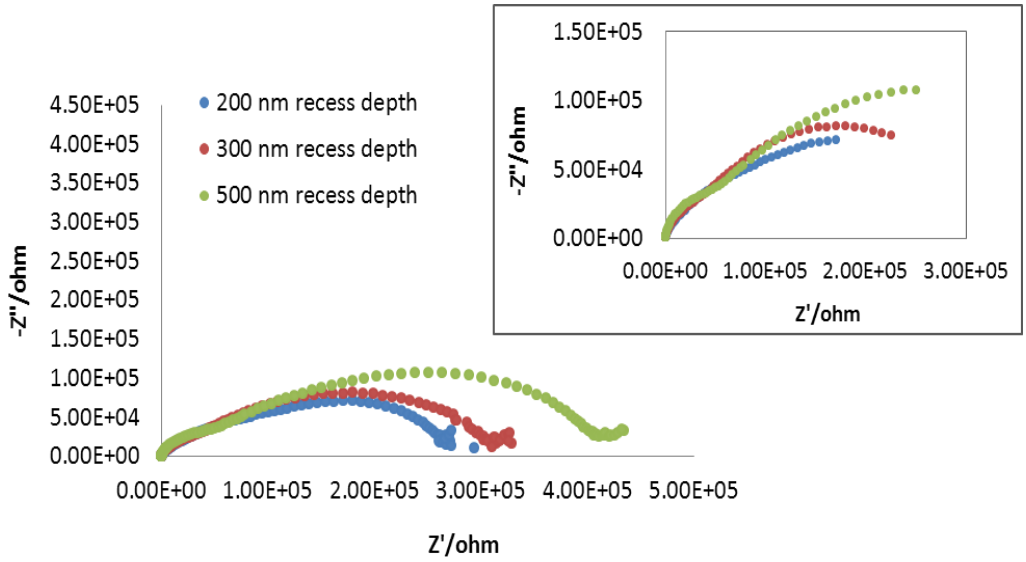


Figure 3.23: Impedance spectra for d1 microdisc arrays with different passivation layers in 1mM FCA in PBS. Frequency range 0.01 Hz -1 MHz and applied amplitude 0.01 V for all arrays. *Inset*: EIS at frequency 200-200,000 Hz.

In general, impedance plot at high frequency (left region on the Nyquist plot) reflects the charge transfer involving non-Faradaic process. Low frequency (right region on the Nyquist plot) on the other hand is indicative on the diffusion mass-charge transfer and associates with Faradaic reaction. Contrary to the situation on a macro dimension, the flux at microelectrode reached a non-zero steady-state value (Fig. 3.24). This is expressed by the impedance diagram that approaches the real axis (*Z'*) at low frequencies in comparison with the typical straight diffusion line as obtained at macroelectrodes [45]. The steady-state value (*i*) decreased as recess depth, *L*, increased hence the switching time from Cottrellian behaviour also increased

accordingly [39]. Given at a very long time i.e. the lowest frequency range (0.1- 0.01 Hz), a linear diffusion could be seen especially at the disc of 500 nm recess depth. This could be attributed to the prevailing linear diffusion within the recess. As follows from Fig. 3.23, as the *L* increased, the Warburg impedance at the lowest frequency became more obvious. The increment of recess depth also has resulted in an increase of both ohmic resistance (real impedance component, *Z'*) and capacitive reaction (imaginary impedance, *-Z''*).

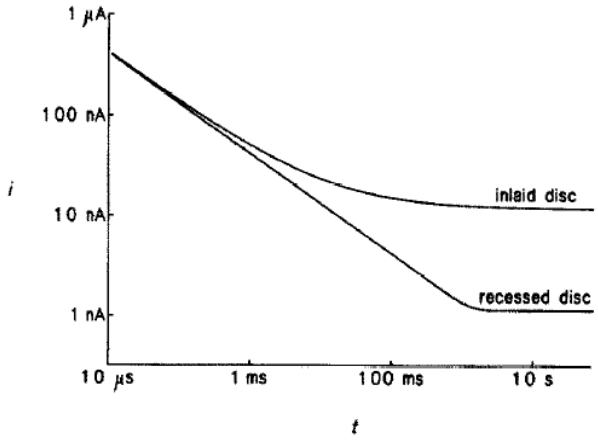


Figure 3.24: The breakdown of Cottrell equation for both inlaid and recessed microdisc. Steady-state behavior is achieved at longer time. Taken from Ref. [46].

For a small recess depth, the recessed microelectrode performs as an inlaid microdisc electrode where the diffusional impedance is similar to the impedance of a microdisc electrode. However as the *L* increased, the spherical diffusion occurring at the edge of the microelectrode is reduced; the linear diffusion dominates in the recess and the diffusional impedance evolves to the Warburg impedance [47]. This is reflected by the 'shoulder' or 'hump' presence at medium to high frequency range particularly for the recess depth 500 nm (200 -200,000 Hz) as shown in inset of Fig. 3.23. The diffusion profiles at the microelectrode thus involved more than one diffusion type i.e. semispherical diffusion at high frequency domain and linear diffusion within the recess trench at the lowest frequency range. This is in accordance with experimental and theoretical work conducted by Gabrille et al. (2006) [48].

The planar diffusional impedance of macroelectrode is a function of the angular frequency (ω) but in the case of microelectrodes, it is a function of the dimensionless parameter ($r^2\omega/D$). As the consequence, the radius of the microelectrode becomes a kinetic parameter of the studied electrochemical system [49]. Therefore, in the case of microelectrode, it is not possible to calculate the usual parameters associated to EIS such as R_s, R_{ct} and C_{dl} from equations used for macroelectrodes as these equations are only applicable in case of planar diffusion.

In the case of planar diffusion associated inlaid disc electrode, the f_{max} value can be determined from the Eq. 3.7 below [50]:

$$\omega_{max} = 2\pi f_{max} = 2.5119\frac{D}{r^2} \qquad \dots (Eq. 3.7)$$

where D is diffusion coefficient ($5.7 \times 10{-}6$ cm^2 s^{-1}) and r is a disc radius (5×10^{-4} cm for the case of 10 μm microdisc). The f_{max} calculated was 9.11 Hz for an inlaid 10 μm microdisc.

We now consider the microdisc with the thinnest passivation layer (200 nm) and calculate its f_{max} value. Supposedly the thinnest passivation layer behaved like an inlaid one, the f_{max} should be of the same value. However the f_{max} was found to be 2.63 Hz which is obviously deviate greatly with the calculated value. Such frequency dispersion, generally attributed to a "capacitance dispersion" is usually expressed in terms of a constant-phase element (CPE) in an equivalent circuit model [51]. In his textbook, Lvovich (2012) has outlined that variability in the thickness and conductivity of surface coating associated with three-dimensional (3-D) distribution is one of the processes that may lead to the CPE representation [52].

The equivalent circuit suggested for d1 design, based on its associated profiles of diffusion is presented in Fig. 3.25. Similarly an equivalent circuit model also has been proposed in 2006 for recessed microelectrode [48]. The Z_M was accounted for spherical diffusion opening of the recess aperture whilst Z_{DIFF} or Z_w (Warburg impedance) can be attributed to the linear diffusion that prevailed within the recess trench at a low-frequency range.

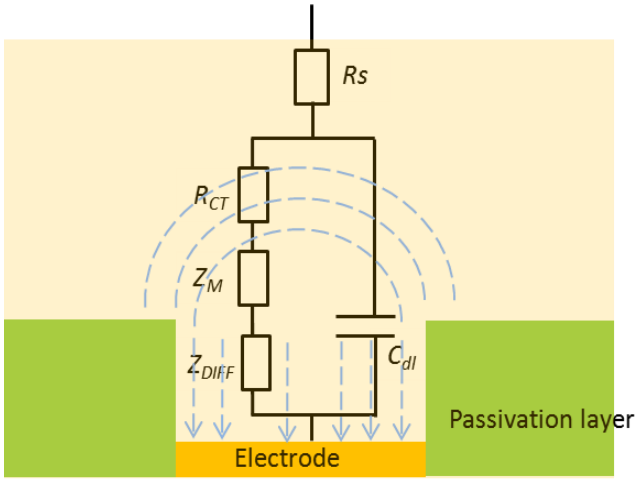


Figure 3.25: Equivalent circuit model suggested for 10 µm microdisc array.

The impedance of d2 however will not be discussed here due to aging factor of the microelectrode at smaller dimensions. This is exhibited by the sluggish CV obtained after several usages. Furthermore the EIS spectra from one microelectrode of the same recess depth varied greatly to another. A simulation however was carried out in order to study the smaller radius impact on impedance curve on an inlaid disc (Fig. 3.26). For the simulation on the ideal impedance measurement, the following equations were used as established by Fleischmann and co-workers (1991) [42]:

$$\mathrm{Re}(Z_d) = \frac{4RT}{\pi n^2 F^2 \sqrt{D\omega}\, a^2 c^{\infty}} \Phi_4\left(\frac{a^2\omega}{D}\right) \quad \ldots (Eq.\,3.8)$$

$$-\mathrm{Im}(Z_d) = \frac{4RT}{\pi n^2 F^2 \sqrt{D\omega}\, a^2 c^{\infty}} \Phi_5\left(\frac{a^2\omega}{D}\right) \quad \ldots (Eq.\,3.9)$$

where Z_d is the diffusion impedance, $\mathrm{Re}(Z_d)$ and $\mathrm{Im}(Z_d)$ are the real and imaginary parts of Z_d respectively, R is the gas constant, T is the temperature, and Φ_4 and Φ_5 are tabulated functions [42]. The magnitude of diffusion impedance was observed to increase inversely with the electrode radius. Such behavior also has been verified by other researcher's simulation on microelectrode embedded in a thin-layer cell [48].

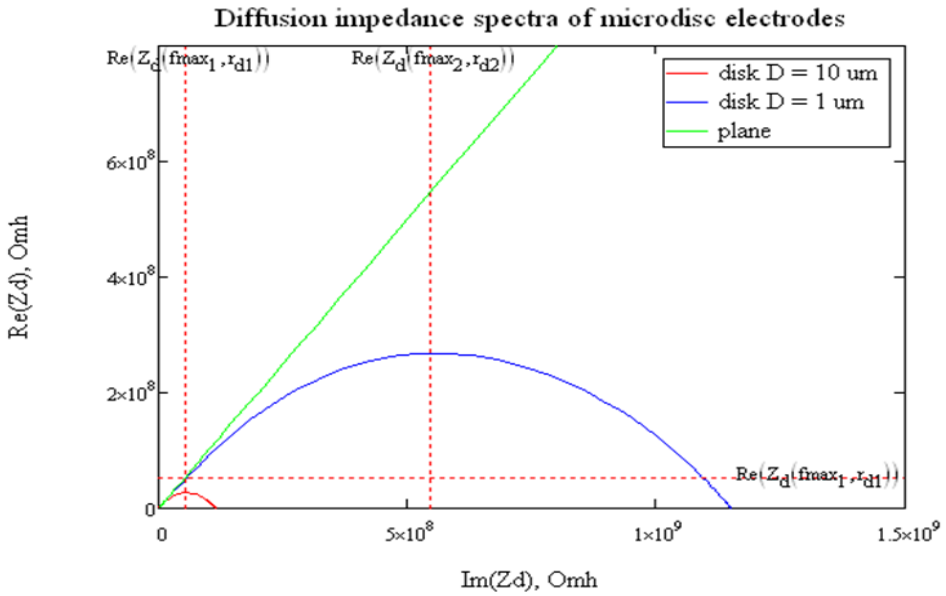


Figure 3.26: Simulated diffusion impedance spectra for a planar macroelectrode and microelectrodes with diameter 10 and 1 μm.

Microband Array Impedance Spectra

For the microband electrode (b1) on the other hand, a semi-circle region followed by a straight line at low frequency was observed (Fig. 3.27). The patterns were similar regardless of the recess depth. Although it was previously reported that only linear diffusion is possible for a recessed microband electrode [29], our earlier CV study and simulation has revealed that a mixed diffusion profile (linear at slow and radial at fast diffusions) were suggested for both b1 and b2. This assumption is valid as microband array possess both micro and macro dimensions [40, 41].

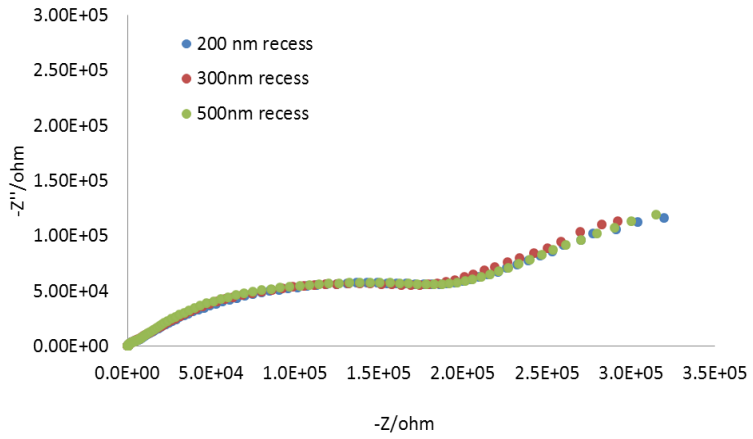


Figure 3.27: Impedance spectra for b1 microband in 1 mM FCA in PBS. Frequency range 0.01-1 MHz and applied amplitude 0.01 V for all recess depths.

According to Kovach et. al (1985), the diffusion to an electrode surface is a function of the electrode geometry and the electrode size [53]. As the width of the b1 consist of smaller dimension (10 μm) which is opposed to its length (500 μm), the diffusion profile at these edges were of approximated with radial diffusion. On a planar band electrode, this non-linear diffusion effect could be prominent [53, 54] but since our microband insulated down in the recess, linear diffusion also may took place in this case (Fig. 3.28).

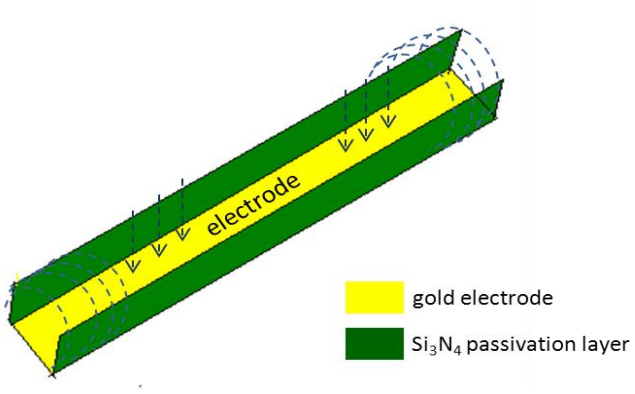


Figure 3.28: Approximation of spherical diffusion at band's width (microscopic) and linear diffusion within the band's length (macroscopic) on the electrode embedded in passivation layer (not to scale).

The first semi-circle of the impedance can be attributed to charge-transfer process and spherical diffusion on the band that occurring at high frequencies i.e. shorter times. However, due to the nature of the macroscopic length of band and the recessed area, the diffusion associated with the Warburg impedance emerged at lower frequency (1 Hz – 0.01 Hz) that correlates well with linear diffusion happening at longer times scale reported [40].

Similar to the microdisc array, due to this mixed diffusions profile; the parameters such as R_s, R_{ct} and C_{dl} could not be determined from this band array impedance spectra by using equations obtained for macroelectrodes.. The aging and factor of the smaller microdisc array dimension of 1 µm also were found to be recurring at the microband hence the results of these dimension were not presented in this thesis. The previous suggested equivalent circuit for the microdisc array hence could be applied in the case of microband array.

EIS Comparison Between Silicon-Based and Glass-Based Microelectrode Array

The EIS for the glass-based microdisc array was also compared to the silicon-based disc array of the same recess depth (200 nm) (Fig. 3.29). It was found that glass-based microdisc array exhibited higher ohmic resistance than the silicon-based microdisc. This could be attributed to the dead electrodes presence in the silicon-based microdisc [8, 24, 55].

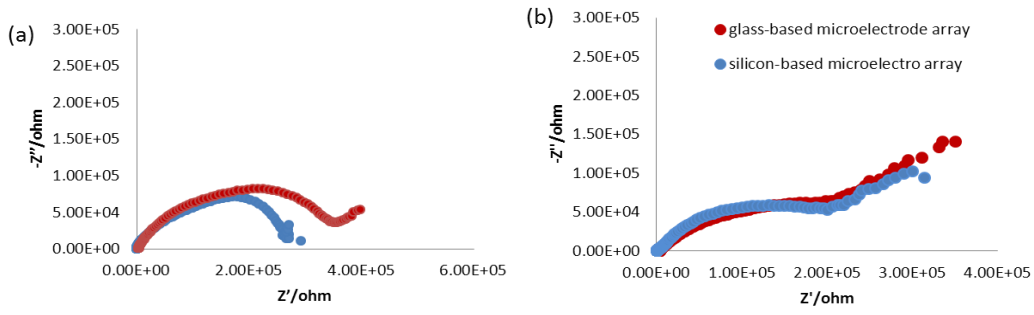


Figure 3.29: EIS comparison for glass-based (red marker) and silicon-based (blue marker) for (a) 10 µm microdisc array and (b) 10 µm for microband array in 1 mM FCA in PBS. Both microelectrode arrays have recess depth of 200 nm. Frequency range 0.01-1 MHz and applied amplitude 0.01 V for all recess.

The EIS curve for microband electrodes for both substrates on the other hand showed a good and similar shape. These studies indicated the performance of the glass-based microelectrode is as good as the silicon-based in terms of CV and EIS at 10 μm dimension.

3.4.5 Influence of Recess Depth on CV and EIS Experiments

The influence of the silicon nitride thickness on both CV and EIS was studied. The relative current is plotted for the different thicknesses for the microelectrodes of d1, d2, b1, b2 and b3 (Figure 3.30). Theoretically, the diffusion limited current decreases as the depth of recess increases. Silicon nitride thickness has very little influence on the current for the designs with bigger diameter for microdisc or recess depth to width (*L/w*) ratio for microband. However, for the electrode where the radius disc is in the same range as the recess depth (d2 design where r = 500 nm and the recess is 200, 300 or 500 nm), the impact is the most pronounced with a loss of up to 50 % of the electrochemical response.

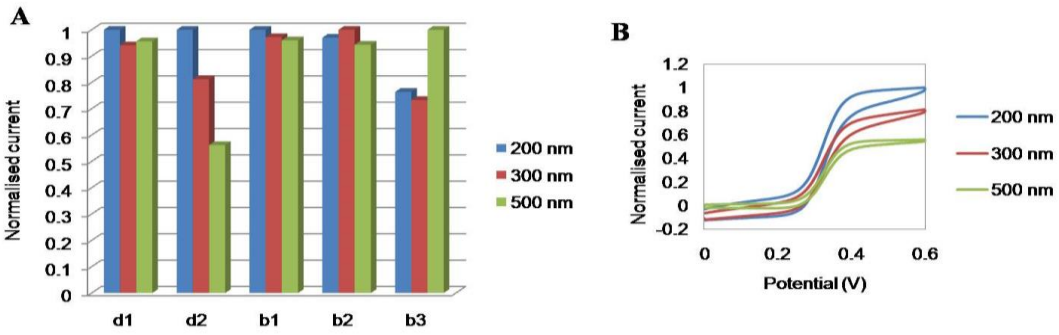


Figure 3.30: (A) Normalised current recorded for d1, d2, b1, b2 and b3 microelectrodes for the different silicon nitride thicknesses; (B) The effect of recess depth is more pronounced in d2 CV

In terms of EIS, the recess of the microdisc array was shown to have impact on the EIS curve. With an increase of the recess, both ohmic and capacitance impedance components increased accordingly. The microband arrays' EIS spectra did not exhibit significant difference for each recess depth. We can relate this with the

percentage of the recess over the electrode's aperture in which for the disc array case, the percentage is 2%, 3% and 5% for the recess depth 200 nm, 300 nm and 500 nm respectively. However for the microband array, the percentage of recess over the electrode's aperture (band's length) is 0.04% for 200 nm recess, 0.06% for 300 nm recess and 0.1% for 500 nm recess. The contribution of electrode recess to the cell impedance becomes negligible small and hence the recess factor may be omitted. However it was reported by Suh & co-workers that recessed silicon dioxide of band electrode may increase the cell capacitance [56].

3.4.6 Influence of the Nature of the Substrate

The study employing silicon-substrates and glass-substrates have allowed us to compare the fabrication and performance of the arrays on both substrates. Each substrate has its own advantages as well as disadvantages. It was found that silicon-based microelectrode array is compatible with both photo-lithography and e-beam lithography techniques. The major concern however is the aging factor and storage stability of the silicon-based microelectrode arrays especially those of smaller dimension. While 10 μm microdisc and microband exhibited good and promising results, the performance for 1 μ and 100 nm of critical dimensions were found to be sluggish and deteriorated over time. Such failure could be due to mechanical stress, film defects, chemical/electrochemical reactions or even combination of mechanical stress and chemical interaction [15]. Fig. 3.31 showed two images on a device prior and after electrochemical testing.

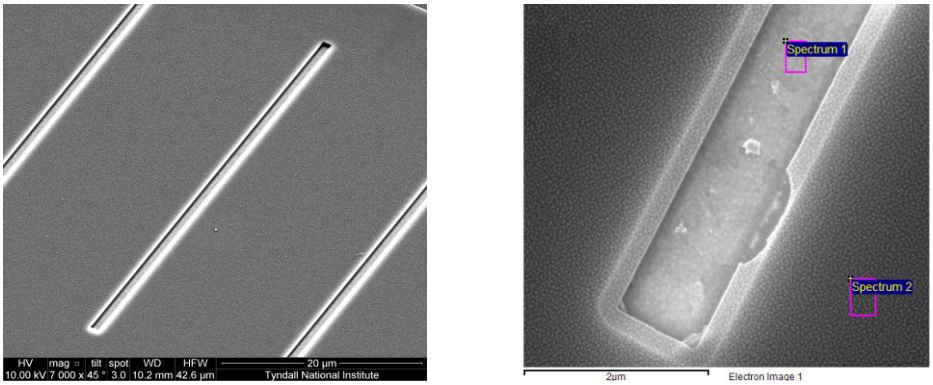


Figure 3.31: Pristine condition on an untested 1 µm silicon-based microband array (left) and cracks and delamination observed on a tested 1 µm band (right).

According to Schmitt et al. (1999), application of silicon based sensors is often hampered as they fail too fast (within minutes or only a few hours) when used in liquid media, particularly electrolyte solutions [57]. The barrier properties of passivation layers against chip degradation on exposure to electrolyte solutions were investigated in 1 M NaCl solution at pH 7. It was found that inorganic passivation layer (SiO_2, Si_3N_4 and duplex layer) exhibit poor protection (Fig. 3.32).

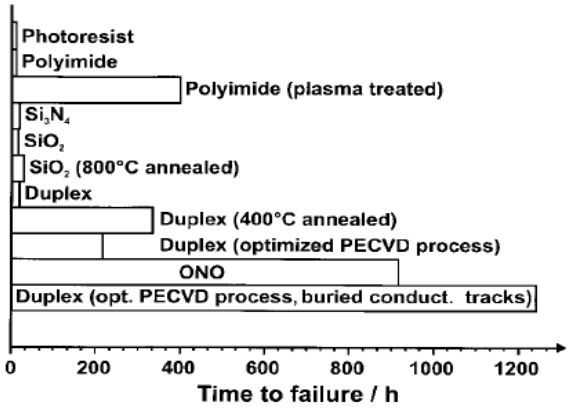


Figure 3.32: Corrosion resistance of several passivation layers over hours studied in 1 M NaCl by Schmitt and co-workers. Taken from Ref. [15].

For the glass-based microelectrode array on the other hand, the e-beam fabrication on the substrate were found to be more complicated. We also have handling issues with the glass-substrates as the dicing process resulted in broken electrodes due to the fragility and brittle nature of the glass itself (Fig. 3.33). At the same time, there was no significant difference observed in electrochemical performance between the microdisc arrays on silicon and glass substrates. Therefore, glass-substrate was not considered for further studies and subsequent fabrication of microelectrochemical cells.

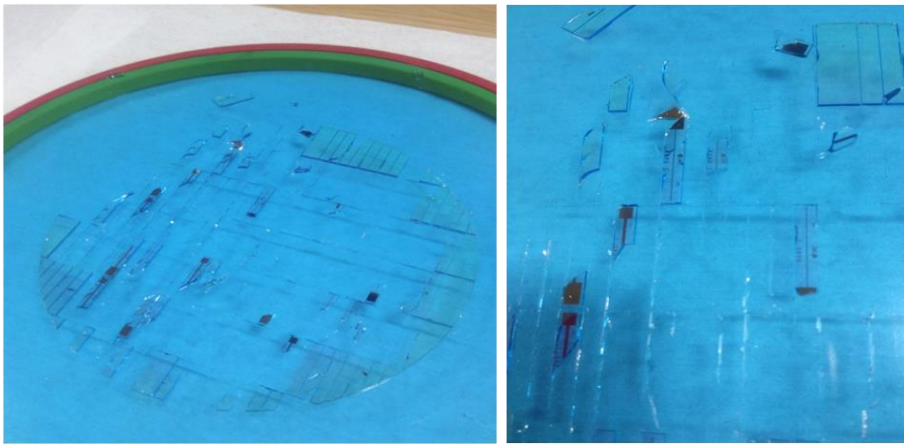


Figure 3.33: The broken microelectrode array on the fabricated glass wafers after dicing process.

3.5 Chemically Modified Electrodes for Recessed Microelectrode Array

In this second part of the chapter, we will look into the chemical modification on the fabricated silicon-based microelectrode arrays. The 10 μm microband and microdisc array were selected in this study due to their stability and reproducibility. Unlike the conventional modification involving dip-coating steps, we are venturing into electrochemical deposition techniques for the chemical modification on the microelectrode array surface. Electrochemical deposition approach is of interest as it selectively modified the area of interest without smearing the passivation tracks or unwanted area.

Two methods of chemical modification were carried out, namely electrochemically assisted self-assembly formation of sol-gel on microband array and gold nanoporous electrodeposition on microdisc array. These two methods were chosen as to our knowledge these two modification methods have not been applied to recessed microelectrode array to date. Furthermore, these methods would be interesting in biosensor application as both sol-gel silica film and nanoporous gold are widely used for biomolecule immobilisation matrix [58-60]. The modified recessed microelectrode array were characterised using both optical and electrochemical techniques. This preliminary study will provide potential insights on various chemical modifications that can be performed on the silicon-based recessed microfabricated electrode array for further biosensing applications.

3.5.1 Electrochemically Assisted Self-Assembly of Silica Film

Extensive reviews on silica-modified electrodes particularly sol-gel for biosensor application have been published by Walcarius within the first decade of year 2000 [61-64] and Gill & Ballesteros [65]. To date, microelectrode modified with sol-gel network were achieved by the means of submersion/dip-coating [66-69], drop-coating [70, 71], spin-coating [72], mixing the sol-gel derived ceramic material homogenously with graphite powder to produce ceramic composite electrodes [73]; and electrodeposition of sol-gel films [74], sol-gel mixture with entrapped enzymes [75-78] and organic/sol-gel hybrid [79]. An approach of using the sol-gel ink in direct-write assembly fabrication of indium-tin oxide also have been reported [80].

Although both dip-coating and drop-coating techniques are straight-forward and simple, nevertheless the major concerns associated with these techniques are that they are confined to flat surface and the lack of selectivity [62]. Under these circumstances, the sol-gel electrodeposition technique lends itself well in offering tunable and controlled film thickness formation on an electrode surface. The work on electrodeposition of sol-gel films have been initially described by Shacham et al. in 1999 [81] and the scope of study has been extended by Walcarius and co-workers [82, 83]. The thickness of the electrochemically deposited sol-gel layers usually ranging from several to hundred micrometers [75]. By applying galvanostatic

conditions (i.e. controlling the current) and varying the deposition time, thickness of the films can be accurately controlled and problems with overpotential can be eliminated [84].

A more ordered electrodeposited sol-gel structure could be accomplished by surfactant-templated silica film on electrode surface via electrochemically assisted self-assembly (EASA). The idea behind the template-based film is to increase the electrode surface roughness thus maximising the surface area for reaction to take place [85].

The general approach of EASA is similar to the two-step of sol-gel preparation procedures involving hydrolysis of the alkoxide at pH 3 (Eq. 3.10) followed by condensation of hydrolysed monomer at pH 9. The condensation leads to the formation of a Si-O-Si bond with the elimination of a water or an alcohol molecule (Eq. 3.11a and 3.11b). In EASA, the pH is being increased by inducing negative potential to the electrode surface [81].

$$Si(OR)_4 + 4H_2O \rightarrow Si\,(OH)_4 + 4ROH \quad \ldots(Eq.\ 3.10)$$

$$Si(OH)_4 + Si\,(OH)_4 \rightarrow (OH)_3Si\text{-}O\text{-}Si(OH)_3 + H_2O \quad \ldots..(Eq.\ 3.11a)$$

$$Si(OH)_4 + Si\,(OH)_4 \rightarrow (OH)_3Si\text{-}O\text{-}Si(OH)_3 + ROH \quad \ldots(Eq.\ 3.11b)$$

The most common precursors for silica are tetramethoxysilane, $Si(OCH_3)_4$, (TMOS) and tetraethoxysilane, $Si(OC_2H_5)_4$, (TEOS) (Fig. 3.34).

(a) (b)

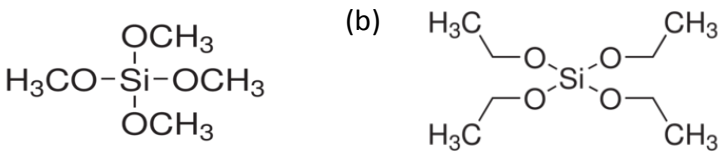


Figure 3.34: Chemical structure of (a) TMOS and (b) TEOS.

In this EASA study, the mesoporous silica films were first formed on the electrode surface by immersion in a pre-hydrolysed precursor solution containing tetraethoxysilane (TEOS) and cationic surfactant of cetyltrimethyl ammonium bromide (CTAB) at pH 3 (Fig. 3.35 top row). A cathodic potential is then applied, increasing the pH and generating hydroxyl ions at the electrode/solution interface. This resulted in the precursors condensation and concomitant growing of a surfactant-templated mesoporous silica film (Fig. 3.35 bottom row). Besides served as template, CTAB also have long been reported in sol-gel preparation as to prevent fracture in the film formation [86] and to stabilize the microscopic structure of the material upon heat-drying [87].

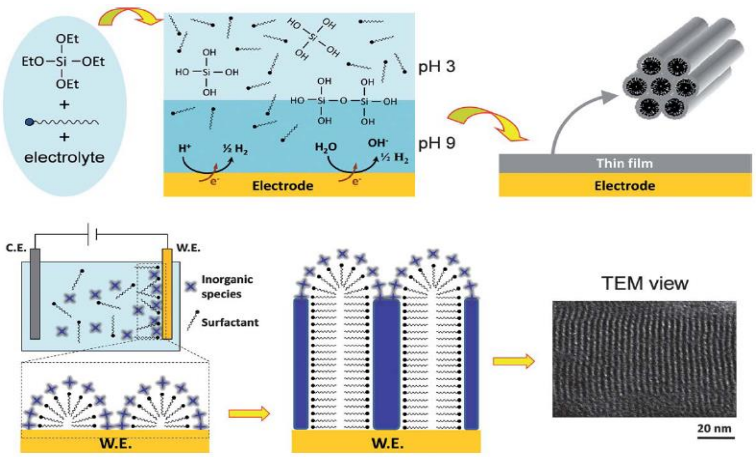


Figure 3.35: Illustration of EASA method in generating ordered and oriented mesoporous silica films on an electrode surface. Taken from Ref. [83].

EASA Silica Film on Gold Surface

The initial approach of electrochemically assisted self-assembly **(**EASA) of sol-gel in this study was first demonstrated on a 1 mm gold disc electrode surface. CTAB and TEOS precursor ratio of 0.32 was employed; as suggested by Goux et al. [84] in order to attain an aggregate-free thin films. Fig. 3.36 shows the comparison of the 1 mm disc gold electrode on an unmodified surface with the electrode after electrodeposition of organosilica film. As can be seen, the apparent advantage of

EASA deposition is that the sol-gel was being selectively deposited into the desired electroactive working electrode areas without smearing the edges or unwanted areas of the insulating part. The successful deposition of the silica film on the electrode surface in this case can be indicated by changes of the electrode surface colour from pale yellow to bright yellow.



Figure 3.36: Comparison of colour changes observed at 1 mm gold disc electrode surface on an unmodified electrode (left) and on electrode after sol-gel electrodeposition (right).

For more detailed characterisation, cyclic voltammetry (CV) experiments were carried out to investigate the coverage of the electrodes with organosilica films. Comparison of the solid line (CV of the bare gold electrode prior modification) with the dotted lines (CV of the modified electrode) is shown in Fig. 3.37. The change in the CV indicates the presence of the surfactant-templated silica film on the gold electrode. These patterns are similar as reported by Walcarius and co-workers [82]. The shift of the oxidation peak by ca. 200 mV after the sol-gel electrodeposition was explained by Etienne and co-workers [88] where they considered that the neutral redox ferrocene methanol (FcMeOH) has been incorporated into the liquid crystal-like surfactant template via solubilisation and accumulation. The shift in peak potential also agrees well with the electrochemical behaviour of ferrocene derivatives solubilised in CTAB [89].

After an overnight aging at 135°C, the CV response decreased suggesting that the solubilised and accumulated FcMeOH has dried out, leaving only the sol-gel films on

the surface. After the surfactant-template removal, the accessibility through the organosilica film was observed almost similar to the unmodified electrode with CV peaks appearing at the same potential values. While this may indicate the permeatibility of FcMeOH on the organosilica film via the developed mesoporous channels, it also may propose desorption of the whole sol-gel network.

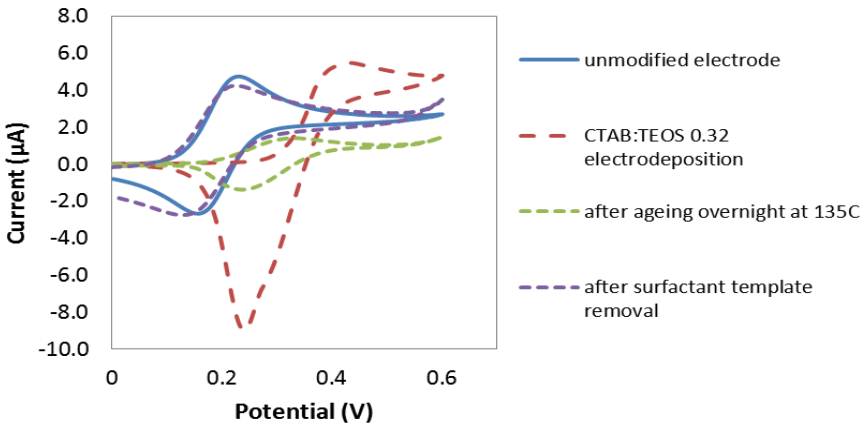


Figure 3.37: Electrochemical monitoring of the permeability of the mesostructured films. CV recorded in 5 mM FcMeOH in 0.1M NaCl (scan rate 50 mVs^{-1}) with unmodified gold electrode (solid blue line), electrode covered with the electrodeposited silica film (red dashed line), after aging overnight (green dashed line) and after surfactant removal via HCl ethanolic rinsing (purple dashed line). Potential achieved: ~-1.5 V, deposition time= 8 secs.

An additional step was then introduced in order to improve the formation and adhesion of the sol-gel particularly on gold electrode surface. This was achieved by pre-treating the gold bare electrode surface with a self-assembly partial monolayer with mercaptopropyltrimethoxysilane (MPTMS) as the thiol-functionalised silica before transferring the electrode into the sol containing CTAB/TEOS:MPTMS (90:10) precursors. The formation of SAM of MPTMS on gold has been proven to act as "molecular glue" between the gold electrode surface and sol-gel derived silica films [90, 91] as shown in Fig. 3.38.

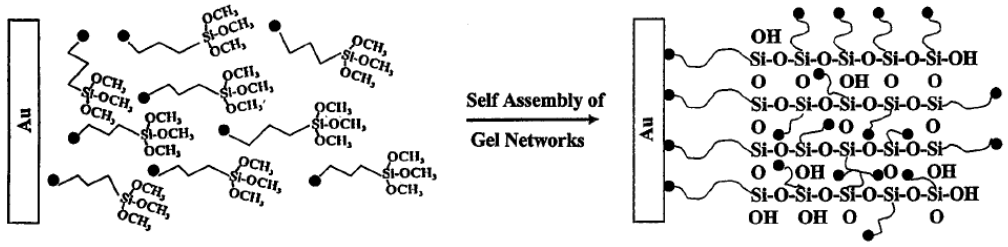


Figure 3.38: Schematic drawing showing the formation of sol-gel surface layers based on the self-assembly of thiol-containing gels. Taken from Ref. [91].

The formation of MPTMS self-assembled partial monolayer on the gold surface was originated from the chemisorptions of strong interaction between the thiol and gold. This monolayer however is still permeable to redox probe in solution due to the non-perfectly self-assembled MPTMS layer which derived from the short contact time for MPTMS on the gold surface.

The CVs after MPTMS–sol-gel film formation followed by ageing and surfactant template removal were recorded as shown in Fig. 3.39. The CV after the MPTMS-sol-gel electrodeposition exhibited a shift to a more positive potential indicating the solubility of the CTAB in FcMeOH as described previous. Upon aging and drying overnight, the sol-gel film seemed to be more repellent as the thiol-functionalised films are hydrophobic hence inducing additional restriction to the mass transport. A better access to the electrode surface was observed after the surfactant template removal which suggests that the template of CTAB surfactant has been successfully removed but the MPTMS with organosilica remained on the gold surface.

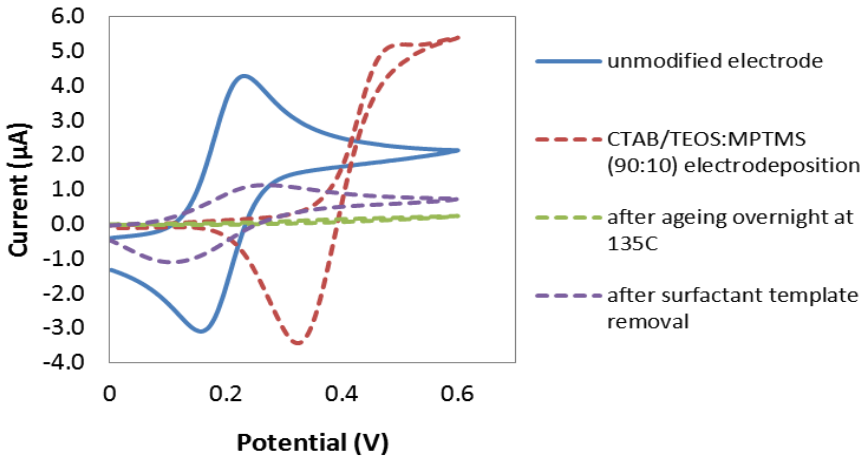


Figure 3.39: CVs of the unmodified gold electrode (solid blue line), electrodeposition of CTAB/TEOS:MPTMS precursors on the surface (red dashed line), after aging overnight at 135°C (green dashed line) and after surfactant template removal (purple dashed line). CV recorded in 5 mM FcMeOH in 0.1M NaCl (scan rate 50 mV s^{-1}). Potential achieved after deposition time of 8 secs was -1.3 V.

The SEM images of the unmodified surface and the modified surface with silica film formed on the gold surface are shown in Fig. 3.40. The diameters of the silica film's spheres were in the range of 380-750 nm. The EDX spectra showed a substantial level of Si, O and Cl in comparison with the unmodified electrode. This indicates the successful formation of the sol-gel layer (Si and O peaks). The Cl peak on the other hand attributed to the sol solution (NaCl). We have also attempted to capture the image using transmission electron microscopy (TEM), however the monolith collapsed as soon as it was being exposed under the scope. It was suggested later that the layer need to be coated with platinum before undergo the TEM imaging. The collapsing also could be avoided by depositing thinner silica film (i.e. shortening the deposition time of sol-gel).

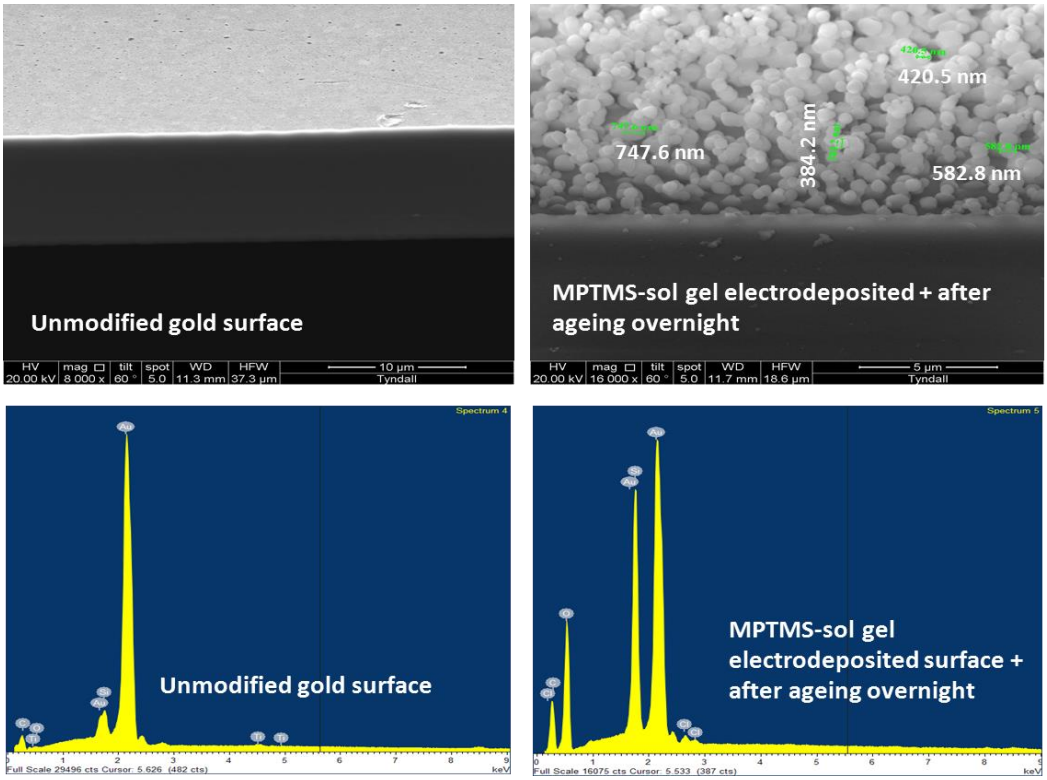


Figure 3.40: *Top row*: SEM images of unmodified and modified with silica film gold electrodes; surface tilted to 60°. *Bottom row*: EDX spectra of the respective electrodes.

EASA Silica Film on Recessed Microband Array

In early 2013, it has been proven that the EASA deposition method had been successfully applied to electrodes with various morphology, geometry and size, namely macroelectrode, microwire, microdisc and Au-CD-trode [83]. However the electrodeposition of silica film on recessed microband array has not been assessed to date.

It was observed that applying the same current density of -0.74 mA cm^{-2} as on earlier study on microelectrode array did not lead to the sol-gel electrodeposition although the deposition time was prolonged from 8 seconds to 16 seconds (Fig. 3.41). The recess microband depth was still the same which signifies that there is no sol-gel layer on the surface.

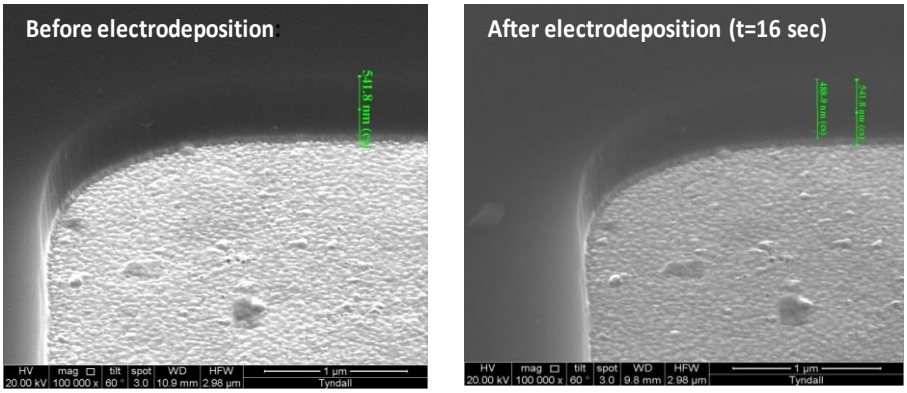


Figure 3.41: SEM images before and after the electrodeposition. Images were taken at the same spot of the particular band to assess the surface modification.

No significant CV changes were observed as well after the sol-gel electrodeposition and ageing overnight steps (Fig. 3.42). The CV after the surfactant template removal also was similar to the blank electrode prior the modification. Hence it can be concluded that no sol-gel layer was formed during the whole process. Furthermore, the potential achieved for the electrodeposition was -0.84 V and did not reach -1.3 V for the hydrolysis potential [81].

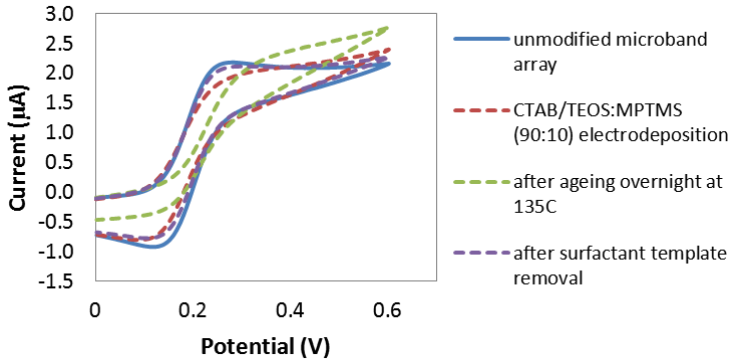


Figure 3.42: CVs of the unmodified microband array (solid blue line), electrodeposition of CTAB/TEOS:MPTMS precursors on the surface (red dashed line), after aging overnight at 135°C (green dashed line) and after surfactant removal (purple dashed line). CV recorded in 5 mM FcMeOH in 0.1M NaCl (scan rate 50 mVs^{-1}). Potential achieved after deposition time of 16 secs was -0.84 V, current density -0.74 mA cm^{-2}.

It was later learnt that when moving from macro- to smaller electrode dimensions, larger current densities need to be applied in ensuring the film deposition. This is attributed to the faster loss of the hydroxyl species in the solution for the diffusion profile of radial or spherical in microelectrode in comparison with linear diffusion on planar macroelectrode [83]. By increasing the current from –0.74 mA cm^{-2} to -7.4 mA cm^{-2} for the recessed microband array, the hydrolysis potential of -1.41 V has been successfully achieved within 8 seconds of electrodeposition (Fig. 3.43).

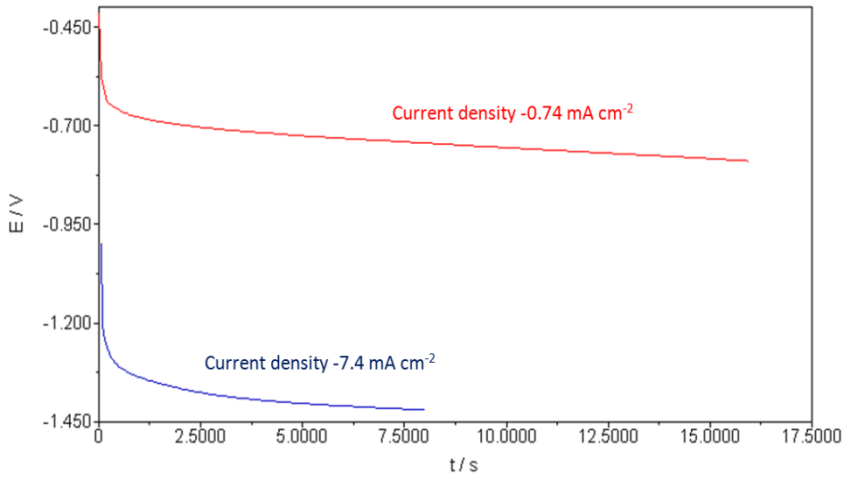


Figure 3.43: Potential as a function of time for the different current density applied for 10 µm microband array. Lower potential achieved for the sol-gel silica film electrodeposition once the current density was increased despite the deposition time. The current density hence needs to be increased when moving from a macro electrode.

However, from the SEM images it was observed that the silica film formed consisted of big granulars (Fig. 3.44). The formation of such big granules could be attributed to several factors. Firstly, it was postulated that current density applied being so high that the film was formed inside the recess before reaching the surface of the silicon nitride thus depositing outside the recess. Interestingly, the cylindrical diffusion process that is commonly associated with microband array could be directly observed in the SEM image. This could be seen on the cylindrical silica-film formed on the

recess. Secondly, the silica film also could be densified during the ageing process where the electrode was placed in an oven with temperature of 135°C. Both chemical and structural transformations can be related to the physical desorption of water and solvents from micropore walls, carbonization and combustion of residual organic groups, condensation polymerization, volume relaxation and viscous sintering [92]. It is proposed that, during gel densification, the desiccated gel become more highly cross-linked while reducing its surface area and free volume [93]. While this effect is not prominent on larger surface, a much smaller surface is greatly affected with the high temperature. This is seconded by Hench & West [94] in 1990 where they reported that the densification temperature decreases as the pore radius decreases and surface area of the gels increases. Although Herzog et al. (2013) did not encounter this densification when modifying the microelectrodes [83], it is noteworthy to mention that the recessed microelectrodes used in this study had different geometry. Furthermore, in his study, a fresh sol solution was made on the day of modification whereas in the presented study we were using a sol that has been prepared fortnight earlier. Although an aged solution plays the least role in forming such formed structure, it is advisable to prepare fresh sol solution prior each modification.

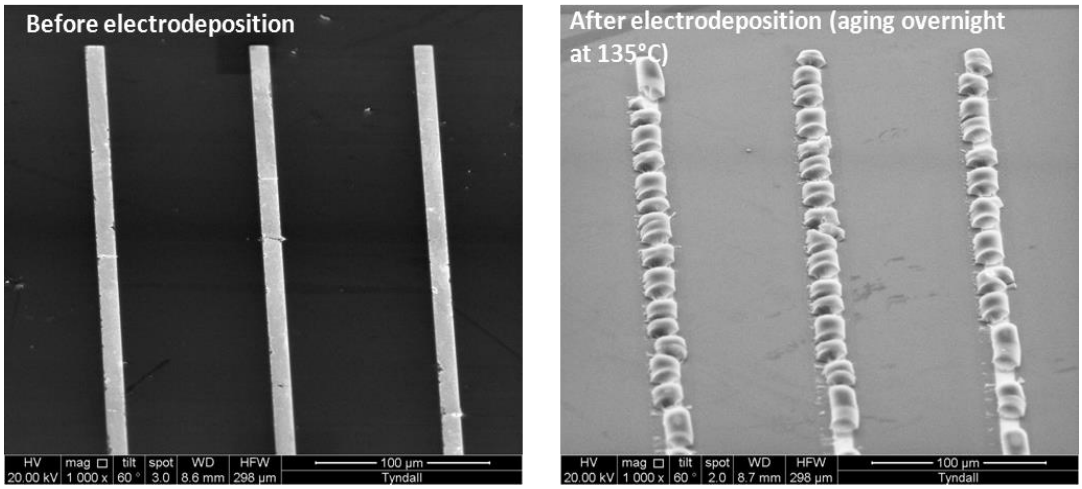


Figure 3.44: SEM images of unmodified microband array (right) and after CTAB/TEOS:MPTMS (90:10) electrodeposition.

The CVs of the unmodified microband array and after application of the electrodeposition steps are shown in Fig. 3.45. The decrease in CV signal after surfactant template removal supported the formation of the silica layer within the recess that hinders penetration of the electrons to the gold surface.

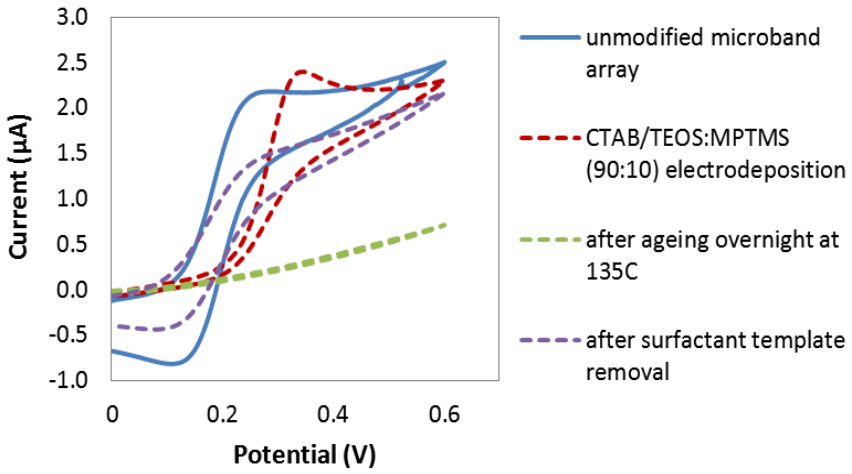


Figure 3.45: CVs of the unmodified microband array (solid blue line), electrodeposition of CTAB/TEOS:MPTMS precursors on the surface (red dashed line), after aging overnight at 135°C (green dashed line) and after surfactant removal (purple dashed line). CV recorded in 5 mM FcMeOH in 0.1M NaCl (scan rate 50 mV s^{-1}). Potential achieved after deposition time of 8 secs was -1.41 V, current density -7.4 mA cm^{-2}.

A fresh solution was then prepared and the electrodeposition on the recessed microband array was performed. The microband electrode was left ageing overnight at room temperature instead of high temperature in the oven. As can be seen from SEM images in Fig. 3.46, smoother silica film with spheres ranging from 300-500 nm was successfully deposited on gold microband array within the recess trench.

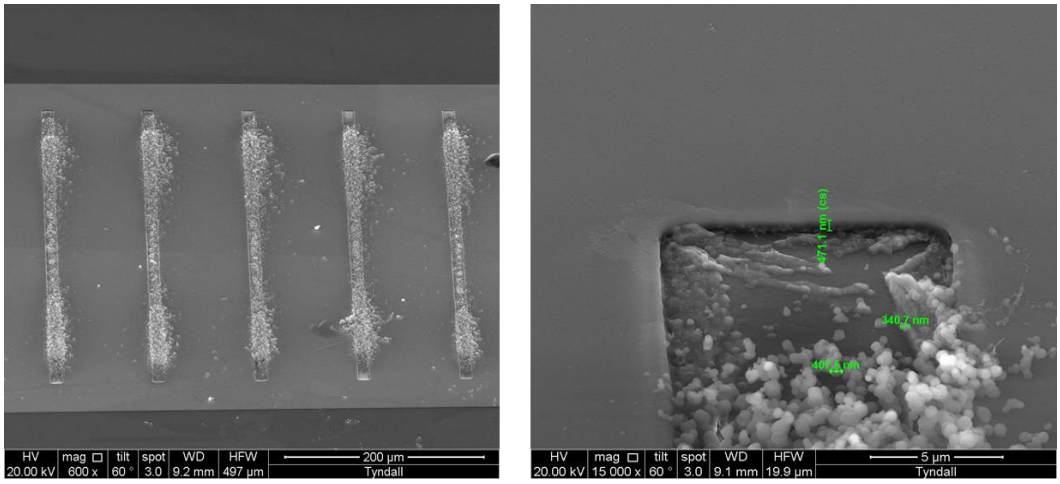


Figure 3.46: SEM images of silica beads successfully deposited on recessed gold microband array (left) with closed up image (right).

The permeability properties of the films were evaluated via CV and EIS in 5 mM ferrocene methanol. From the CV in Fig. 3.47, it can be seen that after an ageing overnight, despite being left at room temperature, a film has been successfully formed. This is indicated by a low and compressed CV signal that correlates to the blocking of electron transfer on the electrode surface. However, after surfactant template removal in ethanolic solution, a better permeability of the film was observed. Interestingly, the modified microband with silica film still retained its microelectrode behaviour. This suggests that the whole band surfaces has opened up several template spots that may be in resemblance with disc hence a steady-shaped voltammogram was observed.

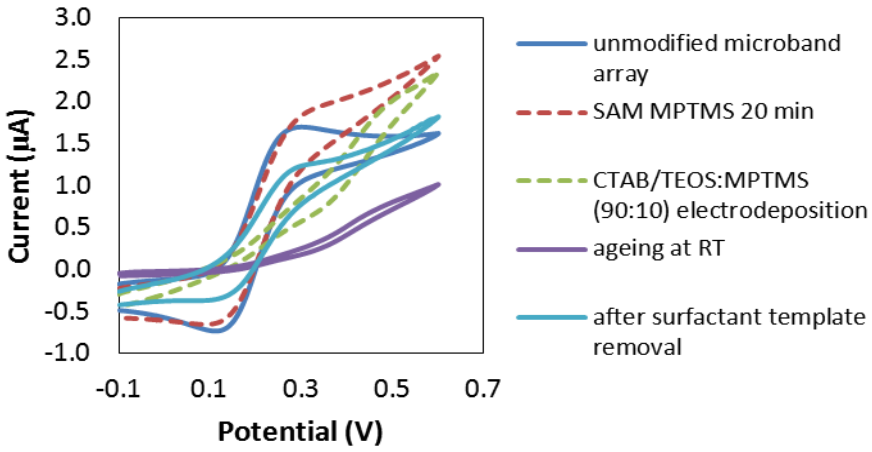


Figure 3.47: CVs of the unmodified microband array (solid dark blue line), after self-assembly MPTMS for 20 minutes (red dashed line), electrodeposition of CTAB/TEOS:MPTMS precursors on the surface (green dashed line), after aging overnight at room temperature (purple solid line) and after surfactant removal (light blue line). CV recorded in 5 mM FcMeOH in 0.1M NaCl (scan rate 50 mV s^{-1}). Potential achieved after deposition time of 8 secs was -1.14 V, current density -7.4 mA cm^{-2}.

The EIS study was also carried out to assess the microelectrode behaviour upon modifications. An impedance spectrum for a typical unmodified microband array in 1 mM ferrocene carboxylic acid redox solution would exhibit a shape representing a semicircle followed by a straight line at the lowest frequency of 0.01 Hz. In Fig. 3.48 however the impedance measurements were limited to 0.1 Hz instead of 0.01 Hz thus the linear straight line region was not observed. Furthermore, the impedance was performed in different redox solution (5 mM ferrocene methanol). Following the partial self-assembly of MPTMS, a shift on the impedance took place (inset, top diagram). A significant increment of the impedance was seen straight after the sol-gel and MPTMS electrodeposition. A massive blocking behaviour was observed after an overnight aging confirming the hardening of the silica film that blocked the electron from reaching the surface. Better permeability occured on the electrode once the surfactant template removal was performed. These results are in agreement with the results obtained by cyclic voltammetry analysis. While the advantage of

microelectrode was maintained after the surfactant removal (steady state CV), EIS study has confirmed the change of the diffusion profile on the modified surface. The impedance is now tending to straight line indicating planar diffusion on the modified electrode. Such behaviour could be attributed to the greater diffusivity of the redox solution within the silica film [95]. Similar pattern has been reported also by Wei & Hillhouse (2007) for their modified cubic silica films in ferrocene dimethanol redox solution [96].

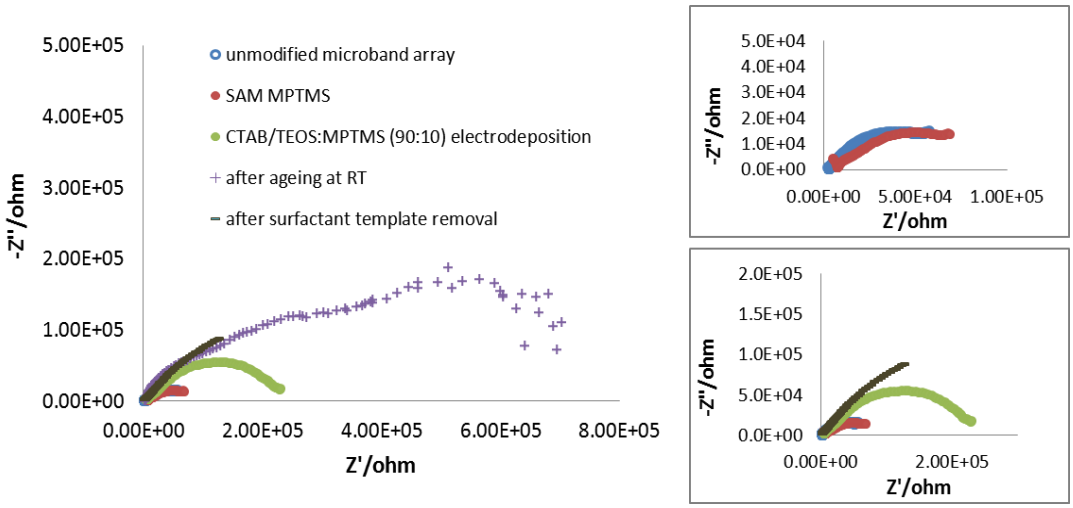


Figure 3.48: EIS of the unmodified microband array (*inset, top diagram*- blue marker), after self-assembly MPTMS for 20 minutes (*inset, top diagram*- red marker), electrodeposition of CTAB/TEOS:MPTMS precursors on the surface (green marker), after aging overnight at room temperature (purple marker) and after surfactant template removal (grey marker). EIS recorded in 5 mM FcMeOH in 0.1M NaCl (0.1-1 MHz).

It was pointed out however that the most concerning issues in modifying the electrodes (particularly the on micro dimension scale) are the lack of the reproducibility for both film formation and properties [83]. A more detailed study is required, for instance to study the thickness of the silica film formed within the recess depth as a function of electrodeposition time. With regard to the future biosensor application, sol-gel network is reported to be superior medium for enzyme

and protein immobilisation/encapsulation in biosensor application. First, this technique does not impair the active biology sites on enzymes or proteins, thus maintaining their native properties and preserving the reactivities. Secondly, leaching or desorption of these entrapped species does not occur or occurs very slowly [58]. However due to the limited resources of the microband electrode available and time constrain, this was by far the best of the study can be conducted. Nevertheless the results obtained in this chapter show and prove that the EASA technique is plausible for surface modification of recessed microelectrode arrays with various geometries and dimensions.

The next mode of chemically modified electrode that will be discussed is the nanoporous gold deposition on microdisc array.

3.5.2 Nanoporous-Gold Modified Surface

The objective of modifying the electrode area with nanoporous gold (NPG) is to increase the active surface area of the gold electrode. The sensitivity of biosensor has been proven to be improved by making the surface porous compared to a planar gold surface [59, 60]. The porosity allows a larger number of biomolecules attachments per surface area resulting in larger signal upon binding with their specifically binding analyte molecules. Apart from biosensors, NPG also have widely being integrated in catalytic applications i.e. in fuel cells [97, 98] owing to its thermal stability and resistance to oxidation.

The work associated with NPG and microelectrode has been reported by several researchers [99, 100] but recessed microelectrode in particular has not been reported. In 2005, Kataky and her co-workers have treated their silicon-based recessed gold microelectrode array with thiolated cyclodextrin nanocavities ensembles in order to mimic the nanoporous electrode behaviour [101] but the work on nanoporous gold electrodeposition was not described.

The NPG process can be briefly described as follows*. $Au_{0.18}Ag_{0.82}$ alloy was first electrochemically deposited on the electrode surface. To produce the NPG, a technique called dealloying was employed. Dealloying is a type of chemical etching process that involves selective metal dissolution. Such an approach has been described by Forty (1979) [102]. It was reported that noble metal alloys (in this case the Au) undergo selective dissolution during anodic corrosion while the less noble component (Ag) is dissolved preferentially. This leads to a depletion gilding of the less noble species and as Ag atoms are dissolved. Au atoms are then clustered and evolved into porous structure. A more detailed mechanism in the dealloying process has been modelled by Erlabacher and co-workers (2001) [103]. The alloy composition $Au_{0.18}Ag_{0.82}$ used in this study gives the highest surface area of NPG (6.9 m^2g^{-1}) and the shortest NPG ligament size (20-30 mm) when dealloyed in 30% nitric acid for 60 minutes [104, 105]. Besides Ag, the use of Zn as the less noble metal also has been reported [100].

The following SEM images show modified 10 μm microdisc electrode array with NPG of different thickness. The thickness of the NPG is controlled by the time of electrodeposition. Prior to the modification, the microdiscs have recess depths of 917 nm (for two electrodes) and 735 nm (one electrode). After the modification, NPG of three different thicknesses has been successfully deposited (122 nm, 252 nm and 6.8 μm) (Fig. 3.49). As can be seen, NPG appears as sponge-like 3D structure with interconnecting pores with ligaments (Fig. 6.15d). Despite its porous structure, it has been shown that NPG can be as strong as bulk Au [103, 106].

* The NPG electrodeposition work on microdisc array was carried out by Dr. Lorraine Nagle from Electrochemical Materials and Energy Group, Tyndall National Institute.

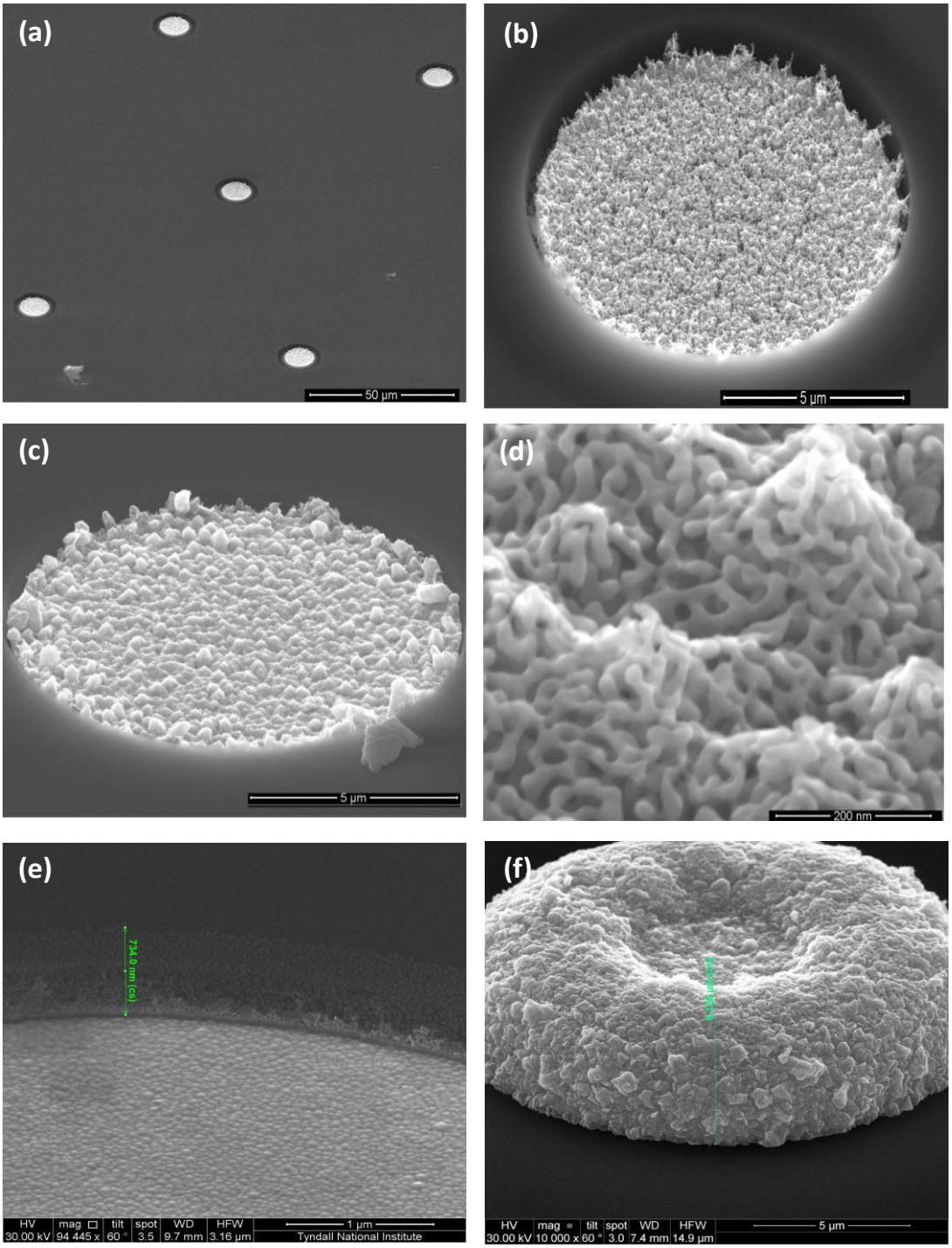


Figure 3.49: SEM images of NPG-modified 10 µm microdisc array with 917 nm recess depth (a-d): (a) microdisc array after modification; (b) 122 nm NPG deposited (c) 252 nm NPG deposited; (d) close-up image of NPG with the joint ligament; and modified microdisc with 735 nm recess depth (e-f): (e) disc before modification; (f) NPG with 6.8 µm NPG deposition. Images are tilted to 60°.

The limiting current for the recess depth thickness after modification was calculated and compared to the obtained experimental limiting current. The following equations describe the limiting current for both recessed microelectrode array and hemisphere electrode [107].

For recessed microdisc array,

$$i_{lim} = \left(\frac{4\pi nFCDr^2}{4L + \pi r}\right)N \quad \ldots.(Eq.3.12)$$

And for hemisphere electrode,

$$i_{lim} = (2\pi nFDCr)N \quad \ldots.(Eq.3.13)$$

where where n is the number of electrons involved in the reaction, F is Faraday constant (96,485 C mol^{-1}), C is the bulk concentration of ferrocene carboxylic acid (mol cm^{-3}), D is diffusion coefficient (5.7×10^{-6} cm^2 s^{-1}), r is the disc radius (cm), L is the silicon nitride thickness (recess depth) (cm) and N is the number of the disc electrodes in an array.

The modified NPG microelectrode exhibits highly improved electrochemical responses compared to the readily fabricated microelectrode, owing to its high surface area. As can be seen from Table 3.5, the experimental limiting currents obtained are twice as large as the theoretical limiting current. This has arisen from the mass transport of the redox solution occurring through porousity of the NPG across the electrode surface.

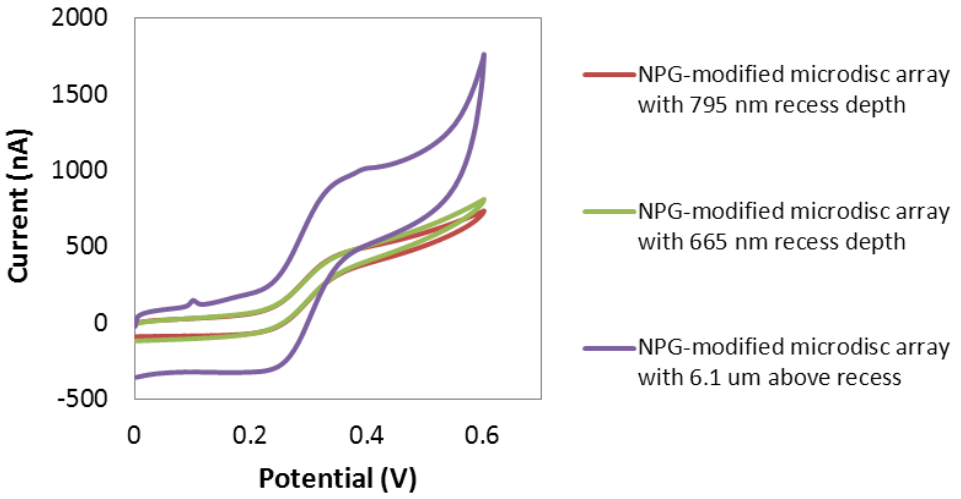


Figure 3.50: CV of the NPG-modified microdisc array of different thicknesses. Scan rate 100 mV s^{-1} in 1 mM FCA in PBS pH7.4.

Table 3.5: Comparison between theoretical current and experimental current for NPG-modified microelectrodes

	Theoretical current (nA)	**Experimental current (nA)**
Initial microdisc recess of 917 nm		
795 nm recess (after 122 nm NPG deposited)	287	564.94 ± 44.49
665 nm recess depth (after 252 nm NPG deposited)	295	627.01 ±97.08
Initial microdisc recess of 735 nm		
Hemisphere electrode of 6.1 µm (after NPG deposition of 6.8 µm)	543	1160 ± 498.97

Kralj and Dryfe (2001) proposed that the density of the porous material on the modified metallic electrode should be taken into account when measuring the limiting current [108], giving the following equation for a recessed microdisc:

$$i_{lim} = \rho A \left(\frac{4\pi nFCDr^2}{4L + \pi r} \right) \quad \ldots (Eq. 3.14)$$

where ρ is the pore density of the porous material and A is the area of the metallic electrode.

However since the pore density of NPG have not been known, and what more the relative density depends on the foam porosity [109], it was postulated from the limiting current calculation that the pore density of NPG deposited in the microelectrode array could be 1.26 x 10^6 pore cm^{-2}. This value is within the close approximation of the pore density of several other materials reported such as PET membrane (1.0 x 10^5 - 5.5 x 10^8 pores cm^{-2}) [108].

From the NPG-modified microelectrodes with recess depth of 795 nm and 665 nm, it was found that the current density with regard to the calculated theoretical current has increased from 1.16 mA cm^{-2} to 2.29 mA cm^{-2} and from 1.2 mA cm-2 to 2.54 mA cm^{-2} respectively. In both cases, a current density increment of twice was observed. Interestingly, the current density obtained is in the same vicinity as reported by Nagle & Rohan (2011) for NPG-modified planar Au electrode (3.1 mA cm^{-2}). The value for the current density at the unmodified planar Au with 5mm diameter macro disc was 2.65 mA cm^{-2} [97]; which indicates that the modified NPG-recessed microdisc array has a current density that is on par with the macrodisc area. For the NPG-modified microdisc electrode with 6.1 μm hemisphere formed above the recess, a current density increment of twice was also observed (from 2.2 mA cm^{-2} to 4.7 mA cm^{-2}).

It was found that the characteristic of microelectrode of having a steady-state CV has diminished for the NPG-modified microelectrode with hemisphere NPG formed above the recess. A broad and peak-shaped CV that corresponds to a macroelectrode CV was attained at scan rate at 100 mV s^{-1}. The respective EIS also has the lowest values in comparison with the unmodified and other NPG-modified microdisc electrodes (Fig. 3.51). This is due to the protruding geometry of the formed NPG-hemisphere that permits easier electron transfer at the surface and hence lower impedance.

The two other NPG-modified microdiscs on the other hand, exhibited steady-shaped voltammograms at 100 mV s^{-1}. The high surface roughness factor and steady-shaped voltammograms indicate that the NPG-modified microdiscs possess high surface area while retaining the advantages of traditional microelectrodes. Supposedly the EIS of the NPG-modified microdisc with 795 nm recess depth exhibited higher impedance compared to the of 695 nm recess depth. According to Seker et al. (2010), the electrode impedance generally decreased with increased film thickness for electrodes with the same initial alloy composition [56].

In this case, for the 665 nm recess depth, 225 nm of NPG was formed hence the film is thicker compared to the 122 nm of NPG formed that resulted in 795 nm recess depth. However no significant difference was observed between the two. This can be addressed to the SEM images as only one disc from the disc array of 314 electrodes was taken. The NPG thickness could be vary from one disc to another disc, and the EIS shows the impedance of total surface area instead of one disc alone. The striking importance however is that a 25-fold decrease in impedance of NPG-modified electrode was reported compared to unmodified gold electrode, as a result of the augmented total surface area [110].

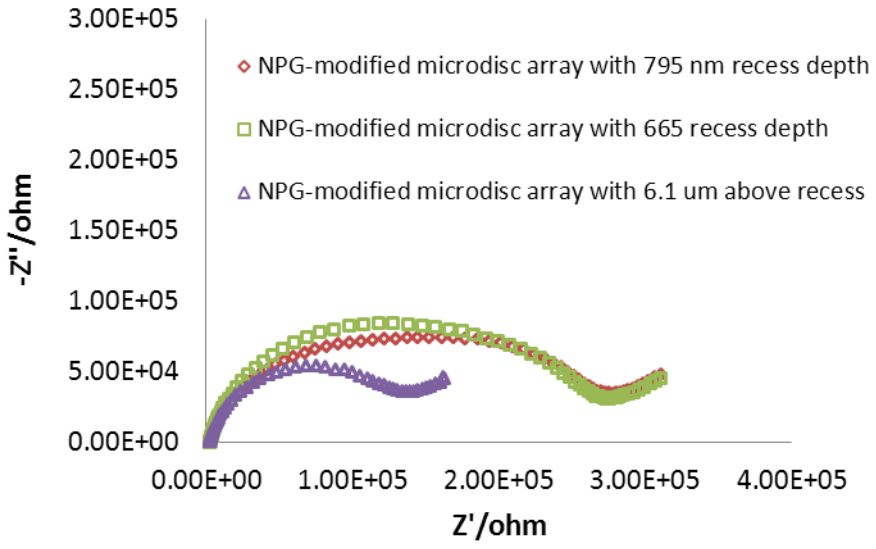


Figure 3.51: EIS of the NPG-modified microdisc array of different thicknesses in 1 mM FCA in PBS. Frequency applied was 0.01-1 MHz.

These interesting features of the NPG-modified microdisc in terms of electrochemistry and surface roughness provide a promising feature for its future application in biosensor area. The surface roughness indeed lends itself well and of important factor in immobilising biological elements. This is supported by the simplicity of the fabrication of the NPG-modified microelectrode.

3.6 Conclusion

The first part of this chapter has described the fabrication and characterisations of micro- and nanoelectrode arrays on two different substrates (silicon and glass) with different thickness of Si_3N_4 passivation layer (200, 300 and 500 nm). Microfabrication involving UV-photolithography technique was employed for the fabrication of microdisc and microband array with 10 μm critical dimension. The microelectrode with smaller dimensions (1 μm and 100 nm) was fabricated by electron beam lithography technique. Only one passivation layer thickness of 200 nm was applied to the glass-based microelectrode array fabrication.

Optical and SEM images have confirmed the dimension and geometry of the fabricated silicon-based microelectrode for all dimensions and recess depths. Accuracy of 10% was achieved for the larger dimensions (d1 and b1) regardless of the Si_3N_4 thickness. However for the smallest features (d2, b2 and b3), the dimensions achieved vary greatly with the thickness. The dimensions achieved for the 500 nm Si_3N_4 thickness wafers were closer to the expected dimensions compared to the wafers with thinner passivation layer suggesting better selectivity of the etching process for Si_3N_4 thickness over the e-beam resist.

The fabricated microelectrode arrays were first characterised using CV technique. All of the silicon-based d1 and d2 for all the three recess depths, and glass-based design d1 of 200 nm recess exhibited steady-state shape peak at 100 mV s^{-1} in 1 mM ferrocenecarboxylic acid (FCA) in PBS pH 7.4. The experimental limiting current obtained for all these microdisc arrays were in the excellent agreement with the calculated theoretical currents, suggesting individual hemispherical diffusion profile for these cases. The CVs for the microband array (b1 and b2) were more inclined to peak/sigmoidal shape at scan rate of 100 mV s^{-1}. In addition, their CVs were greatly

dependant on the scan rate. The suggested diffusion profile for both b1 and b2 was a mixed diffusion layer of individual and overlapping diffusion whilst a total heavily planar diffusion was suggested for b3 (100 nm nanoband). It was learnt that changes in scan rates were able to induce transitions of the CV shapes for the fixed microband array dimension from linear diffusion at slow scan rate to radial diffusion at higher scan rate.

Only microelectrodes with 10 μm dimension were studied for the subsequent EIS characterisation. The performances of the microelectrodes with smaller dimensions were found to be sluggish after several usages, perhaps due to the aging factor and mechanical/electrochemical effect on the passivation layers. Despite having the same surface area, the effect of recess depth was prominent especially in microdisc arrays. The EIS curve for microdisc array appeared to be flattened semi-circles which are in accordance with simulation work reported before. In comparison with disc array, the recess depth on microband array did not significantly affect the EIS curves due to the small and negligible percentage of recess over the electrode's aperture (band's length) (0.04% to 0.1%).

The second part of the chapter demonstrated the possibility of conducting chemical modification on the microelectrode array. This particular study served several purposes, first was to modify and provide the surfaces with immobilisation matrix for further application in biosensing. Secondly, the modification also allows us to increase the surface roughness that can improve the performance of biosensor. Two modification procedures based on electrochemical deposition approach were utilised in this part, namely the sol-gel silica film and nanoporous gold (NPG) electrodeposition.

For the sol-gel silica film formation, both methods employing CTAB:TEOS precursors and with the MPTMS pre-treatment exhibited successful formation of the sol-gel on the gold electrode surface. Adding an MPTMS monolayer helped a better adhesion and better formation of the organosilica on the electrode surface. It also has proven that film deposition is possible on recessed microband array but the characteristics for film formation greatly dependent on the experimental conditions i.e. increasing the current density when moving from macro to micro dimension.

Ageing the microelectrode at high temperature and using a not fresh sol solution only leads to the poor formation of the silica gels.

Apart from that, it also has been demonstrated that NPG-modified recessed microdisc can be conveniently prepared by electrodeposition of $Au_{0.18}Ag_{0.82}$ followed by dealloying steps. This direct and simple method provides a rougher surface with higher current density while maintaining the merit of microelectrode behaviour. The microdisc array still retains its microelectrode behaviour (in the case of presence recessed NPG layer). The integration of surface roughness increment and microelectrode properties may help in improving the biosensing application. The film thickness formed via EASA and NPG for modifying gold electrode surface could be tuned by controlling the electrodeposition parameters (time and ratio of mixtures) thus offering wide range of further biosensor applications.

Overall, the 10 μm microdisc/microband were found to be the most stable and reproducible dimension when compared those with smaller dimension. Although the glass-based microelectrode array exhibited electrochemical performance than on a par with the silicon-based electrode, nevertheless the handling issues concerning the fragility and brittleness of the glass substrate is the major hindrance for its practical use. Chemical modifications conduction also had shown that surface modification is possible on these recessed microelectrodes. Therefore, silicon-based microfabricated electrode/arrays with 10 μm dimension (or greater) will be utilised for the further fabrication and in the following chapters in this thesis.

3.7 References

1. Zoski, C.G., *Ultramicroelectrodes: design, fabrication, and characterization.* Electroanalysis, 2002. **14**(15-16): p. 1041-1051.
2. Lanyon, Y.H. and D.W.M. Arrigan, *Recessed nanoband electrodes fabricated by focused ion beam milling.* Sensors and Actuators B: Chemical, 2007. **121**(1): p. 341-347.
3. Fletcher, S. and M.D. Horne, *Random assemblies of microelectrodes (RAM™ electrodes) for electrochemical studies.* Electrochemistry Communications, 1999. **1**(10): p. 502-512.

4. Wightman, R.M., *Microvoltammetric electrodes.* Analytical Chemistry, 1981. **53**(9): p. 1125A-1134A.
5. Berduque, A., et al., *Voltammetric characterisation of silicon-based microelectrode arrays and their application to mercury-free stripping voltammetry of copper ions.* Talanta, 2007. **71**(3): p. 1022-1030.
6. Buß, G., et al., *Modifications and characterization of a silicon-based microelectrode array.* Electrochimica Acta, 1999. **44**(21–22): p. 3899-3910.
7. Moujahid, W., et al., *Microelectrochemical Systems on Silicon Chips for the Detection of Pollutants in Seawater.* Electroanalysis, 2011. **23**(1): p. 147-155.
8. Herzog, G., et al., *On-chip electrochemical microsystems for measurements of copper and conductivity in artificial seawater.* Talanta, 2013. **116**(0): p. 26-32.
9. Beni, V. and D.W. Arrigan, *Microelectrode arrays and microfabricated devices in electrochemical stripping analysis.* Current Analytical Chemistry, 2008. **4**(3): p. 229-241.
10. Sandison, M.E., et al., *Optimization of the geometry and porosity of microelectrode arrays for sensor design.* Analytical Chemistry, 2002. **74**(22): p. 5717-5725.
11. Compton, R.G., et al., *Design, fabrication, characterisation and application of nanoelectrode arrays.* Chemical Physics Letters, 2008. **459**(1): p. 1-17.
12. Kawagoe, J.L., D.E. Niehaus, and R.M. Wightman, *Enzyme-modified organic conducting salt microelectrode.* Analytical Chemistry, 1991. **63**(24): p. 2961-2965.
13. Morita, K. and Y. Shimizu, *Microhole array for oxygen electrode.* Analytical Chemistry, 1989. **61**(2): p. 159-162.
14. Lanyon, Y.H., et al., *Fabrication of nanopore array electrodes by focused ion beam milling.* Analytical Chemistry, 2007. **79**(8): p. 3048-3055.
15. Schmitt, G., et al., *Passivation and corrosion of microelectrode arrays.* Electrochimica Acta, 1999. **44**(21): p. 3865-3883.
16. Faßbender, F., et al., *Optimization of passivation layers for corrosion protection of silicon-based microelectrode arrays.* Sensors and Actuators B: Chemical, 2000. **68**(1–3): p. 128-133.

17. Bard, A.J., Faulkner, L.R, *Electrochemical Methods, Fundamentals and Applications.* 2001.
18. Zuliani, C., et al., *Formation and Growth of Oxide Layers at Platinum and Gold Nano- and Microelectrodes.* Analytical Chemistry, 2010. **82**(17): p. 7135-7140.
19. Dawson, K., et al., *Electroanalysis at Single Gold Nanowire Electrodes.* The Journal of Physical Chemistry C, 2012. **116**(27): p. 14665-14673.
20. Kounaves, S.P., et al., *Iridium-based ultramicroelectrode array fabricated by microlithography.* Analytical Chemistry, 1994. **66**(3): p. 418-423.
21. Narayanan, S., et al., *Method to quantify the effect of passivation layer in bio-impedance sensors.* Conference proceedings : ... Annual International Conference of the IEEE Engineering in Medicine and Biology Society. IEEE Engineering in Medicine and Biology Society. Conference, 2009. **2009**: p. 3783-6.
22. Narayanan, S., et al., *Analysis of the passivation layer by testing and modeling a cell impedance micro-sensor.* Sensors and Actuators A: Physical, 2010. **159**(2): p. 241-247.
23. Guo, J. and E. Lindner, *Cyclic voltammograms at coplanar and shallow recessed microdisk electrode arrays: guidelines for design and experiment.* Analytical Chemistry, 2008. **81**(1): p. 130-138.
24. Menshykau, D., et al., *Investigating the concept of diffusional independence. Potential step transients at nano- and micro-electrode arrays: theory and experiment.* Analyst, 2009. **134**(2).
25. Davies, T.J. and R.G. Compton, *The cyclic and linear sweep voltammetry of regular and random arrays of microdisc electrodes: Theory.* Journal of Electroanalytical Chemistry, 2005. **585**(1): p. 63-82.
26. Scanlon, M.l.D., et al., *Ion-Transfer Electrochemistry at Arrays of Nanointerfaces between Immiscible Electrolyte Solutions Confined within Silicon Nitride Nanopore Membranes.* Analytical Chemistry, 2010. **82**(14): p. 6115-6123.
27. Rimboud, M., et al., *Electrochemical behaviour and voltammetric sensitivity at arrays of nanoscale interfaces between immiscible liquids.* Analyst, 2011. **136**(22): p. 4674-4681.

28. Bond, A.M., K.B. Oldham, and C.G. Zoski, *Steady-state voltammetry.* Analytica Chimica Acta, 1989. **216**(0): p. 177-230.
29. Alden, J.A. and R.G. Compton, *Microband electrodes of ideal and nonideal geometries: AC impedance spectroscopy.* Electroanalysis, 1996. **8**(1): p. 30-33.
30. Nagale, M.P. and I. Fritsch, *Individually Addressable, Submicrometer Band Electrode Arrays. 2. Electrochemical Characterization.* Analytical Chemistry, 1998. **70**(14): p. 2908-2913.
31. Guerrette, J.P., S.J. Percival, and B. Zhang, *Voltammetric Behavior of Gold Nanotrench Electrodes.* Langmuir, 2011. **27**(19): p. 12218-12225.
32. Streeter, I., et al., *Voltammetry at Regular Microband Electrode Arrays: Theory and Experiment.* The Journal of Physical Chemistry C, 2007. **111**(32): p. 12058-12066.
33. Caston, S.L. and R.L. McCarley, *Characteristics of nanoscopic Au band electrodes.* Journal of Electroanalytical Chemistry, 2002. **529**(2): p. 124-134.
34. Berduque, A., et al., *Voltammetric characterisation of silicon-based microelectrode arrays and their application to mercury-free stripping voltammetry of copper ions.* Talanta, 2007. **71**(3): p. 1022-1030.
35. Said, N.A.M., et al. *Fabrication and Electrochemical Characterization of Micro-and Nanoelectrode Arrays for Sensor Applications*. in *Journal of Physics: Conference Series*. 2011. IOP Publishing.
36. Godino, N., et al., *Mass Transport to Nanoelectrode Arrays and Limitations of the Diffusion Domain Approach: Theory and Experiment.* Journal of Physical Chemistry C, 2009. **113**(25): p. 11119-11125.
37. Ferrigno, R., P.F. Brevet, and H.H. Girault, *Finite element simulation of the amperometric response of recessed and protruding microband electrodes in flow channels.* Journal of Electroanalytical Chemistry, 1997. **430**(1–2): p. 235-242.
38. Amatore, C. and B. Fosset, *Equivalence between Microelectrodes of Different Shapes: Between Myth and Reality.* Analytical Chemistry, 1996. **68**(24): p. 4377-4388.

39. Bartlett, P.N. and S.L. Taylor, *An accurate microdisc simulation model for recessed microdisc electrodes.* Journal of Electroanalytical Chemistry, 1998. **453**(1–2): p. 49-60.
40. Amatore, C., et al., *Mass Transport at Microband Electrodes: Transient, Quasi-Steady-State, and Convective Regimes.* ChemPhysChem, 2012. **13**(6): p. 1562-1568.
41. Wehmeyer, K.R., M.R. Deakin, and R.M. Wightman, *Electroanalytical properties of band electrodes of submicrometer width.* Analytical Chemistry, 1985. **57**(9): p. 1913-1916.
42. Fleischmann, M., S. Pons, and J. Daschbach, *The ac impedance of spherical, cylindrical, disk, and ring microelectrodes.* Journal of Electroanalytical Chemistry and Interfacial Electrochemistry, 1991. **317**(1–2): p. 1-26.
43. Amatore, C. and I. Svir, *A new and powerful approach for simulation of diffusion at microelectrodes based on overlapping sub-domains: application to chronoamperometry at the microdisk.* Journal of Electroanalytical Chemistry, 2003. **557**(0): p. 75-90.
44. Ferrigno, R. and H.H. Girault, *Finite element simulation of electrochemical ac diffusional impedance. Application to recessed microdiscs.* Journal of Electroanalytical Chemistry, 2000. **492**(1): p. 1-6.
45. Bruce, P.G., et al., *Electrochemical impedance spectroscopy at an ultramicroelectrode.* Journal of Electroanalytical Chemistry, 1994. **367**(1-2): p. 279-283.
46. Bond, A.M., et al., *A comparison of the chronoamperometric response at inlaid and recessed disc microelectrodes.* Journal of Electroanalytical Chemistry and Interfacial Electrochemistry, 1988. **249**(1–2): p. 1-14.
47. Murtomäki, L. and K. Kontturi, *Electrochemical characteristics of the microhole ITIES.* Journal of Electroanalytical Chemistry, 1998. **449**(1–2): p. 225-229.
48. Gabrielli, C., et al., *Electrochemical impedance spectroscopy investigations of a microelectrode behavior in a thin-layer cell: Experimental and theoretical studies.* The Journal of Physical Chemistry B, 2006. **110**(41): p. 20478-20485.

49. Los, P. and P.G. Bruce. *AC impedance measurements at ultramicroelectrodes*. in *Electrochemical Measurement, IEE Colloquium on*. 1994.
50. Navarro-Laboulais, J., J. García-Jareño, and F. Vicente, *Kramers–Kronig transformation, dc behaviour and steady state response of the Warburg impedance for a disk electrode inlaid in an insulating surface.* Journal of Electroanalytical Chemistry, 2002. **536**(1): p. 11-18.
51. Jorcin, J.-B., et al., *CPE analysis by local electrochemical impedance spectroscopy.* Electrochimica Acta, 2006. **51**(8): p. 1473-1479.
52. Lvovich, V.F., *Impedance spectroscopy: applications to electrochemical and dielectric phenomena*2012: John Wiley & Sons.
53. Kovach, P.M., et al., *Faradaic electrochemistry at microcylinder, band, and tubular band electrodes.* Journal of Electroanalytical Chemistry and Interfacial Electrochemistry, 1985. **185**(2): p. 285-295.
54. Deakin, M.R., R.M. Wightman, and C.A. Amatore, *Electrochemical kinetics at microelectrodes: Part II. Cyclic voltammetry at band electrodes.* Journal of Electroanalytical Chemistry and Interfacial Electrochemistry, 1986. **215**(1–2): p. 49-61.
55. Ordeig, O., et al., *Regular arrays of microdisc electrodes: simulation quantifies the fraction of 'dead' electrodes.* Analyst, 2006. **131**(3): p. 440-445.
56. Suh, D.H., et al., *Characterization of three-dimensional capacitor prepared by oxide recess in shallow trench isolation.* Journal of the Electrochemical Society, 2005. **152**(1): p. G107-G109.
57. Schmitt, G., et al., *Passivation and corrosion of microelectrode arrays.* Electrochimica Acta, 1999. **44**(21–22): p. 3865-3883.
58. Salimi, A., R.G. Compton, and R. Hallaj, *Glucose biosensor prepared by glucose oxidase encapsulated sol-gel and carbon-nanotube-modified basal plane pyrolytic graphite electrode.* Analytical biochemistry, 2004. **333**(1): p. 49-56.
59. van Noort, D. and C.-F. Mandenius, *Porous gold surfaces for biosensor applications.* Biosensors and Bioelectronics, 2000. **15**(3–4): p. 203-209.

60. Hu, K., et al., *Electrochemical DNA biosensor based on nanoporous gold electrode and multifunctional encoded DNA− Au bio bar codes.* Analytical Chemistry, 2008. **80**(23): p. 9124-9130.
61. Walcarius, A., *Electroanalysis with Pure, Chemically Modified and Sol-Gel-Derived Silica-Based Materials.* Electroanalysis, 2001. **13**(8-9): p. 701-718.
62. Walcarius, A., et al., *Exciting new directions in the intersection of functionalized sol–gel materials with electrochemistry.* Journal of Materials Chemistry, 2005. **15**(35-36): p. 3663-3689.
63. Walcarius, A., *Electroanalytical applications of microporous zeolites and mesoporous (organo) silicas: Recent trends.* Electroanalysis, 2008. **20**(7): p. 711-738.
64. Walcarius, A., *Electrochemical Applications of Silica-Based Organic−Inorganic Hybrid Materials.* Chemistry of Materials, 2001. **13**(10): p. 3351-3372.
65. Gill, I. and A. Ballesteros, *Bioencapsulation within synthetic polymers (Part 1): sol–gel encapsulated biologicals.* Trends in biotechnology, 2000. **18**(7): p. 282-296.
66. Adams, K.L., et al., *Highly Sensitive Detection of Exocytotic Dopamine Release Using a Gold-Nanoparticle-Network Microelectrode.* Analytical Chemistry, 2010. **83**(3): p. 920-927.
67. Fontaine, O., C. Laberty-Robert, and C. Sanchez, *Sol–gel route to zirconia–Pt-nanoelectrode arrays 8 nm in radius: their geometrical impact in mass transport.* Langmuir, 2012. **28**(7): p. 3650-3657.
68. Pierce, A.L., et al., *Thin-film silica sol–gel coatings for neural microelectrodes.* Journal of Neuroscience Methods, 2009. **180**(1): p. 106-110.
69. Hu, Z. and W.R. Heineman, *Oxidation-State Speciation of [ReI (DMPE) 3]+/[ReII (DMPE) 3] 2+ by Voltammetry with a Chemically Modified Microelectrode.* Analytical Chemistry, 2000. **72**(11): p. 2395-2400.
70. Njagi, J., et al., *Amperometric detection of dopamine in vivo with an enzyme based carbon fiber microbiosensor.* Analytical Chemistry, 2010. **82**(3): p. 989-996.

71. Shin, J.H., S.W. Weinman, and M.H. Schoenfisch, *Sol-gel derived amperometric nitric oxide microsensor.* Analytical Chemistry, 2005. **77**(11): p. 3494-3501.
72. Yantasee, W., et al., *Nanoengineered electrochemical sensor based on mesoporous silica thin-film functionalized with thiol-terminated monolayer.* Analyst, 2003. **128**(7): p. 899-904.
73. Tsionsky, M., et al., *Sol-Gel-Derived Ceramic-Carbon Composite Electrodes: Introduction and Scope of Applications.* Analytical Chemistry, 1994. **66**(10): p. 1747-1753.
74. Fink, L. and D. Mandler, *Thin functionalized films on cylindrical microelectrodes for electrochemical determination of Hg(II).* Journal of Electroanalytical Chemistry, 2010. **649**(1–2): p. 153-158.
75. Tian, F., et al., *A microelectrode biosensor for real time monitoring of l-glutamate release.* Analytica Chimica Acta, 2009. **645**(1–2): p. 86-91.
76. Kowalska, M., et al., *Prussian Blue acts as a mediator in a reagentless cytokinin biosensor.* Analytica Chimica Acta, 2011. **701**(2): p. 218-223.
77. Tian, F., E. Llaudet, and N. Dale, *Ruthenium purple-mediated microelectrode biosensors based on sol-gel film.* Analytical Chemistry, 2007. **79**(17): p. 6760-6766.
78. Harrell, T.M., et al., *Selective deposition of biocompatible sol-gel materials.* Journal of sol-gel science and technology, 2004. **31**(1-3): p. 349-352.
79. Mosa, J., et al., *Synthesis of poly(phenylene oxide)-based fluoro-tin-oxide/ZrO2 nanoelectrode arrays by hybrid organic/inorganic approach.* Electrochimica Acta, 2011. **56**(20): p. 7155-7162.
80. Ahn, B.Y., et al., *Direct-write assembly of microperiodic planar and spanning ITO microelectrodes.* Chemical Communications, 2010. **46**(38): p. 7118-7120.
81. Shacham, R., D. Avnir, and D. Mandler, *Electrodeposition of Methylated Sol-Gel Films on Conducting Surfaces.* Advanced Materials, 1999. **11**(5): p. 384-388.
82. Walcarius, A., et al., *Electrochemically assisted self-assembly of mesoporous silica thin films.* Nat Mater, 2007. **6**(8): p. 602-608.

83. Herzog, G., et al., *Electrochemically assisted self-assembly of ordered and functionalized mesoporous silica films: impact of the electrode geometry and size on film formation and properties.* Faraday Discuss., 2013.
84. Goux, A., et al., *Oriented mesoporous silica films Obtained by electro-assisted self-assembly (EASA).* Chemistry of Materials, 2009. **21**(4): p. 731-741.
85. Walcarius, A., *Template-directed porous electrodes in electroanalysis.* Analytical and bioanalytical chemistry, 2010. **396**(1): p. 261-272.
86. Li, J., S.N. Tan, and H. Ge, *Silica sol-gel immobilized amperometric biosensor for hydrogen peroxide.* Analytica Chimica Acta, 1996. **335**(1): p. 137-145.
87. Rottman, C., et al., *Surfactant-Induced Modification of Dopants Reactivity in Sol−Gel Matrixes.* Journal of the American Chemical Society, 1999. **121**(37): p. 8533-8543.
88. Etienne, M., J. Cortot, and A. Walcarius, *Preconcentration Electroanalysis at Surfactant-Templated Thiol-Functionalized Silica Thin Films.* Electroanalysis, 2007. **19**(2-3): p. 129-138.
89. Ryabov, A.D., et al., *Mechanism of a "jumping off" ferricenium in glucose oxidase-D-glucose-ferrocene micellar electrochemical systems.* The Journal of Physical Chemistry, 1995. **99**(38): p. 14072-14077.
90. Sibottier, E., et al., *Factors Affecting the Preparation and Properties of Electrodeposited Silica Thin Films Functionalized with Amine or Thiol Groups.* Langmuir, 2006. **22**(20): p. 8366-8373.
91. Wang, J., P.V. Pamidi, and D.R. Zanette, *Self-assembled silica gel networks.* Journal of the American Chemical Society, 1998. **120**(23): p. 5852-5853.
92. Brinker, C., et al., *Sol-gel transition in simple silicates.* Journal of Non-Crystalline Solids, 1982. **48**(1): p. 47-64.
93. Brinker, C.J. and G.W. Scherer, *Sol → gel → glass: I. Gelation and gel structure.* Journal of Non-Crystalline Solids, 1985. **70**(3): p. 301-322.
94. Hench, L.L. and J.K. West, *The sol-gel process.* Chemical Reviews, 1990. **90**(1): p. 33-72.

95. Etienne, M., et al., *Electrochemical approaches for the fabrication and/or characterization of pure and hybrid templated mesoporous oxide thin films: a review.* Analytical and bioanalytical chemistry, 2013. **405**(5): p. 1497-1512.
96. Wei, T.-C. and H.W. Hillhouse, *Mass transport and electrode accessibility through periodic self-assembled nanoporous silica thin films.* Langmuir, 2007. **23**(10): p. 5689-5699.
97. Nagle, L.C. and J.F. Rohan, *Nanoporous gold catalyst for direct ammonia borane fuel cells.* Journal of the Electrochemical Society, 2011. **158**(7): p. B772-B778.
98. Nagle, L.C. and J.F. Rohan, *Nanoporous gold anode catalyst for direct borohydride fuel cell.* International Journal of Hydrogen Energy, 2011. **36**(16): p. 10319-10326.
99. Lang, X.Y., et al., *Nanoporous gold supported cobalt oxide microelectrodes as high-performance electrochemical biosensors.* Nature Communications, 2013. **4**.
100. Jiang, J. and X. Wang, *Fabrication of high-surface nanoporous gold microelectrode.* Electrochemistry Communications, 2012. **20**(0): p. 157-159.
101. Grancharov, G., et al., *Individually addressable recessed gold microelectrode arrays with monolayers of thio-cyclodextrin nanocavities.* Analyst, 2005. **130**(10): p. 1351-1357.
102. Forty, A., *Corrosion micromorphology of noble metal alloys and depletion gilding.* 1979.
103. Erlebacher, J., et al., *Evolution of nanoporosity in dealloying.* Nature, 2001. **410**(6827): p. 450-453.
104. Ji, C. and P.C. Searson, *Synthesis and characterization of nanoporous gold nanowires.* The Journal of Physical Chemistry B, 2003. **107**(19): p. 4494-4499.
105. Liu, Z. and P.C. Searson, *Single nanoporous gold nanowire sensors.* The Journal of Physical Chemistry B, 2006. **110**(9): p. 4318-4322.
106. Biener, J., et al., *Size effects on the mechanical behavior of nanoporous Au.* Nano letters, 2006. **6**(10): p. 2379-2382.
107. Arrigan, D.W., *Nanoelectrodes, nanoelectrode arrays and their applications.* Analyst, 2004. **129**(12): p. 1157-1165.

108. Kralj, B. and R.A. Dryfe, *Membrane voltammetry: the metal/electrolyte interface.* Physical Chemistry Chemical Physics, 2001. **3**(15): p. 3156-3164.
109. Hodge, A.M., et al., *Characterization and mechanical behavior of nanoporous gold.* Advanced Engineering Materials, 2006. **8**(9): p. 853-857.
110. Seker, E., et al., *The fabrication of low-impedance nanoporous gold multiple-electrode arrays for neural electrophysiology studies.* Nanotechnology, 2010. **21**(12): p. 125504.

CHAPTER 4

DEVELOPMENT OF AN ON-CHIP MICROELECTROCHEMICAL CELL

4.1 Introduction

One of the ultimate objectives in biosensor development is its viability to carry out the analysis on field site i.e. outside the laboratory. This necessitates the miniaturization as well as the portability of the whole biosensor system. With regard to the biosensor measurement, electrochemical biosensors are still favoured over the other biosensor approaches (optical, mass etc.) owing to their stability and simple procedure (elimination of sample pre-treatment). In order to achieve the miniaturization concept and to complement the handhold-sized electrochemical analyser/potentiostats which are commercially ready in market, the fabrication of three-cell electrodes (RE, CE and microarray WE) integrated on a single chip is of paramount importance. Thus, one of the objectives of this thesis is to develop, fabricate and characterise the on-chip microelectrochemical cell with selected dimensions. Often referred as lab-on chip, on-chip devices or biochip, this device lends itself well in providing a portable sensor platform that allows miniaturization of biosensor for *in-situ* measurements [1, 2].

As discussed before, microelectrode arrays offer a number of advantages which include: improved mass transport and increased sensitivity (due to hemispherical diffusion), achieving steady state (or quasi-steady state) responses for Faradaic processes, reduced ohmic (*i*R) drop and most importantly when used in sensing, improved signal-to-noise ratios allowing low detection levels to be reached compared to macroscopic electrodes [3]. Thus, microfabricated electrochemical sensors with WE using microelectrode array can provide sufficient sensitivity and

achieve required limits of detection for practical applications due to improved mass transfer and signal to noise ratio [4].

The successful fabrication and application of the integrated chips have been reported over the past few years. A lab-on-chip fabricated on silicon substrates, referred as silicon chips, has been demonstrated to be viable for the detection of pollutants in seawater for the development of robotic fish [4, 5]. Tan and co-workers also have fabricated an integrated microelectrode arrays via screen-printed technique and demonstrate proof-of-concept in detecting chromium (VI) in environmental (canal water) sample [6]. Needle-type electrochemical sensors that integrate all the RE, CE and a single microelectrode electrode also have been reported for the simultaneous detection of nitrite and dissolved oxygen [7]. Parker and co-workers also have utilised the microfabricated immunochip for aflatoxin M_1 detection with adaptation of the competitive enzyme-linked immunosorbent assay (ELISA) format in their electrochemical biosensor study [8]. A wearable screen-printed electrode has also been developed in 2011 with three electrodes configuration based on the elastic neoprene substrate that can be attached directly on the diving suits. This wearable and portable sensor-potentiostat microsystem will allow the divers to have a visual indication on the water quality (environmental pollutants) and security threats in marine environments [9].

Following the successful fabrication and characterisation of the microelectrode array as described in previous chapter, a microelectrode array WE integrated with RE and CE was developed on a single chip. We refer this as the ‘on-chip microelectrochemical cell’ and this term will be used hereafter. This microelectrochemical cell consists of Ag/AgCl reference electrode (RE), Pt auxiliary/counter electrode (CE) and an array of microdisc or microband gold working electrode with chip dimension of 100 mm (width) x 380 mm (length) as shown in Fig. 4.1. The design also includes contact pads with associating lines that connect to the corresponding electrodes. The chip will be connected to the instrumentation by sliding the transducer pads into the appropriate connector. Thus, the following requirements on the minimum distance between connector and electrodes (5.00 mm), connector slot (10.50 mm) and pad width and length (2.00 x 5.00 mm) were taken into account in this design.

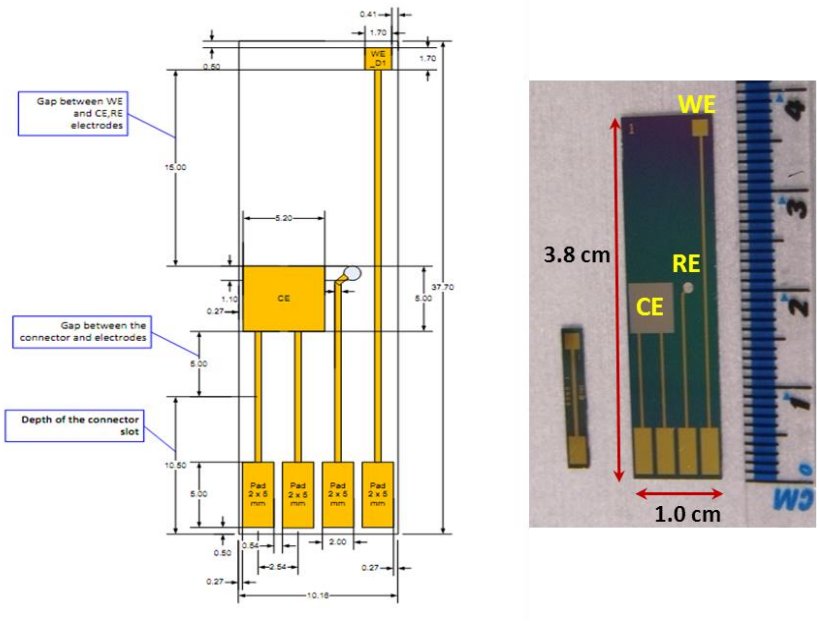


Figure 4.1: Layout and picture of fabricated microelectrochemical cell in comparison with the first version of microelectrode array.

The on-chip microelectrochemical cell was designed in such features considering several important aspects for further applications after the electrode fabrication. Firstly, unlike most of lab-on-chip/chip-on-board/biochips production which requires additional separate integration process [5, 10-15] to assemble the different parts of the electrodes, the developed microelectrochemical cell does not required packaging. This indirectly will reduce the production cost. This microelectrochemical cell can be used straight away in the next step of bio-functionalisation after the fabrication process with simple post production treatment (e.g. oxygen plasma) without the risk of epoxy contamination that derived from the packaging step. Secondly, the working electrode (WE) on the microelectrochemical cell is placed further down the end of the chip. The WE is designed in such way so that the modification of the working electrode surface that will be carried out for surface functionalisation purpose would not interfere and affect both RE and CE surface. Surface functionalisation has been proven to provide and enhance the selectivity and sensitivity of the recognition of target elements in sample analyte [16]. Nevertheless if all the fabricated electrodes are designed adjacently to each other, it is indeed a challenge to modify the WE surface without interfering both RE and CE surface particularly if it involves small

WE area. Modification of working electrode on a biochip for immobilising antibody has been described using aminosilane silanizaton protocol [8] and self-assembly monolayer of 11-mercaptoundecanoic acid [10]. However in these reports, it was not mentioned how both RE and CE on the biochip were 'protected' from the modification chemicals. A few drops of chemical solutions will surely disperse and smear on the whole surface area. Sealing the RE and CE with masking tape or the use of spin-coater is not feasible. Therefore, by having the working electrode of microelectrode array placed further down from the RE and CE, such modification will only affect the area of interest without passivating the other surfaces (Fig. 4.2). To sum up, the aim of the whole cell design is to facilitate the WE surface biomodification.

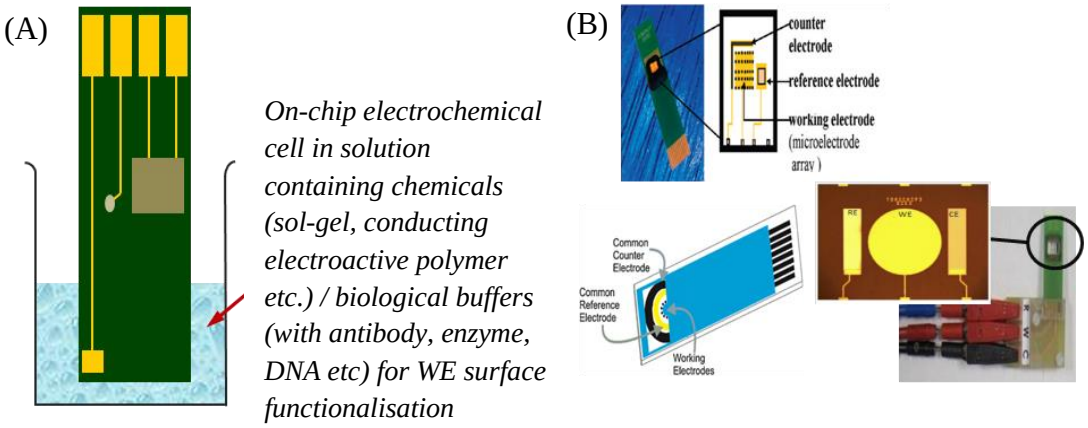


Figure 4.2: Illustration of the idea behind the on-chip microelectrochemical cell design, i.e, modification at the microelectrochemical cell's WE surface without interfering/passivating the RE and CE (A), in comparison with several other biochips'/lab-on-chips' designs (B).

In this study, the fabricated on-chip microelectrochemical cells have two different geometries of WE, i.e. microdisc and microband array. Each geometry designs have a fixed dimension of 10 μm diameter (microdisc) or 10 μm width (microband) but different parameters were studied, i.e. different spacing centre-to-centre distance (*d*) (*d*=100 μm and 50 μm) and different number of electrodes in the array (*N*). All discs array designs were arranged in hexagonal arrays instead of cubic arrays as this

arrangement provides mode space-saving placement of the discs on the available WE area.

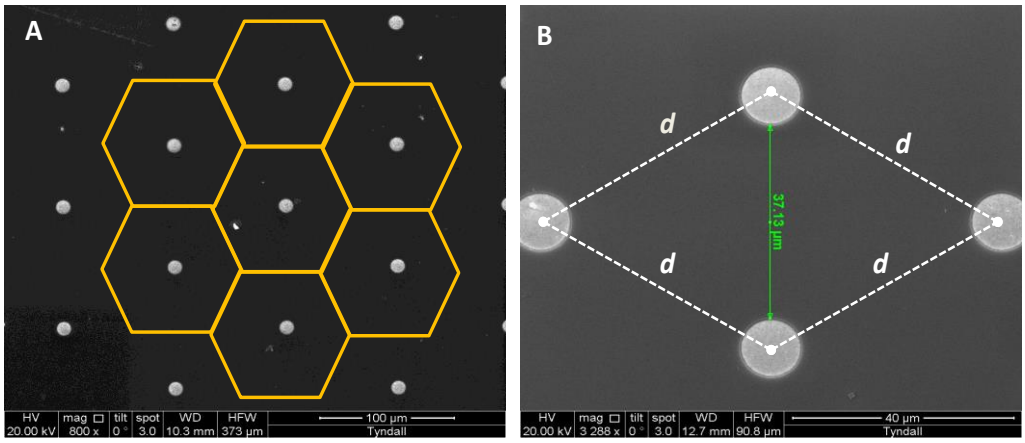


Figure 4.3: (A) Arrangement of fabricated discs array in hexagonal array; and (B) description of centre-to-centre spacing (noted by *d*) in disc array.

The density placement of the discs on the available WE area is characterised by the ratio *d*/*r* where *d* is the centre-to-centre distance between microdiscs and *r* the radius of the microdisc. According to Saito at al. (1968), the ratio of *d/r* can be used to delineate the defined regimes of individual and overlapping diffusion [17]. The independent behaviour of the microdisc electrode, i.e. individual diffusion profile could be achieved at *d/r*>12 [18], with other reported at *d/r*>20 [19]. However these values also greatly dependent on the timescale of the experiments (i.e. diffusion layer thickness) whereby at larger time scale (larger scan rate), all the individual diffusion layers may merge to form linear diffusion layer [18].

In this chapter, an experimental approach is used to study the effect of the *d/r* ratio, together with different numbers of electrodes in the array, towards electrochemical response. The first two wafers of both disc and band array (Wafer 1 and Wafer 2) have a fixed *d/r*=20 (*d/r*>12) while the following Wafer 3 (disc array) and Wafer 4 (band array) have fixed *d/r*=10 (Table 4.1 and Table 4.2).

Table 4.1 Geometrical parameters description for on-chip microelectrochemical cell consisting disc array (denote as D)

	Design	Geometry	Diameter (µm)	*d*, Spacing (centre-to-centre) (µm)	*N*, number of electrodes	Surface area (cm^2)
Wafer 1	D1	Disc	10	100	314	2.466×10^{-4}
	D2				150	1.178×10^{-4}
	D3				86	6.755×10^{-5}
Wafer 3	D4			50	314	2.466×10^{-4}
	D5				150	1.178×10^{-4}
	D6				86	6.755×10^{-5}

Table 4.2 Geometrical parameters description for on-chip microelectrochemical cell consisting band array (denote as B)

	Design	Geometry	Width (µm) x length (µm)	*d*, Spacing (centre-to-centre) (µm)	*N*, number of electrodes	Surface area (cm^2)
Wafer 2	B1	Band	10x500	100	18	9.0×10^{-4}
	B2				9	4.5×10^{-4}
	B3				5	2.5×10^{-4}
Wafer 4	B4			50	18	9.0×10^{-4}
	B5				9	4.5×10^{-4}
	B6				5	2.5×10^{-4}

The objectives of this study were to study the viability of the fabricated on-chip microelectrochemical cell; and to find the optimal design that can retain the microelectrodes properties (non-overlapping diffusion profile providing sigmoidal voltammogram and galvanogram with steady-state current).

4.2 On-Chip Microelectrochemical Cell Fabrication

The electrodes on the on-chip microelectrochemical cell were pre-patterned on a Si substrate and fabricated by standard photolithography and lift-off techniques. For WE fabrication, the process described earlier in Chapter 3 was applied. Additional fabrication process entailing the CE and RE are described here. They included Pt e-beam evaporation for the CE construction. Titanium was used in the proportion of 20:100 Ti:Pt to ensure appropriate adhesion of the Pt layer on the silicon. After metal evaporation, the excess metal and photoresist were lifted off in R1165 resist stripper.

The Ti:Ni:Ag layer (20:50:250) was only evaporated after the passivation etch as etch chemistry would damage the Ag layer. The Ag electrodes were then treated with $FeCl_3$ [20] followed by the lift-off technique. Following fabrication, the on-chip electrochemical cells wafers were diced and no further electrodes packaging were required. All microfabrication processing was carried out at the Central Fabrication Facility at Tyndall National Institute*.

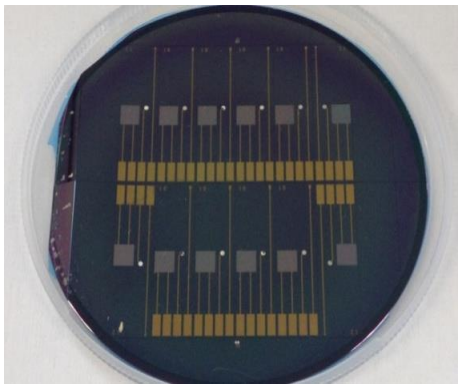


Figure 4.4: Silicon wafer containing fabricated on-chip microelectrochemical cell. Each wafer could produce up to 12 chips.

The following schematic diagrams depict the fabrication for each part of the microelectrochemical cell (Fig. 4.5).

* Fabrication by Mr. Dan O'Connell from Central Fabrication, Tyndall National Institute

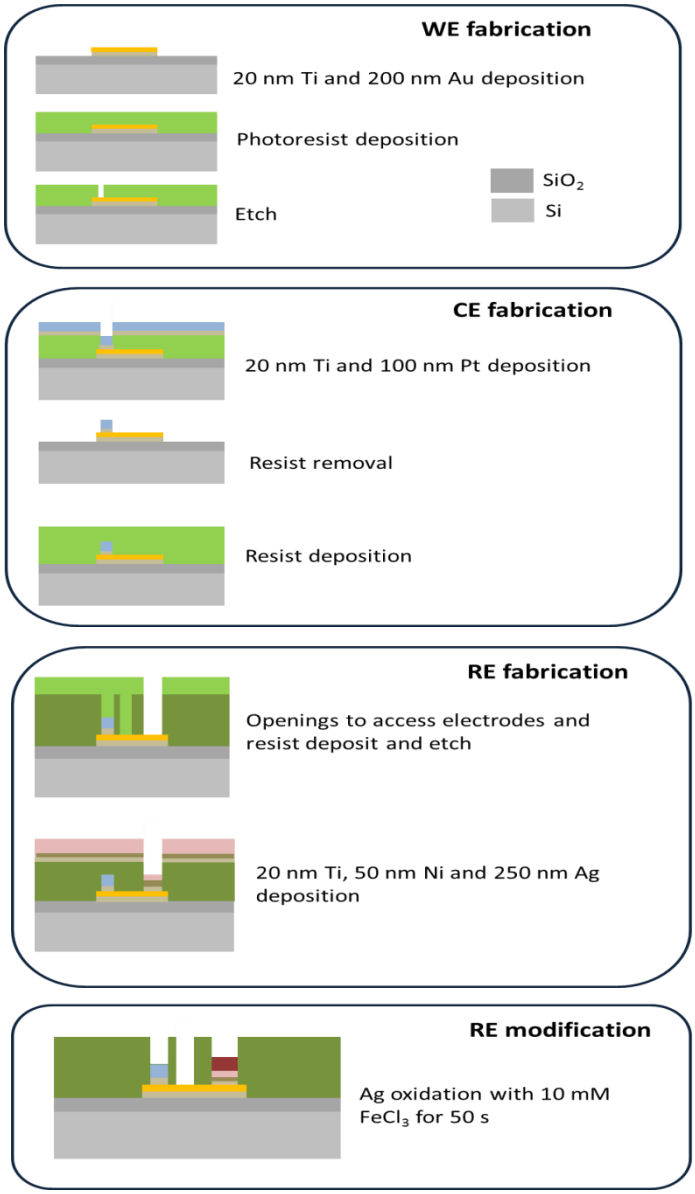


Figure 4.5: Simple schematic diagram showing the fabrication of the different parts (WE, CE and RE) on the on-chip microelectrochemical cell (not to scale).

4.3 Optical Study for Visual Characterisation

The fabricated on-chip microelectrochemical cells were inspected using scanning electron microscopy (SEM) to verify the dimensions of the array geometries, including the recess depth. The energy-dispersive X-ray spectroscopy (EDX) analysis was utilised to analyse the presence of gold, silver and platinum layers on the working, reference and counter electrodes respectively.

From the SEM images*, microdisc arrays were confirmed to have diameter of 10 µm. There is a slight difference in the diameter measurements of the disc when taken during the tilted position and in flat surface position. The tilted position is meant to measure the recess depth, however the reading on the tilted measurements have some corrected cross section measurements hence the differences. The recess depth was found to be an approximate of between 400-720 nm, deviation of 20-44% from the expected 500 nm recess depth. The distance between two discs were found to be in the vicinity of 86 µm and 37 µm which will made up the disc's centre-to-centre spacing approximated to 96 µm for the 100 µm spacing and 47 µm for the 50 µm spacing respectively (Fig. 4.6).

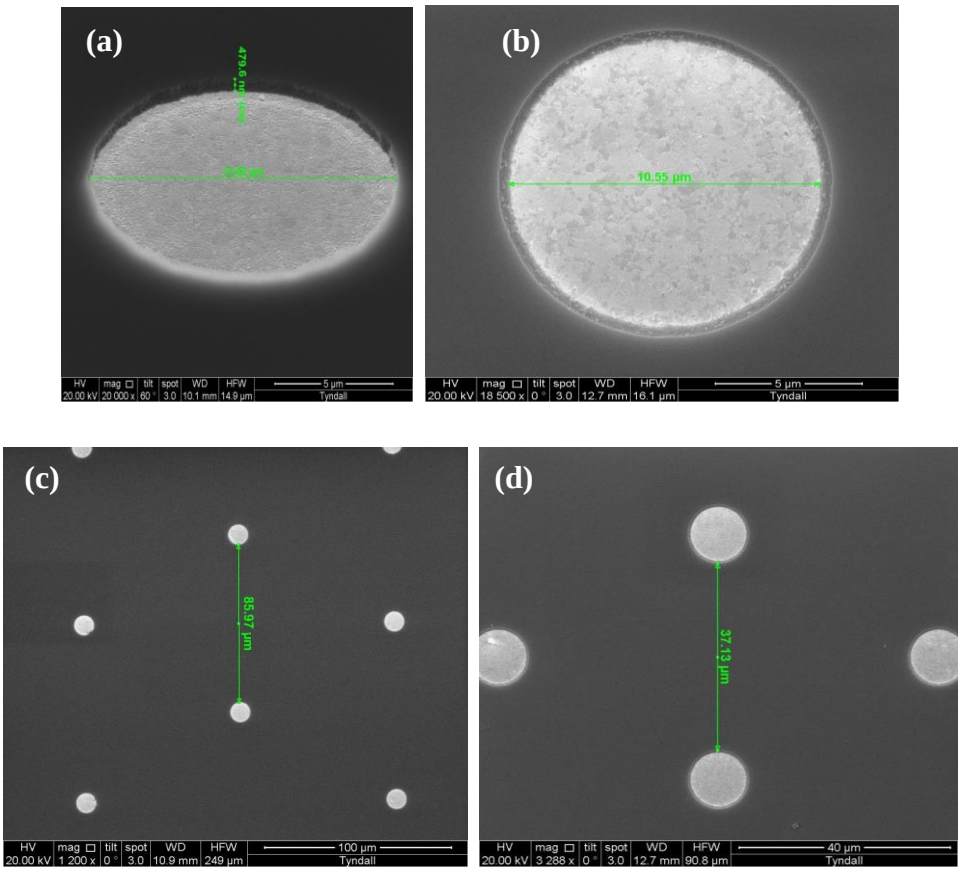


Figure 4.6: SEM images for on-chip microelectrochemical cell with disc arrays. Disc's diameter and recess measurements (a,b); and centre-to-centre distance expected for 100 µm spacing (c) and 50 µm spacing (d).

* SEM images and measurements by Mr. Vince Lodge from Central Fabrication Lab, Tyndall National Institute

For the microband array on the other hand, the achieved dimensions for the fabricated electrodes were in good agreement with the dimensions expected. The band lengths were confirmed to have 493.5 nm which is close to 500 nm as expected. The width of the band was found to be 11.51 μm on tilted position with the range of 600 nm recess depth (Fig. 4.7).

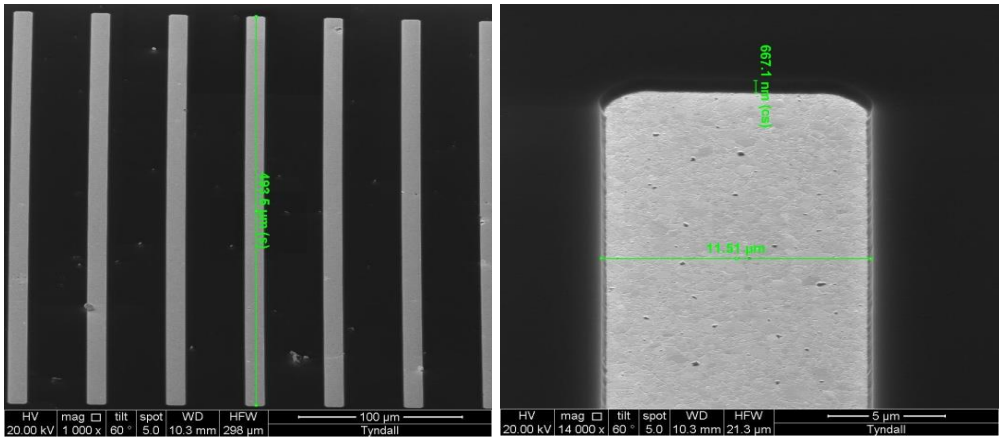


Figure 4.7: SEM images for on-chip microelectrochemical cell with band arrays.

The EDX analysis* confirmed the presence of gold for the WE surface, silver for RE surface and platinum for CE surface (Fig. 4.8). However there was no chloride detected in the RE component, suggesting the instability of the Cl layer formed on the electrode from the Cl treatment. The Cl counterpart might have been peeled off during the lift-off process in fabrication or after several electrochemical measurements. Ti element was present in all the spectra as Ti was used to adhere the electrode metals on the silicon substrate. The presence of Ni on the RE surface may also suggest that some amount of Ni was used as well to adhere the Ag metal on the silicon besides Ti as used in the pyrex/silicon substrate [21]. Some traces of Fe, C, N and K were also found in the RE EDX spectra, which could be derived from the potassium hexaferricyanide solution in sodium chloride used to do some electrochemical measurements of the on-chip microelectrochemical cell prior the SEM/EDX analysis.

* EDX analysis also by Mr. Vince Lodge, Central Fabrication Lab, Tyndall National Institute

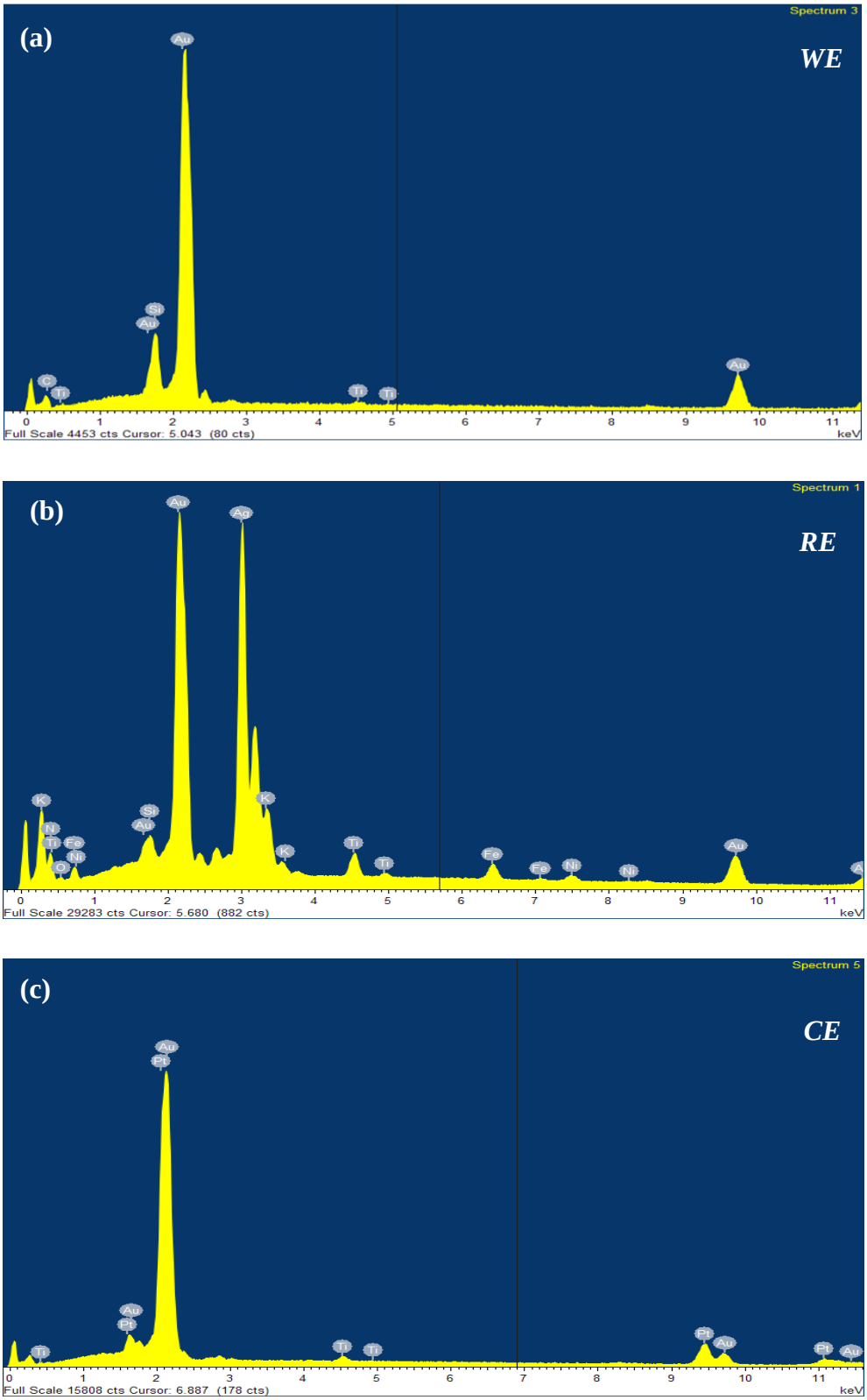


Figure 4.8: EDX spectrum of the Au microelectrode array (a); Ag reference electrode (b); and Pt counter electrode (c).

4.4 Electrochemical Characterisation

All electrochemical characterisations were carried out in 0.1 M ferrocenecarboxylic acid in PBS (pH 7.4). A customised connector (Uniscan Limited, Buxton, UK) was used to hold the on-chip microelectrochemical cell. The on-chip microelectrochemical cell was plasma cleaned for 10 minutes first prior electrochemical measurements. It was found that by prolonging plasma cleaning time, though clean the microelectrode array better; would damage the silver layer on the reference electrode surface. This correlates to the fact that ion etching destroying the Ag layer as discussed in the fabrication part. The suggested 10 min is the optimal time providing trade-off between electrodes clearing and on-chip microelectrochemical cell reliability

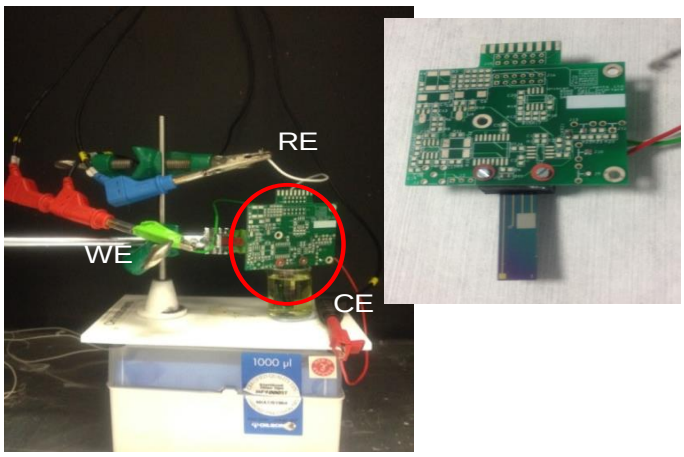


Figure 4.9: Experimental set-up of the on-chip microelectrochemical cell with customised connector for electrochemical measurements.

Although EDX analysis has confirmed the successful deposition of Ag and Pt on RE and CE respectively, electrochemical measurements using commercial Ag/AgCl reference electrode and Pt wire were also taken (hereafter referred as *off-chip* measurements/reading) and compared with the measurements using on-chip's RE and CE (hereafter referred as *on-chip* measurement/reading). This aspect is vital in order to study the electrochemical viability of the fabricated electrodes.

4.4.1 Cyclic Voltammetry Studies

Characterisation of On-chip Electrodes and Commercial Electrodes

The electrochemical performance of the fabricated on-chip Ag reference electrode and Pt counter electrode were first evaluated by comparing the CVs taken from the on-chip cell as a one-piece device and WE from the chip with the external commercial Ag/AgCl and Pt wire electrodes. Four modes of measurements were performed: (i) all-on-chip reading (using both RE and CE on the on-chip microelectrochemical cell); (ii) CE commercial (RE on-chip); (iii) RE commercial (CE on-chip); and (iv) both RE and CE commercial. The voltammograms were obtained in 3 repetitions at a scan rate of 100 mV s^{-1}. As shown in Fig. 4.10, the voltammograms displayed identical peak shapes and currents, but different peak potentials, which can be attributed to the properties of the reference electrodes [5]. Moreover, all voltammograms were obtained with good reproducibility, stability, and reversibility, indicating the successful operability of the fabricated Ag/AgCl reference electrode and platinum counter electrode.

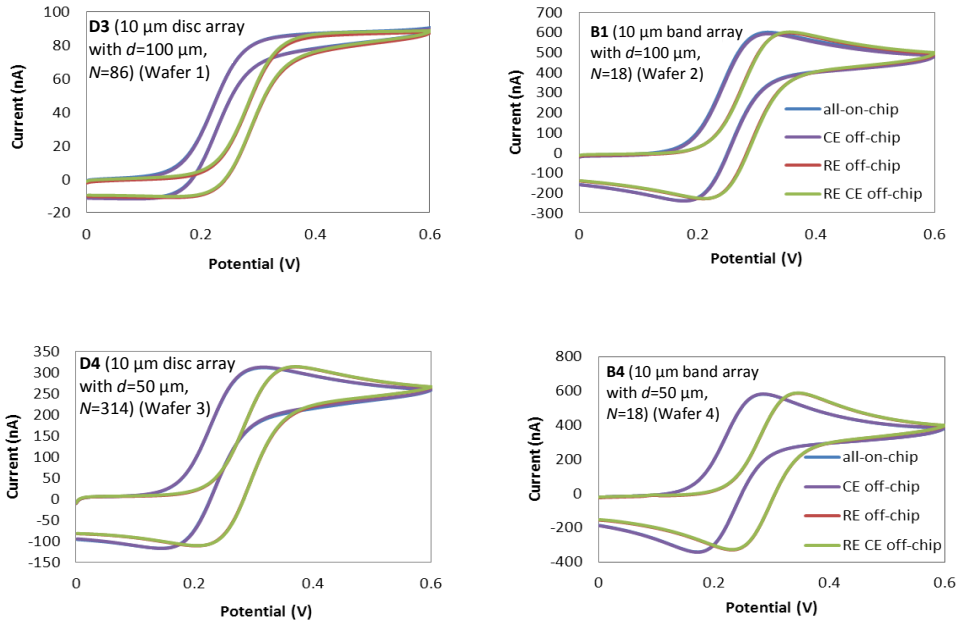


Figure 4.10: On-chip measurements for fabricated microelectrochemical cells (one design from each wafer) compared with readings from commercial RE and CE in 1 mM FCA in PBS, scan rate of 100 mV s^{-1}.

Similar results for the peak shift using commercial Ag/AgCl reference electrode in comparison with on-chip RE were also reported before by Moujahid et al. (2011) [5] and Chen et al. (2000) [15]. In both cases, the RE layer on-chip was retreated with silver and chloride ion was oxidised in either HCl or KCl to form AgCl. In our study, the formation of AgCl was carried out after the deposition of Ti:Ni:Ag layer by submerging the wafers in the $FeCl_3$ solution for 50 seconds as described by Polk et al. (2006) [20].

The shift of the potential separation was due to the commercial RE inner solution (1M KCl) and the concentration of the chloride in the PBS solution (0.05 M). The potential difference between the on-chip and commercial RE can be determined according to the Nernst equation:

$$E_{Ag|AgCl} = E^0_{Ag|AgCl} + \frac{RT}{nF} \ln a_{Cl^-} \quad \ldots . (Eq. 4.1)$$

where $E_{Ag|AgCl}$ is the standard potential for the Ag/AgCl electrode ($E_{Ag|AgCl}$ is 0.2223) and a_{Cl^-} is the chloride activity which can be approximated to the chloride concentration in the solution. The results obtained for the expected potential according to the equation were 0.1467 V for the chloride in 1 mM FCA in PBS and 0.2223 V for the chloride in 1M potassium chloride. The potential on the on-chip RE measurements were found 0.1531 ± 0.014 V, which were close with the calculated ones.

The experimental limiting current, i_{lim}, for the different microelectrochemical cell designs were obtained by averaging three readings or more from one or more measurements (Table 4.3). The values were then compared with theoretical current calculated with previous equations as presented previously in Chapter 3 (Eq. 3.4 for microdisc array and Eq. 3.6 for microband array). All measurements were taken using all-on-chip electrochemical reading.

Table 4.3 Comparison between the theoretical current and experimental current for microelectrode array working electrode for on-chip electrochemical cell

Design	Recess depth (nm)*	Theoretical current, nA	Experimental current, nA
D1	715	292	301.8 ± 26.01
D2	748	139	160.3 ± 3.42
D3	660	81	80.7 ± 6.42
D4	778	288	268. 6 ± 7.28
D5	479	147	156.1 ± 2.73
D6	612	79.9	119.4 ± 2.56
B1	765	622	550 ± 9.75
B2	675	314	223.3 ± 17.75
B3**	n/a	173	151.3 ± 0.64
B4	681	628	500.9 ± 28.3
B5	667	315	218.7 ± 9.15
B6	656	175	142.5 ± 28.88

In the first three disc designs (D1-D3) with interspacing distance of 100 μm, sigmoidal shape CV was observed indicating the occurence of hemispherical diffusion of the ferrocenecarboxylic acid towards the microdiscs with non-overlapping diffusion zones between the neighboring microdiscs. This is validated by the experimental limiting currents achieved for those designs are relatively close with the theoretical current. Such results were similar as obtained for the single WE microelectrode array of 10 μm microdisc array as reported in previous Chapter 3.

The excessive current could be due to 'edge effect' of convergent diffusion at disc microelectrodes. Convergent diffusion is particularly dominant in microelectrodes in comparison with macroelectrodes, as more than 95% of the current collected arises from convergent diffusion to the edges of the microelectrode rather than across the entire electrode surface [22]. In some cases, organic residues on the substrate surface

* Recess depth measurements were determined from SEM images on respective chips. This was done by Mr. Vince Lodge

** A substitute chip with same parameters (spacing and number of array) was used

also could contribute to a faradaic current as reported by Franks et al (2005) on their microfabricated silicon-based Pt macro- and microelectrode [23]. In order to overcome this, their macro- and microelectrodes were further treated by six cycles of cyclic voltammetry from to -1.0 V to +1.0 V after plasma cleaning step. In our studies where the cyclic voltammetry cleaning was not applied, current depletion was observed on subsequent characterisation measurements using the same electrodes on different days; suggesting the excessive current could be derived from the organic traces left on the chips. This however did not greatly affect the first version of microelectrode array single chip, presumably due to its small size in comparison with the on-cell electrochemical chip size. Despite the current depletion and large standard deviation for D1 particularly, the experimental limiting current in comparison with their theoretical value is still acceptable.

For the following disc designs with centre-to-centre interspacing distance of 50 μm (D4-D6), experimental limiting currents for D4 and D5 show good agreement with the theoretical values. The experimental current for D4 was 7% less in comparison with the theoretical current which may suggest that the overlapping diffusion current has taken place once the disc spacing was reduced. In D6 however, the current obtained was 49% higher compared to the theoretical one. With decreasing number of disc array (N=86) and insufficient interspacing distance between the discs to allow individual diffusion profile, this pattern could be attributed to the planar or mixed diffusion which has taken over the hemispherical diffusion. The effect of having 50 μm interspacing distance instead of 100 μm for microdisc array is so apparent in a way that the sigmoidal current has diminished and shifted to a peak-shaped CV (Fig. 4.11) [24].

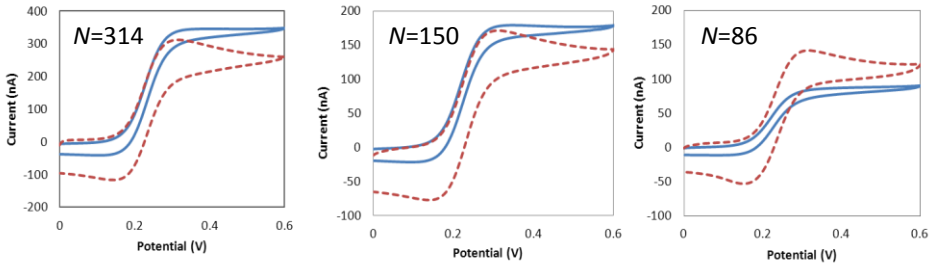


Figure 4.11: The diminishing sigmoidal signal as the distance between the disc's interspacing was reduced from *d*=100 µm (blue line) to *d*=50 µm (red dotted line). Scan rate 100 mV s^{-1} in 1mM FCA in PBS.

The experimental limiting currents increased linearly with the number of microdiscs in array with a determination coefficient r^2=0.9923 for disc centre-to-centre separation 100 µm (inset Fig. 4.12A) and r^2=0.9986 (inset Fig. 4.12B). The CV signal also decreased accordingly, except for D6 which has clearly did not behave as an ideal microelectrode.

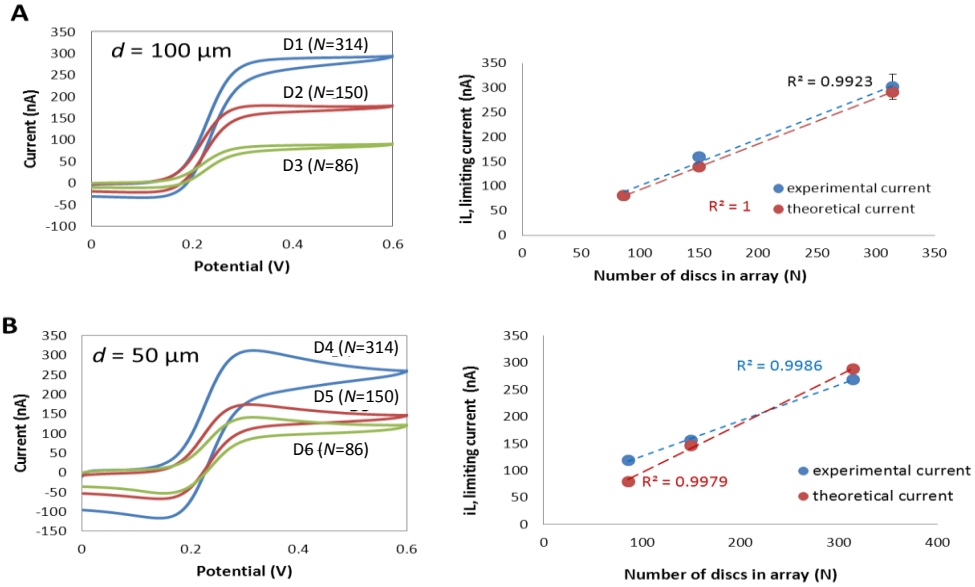


Figure 4.12: Cyclic voltammetry of disc microelectrode array fabricated on microelectrochemical cell for (A) D1-D3 (Wafer 1); and (B) D3-D6 (Wafer 3). Measurements were carried out using on-chip electrochemical cell with scan rate of 100 mV s^{-1} in 1mM FCA in PBS. *Insets*: i_{lim} as a function of *N* for both experimental (blue marker) and theoretical currents (red marker).

For a microelectrochemical cell with the microband array, the theoretical limiting current exceeded the experimental values with discrepancy between current values in the range of 11-31%. As discussed in the previous chapter, the diffusion profile suggested for the fabricated band array was a mixed diffusion profile (individual with overlapping diffusion profile); hence this can be accounted for the large difference between the current values. Probable occurance of planar diffusion also could contribute to the difference.

The voltammogram shapes obtained for the band interspacing centre at 100 µm (B1-B3) showed typical quasi-steady state voltammograms as reported for microband array [25]. This voltammogram however has shifted to a more pronounced peak-shaped CV when the interspacing was reduced by half to 50 µm (Fig. 4.13) for B3-B6. This effect was clearly obvious when the number of array has greatly decreased (N=5). The diffusion profile that would be suggested for the B6 is a planar diffusion, which happens when insufficient spacing is designed on an electrode [26].

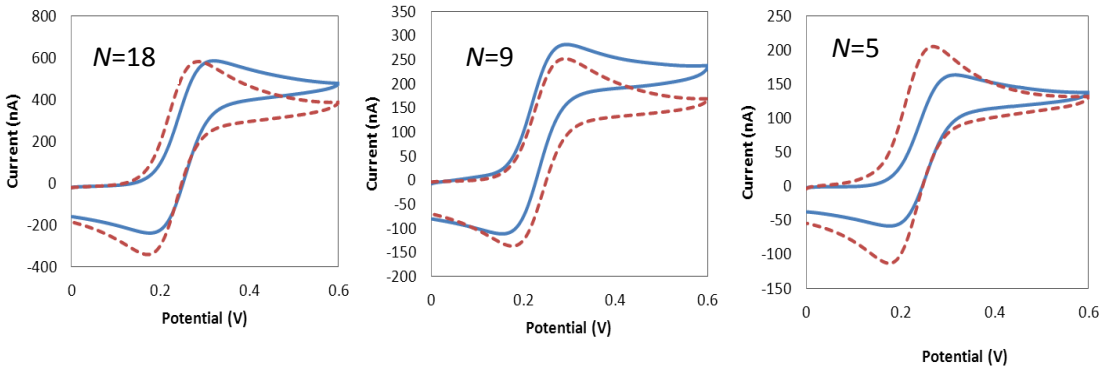


Figure 4.13: The voltammogram has shifted to a peak-shaped CV when band spacing distance was reduced from 100 µm (blue line) to 50 µm (red dotted line). Scan rate100 mV s^{-1} in 1 mM FCA in PBS.

To compare the effect of having a fixed electrode area with reduced interband spacing, a current density study was plotted (Fig. 4.14). It was found that reducing the interband spacing also has resulted in decrease of current density although having

the same area. Overlapping current or planar diffusion is hence suggested for B4-B6 which takes place once the spacing is reduced. This is in agreement with Compton and co-workers who reported that current density at individual electrodes is much greater than a macroelectrode under planar diffuson [22]. Thus B4-B6 had lost their ideal microelectrode properties and no longer behaves as two microelectrode arrays.

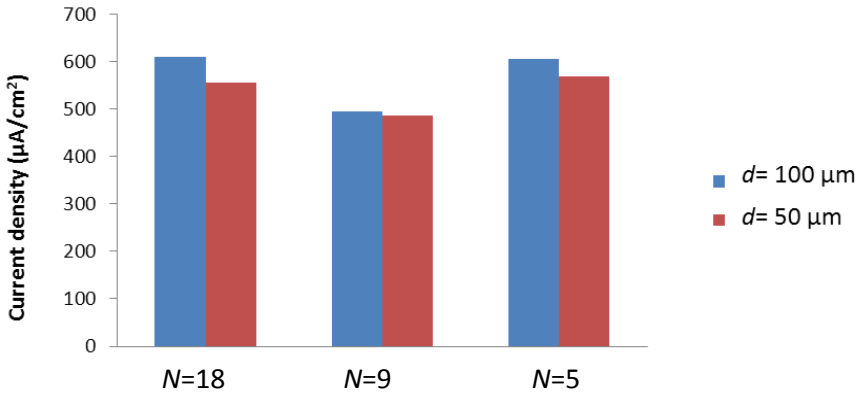


Figure 4.14: Current density of the different interband spacing with the same electrode area (cm^2).

The linearity of the experimental current for the microband electrode for the on-chip microelectrochemical cell were excellent with r^2=0.989 and r^2=0.9948 respectively for interband distance of 100 µm and 50 µm respectively (inset Fig. 4.15 A and B). The r^2 value for theoretical limiting current for B1-B3 however was 0.9987 and not 1 as expected due to the fact that a substitute chip was used to replace the B3 and the recess depth was not checked through SEM, instead it was estimated to be 700 nm. Comparing the CV for B4-B6, the B6 design has similarity with previous reported D6 where their experimental currents deviate significantly from the theoretical current indicating overlapping/planar diffusion that has taken place in the system.

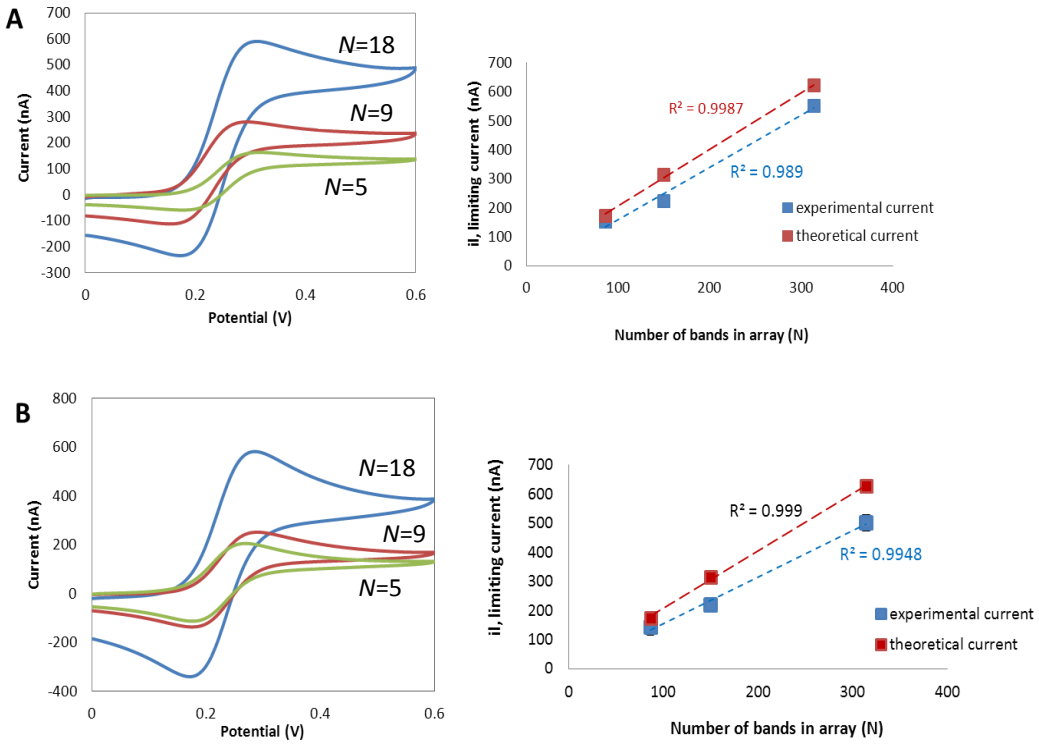


Figure 4.15: Cyclic voltammetry of microelectrochemical cell with band microelectrode array for (A) B1-B3 (Wafer 2); and (B) B3-B6 (Wafer 4). Measurements were carried out in 1 mM FCA in PBS with scan rate of 100 mV s^{-1}. *Insets*: i_{lim} as a function of N for both experimental (blue marker) and theoretical currents (red marker).

To conclude all the fabricated on-chip microelectrochemical cells for the limiting current study, the correlation between theoretical and experimental current for all designs were presented in Fig. 4.16 The correlation gave a good r^2 value of 0.9508 considering the fact that irregularity in the recess depth fabricated was noted.

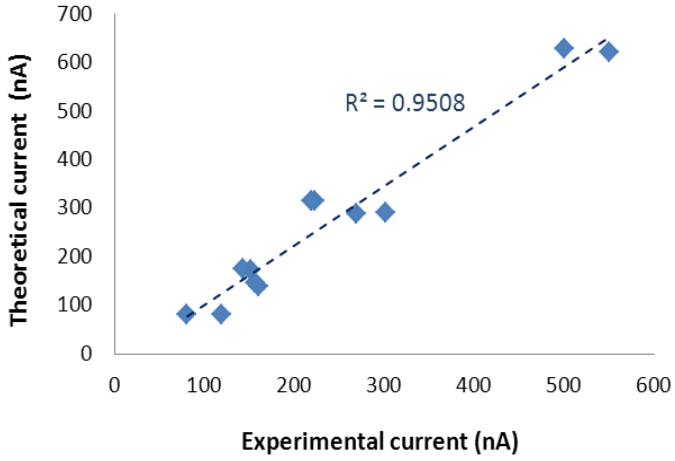


Figure 4.16: Correlation between experimental and theoretical current for all fabricated on-chip microelectrochemical cell.

The effect of reducing the interspacing disc/band array on microelectrodes scan rates were next reported.

Scan Rate Effect on Voltammogram for Different Centre-to-Centre Spacing

For the scan rate study on voltammogram for different centre-to-centre spacing (*d*), only 9 on-chip microelectrochemical cells that were available for further testing. The other three on-chip microelectrode cells namely D2, D6 and B3 were found no longer active due to the presence of dead electrodes and delamination of the band electrodes. The constrain of having subsequent studies for the failed electrodes also are due of limited number of those on-chip microelectrochemical cells fabricated on the wafer, and worse in some cases, both/all electrodes of similar design fail to work.

Lithographic fabrication procedures used are known to be associated with the presence of dead or inactive electrodes which eventually lead to a lower limiting current [4, 27, 28]. Although it was reported that copper electroplating technique was employed to identify the presence of dead electrodes visually [27, 28], the presence of active/inactive electrodes also could be simply investigated by fluorescent

microscope or SEM. The latter technique with EDX analysis is more precise as it is able to inspect the presence/absence of gold layer.

Fig. 4.17 compares two microdisc designs (D2 and D3). As one can see D2 consisted of dead electrodes whilst all the electrodes in D3 were active. The presence of active electrodes could be indicated by the gold layer which seen underneath the microdiscs. On the other hand, if the electrodes are dead, black dots were observed representing the absence of gold. The inset figure in Fig. 4.17(A) shows the massive depletion of current that indicates the electrode has deteriorated hence leaving *ca.* less 50% of active sites.

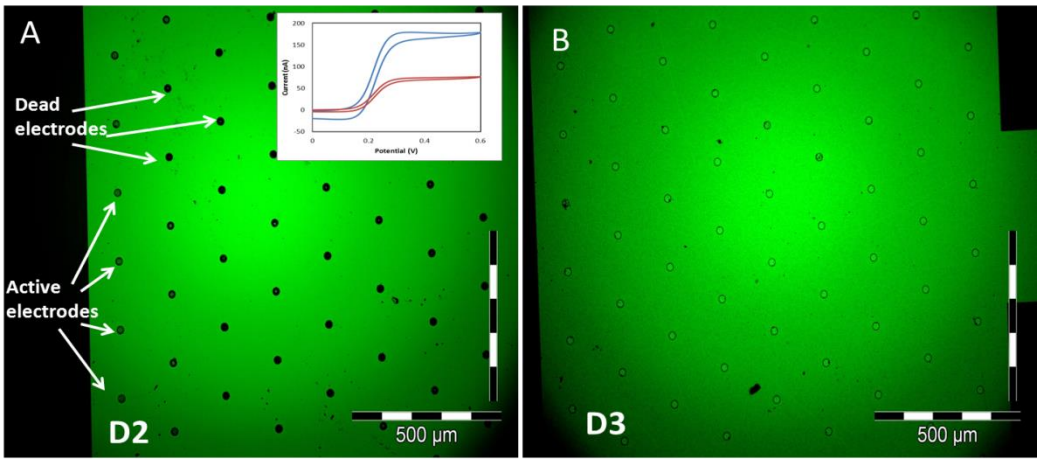


Figure 4.17: Fluorescent microscope image of (A) dead discs on design D2 (*N*=150, *d*=100 µm), represented by black dots (*inset*: current depletion voltammogram in 1 mM FCA in PBS of 100 mv s^{-1} scan rate, before (blue line) and after (red line) dead electrode occurance); and (B) image of active disc electrodes on D3 (*N*=86, *d*=100 µm) with gold layer underneath the discs. Magnification 20x.

For the microband electrode of B3, it also observed that no gold layer left within the recess surface. In comparison, an active microband would have a layer of gold presence as in Fig. 4.18B. We could attribute this to the lamination of the band electrode. Lamination is one of the defect or failure mode that normally occurs in silicon based microsensors [29, 30]. Interestingly, non-uniform current densities on

the electrode surface also have been reported to contribute on electrodes damage [31, 32].

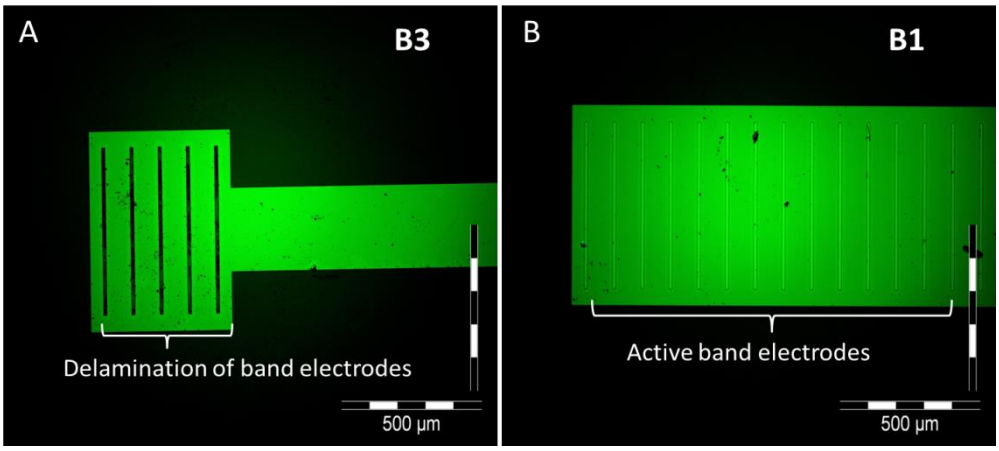


Figure 4.18: Fluorescent microscope image of (A) lamination of gold microband array as observed in B3 (N=5, d=100 µm) design, in comparison with (B) active microband with gold layer as for design B1 (N=18, d=100 µm). Magnification 10x.

The scan rate impacts on voltammogram for the remaining nine on-cell electrochemical chips are now discussed. Microdisc array with interspacing of 100 µm was able to retain its sigmoidal shape if scan rate was increased (Fig. 4.19-top row). When the interspace distance was reduced, the exclusivity of having microelectrode properties has diasppared as indicated by the arisen of peak-shaped voltammogram that changed accordingly with the scan rate increment (Fig. 4.19-bottom row). This implies a diffusion domain has overlapped at the measured scan rate. The reduction peak current (I_{pc}) of FcCOOH, becomes less pronounced for D4 and D5 at higher scan rates where overlapping occurred due to the dominating approach of semi-infinite linear diffusiont [24].

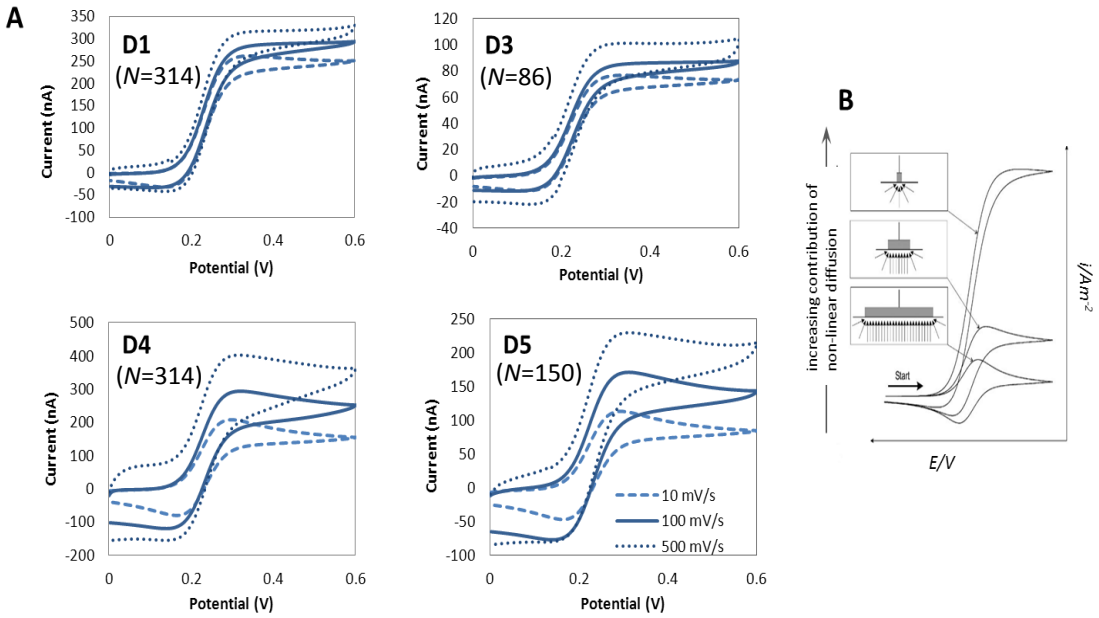


Figure 4.19: (A) Scan rate study for on-chip electrochemical cell with microdisc array working electrode with *d*=100 μm (top row) and *d*= 50 μm (bottom row). Measurements were carried out using all-on-chip reading in 1 mM FCA in PBS with various scan rates. (B) Schematic diagram showing the relationship beween the size of electrode (with respect to the diffusion layer thickness) and the contribution of convergent diffusion to the observed voltammetry (Taken from Ref. [33]).

The cyclic voltammetry peak-shaped response as obtained for the reduced disc interspacing (*d*=50 μm) is a feature of linear diffusion. When it occurs, the diffusion layer is almost flat in shape. On the other hand, the steady-state limit is a characteristic of convergent diffusion and an approximately hemispherical shaped diffusion layer for the diffusion layers associated with different types of voltammogram [34]. The following Fig. 4.20 show that for both D1 and D3 where the disc interspacing is sufficient to allow indivisual hemispherical diffusion (*d*=100 μm), the sigmoidal current stays within the same range although scan rate was increased. However for D4 and D5, the current increased gradually accordingly with the increased scan rate indicating the diminishing of the individual diffusion layer and that dominating overlapping diffusion is occuring.

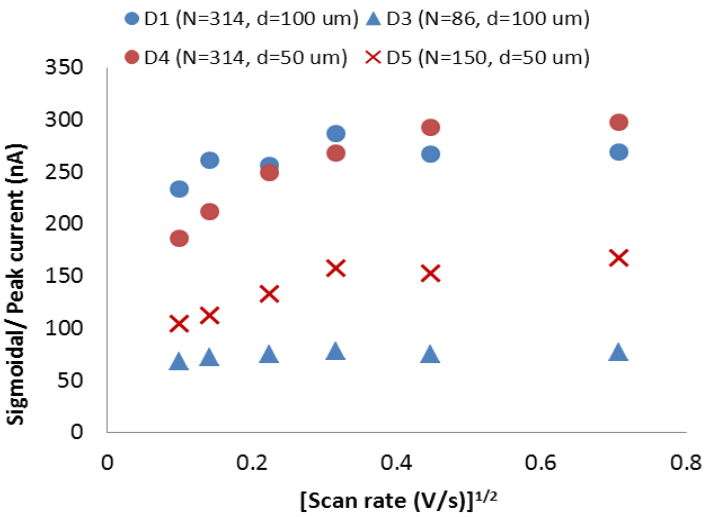


Figure 4.20: Sigmoidal current change as a function of square root of scan rate for microdisc array on-cell electrochemical chip with different disc interspacing, *d*=100 μm (blue marker) and *d*=50 μm (red marker). Red dotted line represents current increment with increasing scan rate for design D4 and D5. For both D1 and D3 with disc interspacing 100 μm (blue marker), there is no current increment observed.

Although microband electrodes were reported to exhibit sigmoidal-shaped CV at slow scan rates (<1 V s^{-1}) [35, 36], nevertheless in our study, the CV shape obtained at scan rate of 10 mV s^{-1} was more of quasi-sigmoidal voltammogram and it was more inclined to peak-shaped CV at 100 mV s^{-1}. These discrepancies could be due to the size of microband employed in the microcell. In Nagale & Fritsch's study (1998), the microbands have width of 25.3-143.5 nm whilst in our study the width is ten times larger i.e. 10 μm. Furthermore in their investigation, the microbands were not recessed but were of protruding bands fabricated on multilayer materials [36]. At higher scan rate, it was observed that CV has more pronounce peak-shape CV, presumable due to an increasing contribution from linear diffusion [34, 36]. The CV shape for B6 at 500 mV s^{-1} showed a 'distorted' CV due to the leaky/crack band electrodes related to delamination that takes place during the CV experiment [30].

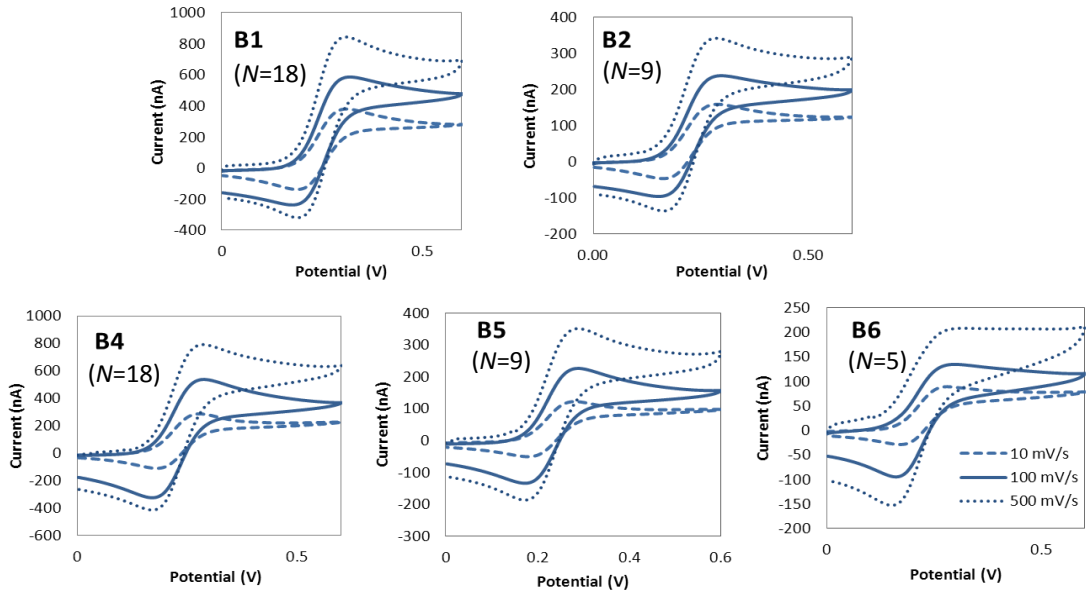


Figure 4.21: Scan rate study on on-chip electrochemical cell with microband array working electrode with *d*=100 μm (B1-B2) (top row) and *d*= 50 μm (B4-B5) (bottom row).

All the band electrodes had scan-rate dependant CVs regardless of the band interspacing distance (Fig. 4.22). It is deduced from the diffusion classification introduced by Compton's group [19, 34] (Fig. 4.22) and as reported previously in Chapter 3, that B1-B3 designs (band interspacing of 100 μm) has mixed diffusion layer (Category 3); and B4-B6 designs (reduced band interspacing of 50 μm) have planar diffusion layer (Category 4) hence act like a macroelectrode.

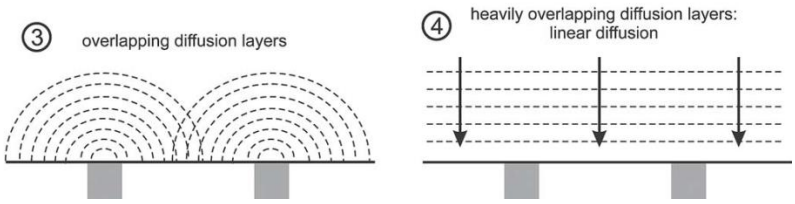


Figure 4.22: Schematic diagram of Category 3 and 4 diffusion profile of microelectrode array suggested for B1-B3 and B4-B6 design respectively. Taken from Ref. [19].

The Category 4 case is decribed when strong overlap of the diffusional fields leading to the entire array behaved as single microelectrodes of the same total area as the microdisc plus insulator area. As seen from the previous Fig. 4.21, the peak currents increased accordingly with the scan rate as expected for a single macroelectrode (Fig. 4.23). Although there is the same trend observed for B1 and B2 CVs, we shall stick these results to the Category 3 which is intermediate between Category 2 (individual diffusion) and Category 4.

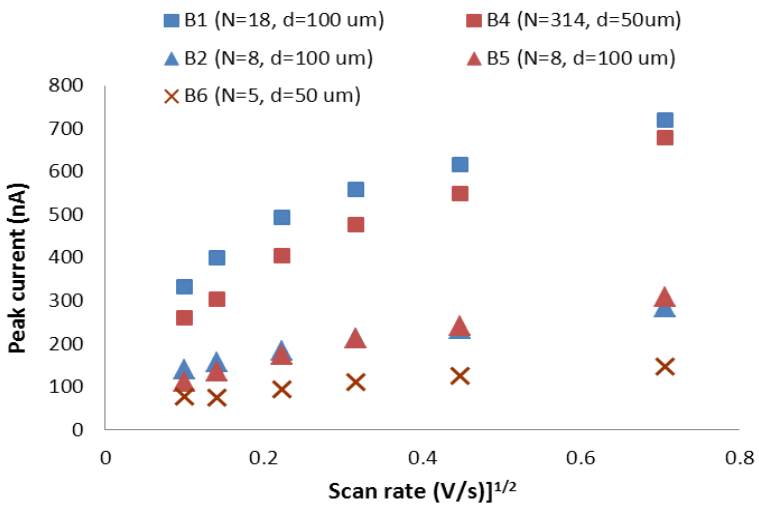


Figure 4.23: Square root of scan rate as a function of the peak current change for microband array on-cell electrochemical chip with different band interspacing, d=100 µm (blue marker) and d=50 µm (red marker).

4.4.2 On-chip RE Stability Study

A stability study on the fabricated Ag RE surface with $FeCl_3$ treatment was studied using open-circuit potential in 1M KCl against commercial Ag/AgCl electrode (3M KCl filling). Readings for the first two electrodes were taken on a replicate of three days experiments for over 6 hours.

As can be seen from Fig. 4.24, both commercial and on-chip RE electrodes reached the steady-state potential within an hour. However, the on-chip Ag/AgCl required more time to achieve steady state potential and the difference between starting and

steady-state potential is larger in comparison with commercial Ag/AgCl RE (167 mV against 218 mV). In a longer time scale (Fig. 4.24b) the advantage of commercial RE over on-chip RE became more obviously as the potential of on-chip RE increased gradually with a slope of R^2=0.7487. The potential of the microfabricated "quasi-reference" electrode (without KCl-containing membrane) was reported to be stable up to 10 hours [37]. The commercial RE however was able to retain the constant potential within 4 hours before the potential drop of 27 mV was observed.

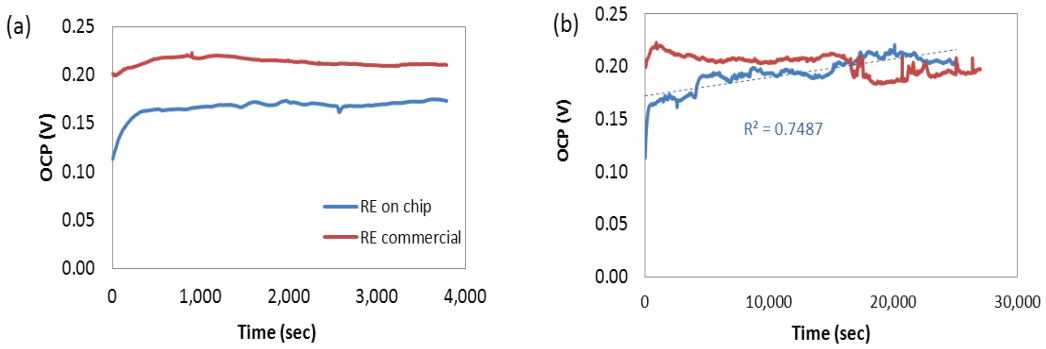


Figure 4.24: Open circuit potentials of on-chip Ag/AgCl on-chip (blue line) and commercial Ag/AgCl (red line) on (a) shorter time scale of 1 hour; and (b) over 6 hours.

It is hence advisable to re-treat the on-chip RE layer with chloride treatment to form the a more robust and reliable chloride counterpart [20] if the on-chip electrochemical study were to be used at longer timescale. Among the treatment of Cl^- on the RE surface post-fabrication that can be suggested is the coating of the surface with silver paint followed by curing at 120°C for 60 minutes. The silver layer then was oxidised to form Ag/AgCl by voltammetric cycling in 1 M KCl [4]. Deposition of additional KCl-containing agar on the silicon-chip electrodes with different coatings (i.e. Nafion and poly-(2-hydroxyethyl (pHEMA)) also has been described to retain the Cl^- leaching properties and to prevent the AgCl layer becoming worn over time [37].

4.4.3 Electrochemical Impedance Spectroscopy Study

As a beginning, a comparative study between EIS using all-on-chip electrodes with off-chip (commercial) RE and CE was carried out. This is to ensure that all on-chip EIS measurements are reliable as with the commercial electrodes. All EIS measurements were taken with minimum of two readings and the average was taken to plot the respective Nyquist plot.

Both EIS curves using on-chip RE and CE were comparable with commercial electrodes measurements (Fig. 4.25) with overlapping of diffusion zones seemed to occur at frequency below of 0.119 Hz. For the on-chip electrochemicall cell, it is noted that the CE surface is larger than the WE of microelectrode array. When the impedance between a small electrode and a large counter electrode is measured, the measured impedance will be dominated by the small electrode impedance [38]. The similarity exhibited between these two modes of measurement hence proved the realiability of the microfabricated RE and CE and thus allowed us to characterise the remaining microelectrochemical cells using all-on-chip measurements.

Another objective by undertaking this experiment is to study the adequacy of the on-chip microelectrochemical cell design with the significant space separation between CE, RE and WE. This separation relates to the specificity of transducer application to biosensing where the WE after the transducer fabrication is subjected to surface biomodification as was discussed in the beginning of the chapter. The long distance between RE and WE leads to an increase of the liquid that can affect the impedance spectrum. As one can see there is no significant difference between spectra at the high frequency range that proves the adequacy of the microchemical cell design. An absence of the difference in the spectra also confirms that the obtained stability of the RE is sufficient for applying EIS - which will be the base for biosensor implemention.

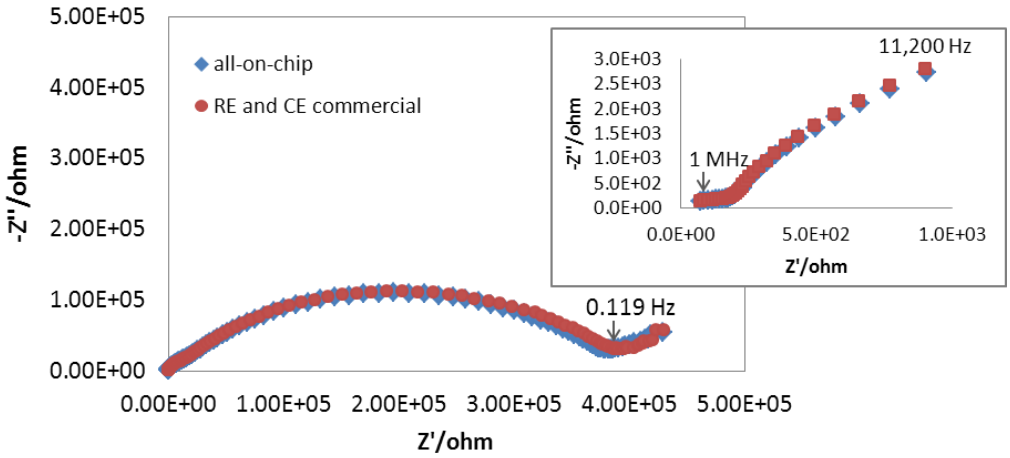


Figure 4.25: Nyquist plot of EIS for D1 microdisc array (*N*=314, *d*=100 µm) design using all-on-chip measurement (blue marker) and off-chip RE and CE (red marker) in 1 mM FCA in PBS. $E_{1/2}$ at 0.29 V, frequency 0.01-1MHz (*Inset*: EIS at higher frequency of 11,200 Hz-1MHz).

Typical Nyquist plot for recessed microdisc array was observed for the microdiscs design of D1 and D3 with disc interspacing 100 µm. For the disc interspacing of 50 µm on the other hand, a straight line is observed in the middle of the real imaginary axis indicating that the presence of linear diffusion on the electrode surface resulted from the overlapping diffusion as suggested (Fig. 4.26B).

For both D1 and D3, linear diffusions at lower frequencies were observed to take place starting from 0.119 Hz (*t*=410 secs) onwards in both cases. When the interspacing was decreased and the electrodes became more closely packed, the frequencies were observed to increase to 0.189 Hz (*t*=375 secs) and 0.352 Hz (*t*=339 secs) respectively for D4 and D5. These values are in agreement with the scan rate studies where at the more packed array, the linear diffusion takes place faster (339 secs) compared to those of largely spaced ones (410 secs).

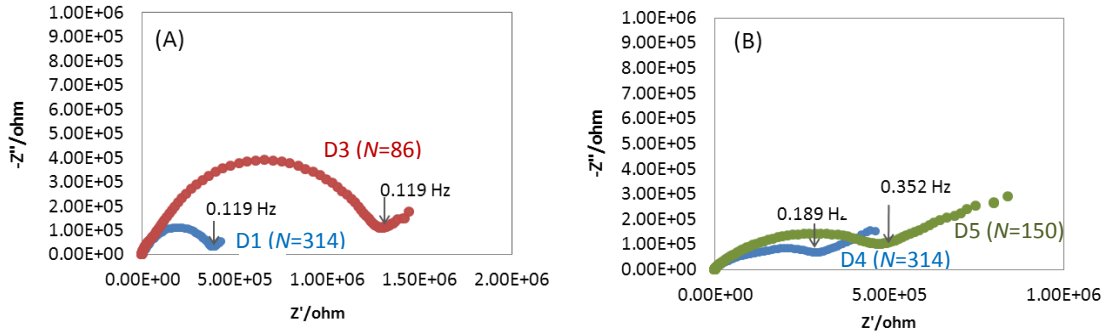


Figure 4.26: EIS spectrum in 1 mM FCA in PBS (frequency 0.01-1MHz, $E_{1/2}$ at 0.29 V) for (A) D1 and D3 (d=100 µm); and (B) D4and D5 (d= 50 µm).

For the microband array, a semi-circle region followed by a straight line at low frequency was observed. The linear part observed at the low frequency range implies a mass-transfer limited process and diffusion that still prevail in the within the recessed band. There was a difference in the semi-circle form and frequency at linear diffusion occurs albeit at the same band array/surface area (Fig. 4.27) hence suggesting different diffusion profile to the electrode surface as suggested earlier. For the band array of 18 electrodes, it can be seen that by reducing the band spacing to half, the linear diffusion took place faster (0.653 Hz, t=316 secs) compared to the 100 µm spacing (0.189 Hz, t=376 secs). The same frequences and times was observed at 9 band electrode array.

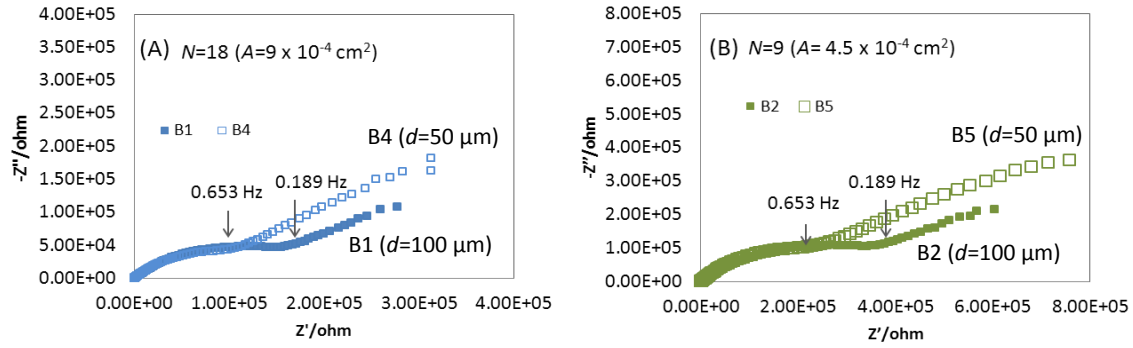


Figure 4.27: EIS spectrum in 1 mM FCA in PBS (frequency 0.01-1MHz, $E_{1/2}$ at 0.29 V) for the band arrays of same surface area (A) A=9x10^{-4} cm^2 (N=18); and (B) A=4.5x10^{-4} cm^2 (N=9). Filled marker indicate d=100 µm while non-filled marker indicate d=50 µm.

For the B6 however, the impedance is similar to a macroelectrode response where a very small semi-cirle at very high frequencies followed by a straight diffusion line (Fig. 4.28). This behaviour impedance as in accordance as reported for the suggested diffusion layer (planar diffusion profile).

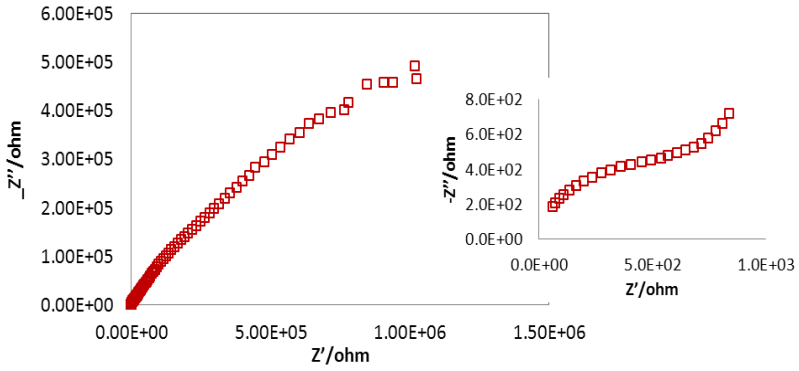


Figure 4.28: Nyquist plot of EIS for B6 microband array (*N*=5, *d*=50 µm) in 1 mM FCA in PBS. $E_{1/2}$ at 0.29 V, frequency 0.01-1MHz (*Inset*: EIS at higher frequency of 28,400 Hz -1MHz).

As discussed earlier in Chapter 3, due to mixed diffusion layer of non-linear and linear diffusion profiles observed on the studied recessed microelectrode array surface, the usual parameters associated to EIS such as R_s, R_{ct} and C_{dl} hence could not be calculated using the angular frequency (ω) function. The suggested an equivalent circuit for all disc designs (D1-D6) and B1-B3 are as given by Gabrielle et al. [39] which incorporate both spherical impedance (Z_M) and diffusion/Warburg impedance (Z_w):

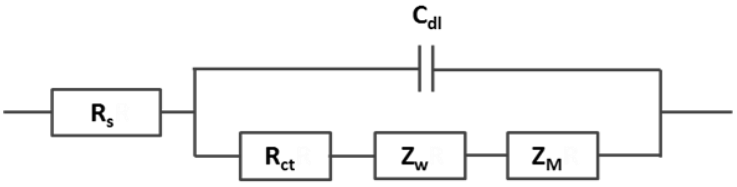


Figure 4.29: Equivalent circuit suggested for microelectrode.

In the case of B4-B6 that was postulated of having macroelectrode behaviour and linear diffusion profile, the Randles circuit was proposed (Fig. 4.30) to model the diffusion:

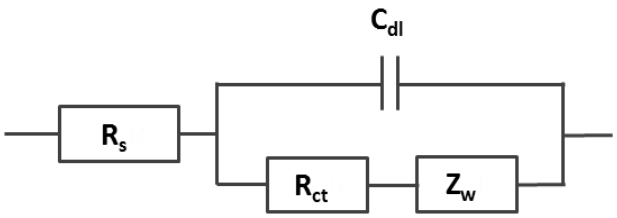


Figure 1.14: Randles circuit model suggested for B6 that behaved like a macroelectrode.

4.5 Conclusion

Overall we can conclude that the design and fabrication of the on-cell microelectrochemical chip were successful. The electrochemical performance (CVs and impedance spectra) of the on-chip electrochemical cell was the same as for gold on silicon WE with external commercial CE and RE electrodes which confirmed the adequacy of the design and fabrication process to the application requirements.

Through the whole 12 designs fabricated, which were investigated in this study, 9 electrodes show good response in terms of small number of dead electrodes, indicating 75% success of the fabrication batch. The occurrence and reoccurrence of dead electrodes were observed at several designs after their use in the saline solutions for electrochemical characterisations, presumably also due to the non-uniform densities of the current on the electrode areas.

We have also proved that interspacing between discs in an array (*d*), apart from the radius of the microdiscs (*r*) are important parameters that influence the type of diffusion (hemispherical, linear or mixed diffusion profile). The impedance study performed correlates well with the limiting current and cyclic voltammetry study, thus supporting the diffusion behaviour proposed for the different geometries and interspacing distance.

The treatment of Cl^- counterpart was carried out with $FeCl_3$ on the wafer prior the lift-off technique for the Ti:Ni:Ag layer. However several post-fabrication steps treatment can be carried out as well in order to ensure the stability of the Ag/AgCl layer over time in future.

4.6 References

1. Nazzaro, F., et al., *Protein Analysis-on-Chip Systems in Foodomics.* Nutrients, 2012. **4**(10): p. 1475-1489.
2. Luong, J.H.T., K.B. Male, and J.D. Glennon, *Biosensor technology: Technology push versus market pull.* Biotechnology Advances, 2008. **26**(5): p. 492-500.
3. Huang, X.J., A.M. O'Mahony, and R.G. Compton, *Microelectrode arrays for electrochemistry: Approaches to fabrication.* Small, 2009. **5**(7): p. 776-788.
4. Herzog, G., et al., *On-chip electrochemical microsystems for measurements of copper and conductivity in artificial seawater.* Talanta, 2013. **116**(0): p. 26-32.
5. Moujahid, W., et al., *Microelectrochemical Systems on Silicon Chips for the Detection of Pollutants in Seawater.* Electroanalysis, 2011. **23**(1): p. 147-155.
6. Tan, F., J.P. Metters, and C.E. Banks, *Electroanalytical applications of screen printed microelectrode arrays.* Sensors and Actuators B: Chemical, 2013. **181**(0): p. 454-462.
7. Liu, S.-Y., et al., *An Innovative Microelectrode Fabricated Using Photolithography for Measuring Dissolved Oxygen Distributions in Aerobic Granules.* Environmental Science & Technology, 2007. **41**(15): p. 5447-5452.
8. Parker, C.O., et al., *Electrochemical Immunochip Sensor for Aflatoxin M1 Detection.* Analytical Chemistry, 2009. **81**(13): p. 5291-5298.
9. Malzahn, K., et al., *Wearable electrochemical sensors for in situ analysis in marine environments.* Analyst, 2011. **136**(14): p. 2912-2917.
10. Ahmad, A. and E. Moore, *Electrochemical immunosensor modified with self-assembled monolayer of 11-mercaptoundecanoic acid on gold electrodes for*

detection of benzo [a] pyrene in water. Analyst, 2012. **137**(24): p. 5839-5844.

11. Haeberle, S. and R. Zengerle, *Microfluidic platforms for lab-on-a-chip applications.* Lab on a Chip, 2007. **7**(9): p. 1094-1110.
12. Jian, G., et al. *Portable digital microfluidics platform with active but disposable Lab-On-Chip*. in *Micro Electro Mechanical Systems, 2004. 17th IEEE International Conference on. (MEMS)*. 2004.
13. Ghafar-Zadeh, E., M. Sawan, and D. Therriault, *A 0.18-μm CMOS capacitive sensor Lab-on-Chip.* Sensors and Actuators A: Physical, 2008. **141**(2): p. 454-462.
14. Ghafar-Zadeh, E., M. Sawan, and D. Therriault, *A Microfluidic Packaging Technique for Lab-on-Chip Applications.* Advanced Packaging, IEEE Transactions on, 2009. **32**(2): p. 410-416.
15. Chen, Y.-P., et al., *Fabrication and characterization of an innovative integrated solid-state microelectrode.* Electrochimica Acta, 2010. **55**(20): p. 5984-5989.
16. Rusmini, F., Z. Zhong, and J. Feijen, *Protein immobilization strategies for protein biochips.* Biomacromolecules, 2007. **8**(6): p. 1775-1789.
17. Saito, Y., *A theoretical study on the diffusion current at the stationary electrodes of circular and narrow band types.* Rev. Polarogr, 1968. **15**: p. 177-187.
18. Lee, H.J., et al., *Cyclic voltammetry at a regular microdisc electrode array.* Journal of Electroanalytical Chemistry, 2001. **502**(1–2): p. 138-145.
19. Davies, T.J. and R.G. Compton, *The cyclic and linear sweep voltammetry of regular and random arrays of microdisc electrodes: Theory.* Journal of Electroanalytical Chemistry, 2005. **585**(1): p. 63-82.
20. Polk, B.J., et al., *Ag/AgCl microelectrodes with improved stability for microfluidics.* Sensors and Actuators B: Chemical, 2006. **114**(1): p. 239-247.
21. Ahmad, A., *Development of biosensors for the determination of polycyclic aromatic hydrocarbons in environmental monitoring of water*, 2012, Ireland: University College Cork.
22. Compton, R.G., et al., *Design, fabrication, characterisation and application of nanoelectrode arrays.* Chemical Physics Letters, 2008. **459**(1): p. 1-17.

23. Franks, W., et al., *Impedance characterization and modeling of electrodes for biomedical applications.* Biomedical Engineering, IEEE Transactions on, 2005. **52**(7): p. 1295-1302.
24. Rahman, A.R.A. and A. Guiseppi-Elie, *Design considerations in the development and application of microdisc electrode arrays (MDEAs) for implantable biosensors.* Biomedical microdevices, 2009. **11**(3): p. 701-710.
25. Morris, R.B., D.J. Franta, and H.S. White, *Electrochemistry at platinum bane electrodes of width approaching molecular dimensions: breakdown of transport equations at very small electrodes.* The Journal of Physical Chemistry, 1987. **91**(13): p. 3559-3564.
26. Guo, J. and E. Lindner, *Cyclic voltammograms at coplanar and shallow recessed microdisc electrode arrays: guidelines for design and experiment.* Analytical Chemistry, 2008. **81**(1): p. 130-138.
27. Menshykau, D., et al., *Investigating the concept of diffusional independence. Potential step transients at nano-and micro-electrode arrays: theory and experiment.* Analyst, 2009. **134**(2): p. 343-348.
28. Ordeig, O., et al., *Regular arrays of microdisc electrodes: simulation quantifies the fraction of 'dead' electrodes.* Analyst, 2006. **131**(3): p. 440-445.
29. Schmitt, G., et al., *Passivation and corrosion of microelectrode arrays.* Electrochimica Acta, 1999. **44**(21): p. 3865-3883.
30. Caston, S.L. and R.L. McCarley, *Characteristics of nanoscopic Au band electrodes.* Journal of Electroanalytical Chemistry, 2002. **529**(2): p. 124-134.
31. McCreery, D.B., et al., *Charge density and charge per phase as cofactors in neural injury induced by electrical stimulation.* Biomedical Engineering, IEEE Transactions on, 1990. **37**(10): p. 996-1001.
32. Weiland, J.D., et al. *Recessed electrodes formed by laser ablation of parylene coated, micromachined silicon probes*. in *Engineering in Medicine and Biology Society, 1997. Proceedings of the 19th Annual International Conference of the IEEE*. 1997. IEEE.
33. Banks, C.E., et al., *Electrocatalysis at graphite and carbon nanotube modified electrodes: edge-plane sites and tube ends are the reactive sites.* Chemical Communications, 2005(7): p. 829-841.

34. Compton, R.G. and C.E. Banks, *Understanding voltammetry*2007: World Scientific.
35. Nagale, M.P. and I. Fritsch, *Individually Addressable, Submicrometer Band Electrode Arrays. 1. Fabrication from Multilayered Materials.* Analytical Chemistry, 1998. **70**(14): p. 2902-2907.
36. Nagale, M.P. and I. Fritsch, *Individually Addressable, Submicrometer Band Electrode Arrays. 2. Electrochemical Characterization.* Analytical Chemistry, 1998. **70**(14): p. 2908-2913.
37. Simonis, A., et al., *Miniaturised reference electrodes for field-effect sensors compatible to silicon chip technology.* Electrochimica Acta, 2005. **51**(5): p. 930-937.
38. Huang, X., et al. *Impedance based biosensor array for monitoring mammalian cell behavior*. in *Sensors, 2003. Proceedings of IEEE*. 2003.
39. Gabrielli, C., et al., *Electrochemical impedance spectroscopy investigations of a microelectrode behavior in a thin-layer cell: Experimental and theoretical studies.* The Journal of Physical Chemistry B, 2006. **110**(41): p. 20478-20485.

CHAPTER 5

SURFACE BIO-FUNCTIONALISATION FOR BIOMOLECULE IMMOBILISATION

5.1 Introduction

The properties of an electrode surface can be manipulated by chemical, biochemical or molecular reagents for biomolecule immobilisation. Surface biofunctionalisation has contributed to a revival of interest in basic and applied research in electrochemistry and electrochemical devices [1]. For biosensors, electrode biofunctionalisation provides selectivity for the recognition of the specific biotargets [2] generating a measurable signal. As far as the surface functionalisation is concerned, it is also a challenge to immobilise the biomolecules without impairing their stability and specificity [3, 4].

In this chapter, two types of protein, namely histidine-tagged protein and antibody will be immobilised on gold macroelectrode surface. The choice of these two types of proteins is of interest because their immobilisation strategies on solid support are gaining attention in the development of protein microarray [5-9]. The surface modification on solid support at macro-size and flat (planar) electrode would provide us initial insights on modification in terms of its electrochemical and optical properties before embarking on surface modification at recessed microelectrode array. Both histidine-tagged protein and anti-T-2 toxin monoclonal antibody were produced in-house by Microbiology Department, UCC and Queen's University Belfast respectively.

5.1.1 Plasma-Cleaning Effect for Surface Functionalisation

Prior any surface modifications in this study, the electrodes were first treated in plasma-cleaner. Besides removing organic contaminants on the surface, plasma-cleaning also helps to promote hydroxylation on its surface for surface functionalisation [10, 11]. The wettability effect on the plasma-cleaned surface was assessed using contact angle measurement. As can be seen from Fig. 5.1, the hydrophilicity property of the gold electrode surface has greatly increased after plasma-cleaned.

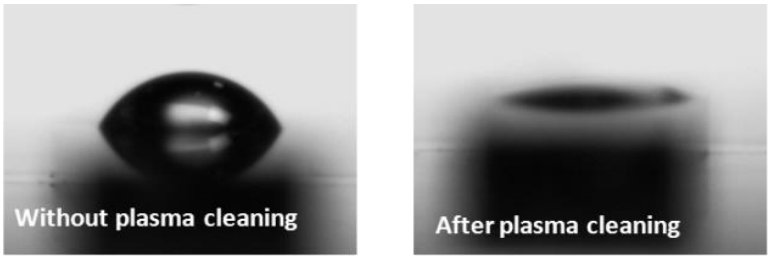


Figure 5.1: Plasma-cleaning effect on gold microelectrode array. Without plasma cleaning the surface is hydrophobic (left) and after plasma cleaning, the surface became hydrophilic (right).

A stability study on the duration of plasma-cleaning effect on the gold surface showed that surface hydrophilicity only lasts within an hour after the plasma-cleaning (Fig. 5.2). The hydrophilicity properties gradually diminished after overnight. Although the surface functionalisation/modification could be carried out several hours after the plasma-cleaning, its hydrophilicity effect is as not as superior as within the first hour of the cleaning. Therefore it was concluded that it's the best to conduct the surface functionalisation as soon as the surface has been plasma-cleaned.

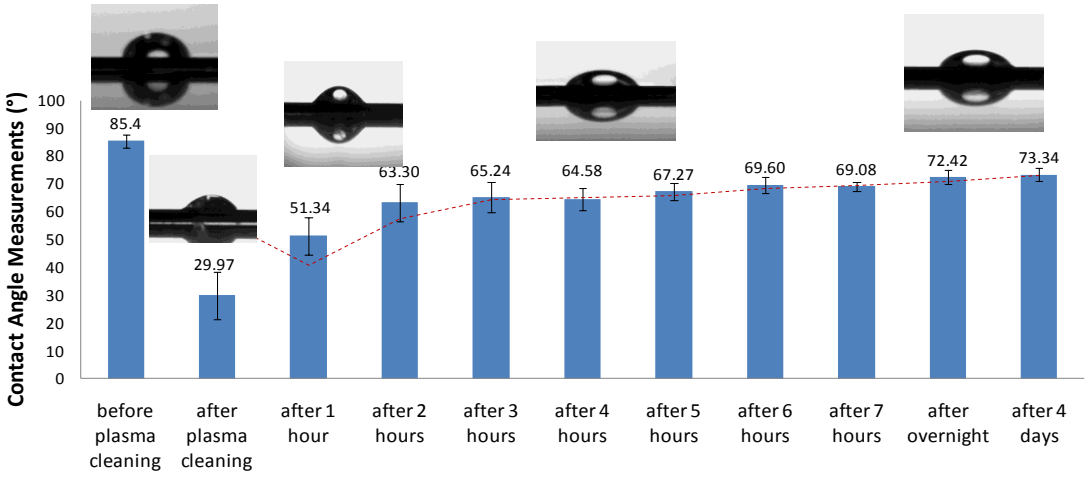


Figure 5.2: The study of plasma-cleaning effect over time.

5.2 Histidine-Tagged Protein Immobilisation on Gold Surface

A histidine-tagged protein is an amino acid protein containing imidazole functional groups that consists of at least six histidine (His) residues, often at the N- or C-terminus of the protein, hence also known as hexa histidine-tag (Fig. 5.3). A number of research groups have reported the immobilisation of His-tag protein for the study of protein-protein interactions [8, 12-16]. A widely reported approach for immobilising His-tag protein on solid was adapted from the immobilised-metal affinity chromatography (IMAC) technique that was originally developed for protein purification purpose. The concept of IMAC was based on the known affinity of transition metal ions such as Zn^{2+}, Cu^{2+}, Ni^{2+} and Co^{2+} to histidine proteins [17, 18] with iminodiacetic acid (IDA) or nitriloactetic acid (NTA) as the chelating ligand [18]. NTA is a tetradentate ligand that have higher affinities for metal ions than the tridentate chelator, IDA. For metal ion immobilisation at the electrode surface, different matrices can be used such as self-assembly monolayer [9, 13, 19-21] or conductive polymers [22, 23].

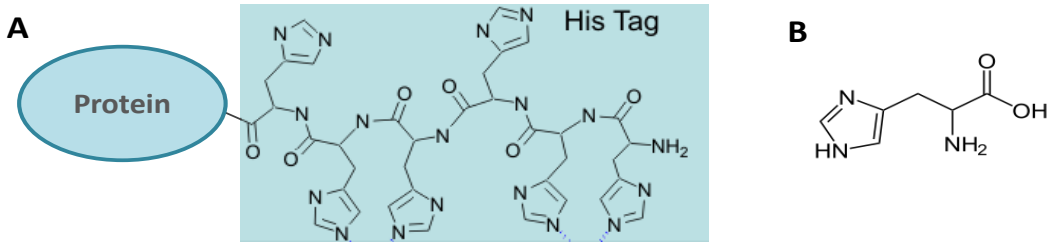


Figure 5.3: (A) A His-tag protein with six histidine groups and (B) structure of L-histidine.

Such application of NTA/histidine-tag immobilisation now has been extensively applied in numerous applications including surface plasmon resonance (SPR) [3, 12, 13, 24] and electrochemistry [20, 25, 26]. This particular immobilisation technique is favoured owing to its controlled protein orientation, specificity, surface regeneration and reversibility characteristics [12, 13, 26].

Here we present an immobilisation method for His-tag protein using self-assembly monolayer and NTA-Cu^{2+} as the metal chelating ligand on a 1-mm gold disc electrode surface. Each modification steps are characterised electrochemically using CV and EIS techniques. All electrochemical characterisations were carried out in 1 mM FCA in PBS pH 7.4 using a two electrode system with Ag/AgCl RE merged with CE and the gold electrode as the WE. In addition, an atomic force microscopy (AFM) study was carried out at every modification steps. His-tag protein model used in this study was PduA shell protein.

5.2.1 Atomic Force Microscopy

The atomic force microscopy (AFM) is a type of scanning probe microscopes (SPMs) that allow researchers to see, measure, analyse and study surface structure/topography with precise resolution and accuracy. Its application varies from physical and material sciences, nanotechnology, biological and even industrial (e.g. semiconductor industry) [27]. Unlike any other type of microscope that requires lenses for visualising images, AFM generates an image by ‘feeling’ the sample surface

with its cantilever's tip rather than 'looking' at it. An analogy given by Morris et al. (2010) in his textbook is that AFM is in resemblance of a blind person feeling objects with their fingers thus building up the images based on the touch [28].

The schematic in Fig. 5.4 illustrates the main features of an AFM. Here, several important parts and basic concepts of AFM are briefly described.

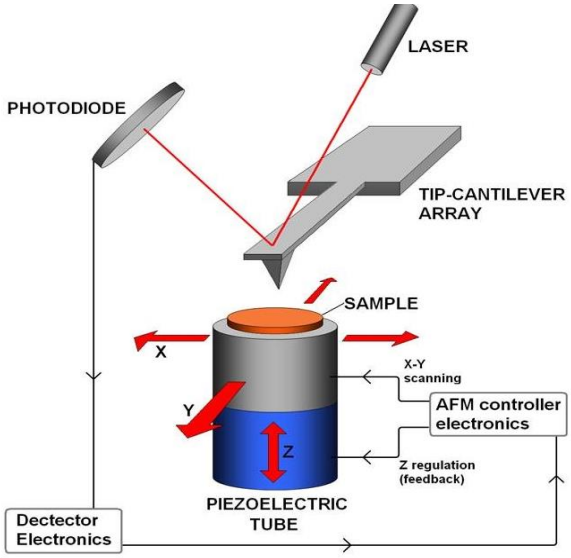


Figure 5.4: Schematic representation of the atomic force microscopy*.

i) AFM cantilevers and probes- the tip/stylus at the end of the cantilever come in contact with the sample surface. They are fabricated using MEMS technology and made of silicon or silicon nitride. The sharpness of the tip determines the resolving power of the instrument. The cantilever allows the tip to move up and down as it tracks the sample and has very low spring constant or force constant.

ii) Piezoelectric transducers – The sample is mounted on top of the piezoelectric transducer that converts electrical potential into mechanical motion.

* Image taken from http://pharm.virginia.edu/AFM.html

iii) Detection mechanism- A laser beam is focused on the end of the cantilever (preferably direct over the tip) and then reflected off onto a photodiode detector. In modern instruments the photodiode is split into four segments (quadrants). As the tip moves in response to changes on the sample topography during scanning, the angle of the reflected laser beam changes, and so the laser spot falling onto the photodiode moves, producing changes in intensity in each of its quadrants.

In life sciences application, AFM imaging on immobilised proteins such as antibodies [29, 30], DNA [31, 32] and even cells [33, 34] to name a few, have been reported. All images in this study were taken by a tip with tapping mode. In the tapping mode, the cantilever is externally oscillated at its fundamental resonance frequency (~300 kHz) (Fig. 5.5). A piezoelectric on top of the cantilever is used to adjust the amplitude of oscillation as the probe scans across the surface. The deviations in the oscillation frequency or amplitude due to interactions between the probe and surface are measured, and provide information about the surface or types of material present in the sample. This method is gentler than contact AFM since the tip is not dragged across the surface, but it does require longer scanning times. It also tends to provide higher lateral resolution than contact AFM [28]. The exerted forces are in pN range hence less destructive in comparison with the contact mode.

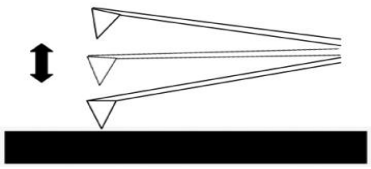


Figure 5.5: Diagram of probe and surface interaction in tapping mode.

Generally AFM use is easier than an electron microscope as there is a minimal sample preparation (SEM and TEM operate in vacuum hence require further treatment if the sample is non-conductive) and almost any sample can be measured. Nevertheless the drawback of AFM is that its image recording is usually slower than the SEM.

5.2.2 PduA Shell Protein

PropaneDiol Utilization (Pdu) is a type of shell protein that can be found in many bacteria, which can make bacterial microcompartments (BMC). Bacterial microcompartments are functionally diverse groups of proteinaceous organelles that confine specific reaction pathways in the cell within a thin-protein based shell [35]. The Pdu microcompartment, for instance, provides reactions for metabolizing 1,2-propanediol in certain enteric bacteria. The Pdu segment contains about 20 genes with different function, like PduA, PduB, PduJ, PduK, which are proved to be shell proteins of the microcompartment (Fig. 5.6).

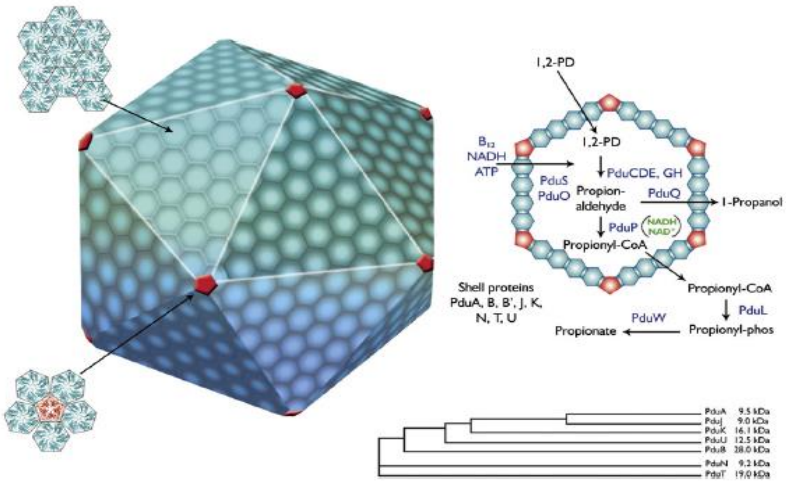


Figure 5.6: The bacterial microcompartment (BMC) and the associated shell proteins. The faces of the BMC structure are formed from the association of hexagonal shell proteins, with the most abundant PduA, PduB, and PduJ shell proteins. The vertex of the assembly is formed with a pentameric shell protein, which in the propanediol metabolosome is thought to be PduN (highlighted in red). The metabolism associated with 1,2-propanediol (1,2-PD) is shown schematically. Taken from Ref. [36].

The Pdu shell proteins are particularly interesting to study as it houses enzymes conversion besides protecting the cell from toxicity of the reactive aldehyde intermediate that is formed during their catabolism. Moreover, Pdu proteins have

potentially interesting electrochemical properties. The choices of PduA in particular, on the other hand, is due to the abundance of this shell proteins in the BMC [36].

PduA forms a symmetric homohexamer whose central pore appears tailored for facilitating transport of the 1,2-propanediol substrate [35]. The Pdu microcompartments are heterogenous in size, with diameter ranging from 100-160 nm [35, 37] and are composed of a proteinaceous interior surrounded by a 3- to 4-nm protein shell [37]. Pdu microcompartment proteins can be expressed from bacterias such as *Salmonella* and *Citrobacter*. However PduA shell protein produced in this study was from *Lactobacillus reuteri* in the same manners as described in the literature [38] with His-tag group bounded to N-terminus of the protein.

5.2.3 Gold Surface Modification

The electrode used in this study was a 1 mm in diameter gold disc with chip dimension of 3 mm x15 mm (Fig. 5.7A). The electrode was fabricated by standard lithography technique consisted of the fabrication steps as presented in Fig. 5.7B.

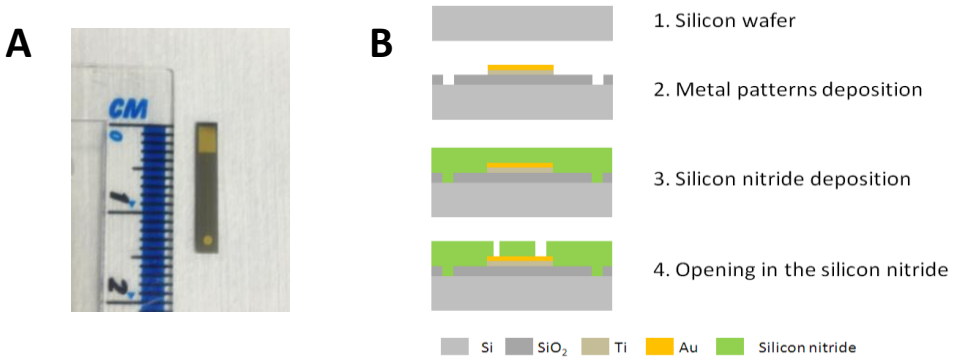


Figure 5.7: (A) Picture of gold electrode with 1mm disc used in this study; and (B) simplified fabrication process for the electrode.

Prior the modification, gold electrode was first plasma cleaned for 10 minutes with the highest UV light setting (100 W, 600mTorr). The gold surface was then activated

with self-assembly monolayers (SAM) of long chain 11-mercaptoundecanoic acid (11-MUA). The SAM method is a renowned method in modifying gold surface where the functional group of disulfides (R-S-S-R), sulfides (R-S-R) and thiols (R-SH) strongly bind on metal particularly gold surface [39] while the other end site remains open for subsequent layer modification. We particularly chose 11-MUA, alkanethiols with a longer chain length as it gave a higher degree of surface coverage with less defects and a higher electron transfer resistance [40]. Long chain alkanethiols (number of methylene groups n>10) assemble in a crystalline-like way and the reduction in the chain length merely leads to less ordered structures [41].

An intermediate ester was then formed with 1-ethyl-3-(3-dimethylaminopropyl)-carbodiimide (EDC) and N-hydroxysuccinimide (NHS) reaction. After the coupling step of the primary amino group of the NTA derivative to the carboxyl terminal group of the SAM, the surfaces were then incubated in diethanolamine solution (as a substitution to the ethanolamine) in order to block unreacted activated carboxyl groups. The Cu^{2+} complex was then introduced and this should be done at pH >4 as acidic media with pH less than 4 will prevent Cu^{2+} coordination [23]. Although Ni^{2+} was widely favoured to be used as the transition metal, nevertheless Cu^{2+}-NTA links to His-tags protein more strongly than cobalt or nickel [42]. Furthermore in terms of occupational safety and health with regard to hazard issue, Cu^{2+} poses less health risk as long exposure to Ni^{2+} was known for being carcinogenic [43-46]. Besides Cu^{2+} and Ni^{2+}, the usage of Co^{2+} [47] and Zn^{2+} [48] were also reported in His-tag protein immobilisation.

The PduA shell His-tag protein was subsequently bound to the NTA-Cu^{2+} complex. The schematic diagram for the gold surface modification is illustrated in Fig. 5.8. Apart from His-tag immobilisation, NTA-Cu^{2+} metal ligand also has been reported for its successful immobilisation for other class of proteins such as antibodies [22, 49], peptides [3], lipopolysaccharide [50] as well as plasmid DNA, RNA and endotoxin [51].

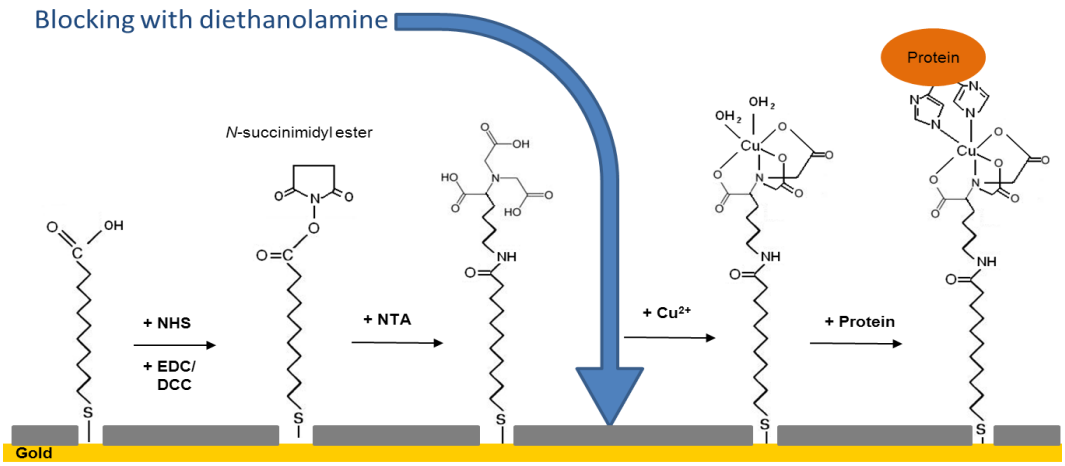


Figure 5.8 : Procedure of gold surface modification involving 11-MUA SAM and immobilisation of His-tag protein onto an alkanethiol SAM.

The NTA-metal complex of Cu^{2+}, Ni^{2+}, Zn^{2+} and Co^{2+} exhibits affinities and specificities toward histidines as illustrated in Fig. 5.9 [51], similar to reported for the IDA-metal complex [52-54]. While Ni^{2+} is the most widely available metal ion for purifying histidine-tagged proteins which provides good binding efficiency to His-tag proteins, it also tends to bind non-specifically to endogenous proteins that contain histidine clusters. Co^{2+} on the other hand, exhibits the most specific interaction with His-tags, resulting in the least nonspecific interaction. However its poor binding is the major drawback. In comparison, Cu^{2+} binds His-tags more strongly than cobalt or nickel. This provides the highest possible binding capacity but also the poorest specificity. For this reason, Cu^{2+} is usually used only for binding applications in which purification is not the objective.

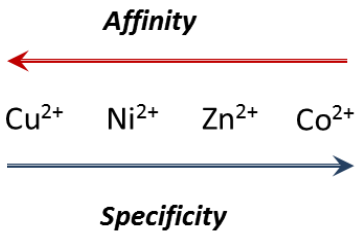


Figure 5.9 : Affinity and specificity for the transition metals binding with His-tag protein

5.2.4 Results and Discussions

Evaluation of Immobilisation Procedure Using a Fluorescent Model

The feasibility and operability of the proposed immobilisation method was conducted by an initial study using Alexa Fluor® 488; a Penta-His fluorophore dye conjugates with excitation and emission wavelength at 494 nm and 519 nm respectively. Using a fluorescent model will allow us to evaluate the immobilisation procedure optically. Green fluorescent tag colour emitted under the selected filter of the microscope will indicate the viability of the immobilisation procedure and vice versa. Alexa Fluor used in the immobilisation study was prepared with dilution of 40x in PBS pH 7.4.

Two control surfaces consisted of unmodified electrode without any modification (Fig. 5.10A) and surface modification with SAM-NTA without Cu^{2+} have been employed (Fig. 5.10C). As can be seen under the fluorescence microscope, no significant green fluorophore were observed in when there is no metal ion being coordinated to the NTA. This proved that coordination of NTA-Cu^{2+} helps to form a significant distribution and orientation of the immobilised Alexa Fluor (Fig. 5.10B).

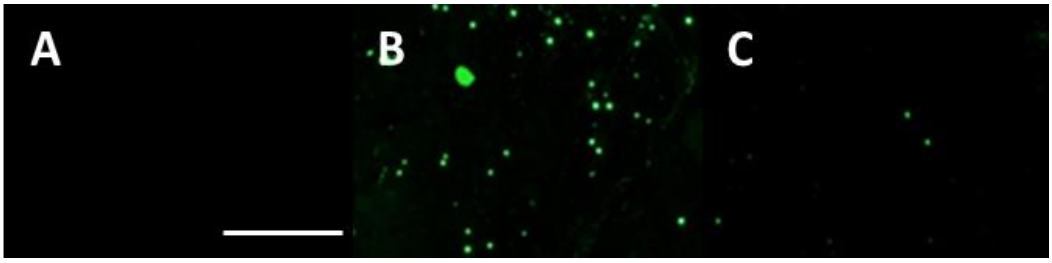


Figure 5.10 : (A) Control gold unmodified electrode ; (B) Alexa Fluor immobilisation on gold electrode using SAM-EDC/NHS-NTA-Cu^{2+} approach ; (C) Alexa Fluor random orientation on gold surface when Cu^{2+} step is omitted. Scale bar 200 μm.

The immobilisation technique using the real His-tag model (PduA shell protein) is now discussed.

PduA Shell Protein Adsorption Study

The idea of having an initial protein adsorption study via AFM was to investigate the PduA protein size in its crude solution. Physical adsorption of protein is indeed the easiest and quickest mode for biomolecule immobilisation on metal surfaces.All AFM images in this study were taken by tapping mode and analysed using SPIP (Scanning Probe Image Processor) software version 4.7.2.

PduA shell protein adsorption on gold surface was confirmed by the increment of surface roughness on the electrode surface. The protein adsorption has resulted surface roughness to increase from 1.86 ± 0.89 nm on an unmodified electrode to 18.3 ± 3.83 nm on an adsorbed one (Fig. 5.11). Such an observation is similar with other researchers that reported the increment of surface roughness upon the adhesion of proteins to the sensor surface [55-58]. Particle analysis conducted suggests that the adsorbed proteins have diameter of 100-150 nm and height of 40-50 nm; both are in consensus with dimensions reported for Pdu microcompartments [35, 37]. X-ray crystal structures of shell proteins also revealed that this type of proteins have flat, 6-fold symmetric hexamers capable of packing in tile-like two-dimensional molecular layers [35].

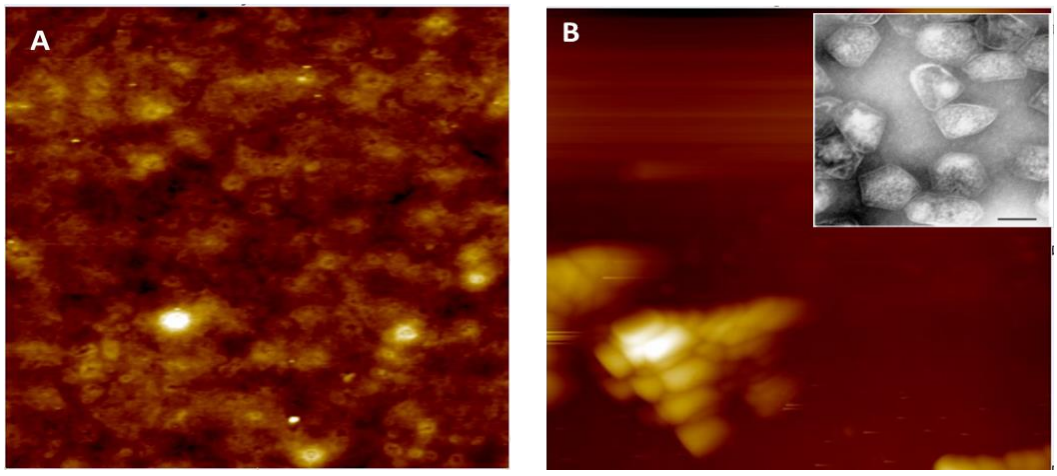


Figure 5.11 : AFM images of (A) unmodified gold surface; and (B) adsorbed PduA shell protein (*inset*: transmission electron micrograph of purified Pdu microcompartment (bar, 100 nm). Taken from Ref. [35]). AFM images of 2 x 2 μm scale, *Z*-scale of 200 nm.

Electrochemical characterisations confirmed the adsorption of the protein on the gold surface based on the shift in CV and spectra changes in EIS analysis presented in Fig.5.12A and Fig 5.12B correspondingly. Electrochemical experiments were performed in 1 mM FCA in PBS 0.01 M pH 7.4 with 2 electrodes system. WE used was the microfabricated 1 cm disc gold electrode and CE was merged with RE where RE is the Ag/AgCl electrode. CVs were taken in the potential range of 0 to + 0.6 V at scan rate of 100 mV s^{-1}. EIS was taken in frequency range of 0.01-100,000 Hz at stimulation ac amplitude equal to 0.001 V and bias potential ($E_{1/2}$) equal to 0.29 V.

As one can see from the CVs upon the protein adsorption (Fig. 5.12A), the formation of inert protein layer caused a decrease in the electron transfer in the redox reaction of Fc/Fc^{+} ions at the electrode surface. In CV it visualised in a decrease of the peak values of oxidation and reduction currents and in a shift of associated oxidation and reduction potentials to the side of higher and lower values, respectively. This finding is similar with Guo et al. (1996) reported in his study of serum albumin adsorption on metal electrodes [59].

From the EIS spectra presented in Fig.5.12B, the adsorbed protein layer on the electrode surface has resulted in a shift of the real impedance at the point where imaginary impedance took the minimum to the larger values. Simultaneously, the protein layer formation visualised in pronounced semi-circle located at high frequencies. In case of unmodified electrode this semi-circle reduced to a very small part in the form of incline line. In both cases, only partial semi-circles were observed for both electrodes (unmodified and with adsorbed protein) due to the limited value of the maximum frequency (instrumentation limit) and number of sampling points within the frequency range (50 points). By having the highest frequency range of 1 MHz and taking more points in future, this will allow us to probe the R_s values and accurately calculate the R_{ct} values for both electrodes. However, in the current case only R_s+R_{ct} values were able to determine as R_s values were not obtained from the impedance spectra.

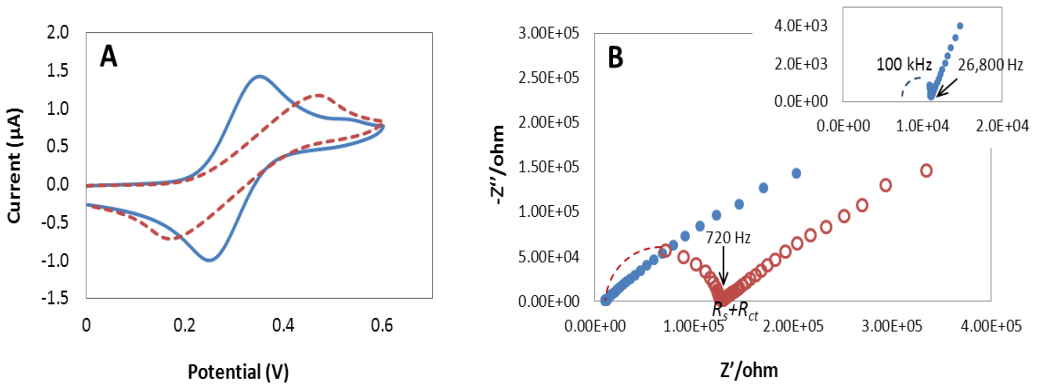


Figure 5.12 : (A) CV of scan rate 100 mV s^{-1}; and (B) EIS studies of adsorbed PduA shell protein (red line/marker) on gold surface in comparison with the unmodified electrode (blue line/marker) in 1 mM FCA in PBS. *Inset*: impedance of unmodified electrode at high frequency. Frequency for EIS 0.01-100,000 Hz

As follows from Fig.5.12B, R_s+R_{ct} increased by 116 kΩ indicating that the protein adsorption with formation of the protein film on the electrode surface has successfully taken place. Gu et al. also has reported an increment of semicircle formation from R_{ct} 950 Ω on the bare gold electrode to R_{ct} value of 2.9× 10^4 Ω after immersing the electrode in cysteamine aqueous solution [60]. In 2005, Wang et al. has observed that R_{ct} value of the adsorbed haemoglobin increased within 1-5 kΩ depending on the duration of the incubation time on the macroporous gold electrode [61].

From electrical equivalent circuit approach this changes in spectra can be explained as follows. As well-known, impedance of a macroelectrode can be represented with the Randles equivalent circuits presented in Fig. 5.13A. It consists of R_s, which is solution resistance; C_{dl}, which is double-layer capacitance; R_{ct}, which is charge transfer resistance and Z_d, which is diffusion impedance. In case of macro electrode associated with plane 1-D diffusion, Z_d is represented by complex Warburg impedance:

$$Zd = \frac{W}{\sqrt{j\omega}} = \frac{W}{\sqrt{\omega}} - j\frac{W}{\sqrt{\omega}} \qquad \ldots (Eq.\ 5.1)$$

where W is Warburg coefficient (or Warburg constant). At high frequencies where $R_{ct}>>|Z_d|$, diffusion impedance can be neglected. Thus, the equivalent circuit is reduced to the circuit presented in Fig. 5.13B. The impedance spectrum of this circuit is a semicircle with the radius equal to R_{ct} and the frequency where the imaginary part of impedance takes its maximum values equal to $f_{max}=1/(2\pi C_{dl}R_{ct})$ [62]. The semicircle starts from R_s and ends at R_s+R_{ct} on the real axis.

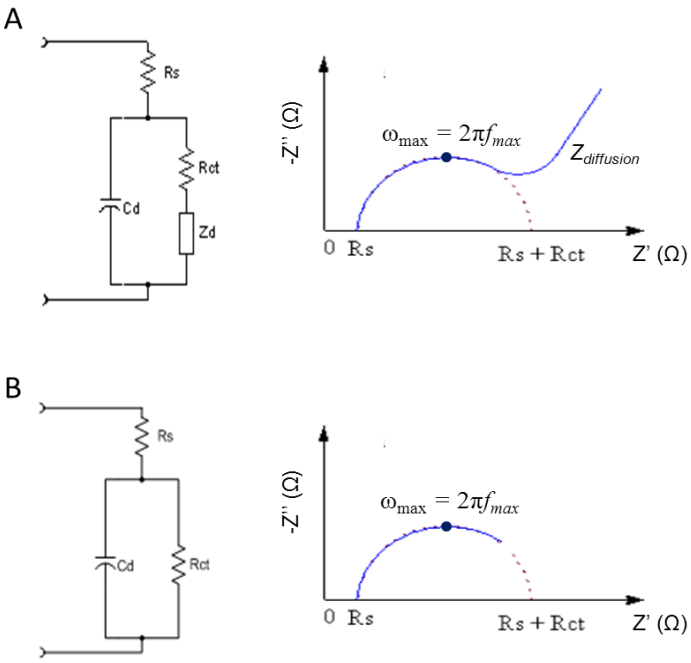


Figure 5.13: (A) A complete Randles equivalent circuit; (B) A reduced Randles equivalent circuit at the high frequencies, with the correspond Nyquist plots (*inset*).

Electrochemical Characterisation of Immobilised PduA Shell Protein

Electrochemical examination (CV and EIS) and atomic force microscopy (AFM) were employed in this study at each step of the gold surface modifications for the His-tag protein immobilisation. Although many researchers have reported CV and EIS for each immobilisation step from an unmodified electrode to protein

immobilisation on the electrode surface, but to our knowledge to date, there is no concurrent study that applies the AFM at each step as well.

Fig. 5.14 shows CV for the seven different steps of the gold electrode surface modification including: unmodified electrode, modification with 11-MUA, ester formation of EDC/NHS reaction, NTA complex formation, surface blocking with diethanolamine, Cu^{2+} coordination and PduA shell protein immobilisation. PduA protein dilution used in the immobilisation study was 0.2 mg mL^{-1} in PBS pH 7.4

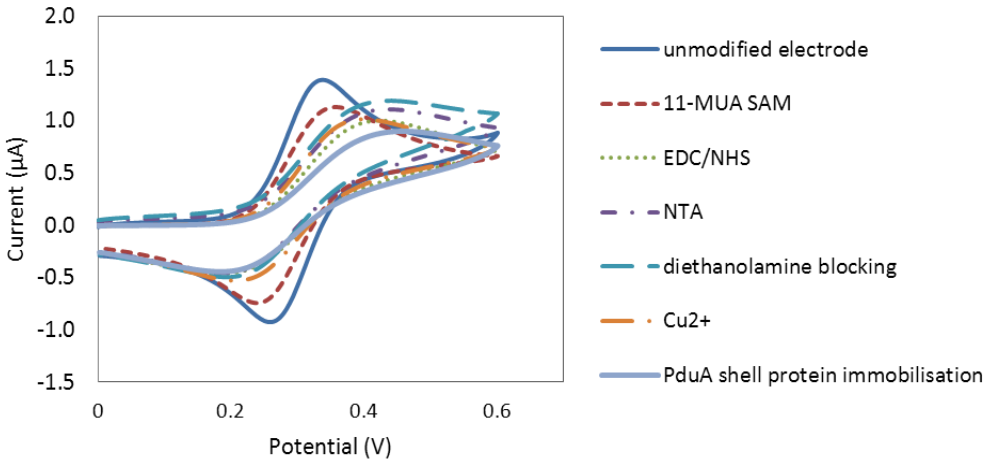


Figure 5.14 : CV study for PduA shell protein immobilisation on gold surface in 1 mM FCA in PBS. Scan rate100 mV s^{-1}.

The cyclic voltammograms with modified surface show quasi-reversible electrochemistry. Each next step of surface modification generally resulted in decreasing of peak currents associated with increasing of peak potentials difference (peak-to-peak separation) as shown in Fig. 5.15. These observations are consistent with the consecutive formation of the thicker blocking layer on the surface at each modification step, which hinders access of the redox probe thereby reduces currents and increases potential difference (peak separations) to drive the redox process.

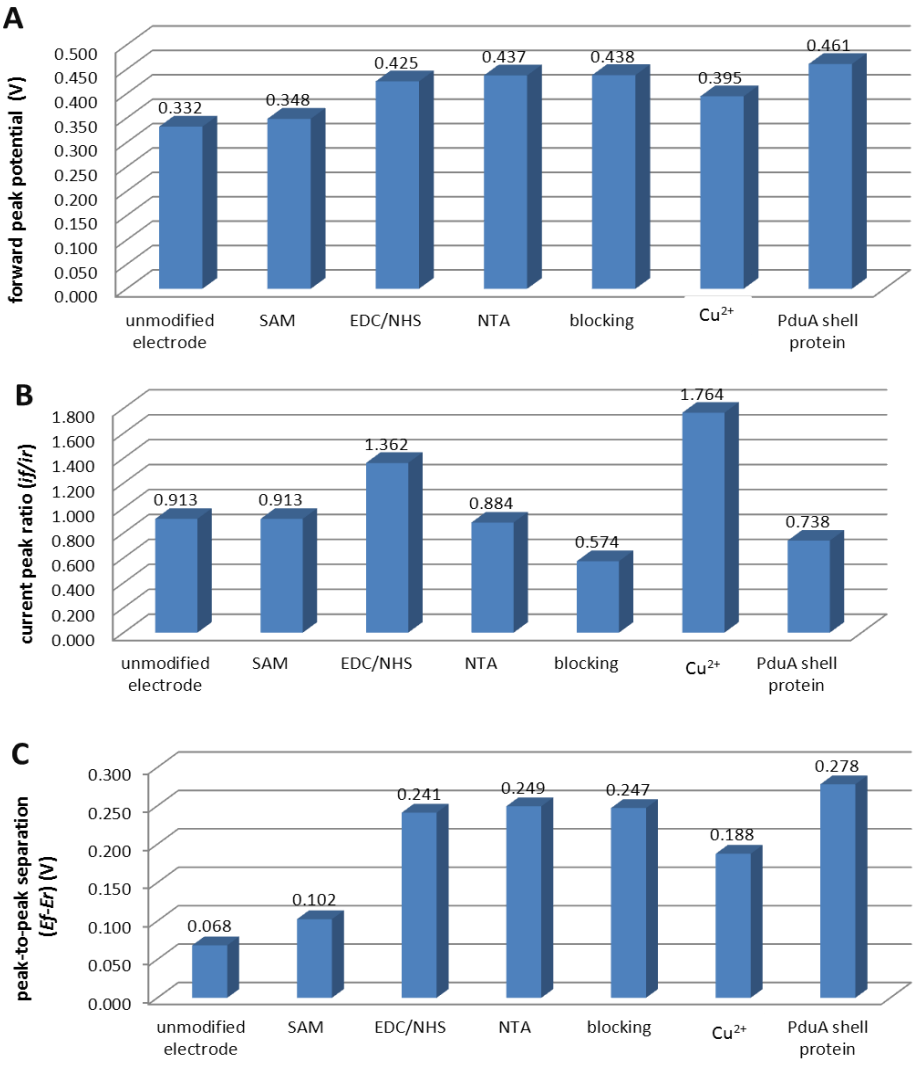


Figure 5.15: Cyclic voltammograms analysis for gold electrode modifications: (A) forward peak potential; (B) ratio for peak current (i_f/i_r); and (C) peak-to-peak separation.

The obtained impedance spectra represented typical Randles circuit responses where a semicircle region followed by a straight line (Fig. 5.16). Diameter of the semicircle increased with the SAM formation, which confirms formation of the isolation monolayer on the gold surface. The steric hindrance packing of the NHS ester has resulted in an increment change of the impedance spectra for the EDC and NHS steps. Normal perception would assume that the impedance spectra will generally increase accordingly with surface modification. Nevertheless, our result has shown

that a mixed layer was obtained alongside the modification which can be attributed to the rearrangement in the structure of SAM. Hleli and co-workers also has reported decreasing EIS spectrum in the modification of gold electrode with mixed SAM with immobilised antibody for the detection of atrazine [63] and haemoglobin [64]. Similar patterns were obtained by other co-workers [65, 66] in interdigitated microelectrodes.

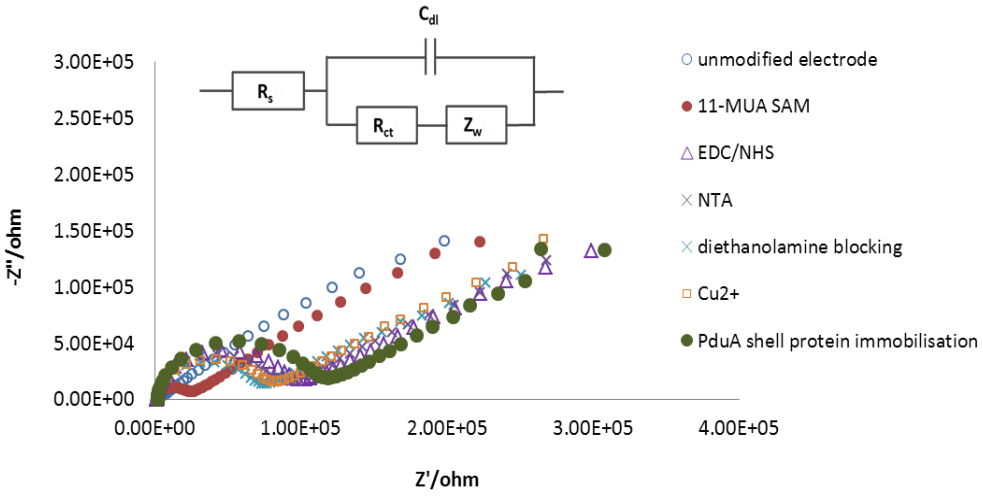


Figure 5.16 : EIS study for PduA shell protein immobilisation on gold surface in 1 mM FCA in PBS (Frequency 0.01-100 MHz). *Inset*: Equivalent circuit used to model impedance data in the presence of the redox couple. R_s, R_{ct}, Z_w and C_{dl} represent the solution resistance, charge transfer resistance, Warburg diffusion and double-layer capacitance respectively.

The parameters associated with EIS parameters on 1-D plane diffusion were presented in Table 5.1. The C_{dl} value was determined from the angular frequency value, $\omega_{max}=2\pi f_{max}=1/R_{ct}C_{dl}$ [62]. As can be seen, the R_{ct} values increased accordingly with the first two surface modifications, i.e. the self-assembly monolayer and EDC/NHS, with decreasing f_{max} and C_{dl} values. The R_{ct} remains within the same range for the following modifications with constant f_{max} observed (100Hz). The R_{ct} remained within the same range for the following steps from NTA formation until Cu^{2+} attachment.

Following the EDC/NHS step, EIS spectra for NTA complex showed lower impedance. This is because no addition layer was added to the surface but merely a replacement in the functional group substitution took place. Additionally, lower resistance for the redox probe may imply that SAM abundant with lysine group provides a positively charged surface and thus the surface improved the ability of the redox probe to access the layer [67]. The same pattern of spectrum with decrease of impedance value after NTA attachment was also observed in Cho et al. (2012) publication [50]. Following the attachment of the PduA shell proteins, the charge-transfer resistance of the impedance spectra (R_{ct}), which relates to the semicircle diameter, continue to increase to the range of 112 kΩ indicating the successful immobilisation of the His-tag protein on the surface.

Table 5.1 R_s and R_{ct} values for unmodified gold electrode and protein adsorption

Steps	R_s **(Ω)**	R_{ct} **(Ω)**	f_{max} **(Hz)**	C_{dl} ***(nF)***
1. Unmodified electrode	1.52×10^3	60	51,800	51.2
2. SAM	1.50×10^3	2.06×10^4	373	20.7
3. EDC/NHS	1.75×10^3	8.75×10^4	100	18.2
4. NTA	1.64×10^3	8.32×10^4	100	19.1
5. Blocking with DEA	1.83×10^3	7.90×10^4	100	20.1
6. Cu^{2+}	1.87×10^3	8.07×10^4	100	19.7
7. PduA shell protein immobilisation	1.93×10^3	1.12×10^5	72	19.8

AFM Study of Immobilised PduA Shell Protein

The AFM images for each modification steps are presented in Fig. 5.17 as follows:

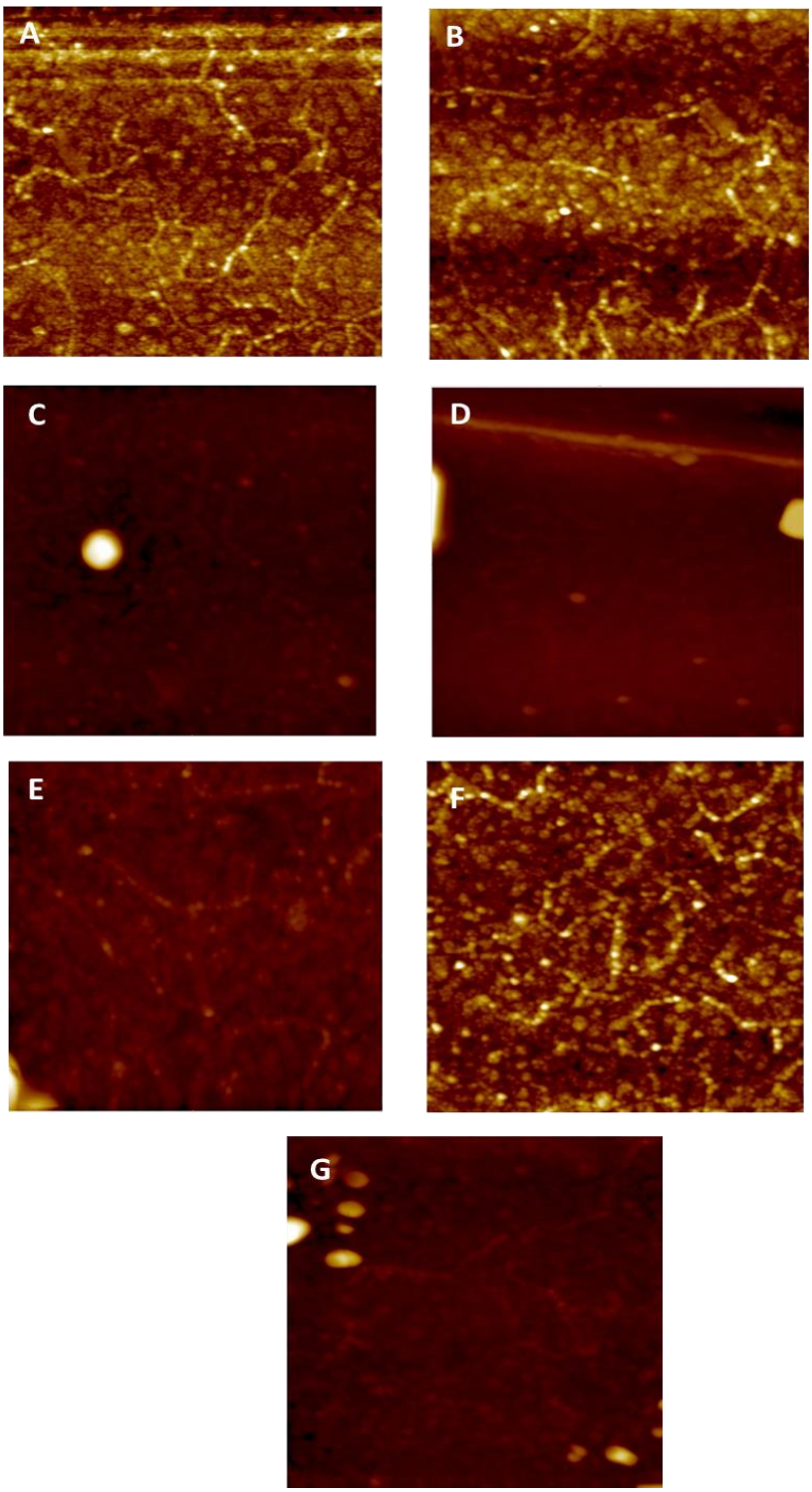


Figure 5.17 : AFM images of each modification steps in immobilising PduA shell protein; (A) gold unmodified electrode, (B) SAM with 11-MUA, (C) EDC-NHS step, (D) NTA complex formation. (E) blocking with diethanolamine, (F) Cu^{2+} coordination, and (G) PduA shell protein immobilisation. AFM images of 2 x 2 µm scale, *Z*-scale of 200 nm.

The surface roughness of the AFM images from step (A) to (G) in Fig. 5.17 was also evaluated as shown in Fig. 5.18. The surface roughness shows an increasing trend from unmodified electrode to NTA steps, and decrease upon surface blocking. This verifies the blocking solution has successfully blocked the electrode surface hence leaving the surface less rough. Roughness peak with height of 100 nm as obtained in EDC and NHS could be attributed to salt residue [68].The roughness increased after Cu^{2+} addition and decreased when PduA shell protein immobilisation took place. This suggests that surface with PduA shell protein had fewer peaks and pits and surface became more even and distributed after the PduA immobilisation.

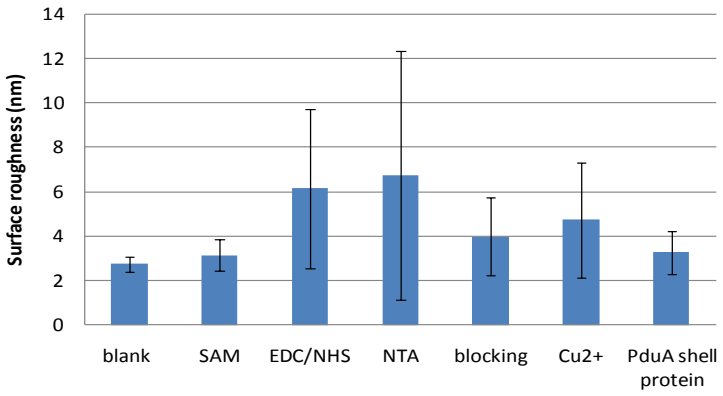


Figure 5.18: Surface roughness of the modified gold electrode surface.

In relation with this, Cacciafesta et al. (2001) also has studied a series of titanium surfaces with different treatments for human plasma fibrinogen adsorption and found that roughness varied enormously with surface treatments [69]. We can hence conclude from this, that surface roughness could be correlated with the availability of the functional groups and derivatives that are readily open for the subsequent surface modification.

The AFM image with PduA shell immobilisation via NTA-Cu^{2+} was analysed using particle and height analysis. The immobilised shell protein also was compared with the adsorbed protein as studied earlier (Fig. 5.19). It was found that the PduA protein immobilised has height ranging from 40-50 nm and diameter around 100-150 nm,

suggesting that they are PduA shell protein as observed from the protein adsorption study. The protein size attained from the particle analysis of the AFM images is in good agreement with the Pdu microcompartments size as described in the literature [35, 37] hence confirming that they are of Pdu proteins.

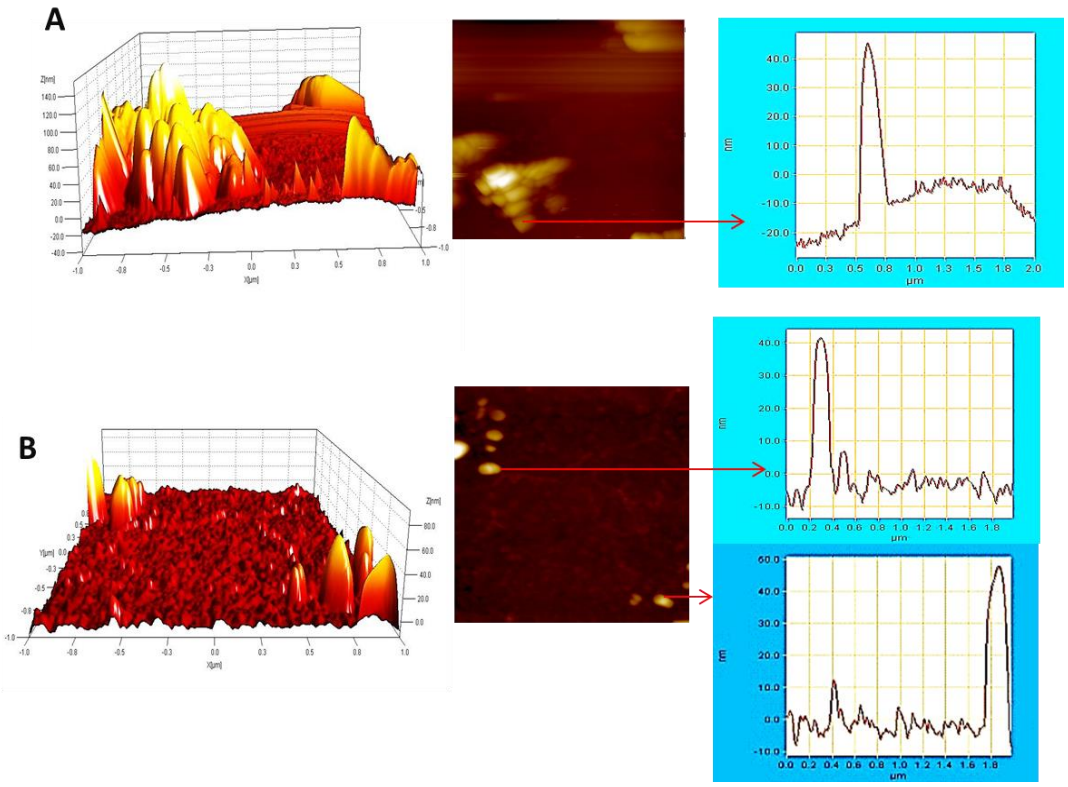


Figure 5.19: Comparison of the (A) adsorbed; and (B) immobilised PduA shell protein. The 3-D images of the scanned AFM images with the measured PduA shell proteins were presented. All measured proteins have the same dimension with average heights of 40-50 nm with diameter 100-200 nm.

AFM image quality and sharpness deteriorated as the immobilisation process was approached to the end of procedure. This can be addressed to the quality of the tip that has been extensively used along the immobilisation procedure characterisation. In AFM terminology, this is referred as probe artefacts. Contamination of AFM probes is quite common, and scanning certain samples, especially biological samples, leads to dirty probes more quickly than others. In particular, biological or soft samples, or any sample with loose material at the surface, tend to contaminate

probe tips quickly, leading to image degradation [70]. The quality of AFM images could also be improved by separating the AFM from environmental noise. Floor and acoustic noise will lead to results of poor feedback settings and can also appear to give rise in noise in AFM images [27].

In conclusion, the decrease in CV signal, increment of the EIS spectra and the AFM images had confirmed the successful immobilisation of PduA shell protein on the gold surface. The dimensions measured from the AFM images of the immobilised protein matched with both the dimension of the adsorbed protein and as known from literature. The protein shell outer layer estimated of 3 nm however is too thin to be seen under the AFM. Although the specificity of the Cu^{2+} was not further investigated, it is known from literature that Cu^{2+} has the most affinity compared to the other transition metal [42]. Despite being the least specific, Cu^{2+} is able to bind to its specific protein five times higher than the other biological species [50].

5.3 Antibody Immobilisation on Gold Surface

Before venturing on surface functionalisation at a recessed microelectrode array for antibody immobilisation, the study was first implemented on a macroelectrode surface. The microfabricated silicon-based electrode used in this section had a rectangle shape with dimension of 20 mm (*width*) x 70 mm (*length*) (Fig. 5.20). It was produced with fabrication process as was described in Section 5.2.3.

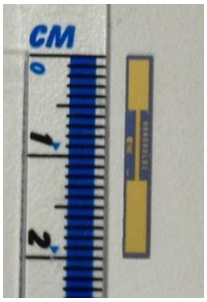


Figure 5.20: Picture of gold macroelectrode with 20 mm x 70 mm surface.

Three surface functionalisation methods were considered at this first stage, namely carboxymethyl dextran (CM-Dextran), and silanisation using (3-glycidyloxypropyl)trimethoxysilane (GOPTS) and (3-aminopropyl) triethoxysilane

(APTES)[*]. The choice of these immobilisation procedures was due their establishment for antibody immobilisation in biosensing. The CM-Dextran method is a renowned technique adapted from the SPR chip [71] while GOPTS and APTES are the most common silanisation agents used for antibody microarray on glass slides [72].

The aforementioned three techniques were investigated by means of electrochemical impedance spectroscopy. The goal of this initial study was to compare the stability and viability of the selected procedures for antibody immobilisation and to find the best immobilisation approach that can be further employed on microelectrode array surface for the subsequent study in developing T-2 toxin labelless immunosensor (Chapter 6).

5.3.1 Carboxymethyl Dextran

Carboxymethyl dextran or abbreviated as CM-Dextran, is a polyanionic derivative of Dextran. CM-Dextran coated sensor chip has been extensively used in SPR-based biosensor immunoassay for immobilising antibodies [73, 74]. CM-dextran in conjunction with EDC and NHS amine coupling has demonstrated to provide a high-density surface for antibody fragment immobilisation [71, 75].

5.3.2 Surface Silanisation Using GOPTS and APTES

Another class of self-assembled monolayer besides thiols is the silane. Unlike thiols that are widely used on gold surface, silanisation is well-associated with silica or glass surface [76]. A large range of silane compounds are available with various functional groups (amino, thiol, carboxyl, epoxide etc.). Each functional group bears different properties, e.g. alkylsilanes is cell repellent while aminosilanes group suits cell surface adhesion [77]. In this part, two types of silanes were looked into, namely APTES and GOPTS (Fig. 5.21).

[*] Surface functionalisation at macroelectrodes were prepared by Dr. Terry McGrath of Queen's University Belfast, Northern Ireland and Dr. Karen Twomey of Tyndall National Institute, Cork

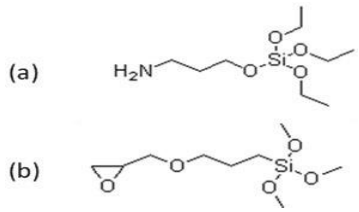


Figure 5.21: Chemical structure of (A) APTES (containing amino functional group); amd (B) GOPTS (containing epoxide functional group).

The silanization process is initialized by hydrolyzation of the alkoxysilane molecules. The silanols (Si–O–H) generated will coordinate with the inorganic surface hydroxyls through a condensation reaction, forming siloxane bonds (Si–O–Si) to anchor the silane to the silica surface. Usually this silane SAM will undergo curing process (heating at high temperature) to remove water molecules and to cross-link adjacent silanols forming stable siloxane linkages [76].

For the GOPTS, a heterofunctional linker (Poly-(ethelene glycol diamine) 2000 g mol^{-1}, abbreviated as DAPEG) and disuccinimidyl carbonate (DSC) are used for the anti-T-2 toxin monoclonal antibody attachment (Fig. 5.22).

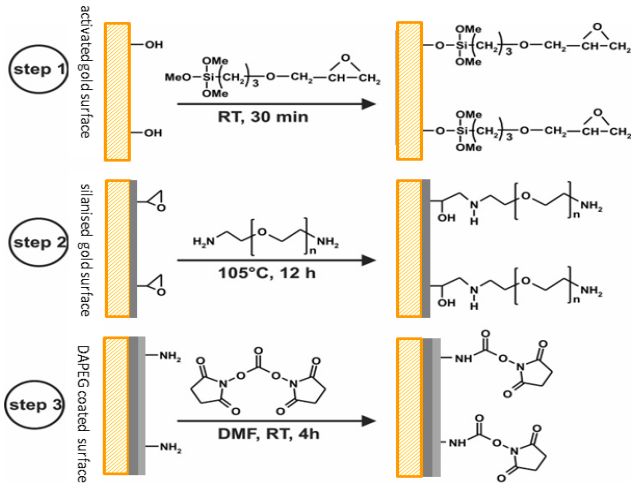


Figure 5.22: Scheme of PEG layer activated gold substrates. Step (1): Silanized gold surface with GOPTS; Step (2): The monolayer of epoxides on the gold surface reacts with DAPEG smelter; and Step (3): DAPEG-coated gold surface are activated with DSC for antibody binding. Taken and adapted from Ref. [78].

Meanwhile 1,4-Phenylene diisothiocyanate (PDITC) was selected as antibody cross-linker on APTES modified surface as described by Raj and co-workers (2009) [10, 79]. PDITC is a homobifunctional cross-linker containing two amine reactive isothiocyanate groups on a phenyl ring. Reaction with the amine group on silanised surface forms a thiourea linkage leaving the second isothiocyanate group free to couple with amine groups on the antibody (Fig. 5.23).

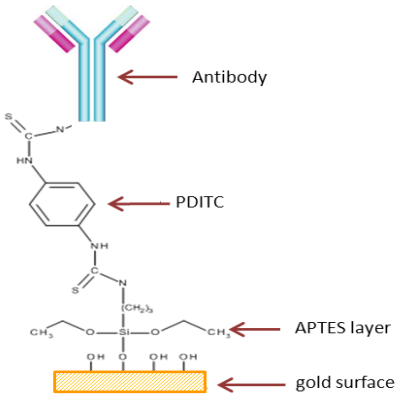


Figure 5.23: Schematic diagram of APTES-activated gold surface with antibody binding via PDITC linker.

5.3.3 Results and Discussions

The CV and EIS for unmodified electrodes were first presented and discussed here. Four unmodified electrodes were taken randomly in order to assess the uniformity of the electrochemical readings for each fabricated electrode. As can be seen from Fig. 5.24, CV for the macroelectrode in 1 mM FCA in PBS has redox potentials at +0.32 V and + 0.26 V, similar as obtained for 1 mm gold disc previously (Section 5.2.4, Fig. 5.12). The peaks potentials observed are typical in a reversible CV system in ferrocene carboxylic acid redox probe (Fc/Fc^{+}) for unmodified gold electrodes as reported before [80]. The EIS Nyquist plot exhibited a straight line with 45° angle, indicating typical Warburg impedance associated with planar diffusion. Overall, all the four random electrodes show uniform CV and EIS signal with R_s+R_{ct} value of 80.25 ± 13.77 Ω.

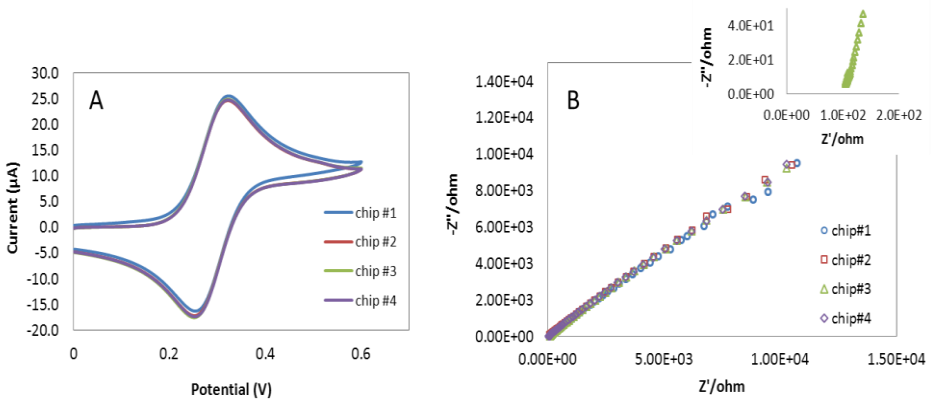


Figure 5.24: CV (scan rate 100 mV s^{-1}); and (b) EIS for four unmodified electrodes in 1 mM FCA in PBS. Frequency for EIS 0.01–100 kHz, $E_{1/2}$ 0.29 V. *Inset:* EIS at high frequency range for chip #3 (146 – 100 kHz).

EIS Study on Different Surface Functionalisations for Antibody Immobilisation

For the immobilisation study, experiments were carried out on minimum of four electrodes to investigate the reproducibility of each electrode. The comparisons were made on the base of impedance spectra. Anti-T-2 toxin antibody concentration that was being used for the immobilisation study was 0.1 mg mL^{-1}. Stability of electrodes for each modification is displayed in bar chart as the function of R_{ct} differences obtained from the impedance spectroscopy (Fig. 5.25). Although CM-Dextran with 0.1 mg mL^{-1} exhibited the largest R_{ct} difference after surface functionalisation (in kΩ magnitude), the main concern was the vast electrochemical signal discrepancy obtained between the electrodes. The other two surface functionalisation methods on the other hand, despite having lower signal than the CM-Dextran modified electrodes, produced more uniform signal response with acceptable standard deviation.

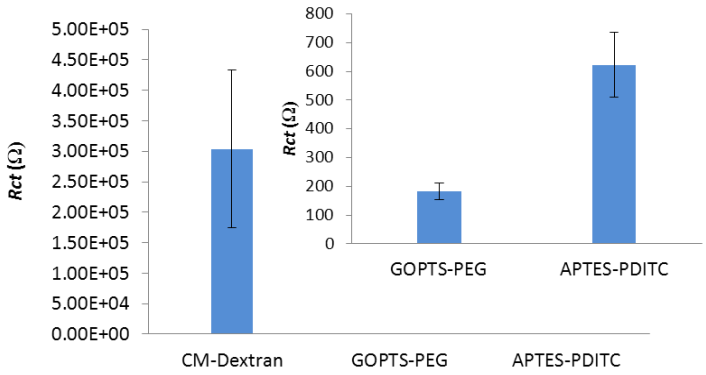


Figure 5.25: Electrodes with different surface biofunctionalisation for 0.1 mg mL-1 anti-T-2 toxin antibody concentration; CM Dextran and (*insets*) GOPTS-PEG and APTES-PDITC.

The CM-Dextran surface functionalisation was repeated on several electrodes with higher antibody concentration (1 mg mL^{-1}), however, the recurrence of electrochemical signal instability became a major drawback for selection of this technique for subsequent studies (Fig. 5.26). Although CM-dextran surfaces provide a reliable and rapid detection particularly in SPR biosensor application, nevertheless its issue of non-specific binding and matrix interference remains the major concern among researchers [74]. This method is therefore deemed unsuitable for our gold on silicon-based microelectrode.

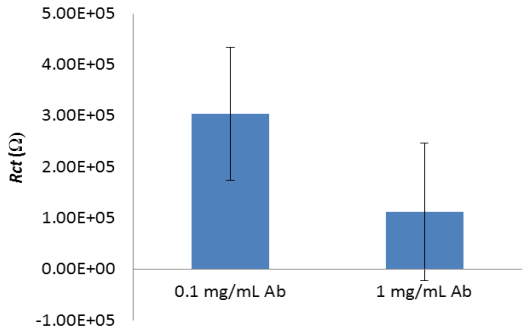


Figure 5.26: Surface functionalisation using CM-Dextran method with different antibody concentrations.

Among all the three surface functionalisations, GOPTS-PEG electrodes exhibited the most stable and uniform current changes. However the main concerns related to this technique were that it produced small R_{ct} changes in comparison with the unmodified electrodes (Fig. 5.27A) i.e. merely within hundreds Ω vicinity. There was also no significant difference when antibody concentration was increased one-fold on the surface (Fig. 5.27B). Although GOPTS silanisation were reported to be superior on glass [72] and silicon nitride substrates [81] with high density protein attachment, nevertheless the result was not encouraging on our gold on silicon electrode. This is perhaps due to the initial treatment on the gold electrode itself [76] that may be lacking of sufficient hydroxyl group to bind with the GPOTS hence affecting the rest of the modification protocols.

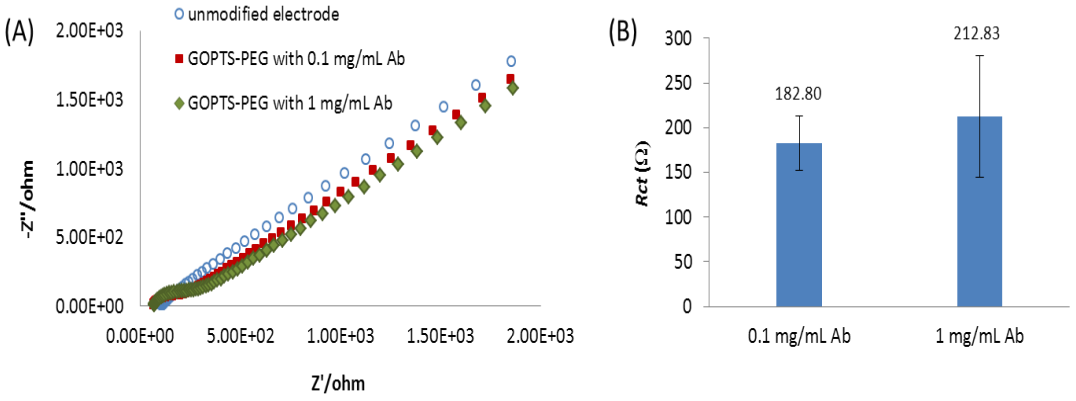


Figure 5.27: (a) Nyquist plot for EIS changes on surface functionalisation with GOPTS-PEG surface functionalisation with anti-T-2 toxin antibody concentrations of 0.1 and 1 mg mL^{-1} in 1 mM FCA in PBS in comparison with the unmodified electrode (Frequency 0.1- 100,000 Ω). (b) Comparison of R_{ct} changes for different antibody concentration on GOPTS-PEG surface functionalisation.

The silanised surface functionalisations (GOPTS-PEG and APTES-PDITC) with 0.1 mg mL^{-1} antibody immobilised were further tested in 0 ppb and 250 ppb of T-2 toxin concentration to screen their electrochemical response on negative and positive toxin stimulation. Comparing both silanisation methods, the APTES-PDITC

technique exhibited R_{ct} changes that were three times greater than the GOPTS-PEG technique (Fig. 5.28A) with lower signal-to-noise ratio of 5.60 ± 0.50 as opposed to 7.39 ± 2.1 for GOPTS-PEG. Even in the presence of low antibody concentration, this particular surface functionalisation was able to detect the 250 ppb T-2 toxin concentration albeit the matrix interference at 0 ppb T-2 toxin concentration (Fig. 5.28B).

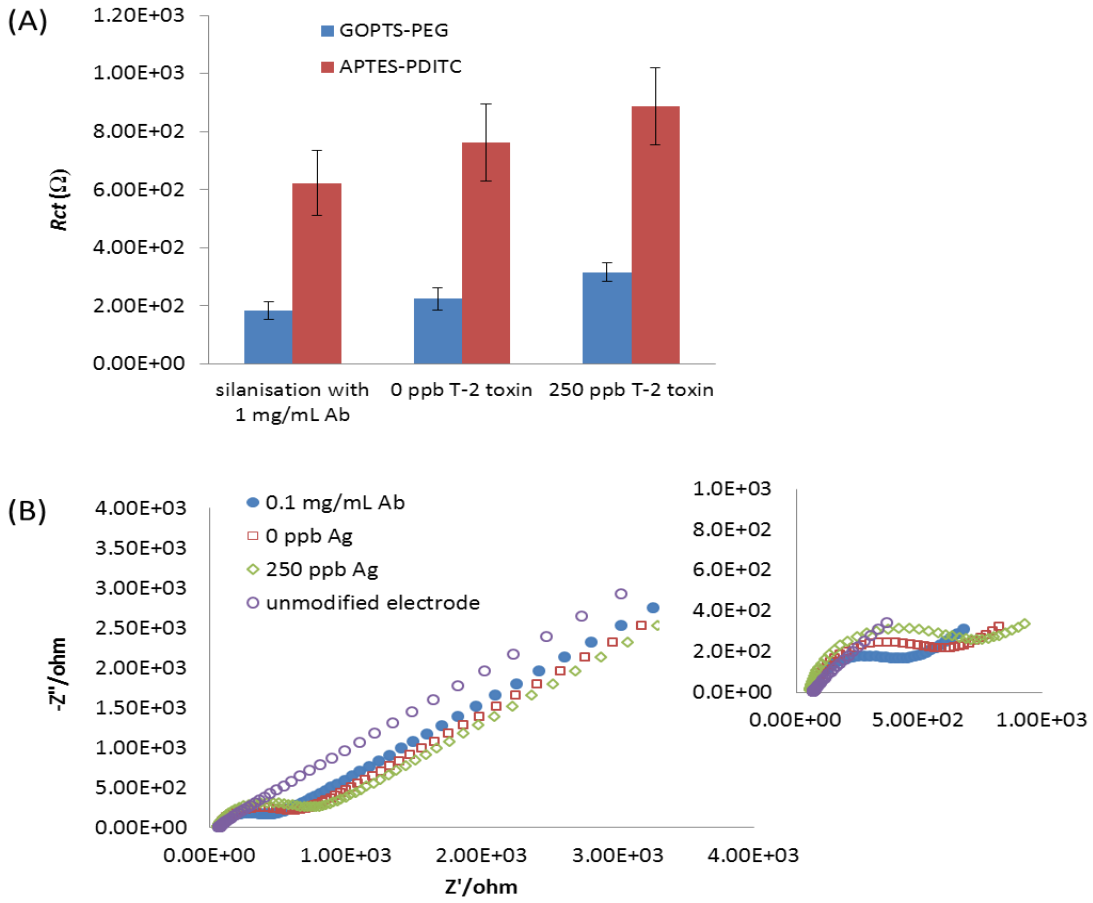


Figure 5.28: (a) Comparison of R_{ct} changes for different silanisation modification with immobilised antibody and subsequent antigen binding; and (b) EIS changes of APTES-PDITC surface functionalisation with 0.1 mg mL-1 immobilised anti-T-2 antibody, 0 ppb and 250 ppb T-2 toxin binding in comparison with unmodified electrode in 1 mM FCA in PBS (0.1-100,000 Hz), (*Inset*: close-up of semi-circle region for frequency range 10-100,000 Hz).

Based on the stability of the APTES-PDITC method on macroelectrode surface, this technique is therefore selected for the following application on microelectrode array as will be discussed in the next chapter. Although both CM-Dextran and GOPTS-PEG were favoured elsewhere for antibody immobilisation for biosensor application, nevertheless our studies have shown that these techniques were not compatible with our microfabricated gold on silicon electrodes. This can be addressed to: (i) Nature of the surface functionalization that requires several days of the entire modification. In CM-Dextran method for instance, long exposure time in SAM solution may improve self-assembly monolayer formation, however continuous treatment that requires long immersion times may impair the SAM formation as well. With regard to this, APTES-PDITC modification steps require only one day hence surface modification is readily available for antibody attachment. (ii) Pretreatment of the surface [82, 83]. Since the methods employed here mostly suit for silica-based substrates, a more robust pretreatment strategy for gold surface should be sought.

Optical Inhibition Study for Immobilised Anti-T-2 Antibody on APTES-PDITC Functionalised Surface

The immobilised anti-T-2 toxin antibody on the APTES-PDITC functionalised surface was further tested by optical inhibition study. In this study, a horseradish peroxidase (HRP) conjugated T-2 toxin can be used to monitor an antibody immobilisation. Figure 5.29 outlines the basic principles involved in this optical method whilst Figure 5.30 describes the principles for showing inhibition which can in turn lead to the production of calibration curves.

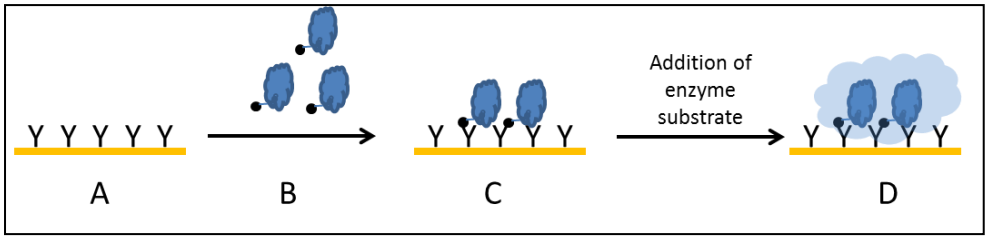


Figure 5.29: Basic principles of optical method used to test immobilisation strategies (**A**: immobilised anti-T-2 toxin antibody on the modified gold surface. **B**: introduction of HRP conjugated T-2 toxin. **C**: Following washing, only the bound toxin remains attached to the immobilised surface. **D**: following addition of enzyme substrate, a colour develops that is proportional to the amount of bound HRP conjugated toxin. This development can be stopped at a given time by the addition of a stop solution and the colour development recorded at 650 nm using a spectrophotometer.

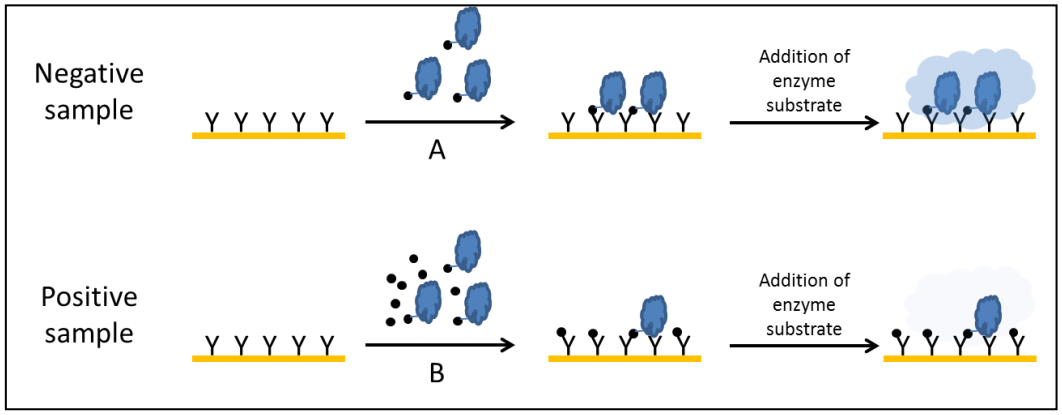


Figure 5.30: Inhibition principles for optical testing method (**A**: for a negative sample, a fixed concentration of HRP conjugated toxin is mixed with a set volume of buffer and left to react on the surface for a set time before washing and the addition of enzyme substrate thus facilitating the development of colour in solution. **B**: for a positive sample the HRP conjugated toxin is mixed with a set volume of unconjugated toxin. The colour development after the addition of enzyme substrate will be less or even none. Calibration curves can be generated by using different concentrations of unconjugated toxin).

The anti-T-2 toxin antibody concentration used in this study was 1 mg mL^{-1}. The experiments were conducted using the competitive direct enzyme-linked immunosorbent assay (ELISA) approach as explained employing only two standard concentrations of 0 and 250 ppb T-2/HT-2 toxin. All the reagents and toxin used in this study was from Veratox® kit, Neogen.

The results of optical inhibition study are presented in Fig. 5.31. As can be seen from the figure, the absorbance of the toxin caused by enzyme-substrate interaction was inversely proportional to the concentration of T-2 toxin. This is typical inhibition signal associated with the ELISA method. Using the APTES-PDITC technique for antibody immobilisation, 78% inhibition was observed indicating the viability of this functionalisation protocol on the gold surface silicon-based macroelectrode.

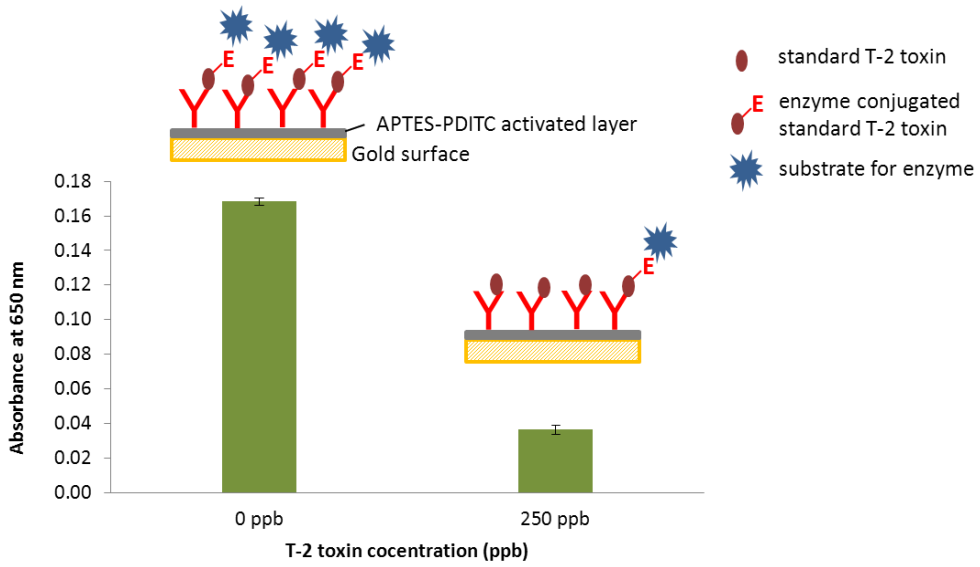


Figure 5.31: Optical inhibition test study on APTES-PDITC functionalised surface with 1 mg mL^{-1} immobilised anti-T-2 toxin antibody. *Inset*: Schematic diagram for direct competitive ELISA happening on the surface. The 0 ppb containing the highest concentration of enzyme-conjugated T-2 toxin produced the highest absorbance as the result of enzyme-substrate interaction.

5.4 Conclusion

This chapter has looked into various surface functionalisation techniques for two types of protein immobilisation for biosensor application, namely Histidine-tagged protein and antibody for mycotoxin T2-toxin. In the beginning, we have also shown how plasma-clean effects the surface wettability property in ensuring a success surface functionalisation/ modification. A stability study of plasma-cleaning effect has proven that the wettability property will be diminished over time and hence it is a prerequisite to plasma-clean the surface prior any modification steps.

In the first part, the immobilisation of histidine-tagged protein with PduA shell protein model using 11-mercaptoundecanoic acid SAM with NTA-Cu^{2+} ligand was found successful. The characterisation studies for this part were comprehensive and consisted of CV, EIS and AFM. The CV had transformed from a reversible to a quasi-reversible system on both adsorbed and immobilised PduA shell protein, confirming the surface modification on the gold electrode. Through EIS study, we have demonstrated that the EIS spectrum did not necessarily increased at each modification steps due to the surface charge and electron permeability. The SAM layer formation could be improved by carrying out the EDC/NHS steps in three cycles as the first cycle only activates the first cycle of EDC/NHS on 11-MUA only activate 50% of the carboxylic acid in the MUA monolayer converted to amides. This limitation is due to the steric packing of the NHS ester intermediate. After three cycles of exposure to EDC/NHS, it was reported that the MUA activation has been enhanced up to 80% [84]. The protein dimensions obtained from the particle analysis of the AFM images are in good agreement with the protein size known from literature. To improve the coordination of Cu^{2+} with NTA, the solutions can be kept under stirring condition during the electrode immersion [23].

The second part of this chapter investigated the compatibility of three different surface functionalization approaches on the gold electrode for antibody immobilisation, i.e. CM-Dextran and silanisation using GOPTS-PEG and APTES-PDITC. This initial study indicated that although CM-Dextran exhibited the largest impedance changes upon surface functionalization and antibody immobilisation, the instability and variation of signal produced by the modified electrode were of major concern. The GOPTS-PEG technique, on the other hand, exhibited the most uniform

and reproducible signal. Nevertheless, due to the lowest impedance signal, this technique also was omitted for the further study. The APTES-PDITC method by far has proven to be viable and compatible on our gold on silicon macroelectrode, as proven by both electrochemical impedance characterisation and optical inhibition study with ELISA approach. The selected method also exhibited low signal-to-noise ratio compared to GOPTS-PEG silanisation method.

The following chapter will discuss the development of T-2 toxin immunosensor using APTES-PDITC method for surface functionalization on the recessed microelectrode array.

5.5 References

1. Wrighton, M.S., *Surface functionalization of electrodes with molecular reagents.* Science, 1986. **231**(4733): p. 32-37.
2. Baldrich, E., et al., *Gold immuno-functionalisation via self-assembled monolayers: Study of critical parameters and comparative performance for protein and bacteria detection.* Journal of immunological methods, 2008. **336**(2): p. 203-212.
3. Bolduc, O.R., et al., *Modified peptide monolayer binding His-tagged biomolecules for small ligand screening with SPR biosensors.* Analyst, 2011. **136**(15): p. 3142-3148.
4. Angenendt, P., *Progress in protein and antibody microarray technology.* Drug Discovery Today, 2005. **10**(7): p. 503-511.
5. Templin, M.F., et al., *Protein microarray technology.* Drug Discovery Today, 2002. **7**(15): p. 815-822.
6. Angenendt, P., et al., *Next generation of protein microarray support materials:: Evaluation for protein and antibody microarray applications.* Journal of Chromatography A, 2003. **1009**(1–2): p. 97-104.
7. Haab, B.B., *Advances in protein microarray technology for protein expression and interaction profiling.* Current opinion in drug discovery & development, 2001. **4**(1): p. 116-123.

8. Du Roure, O., et al., *Functionalizing surfaces with nickel ions for the grafting of proteins.* Langmuir, 2003. **19**(10): p. 4138-4143.
9. Kato, K., H. Sato, and H. Iwata, *Immobilization of histidine-tagged recombinant proteins onto micropatterned surfaces for cell-based functional assays.* Langmuir, 2005. **21**(16): p. 7071-7075.
10. Herzog, G., J. Raj, and D.W. Arrigan, *Immobilisation of antibody on microporous silicon membranes.* Microchimica Acta, 2009. **166**(3-4): p. 349-353.
11. Ahmad, A. and E. Moore, *Electrochemical immunosensor modified with self-assembled monolayer of 11-mercaptoundecanoic acid on gold electrodes for detection of benzo [a] pyrene in water.* Analyst, 2012. **137**(24): p. 5839-5844.
12. Gershon, P.D. and S. Khilko, *Stable chelating linkage for reversible immobilization of oligohistidine tagged proteins in the BIAcore surface plasmon resonance detector.* Journal of immunological methods, 1995. **183**(1): p. 65-76.
13. Sigal, G.B., et al., *A self-assembled monolayer for the binding and study of histidine-tagged proteins by surface plasmon resonance.* Analytical Chemistry, 1996. **68**(3): p. 490-497.
14. Wegner, G.J., et al., *Fabrication of Histidine-Tagged Fusion Protein Arrays for Surface Plasmon Resonance Imaging Studies of Protein−Protein and Protein−DNA Interactions.* Analytical Chemistry, 2003. **75**(18): p. 4740-4746.
15. Sasakura, Y., et al., *Protein Microarray System for Detecting Protein−Protein Interactions Using an Anti-His-Tag Antibody and Fluorescence Scanning: Effects of the Heme Redox State on Protein−Protein Interactions of Heme-Regulated Phosphodiesterase from Escherichia coli.* Analytical Chemistry, 2004. **76**(22): p. 6521-6527.
16. Kröger, D., et al., *Immobilization of histidine-tagged proteins on gold surfaces using chelator thioalkanes.* Biosensors and Bioelectronics, 1999. **14**(2): p. 155-161.
17. Porath, J., *IMAC—Immobilized metal ion affinity based chromatography.* TrAC Trends in Analytical Chemistry, 1988. **7**(7): p. 254-259.

18. Block, H., et al., *Immobilized-metal affinity chromatography (IMAC): a review.* Methods in enzymology, 2009. **463**: p. 439-473.
19. Le, T.T., et al., *A simple method for controlled immobilization of proteins on modified SAMs.* Physical Chemistry Chemical Physics, 2011. **13**(12): p. 5271-5278.
20. Balland, V., et al., *Oriented Immobilization of a Fully Active Monolayer of Histidine-Tagged Recombinant Laccase on Modified Gold Electrodes.* Chemistry-A European Journal, 2008. **14**(24): p. 7186-7192.
21. Wu, C.-C., et al., *Protein immobilization on Ni (II) ion patterns prepared by microcontact printing and dip-pen nanolithography.* Acs Nano, 2010. **4**(2): p. 1083-1091.
22. Hafaid, I., et al., *Effect of electrical conditions on an impedimetric immunosensor based on a modified conducting polypyrrole.* Sensors and Actuators B: Chemical, 2010. **144**(1): p. 323-331.
23. Haddour, N., S. Cosnier, and C. Gondran, *Electrogeneration of a poly (pyrrole)-NTA chelator film for a reversible oriented immobilization of histidine-tagged proteins.* Journal of the American Chemical Society, 2005. **127**(16): p. 5752-5753.
24. Nieba, L., et al., *BIACORE analysis of histidine-tagged proteins using a chelating NTA sensor chip.* Analytical biochemistry, 1997. **252**(2): p. 217-228.
25. Johnson, D.L. and L.L. Martin, *Controlling protein orientation at interfaces using histidine tags: an alternative to Ni/NTA.* Journal of the American Chemical Society, 2005. **127**(7): p. 2018-2019.
26. Ley, C., et al., *Immobilization of histidine-tagged proteins on electrodes.* Colloids and Surfaces B: Biointerfaces, 2011. **88**(2): p. 539-551.
27. Eaton, P.J. and P. West, *Atomic force microscopy*2010: Oxford University Press New York.
28. Morris, V.J., A.R. Kirby, and A.P. Gunning, *Atomic force microscopy for biologists*. Vol. 57. 2010: Imperial College Press London.
29. Ouerghi, O., et al., *Investigating antibody–antigen binding with atomic force microscopy.* Sensors and Actuators B: Chemical, 2002. **84**(2): p. 167-175.

30. You, H.X. and C.R. Lowe, *AFM studies of protein adsorption: 2. Characterization of immunoglobulin G adsorption by detergent washing.* Journal of Colloid and Interface Science, 1996. **182**(2): p. 586-601.
31. Allen, M., E. Bradbury, and R. Balhorn, *AFM analysis of DNA-protamine complexes bound to mica.* Nucleic acids research, 1997. **25**(11): p. 2221-2226.
32. Bezanilla, M., et al., *Adsorption of DNA to mica, silylated mica, and minerals: characterization by atomic force microscopy.* Langmuir, 1995. **11**(2): p. 655-659.
33. Kasas, S., V. Gotzos, and M. Celio, *Observation of living cells using the atomic force microscope.* Biophysical journal, 1993. **64**(2): p. 539-544.
34. Li, Q., et al., *AFM indentation study of breast cancer cells.* Biochemical and biophysical research communications, 2008. **374**(4): p. 609-613.
35. Crowley, C.S., et al., *Structural insight into the mechanisms of transport across the Salmonella enterica Pdu microcompartment shell.* Journal of Biological Chemistry, 2010. **285**(48): p. 37838-37846.
36. Parsons, J.B., et al., *Synthesis of empty bacterial microcompartments, directed organelle protein incorporation, and evidence of filament-associated organelle movement.* Molecular cell, 2010. **38**(2): p. 305-315.
37. Havemann, G.D. and T.A. Bobik, *Protein content of polyhedral organelles involved in coenzyme B12-dependent degradation of 1, 2-propanediol in Salmonella enterica serovar Typhimurium LT2.* Journal of bacteriology, 2003. **185**(17): p. 5086-5095.
38. Pang, A., et al., *Substrate channels revealed in the trimeric Lactobacillus reuteri bacterial microcompartment shell protein PduB.* Acta Crystallographica Section D: Biological Crystallography, 2012. **68**(12): p. 1642-1652.
39. Wink, T., et al., *Self-assembled monolayers for biosensors.* Analyst, 1997. **122**(4): p. 43R-50R.
40. Anandan, V., R. Gangadharan, and G. Zhang, *Role of SAM chain length in enhancing the sensitivity of nanopillar modified electrodes for glucose detection.* Sensors, 2009. **9**(3): p. 1295-1305.

41. Porter, M.D., et al., *Spontaneously organized molecular assemblies. 4. Structural characterization of n-alkyl thiol monolayers on gold by optical ellipsometry, infrared spectroscopy, and electrochemistry.* Journal of the American Chemical Society, 1987. **109**(12): p. 3559-3568.
42. Stora, T., et al., *Metal ion trace detection by a chelator-modified gold electrode: A comparison of surface to bulk affinity.* Langmuir, 1997. **13**(20): p. 5211-5214.
43. Kasprzak, K.S., F.W. Sunderman Jr, and K. Salnikow, *Nickel carcinogenesis.* Mutation Research/Fundamental and Molecular Mechanisms of Mutagenesis, 2003. **533**(1–2): p. 67-97.
44. Dunnick, J.K., et al., *Comparative carcinogenic effects of nickel subsulfide, nickel oxide, or nickel sulfate hexahydrate chronic exposures in the lung.* Cancer research, 1995. **55**(22): p. 5251-5256.
45. Lee, Y., et al., *Carcinogenic nickel silences gene expression by chromatin condensation and DNA methylation: a new model for epigenetic carcinogens.* Molecular and cellular biology, 1995. **15**(5): p. 2547-2557.
46. Salnikow, K., et al., *Carcinogenic nickel induces genes involved with hypoxic stress.* Cancer research, 2000. **60**(1): p. 38-41.
47. Abad, J.M., et al., *Functionalization of Thioctic Acid-Capped Gold Nanoparticles for Specific Immobilization of Histidine-Tagged Proteins.* Journal of the American Chemical Society, 2005. **127**(15): p. 5689-5694.
48. Ordaz, E., et al., *Covalent and Metal-Chelate Immobilization of a Modified 2-Haloacid Dehalogenase for the Enzymatic Resolution of Optically Active Chloropropionic Acid.* Biotechnology Progress, 2000. **16**(2): p. 287-291.
49. Ionescu, R.E., et al., *Label-free impedimetric immunosensor for sensitive detection of atrazine.* Electrochimica Acta, 2010. **55**(21): p. 6228-6232.
50. Cho, M., et al., *Sensitive electrochemical sensor for detection of lipopolysaccharide on metal complex immobilized gold electrode.* Sensors and Actuators B: Chemical, 2012. **174**(0): p. 490-494.
51. Tan, L., et al., *Differential interactions of plasmid DNA, RNA and endotoxin with immobilised and free metal ions.* Journal of Chromatography A, 2007. **1141**(2): p. 226-234.

52. Gaberc-Porekar, V. and V. Menart, *Perspectives of immobilized-metal affinity chromatography.* Journal of Biochemical and Biophysical Methods, 2001. **49**(1–3): p. 335-360.
53. Ueda, E.K.M., P.W. Gout, and L. Morganti, *Current and prospective applications of metal ion–protein binding.* Journal of Chromatography A, 2003. **988**(1): p. 1-23.
54. Porath, J., et al., *Metal chelate affinity chromatography, a new approach to protein fractionation.* Nature, 1975. **258**(5536): p. 598-599.
55. Parker, C.O., et al., *Electrochemical Immunochip Sensor for Aflatoxin M1 Detection.* Analytical Chemistry, 2009. **81**(13): p. 5291-5298.
56. Parra, A., et al., *Cholesterol oxidase modified gold electrodes as bioanalytical devices.* Sensors and Actuators B: Chemical, 2007. **124**(1): p. 30-37.
57. Tsai, Y.-C., J.-D. Huang, and C.-C. Chiu, *Amperometric ethanol biosensor based on poly (vinyl alcohol)–multiwalled carbon nanotube–alcohol dehydrogenase biocomposite.* Biosensors and Bioelectronics, 2007. **22**(12): p. 3051-3056.
58. Vianello, F., L. Zennaro, and A. Rigo, *A coulometric biosensor to determine hydrogen peroxide using a monomolecular layer of horseradish peroxidase immobilized on a glass surface.* Biosensors and Bioelectronics, 2007. **22**(11): p. 2694-2699.
59. Guo, B., J.-i. Anzai, and T. Osa, *Adsorption behavior of serum albumin on electrode surfaces and the effects of electrode potential.* Chemical and Pharmaceutical Bulletin-Tokyo, 1996. **44**: p. 800-803.
60. Gu, H.-Y., A.-M. Yu, and H.-Y. Chen, *Direct electron transfer and characterization of hemoglobin immobilized on a Au colloid–cysteamine-modified gold electrode.* Journal of Electroanalytical Chemistry, 2001. **516**(1–2): p. 119-126.
61. Wang, C., et al., *Adsorption and Direct Electron Transfer from Hemoglobin into a Three-Dimensionally Ordered Macroporous Gold Film.* Advanced Functional Materials, 2005. **15**(8): p. 1267-1275.

62. Lisdat, F. and D. Schäfer, *The use of electrochemical impedance spectroscopy for biosensing.* Analytical and bioanalytical chemistry, 2008. **391**(5): p. 1555-1567.
63. Hleli, S., et al., *Atrazine analysis using an impedimetric immunosensor based on mixed biotinylated self-assembled monolayer.* Sensors and Actuators B: Chemical, 2006. **113**(2): p. 711-717.
64. Hleli, S., et al., *An immunosensor for haemoglobin based on impedimetric properties of a new mixed self-assembled monolayer.* Materials Science and Engineering: C, 2006. **26**(2): p. 322-327.
65. Ramón-Azcón, J., et al., *An impedimetric immunosensor based on interdigitated microelectrodes (IDμE) for the determination of atrazine residues in food samples.* Biosensors and Bioelectronics, 2008. **23**(9): p. 1367-1373.
66. Valera, E., et al., *Impedimetric immunosensor for atrazine detection using interdigitated μ-electrodes (IDμE's).* Sensors and Actuators B: Chemical, 2007. **125**(2): p. 526-537.
67. Li, X.H., et al., *Ionic-Liquid-Doped Polyaniline Inverse Opals: Preparation, Characterization, and Application for the Electrochemical Impedance Immunoassay of Hepatitis B Surface Antigen.* Advanced Functional Materials, 2009. **19**(19): p. 3120-3128.
68. Kharlampieva, E., et al., *Spin-Assisted Layer-by-Layer Assembly: Variation of Stratification as Studied with Neutron Reflectivity†.* Langmuir, 2009. **25**(24): p. 14017-14024.
69. Cacciafesta, P., et al., *Visualisation of human plasma fibrinogen adsorbed on titanium implant surfaces with different roughness.* Surface Science, 2001. **491**(3): p. 405-420.
70. Taatjes, D.J., et al., *Quality assessment of atomic force microscopy probes by scanning electron microscopy: Correlation of tip structure with rendered images.* Microscopy research and technique, 1999. **44**(5): p. 312-326.
71. Vashist, S.K., et al., *Effect of antibody immobilization strategies on the analytical performance of a surface plasmon resonance-based immunoassay.* Analyst, 2011. **136**(21): p. 4431-4436.

72. Kusnezow, W., et al., *Antibody microarrays: an evaluation of production parameters.* Proteomics, 2003. **3**(3): p. 254-264.
73. Haasnoot, W., M. Bienenmann-Ploum, and F. Kohen, *Biosensor immunoassay for the detection of eight sulfonamides in chicken serum.* Analytica Chimica Acta, 2003. **483**(1): p. 171-180.
74. Situ, C., et al., *Reduction of severe bovine serum associated matrix effects on carboxymethylated dextran coated biosensor surfaces.* Talanta, 2008. **76**(4): p. 832-836.
75. Howell, S., et al., *High-density immobilization of an antibody fragment to a carboxymethylated dextran-linked biosensor surface.* Journal of Molecular Recognition, 1998. **11**(1-6): p. 200-203.
76. Vistas, C.R., A.C.P. Águas, and G.N.M. Ferreira, *Silanization of glass chips—A factorial approach for optimization.* Applied Surface Science, 2013. **286**(0): p. 314-318.
77. Corey, J.M., B.C. Wheeler, and G.J. Brewer, *Micrometer resolution silane-based patterning of hippocampal neurons: critical variables in photoresist and laser ablation processes for substrate fabrication.* Biomedical Engineering, IEEE Transactions on, 1996. **43**(9): p. 944-955.
78. Wolter, A., R. Niessner, and M. Seidel, *Preparation and Characterization of Functional Poly(ethylene glycol) Surfaces for the Use of Antibody Microarrays.* Analytical Chemistry, 2007. **79**(12): p. 4529-4537.
79. Raj, J., et al., *Surface immobilisation of antibody on cyclic olefin copolymer for sandwich immunoassay.* Biosensors and Bioelectronics, 2009. **24**(8): p. 2654-2658.
80. Guo, X. and N. Hu, *Increment of Density of Au Nanoparticles Deposited in Situ within Layer-by-Layer Films and Its Enhancement on the Electrochemistry of Ferrocenecarboxylic Acid and Bioelectrocatalysis.* The Journal of Physical Chemistry C, 2009. **113**(22): p. 9831-9837.
81. Psarouli, A., et al., *Covalent Binding vs. Adsorption of Biomolecules on Silicon Nitride Planar Waveguides.* Procedia Engineering, 2011. **25**: p. 350-353.

82. Halliwell, C.M. and A.E. Cass, *A factorial analysis of silanization conditions for the immobilization of oligonucleotides on glass surfaces.* Analytical Chemistry, 2001. **73**(11): p. 2476-2483.
83. Mitchon, L.N. and J. White, *Growth and analysis of octadecylsiloxane monolayers on Al2O3 (0001).* Langmuir, 2006. **22**(15): p. 6549-6554.
84. Frey, B.L. and R.M. Corn, *Covalent attachment and derivatization of poly (L-lysine) monolayers on gold surfaces as characterized by polarization-modulation FT-IR spectroscopy.* Analytical Chemistry, 1996. **68**(18): p. 3187-3193.

CHAPTER 6

DEVELOPMENT OF T-2 TOXIN IMMUNOSENSOR

6.1 Introduction to Immunosensor

A biosensor that utilises antibody or antigen as the biorecognition element is referred to as an immunosensor. Simply put, an immunosensor is an adaptation of immunoassay in biosensor format [1, 2]. The renowned and established immunoassay is the enzyme-linked immunosorband assay (ELISA); and using similar approach, its procedures and reagents can be employed in the labelled-immunosensor development. Such work has been demonstrated by Tothill and co-workers using electrochemical measurement [3-7]. Enzymes such as alkaline phosphatase and horse-radish peroxidase (HRP) are commonly used as the enzyme-label with this regard.

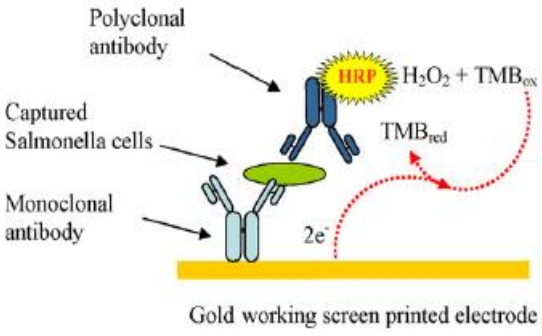


Figure 6.1: Schematic diagram of the electrochemical immunosensor system using an HRP enzyme-label (based on a direct sandwich ELISA) for *Salmonella* detection. Taken from Ref. [4].

In a label-immunosensor, either the antigen or antibody could be labelled in order to obtain a measurable signal. Other than the aforementioned enzyme-label, antibody or antigen also could be labelled with fluorophore [8] and radioactive label [9].

Besides electrochemical, interactions between the immobilised antibody and the target antigen can be monitored using optical [8, 10], mass sensitive [11, 12] or thermoelectric immunosensors (thermistors). The latter detection however has the least application in immunosensing [2]. Although initially optical immunosensor were preferred in late 1990s/early 2000s, current trends have shown that electrochemical immunosensors are gaining considerable attention due to their simplicity, the ease of miniaturisation and the low cost of the instrumentation [13, 14]. The most common electrochemical techniques employed in immunosensor are the CV [5], chronoamperometry [3, 4], EIS [15], capacitance [16] and potentiometry [17]. To gain better insight and understanding of the antibody-antigen interaction, a combination of two or more electrochemical techniques can be used as well [17].

Recently it is becoming of interest to conduct an immunosensor with a label-free approach (i.e. direct detection of antibody-antigen binding). This is reflected by the emerging of over 300 publications through the Web of Knowledge database for the past three years. Getting rid the use of competitive labelled immunoagents may help to accelerate the analysis time by eliminating the long incubation steps. However, a challenge facing label-free immunosensors is the fact that the antibody-antigen binding does not elicit any electrochemical signal hence limiting the electrochemical measurements. Among the most widely reported techniques used in measuring labelless Ab-Ag interaction in real-time is the surface plasmon resonance (SPR) [18]. Lately EIS technique has becoming of interest to probe the antibody-antigen binding owing to its sensitivity of analysing surface phenomena and changes of bulk properties [19]. The work on label-free immunosensor using EIS technique has been demonstrated viable by groups of researchers for the detection of cholera toxin [15], *Salmonella typhimurium* [20], multiple sclerosis [21], *E.coli* [22] and pesticide (atrazine) [23], to name a few.

6.1.1 Antibodies

Antibodies are highly selective glycoproteins, which are produced by mammalian immunological systems in response when being triggered by an antigen [24]. An antigen could be any foreign substance, either protein (bacteris, cells, fungi, virus) or non-living substances (toxin, chemicals, drugs), to one's immune system. Antibody is also known as immunoglobulins (Igs) and be categorised into five different classes of IgG, IgA, IgM, IgD and IgE; depending on the number of domains in the constant regions of the heavy chains and positions of the disulfide bridges (Figure 6.2a). The IgG (immunoglobulin G), the most abundant immunoglobulin species in serum, is the most extensively used in immunoassay application. The structure of antibody is typically represented schematically as a Y-shape, and consists of two identical *Fab* (fragment antibody) portions hinged to an *F*c (fragment crystallizable) part. The *Fab* fragment is a region where binding with antigen takes while the *Fc* region is the tail region of an antibody that interacts with cell surface receptors [24].

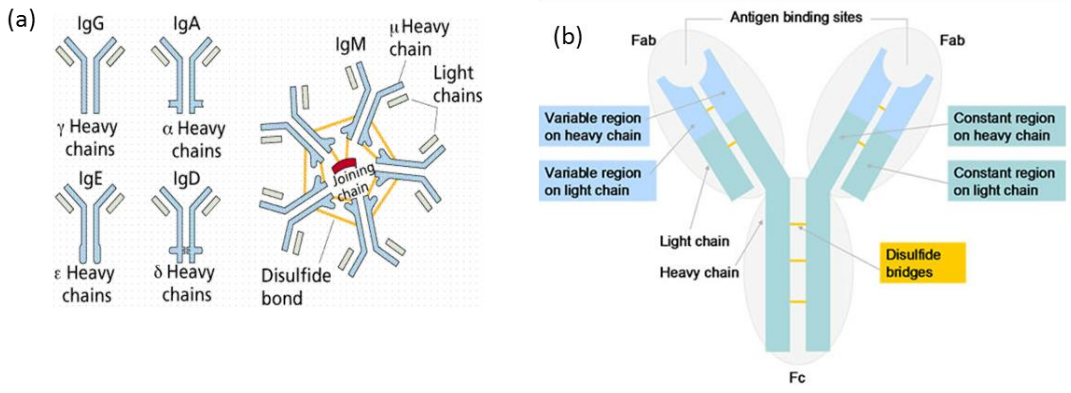


Figure 6.2: (a) The five classes of antibodies (b) Structural regions of an antibody molecule.

Depending on the nature of its production, antibodies can be divided into either monoclonal or polyclonal type antibodies. Monoclonal antibodies are produced by a single clone of antibody-producing cells where spleen cells are taken from the immunised animals for cloning using hybridoma technology [25]. Polyclonal antibodies, on the other hand, are taken from the serum of immunised animals that

will undergo several purification steps and are a mixture of different antibodies produced by different cells [26]. Although the polyclonal antibody production is relatively cheaper and simple, nevertheless the monoclonal antibodies are more specific. Monoclonal antibodies also can be made in cell culture and are therefore also more reproducible from batch to batch than polyclonal antibodies. Table 6.1 shows the difference between monoclonal and polyclonal antibodies.

Table 6.1 Comparison of monoclonal and polyclonal antibodies.

Monoclonal antibodies	**Polyclonal antibodies**
High cost to prepare	Cheaper cost to prepare
High technology and skills required	Technology required is low
Time scale is long for hybridomas	Time scale is short
Can produce large amounts of specific antibodies but may be too specific	Produces large amounts of non-specific antibodies
Same affinities	Different affinities
Monospecific antibody	Could not be reproduced
Detect only one epitope	Recognises multiple epitopes
Efficient for binding of antigens within a mixture of related molecules	Not useful for probing specific domains of antigens

Antibody-Antigen Binding

Antibody–antigen (Ab-Ag) reaction is very specific but its interaction is non-covalent and weak. Each antibody binds to a particular part of the antigen called the antigenic determinant or epitope. The non-covalent bonds involved in Ab-Ag binding are hydrogen bonds, electrostatic forces, Van der Waals forces and hydrophobic bonds (Fig. 6.3). The non-covalent binding involved in the Ab-Ag interaction depends on the proximity of one another. If the antigens and antibodies are close to each other, hydrophobic forces and van der Waals can be formed. Instead, the electrostatic interactions and hydrogen bonds do not require the antigen and antibody to be close.

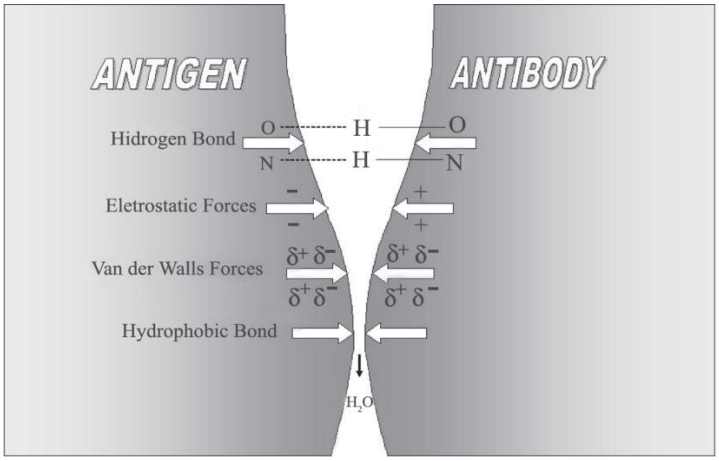


Figure 6.3: Forces involved in antigen-antibody binding. Taken from Ref. [27].

The strength of a single antigen–antibody bond is termed as the antibody affinity. Since each monoclonal antibody has two antigen-binding sites and polyclonal antibodies can bind multiple antigenic determinants, antibodies are multivalent in their reaction with antigen [28]. In some cases, cross-reactivity also can occur where antibodies can recognise other antigens.

6.2 T-2 toxin

T-2 toxin is a type of mycotoxin. Mycotoxins are highly toxic secondary metabolites produced by molds, affecting agricultural industry in particular cereal grains and cereal-based foods [29]. Due to its acute toxicity and carcinogecity, the EU and in fact, many countries, have established a stringent regulation (e.g. setting the permitted level and sample testing) in order to control the contamination [30]. T-2 and its metabolite, HT-2, is a trichothecene type A mycotoxin. Trichothecenes are classified of groups of A, B, C and D; depending on their basic structure and type A trichothecene has no carbonyl group [31]. Fig. 6.4 highlights the structures of the most common accruing trichothecene type A and type B. The clinical signs of trichothecene infection in animals include feed refusal and vomiting, growth retardation, reproductive disorders, blood disorders, dermatitis, oral lesions and depression of the immune response [32].

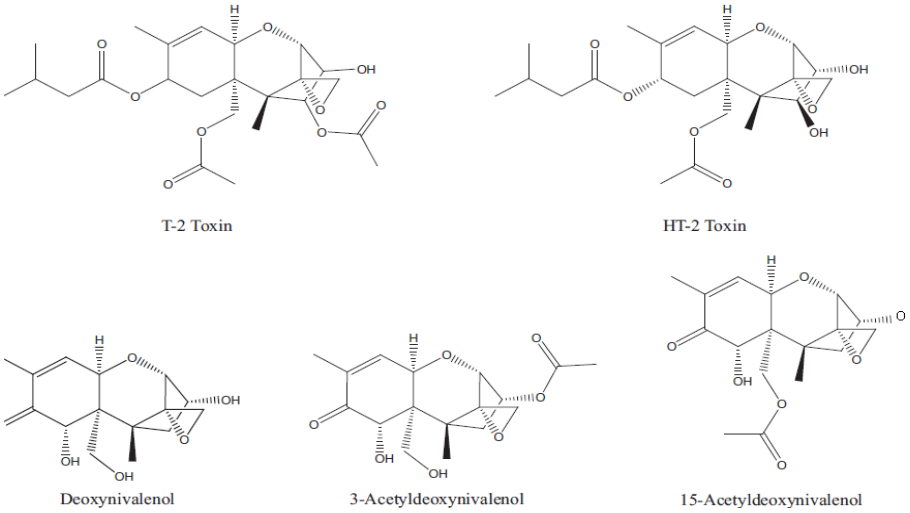


Figure 6.4: Chemical structures of the type A (T-2 and HT-2 toxins) and type B trichothecenes (deoxynivalenol, 3- and 15-acetyldeoxynivalenol). Taken from Ref. [32].

T-2 toxin is naturally occurring mold byproducts of Fusarium spp fungus, which are potent and toxic to both humans and animals. The immunosuppressive effect arose from the toxin has been studied by Rosenstein et al. in 1979 [33]. Lee and co-workers also has reported death of the rats after being fed with crude culture of Fusarium isolates containing T-2 toxin [34]. In cereal production, T-2/HT-2 usually has higher incidences and concentrations on oats, barley and wheat. Its occurance is such prominent in EU countries [35] and has been highlighted in Norway [36], Poland [37], Croatia [38], Turkey [39], Spain [40], and even Pakistan [41]. An isolated case of T-2 toxin detection in rice also has been reported in Nigeria [42]. A survey carried out in 2009 also indicated an increasing rate of T-2 occurrence in Nordic countries reaching concentration as high as 1000 μg/kg, exceeding limit of 500 μg/kg for unprocessed oats [35].

Another concern pertaining to T-2 toxin is the possible misuse of the chemical component as a biological warfare agent [43, 44] since mold-toxins are cheap and easy to obtain [45]. Details of trichothecene use as biological warfare and its series of history has been described in-depth in the textbook of *Medical Aspects of Chemical and Biological Warfare* (Chapter 34) by Wannemacher & Wiener [44]. T-2 toxin as biological warfare agents can be deployed in the form of dusts, droplets,

aerosols, or smoke particles from aircraft, rockets, missiles, artillery, mines, or even portable sprayers. According to Paterson (2006), the T-2 toxin posed a significant threat as bioweapon as this is a valid weapon and the exposure to a few milligrams of the toxin is potentially lethal [46]. T-2 toxin inhibits protein synthesis by binding to ribosomal RNA and disrupts cell membranes.

6.2.1 Conventional and Current Methods for T-2 Toxin Detection

The detection of T-2 toxin could be either based on analytical instrumentation methods (quantitative) or screening (qualitative and semi-quantitative, which are as described below.

Instrumentation Methods

The conventional instrumentation methods such as gas chromatography (GC) and high performance liquid chromatography (HPLC), coupled with various detectors, have long being established for the T-2 detection. GC-mass spectroscopy (GC-MS) is the most widely employed for the T-2 toxin detection, allowing simultaneous analysis of several trichothecenes with high sensitivity [36, 43, 47]. However, GC is tedious, requiring sample extraction and derivatisation, and column clean-up [31]. Besides that, the derivatisation reagents depends on both the type of trichotecenes and detectors used. Besides GC-MS, other T-2 toxin detectors such as electron capture detector (ECD) and flame ionisation detector (FID) were also reported. The HPLC method, on the other hand, does not need sample derivatisation. HPLC coupled with refractive index (LC-RI) and UV [39] detectors have been reported for T-2 toxin detection. The latter however was found unsuitable for T-2 detection as T-2 chemical structure does not contain carbonyl function required for UV adsorption. Although fluorescent labelling could be added, this will only prolong the analysis time. LC-MC was found to be as superior as the GC-MS in terms of sensitivity and the cost but LC-MS does not require the derivatisation step [43]. The major drawback of both GC and HPLC however, are that they require highly-skilled personnel to operate the high-end instrumentations and the extensive use of organic solvents for sample extraction etc. Since this is a lab-based measurement, the

detection of the toxin also is confined only in the lab, limiting the need of performing in-situ field measurement.

Screening Methods

Screening methods provide the simpler approach and involve less complicated instrumentation. However, this mode of detection only provides qualitative and sometimes semi-quantitative indication based on colour changes. T-2 detection using screening methods such as thin layer chromatography (TLC) [38-40] and ELISA [48, 49] have been reported. The advantage of TLC method is that it is a simple, robust, offline method with adjustable detection limit. Nevertheless, this method is susceptible to interference [42] with higher variance [50]. The ELISA kit for the T-2 toxin detection is widely available from various companies such as Ridascreen, Neogen and Bioo Scientific, to name a few. ELISA can also serve as a quantitative method but the drawback derived from ELISA is that it requires lengthy time as it involves an indirect antibody-antigen binding. A more recent trend for screening T-2 toxin is by using immunodiagnostic strip tests (also referred as dipstick or immunochromatographic) based on lateral-flow technology where the antibodies are conjugated with colloidal nano-gold particle (Fig.6.5). However, challenges rely on adjusting the flow properties of the test strip besides reducing matrix background interference [51]. Several immunostrips are commercially available nowadays and can serve as both qualitative and semi-quantitative measurements, however, all of these claimed "rapid tests" are still based on the competitive immunoassay format [51-53]. Furthermore to quantify the concentration, a mini reader instrument is required thus increasing instrumentation cost.

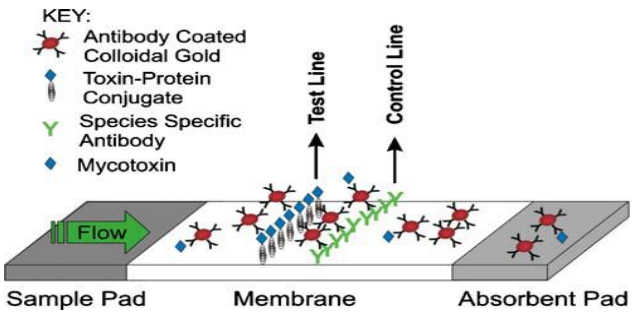


Figure 6.5: Principle of competitive assay in test strip format. Taken from Ref. [51].

Biosensor for T-2/HT-2 Toxin Detection

The first biosensor work on T-2 toxin detection using optical biosensor approach was reported by Williamson et al. in 1989 [9, 54]. In his study, T-2 toxin monoclonal antibody (MAb) was immobilised on quartz fibre and its specific T-2 antigen was labelled with radiolabel [9]. Direct detection of T-2 antibody (both polyclonal and monoclonal) and its specific T-2 toxin has been demonstrated by using total internal reflection ellipsometry (TIRE) supported by QCM impedance methods [55]. An SPR-based biosensor for T-2/HT-2 screening detection in cereals and maized-based baby food was conducted in 2010 by Elliot and co-workers [56]. The following year, Gupta et al. also reported the similar approach using SPR for detecting molecularly imprinted polymer (MIP) T-2 toxin with a little EIS work to study and compare the immobilisation procedure [57]. All of the aforementioned techniques involving both SPR and QCM are based on optical biosensor. The only work based on electrochemical biosensor for T-2 toxin detection by using multichannel electrochemical immunosensors (MEI) on 96-well screen-printed microplate has been published by Piermarini et al. [49]. However, the indirect detection of Ab-Ag was used in this study and the signal generated by the enzymatic subsrates of TMB and T-2 toxin MAb conjugated HRP was measured using intermittent pulse amperometry (IPA) technique.

6.3 Objectives of the Study

Concerning the toxicity posed by T-2 toxin in both agriculture and bioweapon use, it is therefore important to develop a direct and straight forward method for its detection. With this regard, labelless detection of Ab-Ag is required and such can be achieved by EIS. To our best knowledge, there is no work and publication related on labelless detection of T-2 toxin using both microelectrode array and EIS technique that has been reported to date.

Various techniques for immobilising Ab on microelectrode have been reported, most of them employing interdigitated array [15]. In contrast and as continuation the second part of the previous chapter, the objective of this chapter is to study the surface functionalization using APTES-PDITC technique on the microelectrode

array for anti-T-2 toxin antibody in frame of T-2 toxin immunosensor development. Both microdisc and microband array will be employed with this regard. The immobilisation of biological elements at the silicon-based microelectrode array indeed is more challenging as the microelectrode dimensions are much smaller compared with macro counterparts and consist of hundreds of disc array. What makes it more intricate is that all of microelectrodes are the recessed electrodes. The fact that microelectrodes are much smaller than macroelectrodes makes them more susceptible to noise; each modification of electrode array contribute to the total current output thus uniformity of every array is of paramount importance.

6.4 Results and Discussions

Single WE microelectrode array chip was used in this study. The fabrication is as described previously in Chapter 3 (Section 3.2) with 200 nm recess depth. Both of the microband and microdisc dimensions are given in Table 6.2. Such dimensions were selected following the preliminary characterisation and study that have proven these designs have sufficient interspacing distance to allow individual diffusion profiles.

Table 6.2 Dimensions for the microdisc and microband electrode array used in surface functionalization for anti-T-2 toxin antibody immobilisation.

Geometry	Diameter or Width (μm)	Radius or Length (μm)	Centre-to-centre separation (μm) (*d*)	Number of electrodes, *N*	Surface area, A (cm^2)
Disc	10	5	100	323	2.537×10^{-4}
Band	10	500	100	17	8.5×10^{-4}

In our study, the antibody immobilisation on the microelectrode array will be evaluated by both CV and EIS. It was highlighted earlier in Chapter 4 and 5 that parameters associated with EIS (R_s, R_{ct} and C_{dl}) are not possible to determine using equations developed for the electrode with plane diffusion since the microelectrode

arrays possess a mixed diffusion layer. However, it is well known that EIS technique is able to probe the bulk properties happening on the electrode surface. In this case, the change of one impedance element- a resistance or a capacitance- can be monitored the changes upon surface functionalization. In this study, the changes and reading taken from the EIS were from the shift of R_{ct} by extrapolating the R_{ct} semi-circle. This measurement is referred as resistance-based sensors [19].

There were several other approaches on determining and taking the impedimetric readings. Modern impedance analysers are able to provide data evaluation software and fitting programmes which allow the calculation of transfer functions according to an equivalent circuit [19]. Recently, Abdul Rahman and co-workers (2013) measure the conductance and dielectric properties of the bulk samples on the interdigitated array where the electrochemical spectrum analysis algorithm was employed to model the CPE element and curve fitting technique was used to extract values [58, 59]. Similar modelling and fitting analysis also was reported by other researcher in the detection of human-chorionic-gonadotropin [60]. While this indirect analysis method could be accurate nevertheless but development of the fitting procedure is a specific complex task, which was not inside objectives of the current study. Thus, a more straightforward approach demonstrated by other researchers [15, 19, 61-64] and based on estimating and comparing the R_{ct} values was utilised in the EIS discussion in this chapter.

6.4.1 Silanisation Using APTES with PDITC Cross-Linker

The application using similar techniques for antibody immobilisation for Aflatoxin M1 immunosensor had been demonstrated viable as reported by Parker et al. (2009) on gold microelectrode array of [5] and by Herzog et al. (2009) on microporous silicon membranes [65]. In these publications, optical (fluorescence microscopy) and electrochemical characterisations namely cyclic voltammetry were described but none have discussed the EIS approach.

For a beginning, two microdisc electrode arrays were tested with APTES-PDITC surface functionalization with two different concentrations of anti-T-2 toxin antibody immobilised (0.5 mg mL^{-1} and 1 mg mL^{-1}). The CV and EIS were analysed after

each modification steps, i.e. unmodified electrode, after APTES-PDITC activation and after antibody attachment. In the beginning, two different microdisc array electrode with similar EIS curve and limiting current values from were selected. Thus, prior modification, electrodes have limiting current of 401.4 ± 19.1 and 389.35 ± 4.05 (experimental limiting current of 338 nA) (Fig. 6.6) with similar EIS curve and magnitude. The unmodified disc arrays showed a typical flattened semi-circle EIS curves.

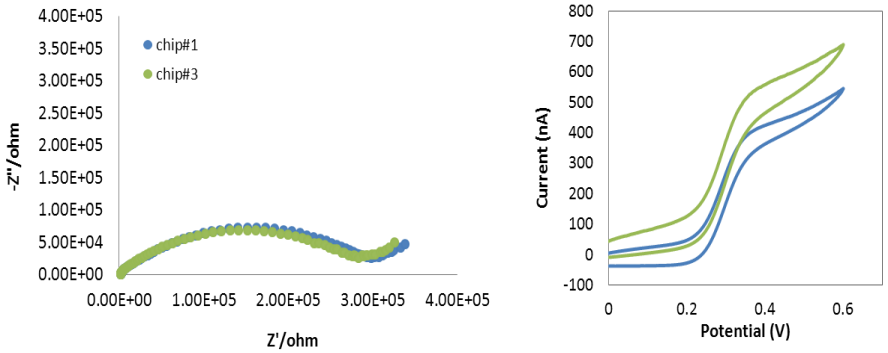


Figure 6.6: EIS (frequency 0.01- 100,000 Hz) and CV (scan rate of 100 mV s^{-1}) performed in 1 mM FCA in PBS for unmodified electrodes.

Upon surface functionalization with APTES silanisation and PDITC attachment (Fig. 6.7), both electrodes exhibited massive impedance difference in the magnitude of 2 MΩ. The two semicircles observed at this stage. The first semicircle can be regarded to the bulk material; the second semi-circle derived from the adsorption on the interface [66]. After antibody immobilisation, the impedance curve decreased, which can be attributed to the rearrangement of the silanisation layer. The first antibody attachment of 0.5 mg mL^{-1} exhibited similar patterns between the two different disc arrays whereby the first semi-circle has imaginary value within 300-400 kΩ. The second small semi-circle had R_{ct} value difference of 500 kΩ approximately. The addition of second concentration of the antibody (1.0 mg ml^{-1}) on the first microdisc array showed no further increment in impedance spectra that can be attributed to the saturation of the antibody immobilisation on the surface. However, for the second microdisc electrode, the addition of subsequent concentration resulted in a decrease of impedance curve. This could be due to the

detachment of the silanisation layer as the APTES-PDITC linker layer obtained on this electrode had different pattern in comparison with the first microdisc electrode.

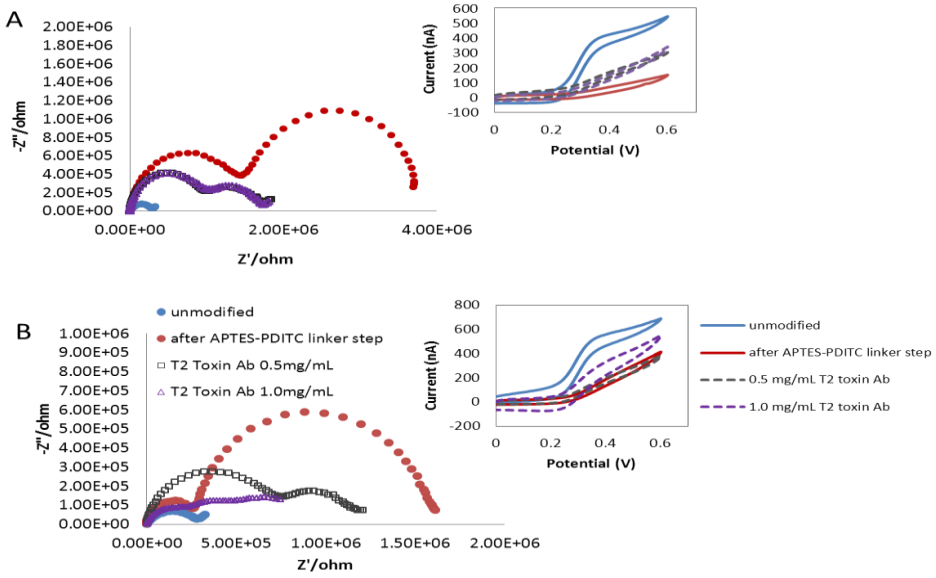


Figure 6.7: EIS (frequency 0.01- 100,000 Hz) and CV (scan rate of 100 mV s^{-1}) comparison for two different 10 µm microdisc electrode array functionalised with APTES silanisation with PDITC linker for two anti-T-2 toxin antibody concentrations immobilisation. Electrochemical measurements were performed in 1 mM FCA in PBS.

Discrepancy in electrochemical impedance signal from both microdisc array may suggest the non-uniformity of the silanisation layer formation that took place on the two different electrodes. This could be seen by the difference in the two semi-circles observed after the APTES-PDITC layer deposition. In terms of limiting current, the currents decreased by 22% after antibody attachment for both microdisc array. The large deviation of impedance reading between two devices using silanisation with PDITC linker also have been reported by Manning and co-workers (2007) for the DNA biosensor on the diamond drilled substrates although they concluded that this method is reproducible compared to the direct immobilisation approach [67].

The surface properties on the two microdisc electrodes were assessed using contact angle measurement before and after the APTES deposition and antibody immobilisation (Fig. 6.8). The unmodified electrodes were found to be hydrophobic with values of 139-160° for both disc arrays. After silanisation and PDITC linkage, the surface was less hydrophobic as the contact angle values obtained were lower. The contact angle values for the unmodified surface and after APTES silanisation were in the close vicinity as reported by Raj et al. (2009) on his silanised cyclic olefin copolymer materials [10]. The two microdisc arrays showed slightly different readings for the unmodified and after APTES-PDITC formation. The second unmodified electrode (chip #3, marked by red bar) had slightly hydrophobic properties and this is reflected by the shift in current reading as obtained in the CV for unmodified electrode (Fig. 6.6). In general, the contact angle readings between the two microdisc electrodes were not of much difference after the first antibody immobilisation. The fact that these readings remained in the same close values after the second concentration of anti-T2 toxin antibody on the first microdisc array could be addressed to the saturation of antibody immobilisation.

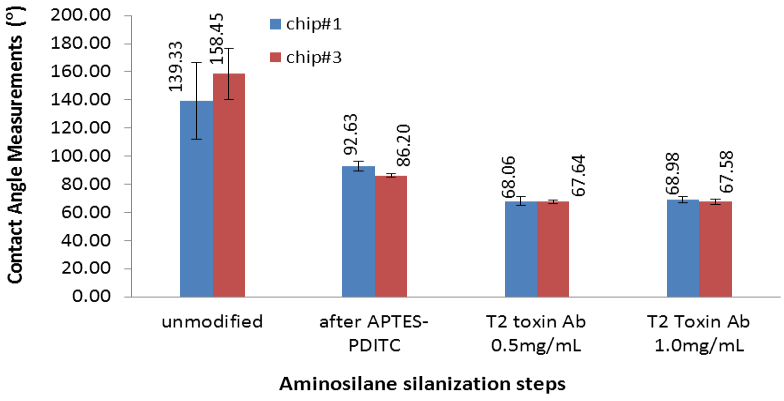


Figure 6.8: Contact angle study of two different silicon-based 10 µm microdisc gold electrode array at different stages of the modification procedures.

The surface functionalization was then applied on microelectrode array with larger surface area i.e. 10 µm microband electrode array. Similar to microdisc array, unmodified electrodes were first tested and screened before proceed to the modification. In this study, three different anti-T-2 antibody concentrations were

used (0.5, 1.0 and 2.0 mg mL^{-1}). The non-uniformity of APTES-PDITC layer formed on these two electrodes can be seen based on the difference of EIS curve generated after this step. An increment (positive shift) on the impedance on both microband electrodes could be due to the formation of APTES-PDITC layer on the surface. What is interesting here is the EIS signal for APTES-PDITC formation on the microband array was found different from the microdisc array. On the microdisc arrays, the EIS for APTES-PDITC shifted to larger impedance and decreased upon antibody attachment. In the case of microband array, the EIS curve for this particular step increased accordingly with the antibody immobilisation. As the result of the non-uniformity layer of the APTES-PDITC layer, the concentration of anti-T-2 toxin antibody that can be attached on the surface also was affected (Fig. 6.9). For instance, the first microband can accommodate up to 2.0 mg mL^{-1} concentration of anti-T-2 toxin (Fig. 6.9A) while the second microband has limitation up to 1.0 mg mL^{-1} (Fig. 6.9B). The limiting current for both electrodes have decreased by 13-16 % after antibody attachment.

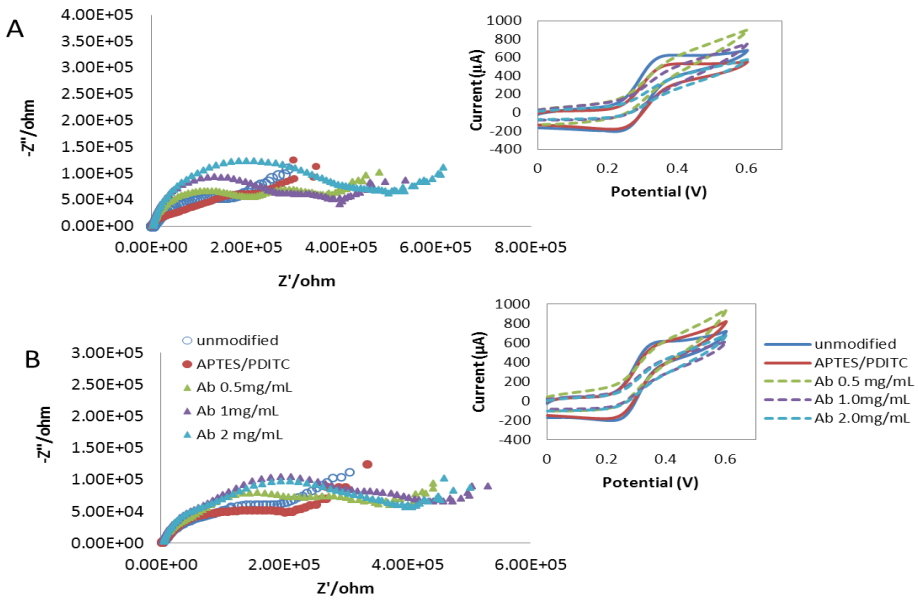


Figure 6.9: EIS (frequency 0.01- 100,000 Hz) and CV (scan rate of 100 mV s^{-1}) comparison for two different 10 µm microband electrode array functionalised with APTES silanisation with PDITC linker for three anti-T-2 toxin antibody concentrations immobilisation. Electrochemical measurements were performed in 1 mM FCA in PBS.

Besides the non-uniformity formation of the APTES-PDITC layer, another drawback that we have to deal with when undertaking these procedures was the presence of scattering electrical noise at high frequency. The scattering impedance noise was recurrence at several microelectrode arrays with MΩ magnitude. In EIS term, such noise could be addressed as R_n (noise resistance) and similar electrical noise with MΩ values also have been reported before by Behzadnasab et al. (2011) on his aminosilane treated nanoparticles [68]. It was found that the noise could be removed or eliminated by vigorously washing the electrode with DW. However such action could impair the modification layer that formed on the surface. Grygoryev (2013) has reported a similar finding in his thesis where it was reported that the deposited APTES using the same procedures as ours had increased the electrode impedance drastically besides producing poor patterning on the silanised microelectrode [69]. This is seconded by another thesis publication by Wen in 2011 whom addressed the noise in EIS measurement to the non-uniformity of APTES formation [70]. The noise level in EIS is dependent on the effective surface area, specific resistance of the bulk and the thickness of insulator [71] and in this case we deduced that the major contribution in the scattering noise was from the organic solvent traces left on the gold surface instead of the APTES itself. According to Mills & Mabbutt (2000) the noise could be due to the small applied voltages used in EIS [72].

Pertaining this surface functionalization procedure, there are several other issues that need to be revised and highlighted such as follows:

1. Pre-treatment of the gold surface. Unlike macroelectrode, the fabricated microelectrode arrays need a more robust pre-treatment due to the smaller and recessed surface area.

2. Albeit PDITC has been reported for successful antibody conjugate [73], nevertheless since PDITC in this study are immersed in DMF and chips were washed with numerous organic solvents prior Ab attachment, another alternative for the cross-linker should be sought. Organic solvent traces left at gold microelectrode array surface lead to scattering of impedance reading when measurement is taken after APTES/PDITC step. Inconsistency in vigorous washing may impair Ab immobilisation.

6.4.2 Silanisation Using APTES with EDC-NHS Amine Coupling

Following the previous discussion, the silanisation using APTES will still be retained in this study while attention will be given on the surface pre-treatment and choices of linker. In 2011, several antibody immobilisation strategies on SPR Au chip has been described by Vashist and co-workers [74]. The described method employing APTES silanisation with piranha solution pre-treatment and the use of EDC-NHS-activation group for antibody immobilisation was proven to be successful for antibody immobilisation as well as in its application in both immunoassay [75, 76] and biosensor performance [74, 77-79]. However such a method has not been applied on microelectrode arrays for antibody immobilisation with EIS characterisation. Thus this second section of the chapter endeavours to apply and study the compatibility of this method with our silicon-based microelectrode array. The schematic diagram of different immobilisation strategies carried out by Vashist et al. (2011) on the SPR Au chip is presented in Fig. 6.10.

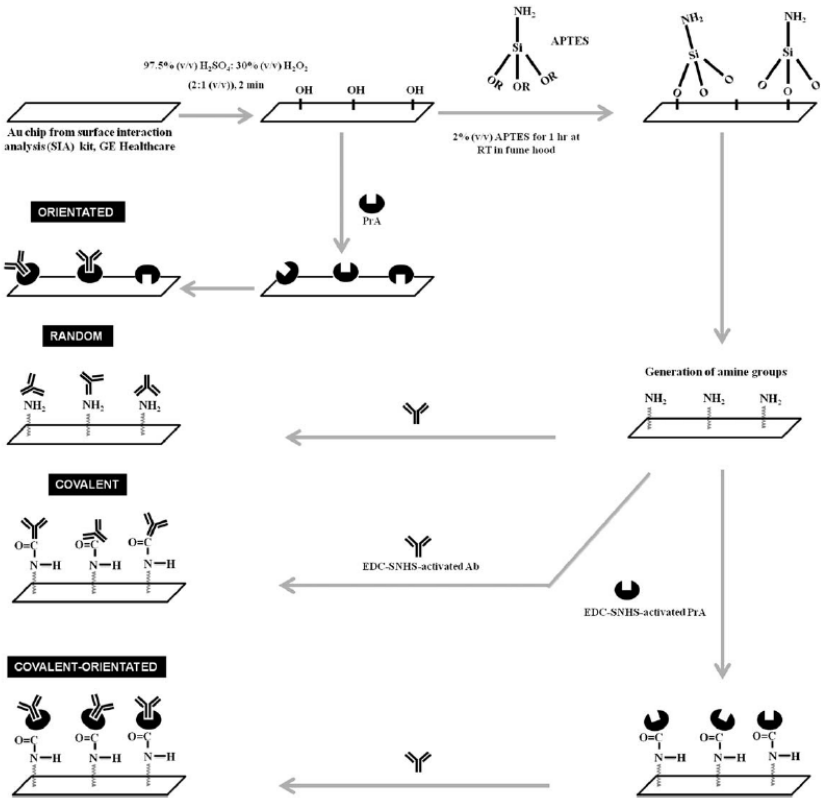


Figure 6.10: Schematic representation of various immobilization strategies employed for the SPR-based immunoassay. PrA is protein A. Taken from Ref. [74].

Based on the immunosensor performance reported [74], we narrowed down our study on two antibody immobilisation procedures, i.e. covalent attachment (EDC-NHS-Ab) and covalent-orientation (EDC-NHS-activated Protein A). The choice of buffer for antibody dilution also has been changed from borate buffer pH 8.0 to PBS pH 7.4 as initial electrochemical study indicated that PBS produced a more positive signal for antibody immobilisation (Fig. 6.11). With regard to this, Williamson and co-workers [9, 54] also performed the anti-T-2 toxin monoclonal antibody dilution in PBS pH 7.4 for the optical study. Such pH has proven to work well with antibody as reported by Nabok et al in [55] where their T-2 polyclonal and monoclonal antibody were diluted in Trizma-HCl buffer with pH 7.5 Antibody dilution in PBS also has been widely used in the work of antibody microarray [78] without compromising the electrochemical signal.

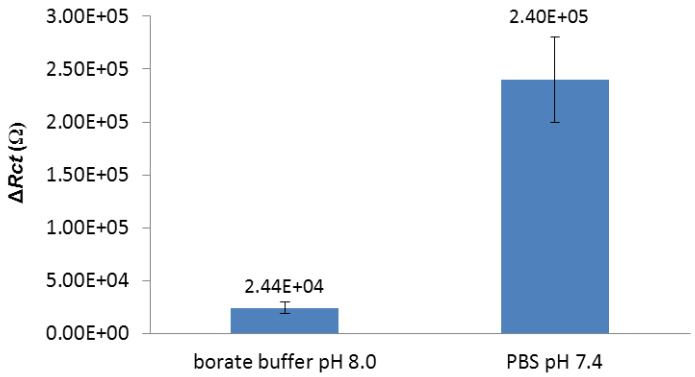


Figure 6.11: Comparison of response unit in terms of ΔR_{ct} for antibody immobilisation with dilution in borate buffer pH 8.0 and PBS pH7.4 with regard to the APTES silanisation layer.

Optical Study Using Fluorescent Labelled-Antigen

The viability of the selected modification for microelectrode arrays was first estimated using Mouse IgG and anti-mouse IgG FITC-conjugate on a 40 μm microband array. Briefly, the gold surface was first pre-treated with piranha solution (30% H_2O_2: H_2SO_4, 1:2) before carrying out the APTES silanisation (2% APTES in DW) for 1 hour. This was followed by addition of pre-mixed antibody (Mouse IgG)

conjugated EDC-NHS on the silane layer before adding its specific antigen (anti-mouse IgG FITC-conjugate). Upon the successful Ab-Ag binding, green fluorescent spotting could be seen, which is indicative of the FITC conjugate fluorescent signal (Fig. 6.12A). A control experiment, which omitted the antibody constituent, was also employed (Fig. 6.12B) to study the selectivity and non-specific binding with this selected procedure. Without the presence of Mouse-IgG, the anti-mouse IgG conjugated FITC was still able to bind with the amine group of the EDC-NHS via its *Fc* fragment hence no fluorescent signal was observed. Although some non-specific binding of the anti-mouse IgG conjugated FITC could take place on the surface, there was however as can be seen in Fig. 6.12B, non-specific binding happened within the first 15 minutes of antigen incubation.

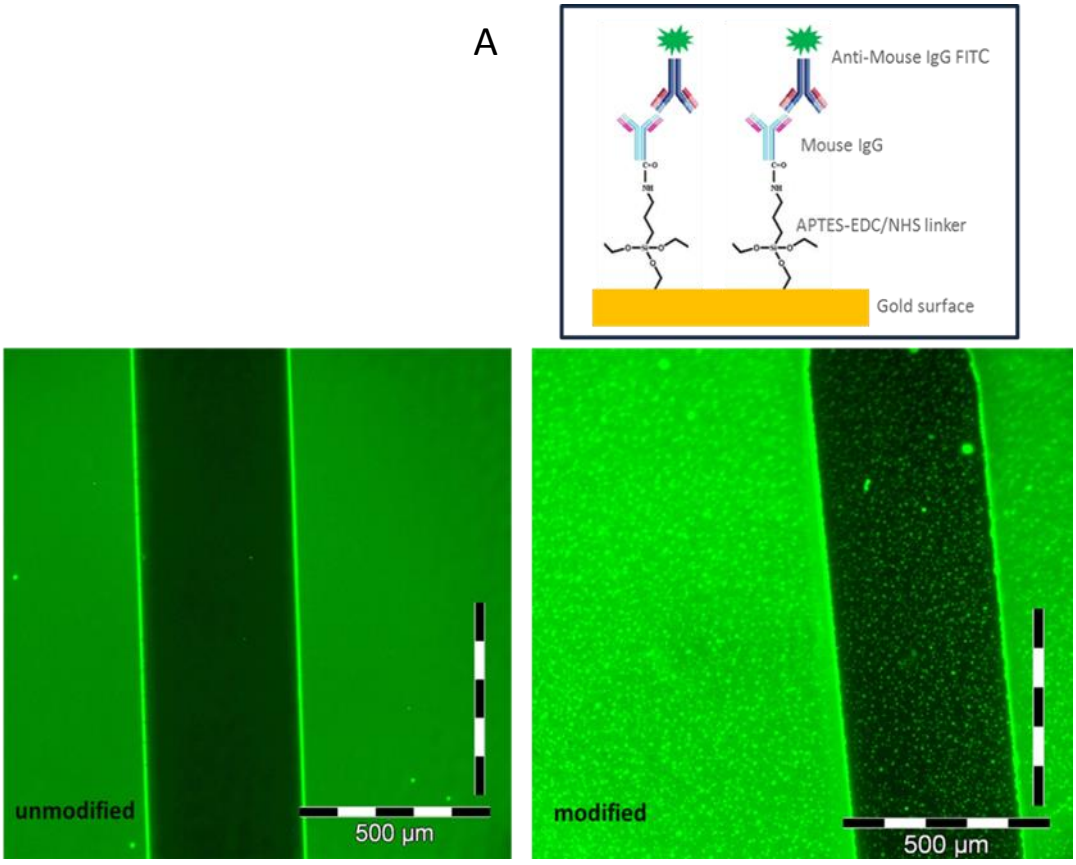


Figure 6.12A: Optical fluorescent microscope image to study the viability of the immobilisation procedure using piranha solution-APTES-EDC/NHS-Ab steps on silicon-based microband array of 40 µm width with the presence of 0.5 mg mL^{-1} mouse IgG concentration in PBS pH7.4 (*Inset*: schematic procedure of mouse IgG immobilisation and its binding with the anti-Mouse IgG conjugated FITC).

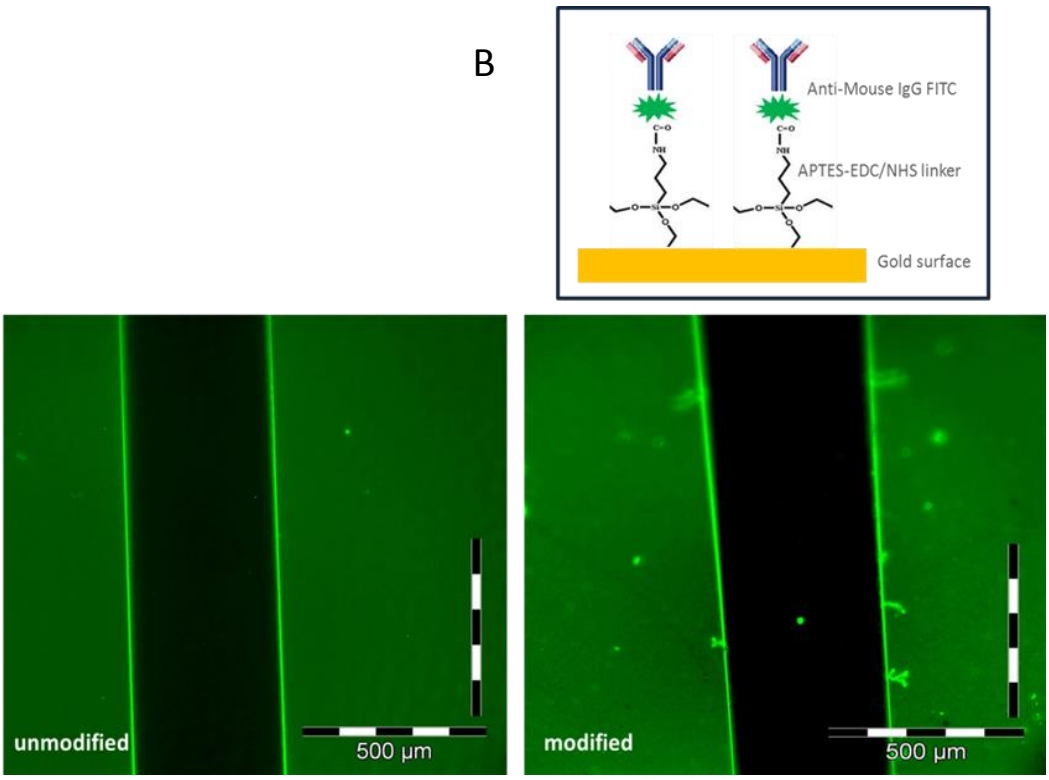


Figure 6.12B: Optical fluorescent microscope image to study the viability of the immobilisation procedure using piranha solution-APTES-EDC/NHS-Ab steps on silicon-based microband array of 40 µm width with the absence mouse IgG. (*Inset*: schematic procedure of anti-Mouse IgG conjugated FITC immobilisation).

The antigen incubation time was also varied and studied between 15 minutes to 1 hour. This indirectly will allow us to optimise the antibody-antigen (Ab-Ag) binding time. By prolonging the incubation time up to 1 hour, this only allowed the non-specific binding of the antibody/antigen on the surface particularly the silicon nitride passivation layer as shown in Fig. 6.13. Hence in order to minimise the non-specific binding of antibody/antigen on the sensor surface, the selected Ab-Ag binding time that will be further used in this study is only 15-30 minutes.

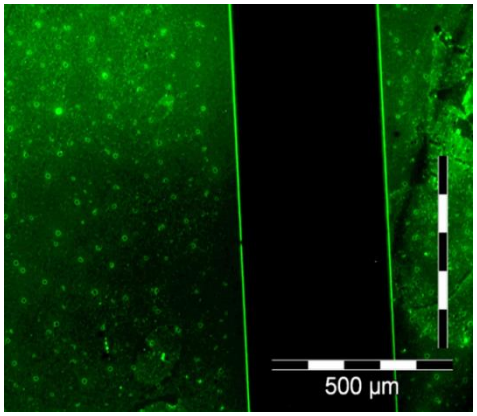


Figure 6.13: Optical fluorescent microscope showing non-specific binding of the anti-Mouse IgG conjugated FITC on the silicon nitride passivation layer when the incubation time was prolonging to 1 hour. However no non-specific binding was observed on the gold surface.

Covalent-Orientated Immobilisation Strategy Using Protein A

It is long known that the antibody orientation in immobilisation protocol played an undoubtedly important role in ensuring the binding with its specific antigen. Such an objective could be achieved with the aid of Protein A or Protein G layer that could capture the *Fc* fragment of antibody and leaving the *Fab* fragment antibody for subsequent binding [11, 60, 80].

The use of Protein A also had been investigated electrochemically in this study. Fig. 6.14 showed an EIS result with EDC-NHS-activated-Protein A. As can be seen, the R_{ct} increased accordingly with the surface functionalization indicating the successful formation of APTES layer and deposition of EDC-NHS-activated Protein A. The increment after BSA blocking could be addressed by the BSA molecule that covered the surface to block any non-specific binding from happening. The concentration of anti-T-2 toxin antibody that could be immobilised within this procedure was found to be limited to only 0.1 mg mL^{-1}. The impedance decreased when anti-T-2 toxin antibody concentration was increased to 0.5 mg mL^{-1} and this could be related to Protein A layer desorption on the gold surface. The EIS increment when adding the antibody concentration of 1.0 mg mL^{-1} could be due to the non-specific binding or adsorption of the antibody on the surface itself. The desorption or leaching of Protein

A is possible to happen as reported before [81] due to the longer immersion time of antibody incubation on the electrode surface. To verify this, a leaching study with Bradford or BCA protein assay could be done in future to assess the leaching property.

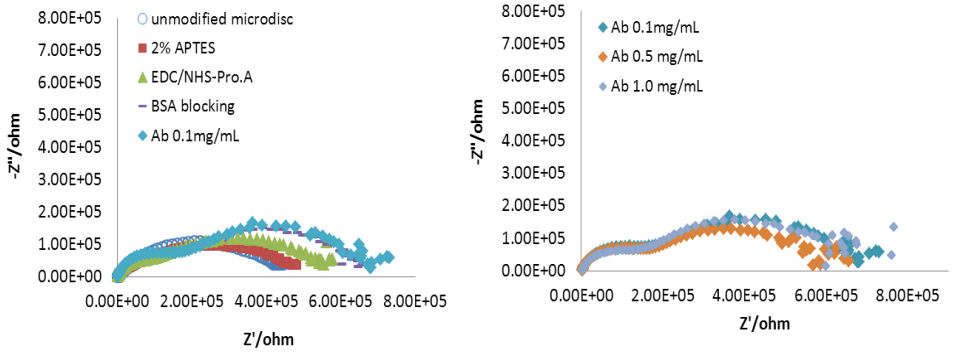


Figure 6.14: EIS (frequency 0.01- 100,000 Hz) of microdisc array with surface functionalization of piranha solution-APTES-EDC-NHS activated Protein A with anti-T-2 toxin immobilisation of three different concentrations in 1 mM FCA in PBS.

The combination of APTES with Protein A had indeed to be superior for antibody immobilisation giving high antigen binding signal [74, 82]. However, concerning the leaching properties and due to the limitation availability of Protein A stock, this immobilisation protocol had to be forgone. Furthermore, according to Kusnezow et al. (2003), the blocking process could affect the spot quality [83] and this certainly pose a risk in case of electrode array of micron dimensions. The immobilisation study thus was continued with the covalent attachment immobilisation procedure without the use of Protein A.

Covalent Attachment of Anti-T-2 Toxin Monoclonal Antibody Using EDC-NHS

The procedure employing piranha solution pre-treatment followed by deposition of 2% APTES in DI water on the microelectrode array was found to be reproducible on more than two electrodes (Fig. 6.15). Piranha solution was used for cleaning the surface and it was assumed that its etching properties [84], which provide ample surface roughness will lend to better formation of the silane layer. There were indeed several variations of APTES layer formation between several electrodes but the difference was not as massive as observed previously on APTES-PDITC procedure on microdisc array. Furthermore no electrochemical impedance noise was observed when switching to this procedure, presumable as there were no organic solvents that were being used for the washing procedures etc. For instance, APTES in this study was diluted in deionised water whilst APTES in the previous procedure was diluted in methanol.

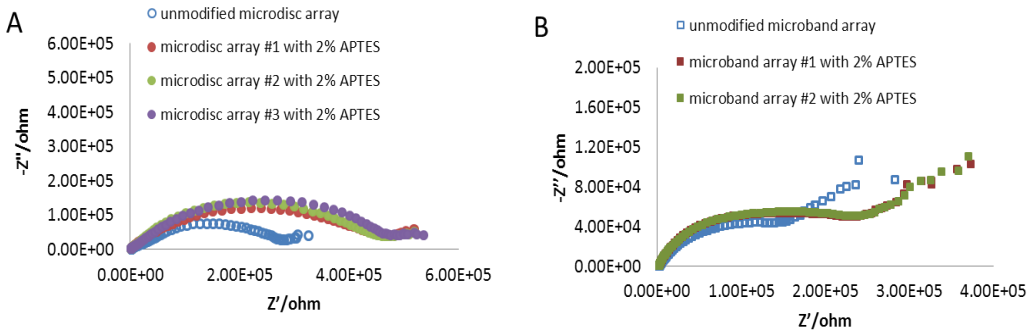


Figure 6.15: Nyquist plot showing comparison of reproducibility of the APTES layer (2% APTES in DW) on two or more microelectrode for (a) microdisc; and (b) microband array (EIS frequency 0.01- 100,000 Hz).

The anti-T-2 toxin antibody in this study was premixed with the EDC-NHS mixture but it also has shown that the antibody molecule can be adsorbed on the APTES layer as well. However antibody binding based on adsorption on aminosilanes have proven to result in lower quality of attachment [83]. This procedure will be further used in establishing the standard curve for the T-2 toxin immunosensor development.

Anti-T-2 Toxin Monoclonal Antibody Calibration Curve

In order to ascertain the concentration of anti-T-2 toxin antibody that can accommodate both microdisc and microband electrode surface area, an optimisation study of the antibody concentration need to be performed beforehand. The concentration was run from 0 to 0.75 mg mL^{-1} fo anti-T-2 toxin antibody, diluted in PBS. Although Kusnezow et al. (2003) reported the optimum antibody concentration that was used in the antibody microarray is 1 mg mL^{-1} regardless of the immobilisation technique [83], however due to the limitation of the antibody resources, the optimisation study had to be restrained to only 0.75 mg ml^{-1}. Besides, much higher concentration would only have adverse effect on microarray performance.

The resistance shift/increment on both microband and microdisc array was seen to increase accordingly with the surface functionalisation and anti-T-2 toxin antibody immobilisation (Fig. 6.16), indicating the presence of bulk material. The electrode surface also was not totally blocked as the redox probe was still permissible to the gold surface layer. The limiting current from the CV also was found to decrease upon the modification.

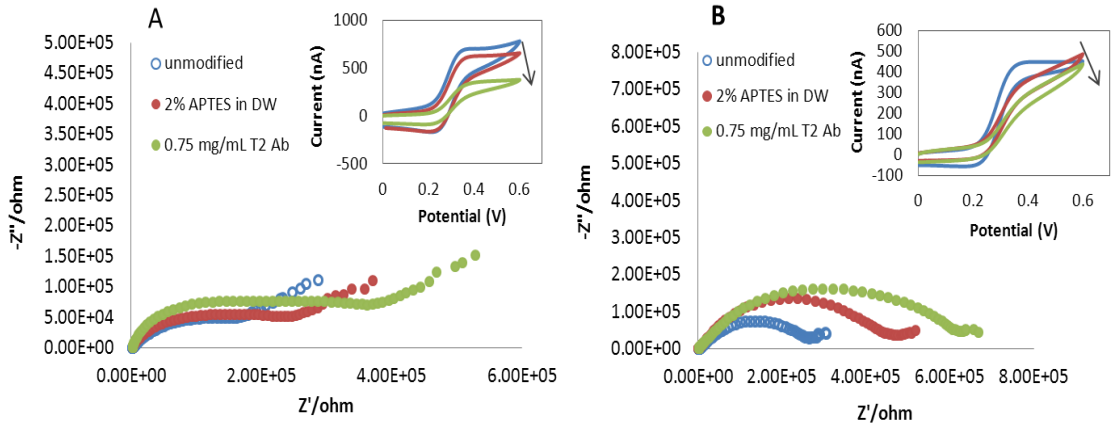


Figure 6.16: R_{ct} change upon surface functionalization with antibody immobilisation. The impedance increment (positive shift) is associated with bulk property and formation of additional layer happening on the microelectrode array surface. Results presented for (A) 10 µm microband array; and (B) 10 µm microdisc array in 1 mM FCA in PBS (Frequency 0.01-100,000 Hz). *Inset*: CV showing the decrease of limiting current accordingly with each surface functionalization steps.

The result for the anti-T-2 antibody immobilisation was first presented here. Fig. 6.17A showed that the both real and imaginary impedance values increased as the concentration of the anti-T-2 toxin antibody was also increased. The calibration curve for the antibody concentration that can be immobilised on the 10 µm microband array was as shown in Fig. 6.17B where the ΔR_{ct} value obtained was calculated in regard with the APTES silanisation layer formed from each microband array.

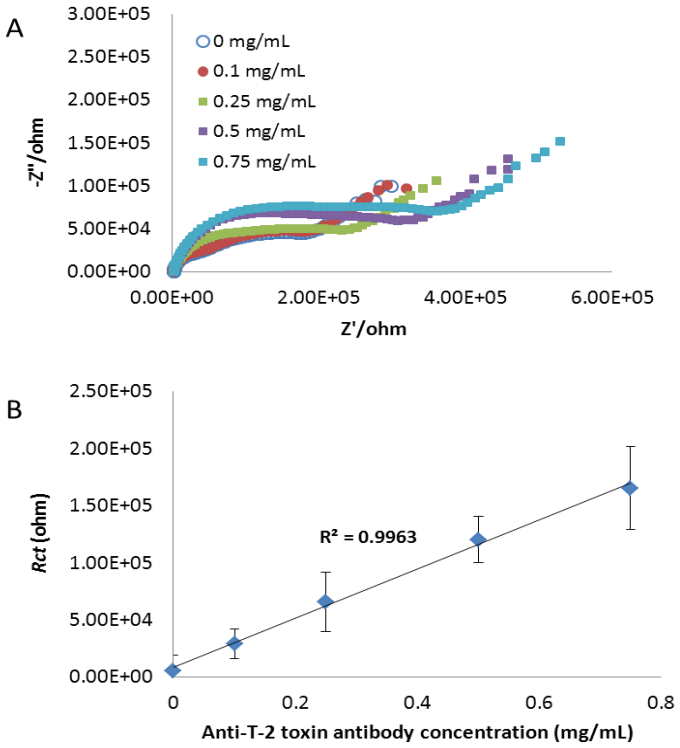


Figure 6.17: (A) Nyquist spectra acquired for different anti-T-2 toxin concentration response on five different microband electrode array; and (B) shift/difference of charge-transfer resistance values with regard to their respective electrodes after APTES functionalization steps as a function of anti-T-2 toxin antibody concentration (n=2).

The linear calibration line with excellent R^2 value was obtained from the calibration curve. It can be assumed that the microband electrode still can accommodate more than 0.75 mg mL^{-1} of antibody concentration since there was no plateau phase yet to be observed within this range. However, as mentioned earlier, due to the limitation

of the antibody stock and so as to not waste the valuable resources the concentration of the anti-T-2 toxin antibody that will be used on the microband array, it was decided to use a concentration of 0.75 mg mL^{-1} antibody.

The limiting currents for the microband arrays were also decreased accordingly with the surface functionalization (Fig. 6.18). Prior modifications, the limiting current of the unmodified ones were 556.26 ± 43.7 (theoretical limiting current of 632 nA). This value was found to be decreased by 3% after 2% APTES formation and up to 44% after 0.75 mg mL^{-1} of anti-T-2 toxin antibody immobilisation.



Figure 6.18: Reduction of limiting current calculated for the 10 μm microband array according to surface functionalization.

For the 10 μm microdisc array on the other hand, the antibody calibration curve obtained was of a sigmoidal pattern as opposed to the microband array (Fig. 6.19). Such difference could be addressed to the geometry of the two electrode arrays. For the first two anti-T-2 toxin antibody concentrations (0 and 0.1 mg mL^{-1}), the R_{ct} response was low and indicative of desorption of the APTES layer. This also could be due to the matrix interference (buffer solution). While this effect is not prominent on the microband array, the matrix effect is more pronounced at disc array area due to the smaller surface or presumably weak hydroxylation on the gold surface. It has been reported that in some cases, procedures that required a modification of the

antibodies are less suited in practical application and eventually will lead to loss of antibody activity [85].

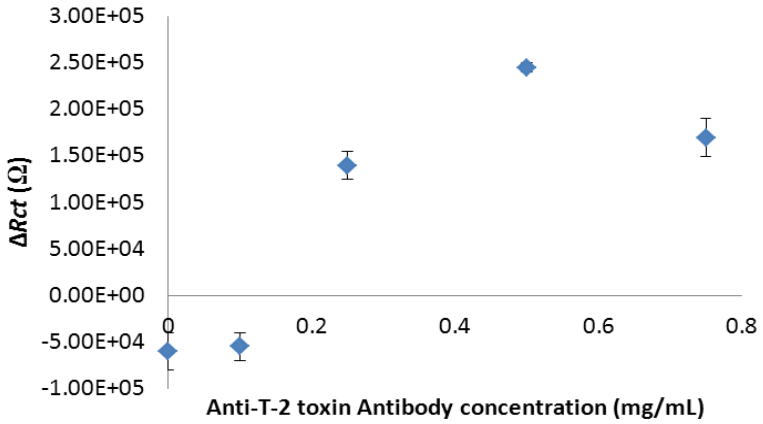


Figure 6.19: Sigmoidal calibration curve achieved for anti-T-2 toxin immobilisation achieved on the 10 µm microdisc array (*n*=2).

Based on the calibration curve, the maximum of the anti-T-2 toxin antibody that can be immobilised on the disc surface was optimised and determined at 0.5 mg mL^{-1}. Further increasing the antibody concentration did not result in *Rct* change, perhaps due to the saturation of immobilisation achieved at the disc surface. In terms of limiting current, the unmodified microdiscs had limiting current of 407.23 ± 52.9 (theoretical limiting current of 338 nA). After the silanisation, the limiting current was found to decrease by 8%, indicating the presence of the silanisation layer. With this regard, APTES has a tendency to form a polymer in the presence of water. This thick polymeric layer was formed in solution and then physisorbed to the electrode surface hence forming the silanisation layer. However the limiting currents were found to be fluctuating upon antibody immobilisation which could be addressed to either the instability of the gold surface disc array or the quality of the silanisation layer itself (Fig. 6.20).

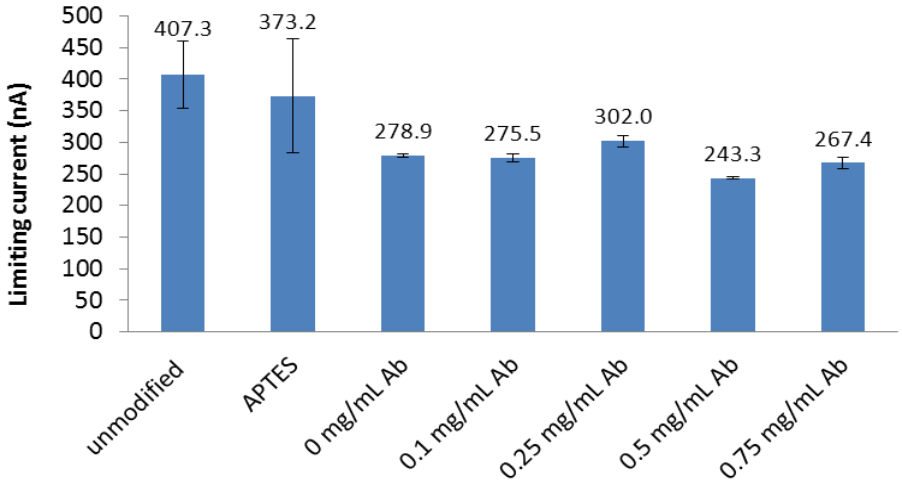


Figure 6.20: Reduction of limiting current for the 10 µm microdisc array upon surface functionalization and antibody immobilisation.

The antibody concentration that would be applied for the immobilisation strategy in detecting its specific T-2/HT-2 toxin in subsequent study was 0.5 and 0.75 mg mL^{-1} for the 10 µm microdisc and microband array respectively. The choice of such concentration is relevant taking into account the total surface area of the two microelectrodes, i.e. 2.537 x 10^{-4} cm^2 for the 10 µm microdisc array and 8.5 x 10^{-4} cm^2 for the 10 µm microband array. It was suggested that when performing concentration determinations of the binding partner, the immobilized molecule should be present at high densities so that mass transport effects predominate [86]. However, balancing the criteria between electrochemical performance and limitation of stock availability, such pre-determined concentrations were employed.

T-2/HT-2 Toxin Calibration Curve

The set detection limits for T-2/HT-2 toxin were 100 µg kg^{-1} for unprocessed cereals and cereal products except 500 µg kg^{-1} for unprocessed oats, 200 µg kg^{-1} for oat products and 50 µg kg^{-1} for infant food [35]. In this study, five calibration points were taken, i.e. 0, 25. 50, 100 and 250 ppb, as supplied in the Veratox® toxin kit by Neogen. The impedance measurements were performed in pure buffer solution as

obtained from the Neogen kit. The change in R_{ct} was calculated by the difference/shift in resistance readings between the attachment of the antigen (Ab-Ag) and the immobilised antibody (n=2 readings). The r^2 value for the 10 μm microband curve was 0.9847 as determined by the Graphpad Prism "one site -Specific binding" curve fitting function software (Fig. 6.21). The analytical limit of quantitation (LOQ) was found to be 4.89 ppb.

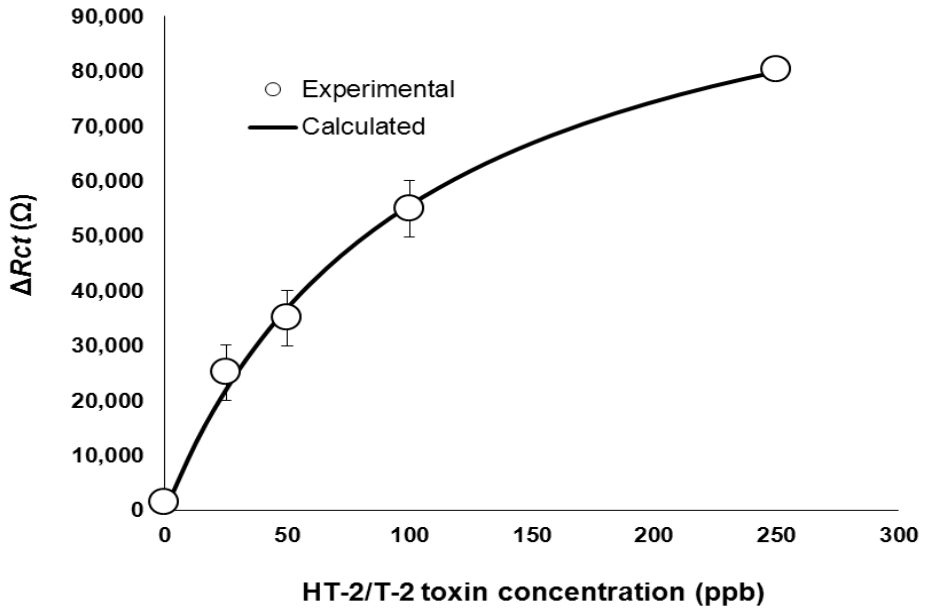


Figure 6.21: Standard curve for T-2/HT-2 toxin detection using the developed microband array in buffer solution. r^2 was found to be 0.9847 as determined from the Graphpad Prism software (n=2).

For the 10 μm microdisc array on the other hand, a poor calibration curve was established for the T-2/HT-2 toxin detection (Fig. 6.22, inset). This emphasized the need of having larger surface area for better antibody immobilisation and its antigen binding. Hence 40 μm microdisc array (N=23) was selected for the further calibration study. The unmodified 40 μm microdisc arrays were screened and studied prior modification. Their experimental current exhibited was 148.9 ± 25.38 nA in comparison with the theoretical current of 99.9 nA.

As expected, the bigger dimension of surface area displayed better antibody immobilisation and antigen binding. The anti-T-2 toxin antibody concentration that was used in the array was still maintained at 0.5 mg mL^{-1} considering the fact that its surface area is of 2.890e^{-4} cm^2; which is still in the same vicinity of the 10 µm disc surface area (2.537 e^{-4} cm^2). As shown in Fig. 6.22, the r^2 value obtained for the T-2/HT-2 calibration curve using 40 µm was 0.959. The analytical sensitivity (LOQ) for the microdisc was 1.53 ppb.

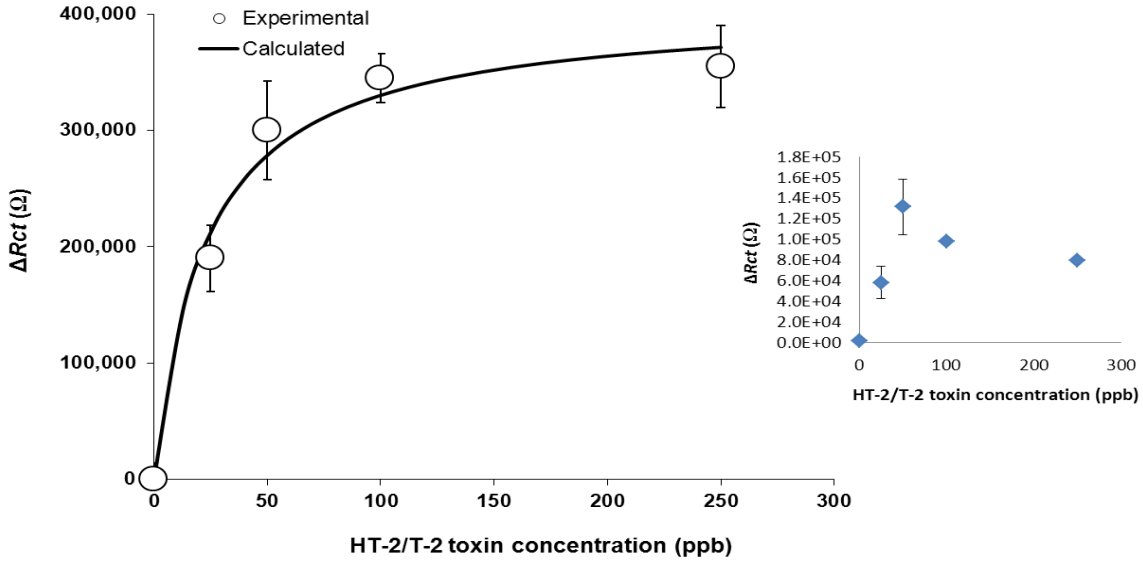


Figure 6.22: Standard curve for T-2/HT-2 toxin detection using the 40 µm microdisc array with r^2 of 0.959 as determined from the Graphpad Prism software (n=2). *Inset*: Toxin calibration curve as obtained from the 10 µm microdisc array.

The results presented here is an initial investigation of a new method in detecting T-2/HT-2 toxin using labelless impedimetric immunosensor, which to our best knowledge, has not been explored yet. The calibration curves established in buffer solution show that the microelectrode arrays were sensitive and were able to detect levels of T-2/HT-2 toxin as low as 25 ppb (25 µg kg^{-1}). The linear range of detection for both microelectrode arrays with the selected surface functionalisation method was between 0-50 ppb, which is as superior to other reported developed biosensors [55] in buffer solution. Although much lower detection limit was also reported

(1ppb) [9], the advantages by using the method developed here is that the immobilisation procedure is straight-forward without the need to further label either the antibody or antigen.

6.5 Conclusion and Suggestions for Future Work

In this final chapter, we have demonstrated a feasible and suitable surface functionalization for antibody immobilisation on silicon-based gold microelectrode array in the preliminary development of T-2 toxin immunosensor. We also have shown that scattering electrical noise encountered at high frequency when carrying out the EIS was attributed to the traces of organic solvent used in the surface functionalization rather that the APTES silanisation itself. The selected surface functionalization (APTES with EDC-NHS) is a straight-forward procedure that did not require the use of excessive organic solvent.

Several other supportive studies could be carried out to solidify the development of this T-2 toxin immunosensor. For example, spiking samples with the T-2/HT-2 toxin, performing recovery tests and interferences study of cross-reaction with several other mycotoxins (e.g. Aflatoxins and Ochratoxins) could be done in future. In order to establish a calibration curve at lower range, several other points were required. This could be achieved by (i) diluting the toxin stock as received from Neogen; or (ii) perform the real toxin dilution in buffer solution. The latter, although was said to produce more reliable standard curve, however pose a major safety concern as the real toxin supplied in powder form which is fatal. The hindrance that we face in this study as well is the type of biosafety cabinet (as well as the suitable lab) that may be required to conduct the real toxin study. The impedance devices such as the interdigitated electrodes (IDE) that is widely employed in impedimetric sensor could also be useful to study since it has been shown that immobilisation of biomolecules requires a larger surface in order to maintain its sensitivity [71]. It is deduced that surface functionalization worked best with larger surface area. This is reflected by the reliability and better results were achieved on the 10 μm microband and 40 μm microdisc electrode arrays in comparison with the 10 μm microdisc array.

When undertaking the surface functionalization, we have also learnt that several little things may affect the antibody-antigen attachment and could not be neglected. For instance, it is very important to have clean glassware, particularly clean microinserts that were used to facilitate the surface modification. Secondly, the use autoclaved pipette tips are always recommended when dealing with biological solutions/samples. Thirdly, the choice of washing solution (e.g. PBS or DW) also played an important role in ensuring a clear impedance signal is obtained.

No stability study was carried out but it was reported that APTES-activated slides has shelf life of two months period at RT [83]. We have also decided to forgo the aid of Protein A for antibody orientation based on leaching properties and limiting resources. Also, given the fact that the array for the band/disc are in micron scale, the attachment of both Protein A and antibody are thus constrained with the small dimensions. And finally, the more complex an attachment process will make the modification process more complicated and lengthy besides wasting valuable resources.

6.6 References

1. Hock, B., *Antibodies for immunosensors a review.* Analytica Chimica Acta, 1997. **347**(1): p. 177-186.
2. Luppa, P.B., L.J. Sokoll, and D.W. Chan, *Immunosensors—principles and applications to clinical chemistry.* Clinica Chimica Acta, 2001. **314**(1): p. 1-26.
3. Sarkar, P., et al., *Amperometric biosensors for detection of the prostate cancer marker (PSA).* International Journal of Pharmaceutics, 2002. **238**(1–2): p. 1-9.
4. Salam, F. and I.E. Tothill, *Detection of Salmonella typhimurium using an electrochemical immunosensor.* Biosensors and Bioelectronics, 2009. **24**(8): p. 2630-2636.
5. Parker, C.O., et al., *Electrochemical Immunochip Sensor for Aflatoxin M1 Detection.* Analytical Chemistry, 2009. **81**(13): p. 5291-5298.

6. Abdul Kadir, M.K. and I.E. Tothill, *Development of an electrochemical immunosensor for fumonisins detection in foods.* Toxins, 2010. **2**(4): p. 382-398.
7. Heurich, M., M.K.A. Kadir, and I.E. Tothill, *An electrochemical sensor based on carboxymethylated dextran modified gold surface for ochratoxin A analysis.* Sensors and Actuators B: Chemical, 2011. **156**(1): p. 162-168.
8. Dill, K., et al., *Antigen detection using microelectrode array microchips.* Analytica Chimica Acta, 2001. **444**(1): p. 69-78.
9. Williamson, M., et al., *Anti-T2 monoclonal antibody immobilization on quartz fibers: stability and recognition of T2 mycotoxin.* Analytical Letters, 1989. **22**(4): p. 803-816.
10. Raj, J., et al., *Surface immobilisation of antibody on cyclic olefin copolymer for sandwich immunoassay.* Biosensors and Bioelectronics, 2009. **24**(8): p. 2654-2658.
11. Babacan, S., et al., *Evaluation of antibody immobilization methods for piezoelectric biosensor application.* Biosensors and Bioelectronics, 2000. **15**(11): p. 615-621.
12. König, B. and M. Grätzel, *Development of a piezoelectric immunosensor for the detection of human erythrocytes.* Analytica Chimica Acta, 1993. **276**(2): p. 329-333.
13. Herzog, G. and D.W.M. Arrigan, *Electrochemical strategies for the label-free detection of amino acids, peptides and proteins.* Analyst, 2007. **132**(7): p. 615-632.
14. Ronkainen-Matsuno, N.J., et al., *Electrochemical immunoassay moving into the fast lane.* TrAC Trends in Analytical Chemistry, 2002. **21**(4): p. 213-225.
15. Chiriacò, M.S., et al., *EIS microfluidic chips for flow immunoassay and ultrasensitive cholera toxin detection.* Lab on a Chip, 2011. **11**(4): p. 658-663.
16. Berggren, C. and G. Johansson, *Capacitance measurements of antibody-antigen interactions in a flow system.* Analytical Chemistry, 1997. **69**(18): p. 3651-3657.
17. Fu, Y., et al., *Study on the immobilization of anti-IgG on Au-colloid modified gold electrode via potentiometric immunosensor, cyclic voltammetry, and*

electrochemical impedance techniques. Colloids and Surfaces B: Biointerfaces, 2005. **40**(1): p. 61-66.

18. Howell, S., et al., *High-density immobilization of an antibody fragment to a carboxymethylated dextran-linked biosensor surface.* Journal of Molecular Recognition, 1998. **11**(1-6): p. 200-203.
19. Lisdat, F. and D. Schäfer, *The use of electrochemical impedance spectroscopy for biosensing.* Analytical and bioanalytical chemistry, 2008. **391**(5): p. 1555-1567.
20. Dong, J., et al., *A Label-free Electrochemical Impedance Immunosensor Based on AuNPs/PAMAM-MWCNT-Chi nanocomposite Modified Glassy Carbon Electrode for Detection of< i> Salmonella typhimurium</i> in milk.* Food Chemistry, 2013.
21. Derkus, B., et al., *Myelin basic protein immunosensor for multiple sclerosis detection based upon label-free electrochemical impedance spectroscopy.* Biosensors and Bioelectronics, 2013. **46**(0): p. 53-60.
22. Barreiros dos Santos, M., et al., *Highly sensitive detection of pathogen Escherichia coli O157:H7 by electrochemical impedance spectroscopy.* Biosensors and Bioelectronics, 2013. **45**(0): p. 174-180.
23. Tran, H., et al., *Label-Free Electrochemical Immunoaffinity Sensor Based on Impedimetric Method for Pesticide Detection.* Electroanalysis, 2013. **25**(3): p. 664-670.
24. Collings, A. and F. Caruso, *Biosensors: recent advances.* Reports on Progress in Physics, 1997. **60**(11): p. 1397.
25. Zola, H., *Monoclonal antibodies: a manual of techniques*1987: CRC press.
26. Zola, H., *Monoclonal Antibodies*, in *eLS*2001, John Wiley & Sons, Ltd.
27. Fernandes, H.P., C.L. Cesar, and M.d.L. Barjas-Castro, *Electrical properties of the red blood cell membrane and immunohematological investigation.* Revista brasileira de hematologia e hemoterapia, 2011. **33**(4): p. 297-301.
28. Kumagai, I. and K. Tsumoto, *Antigen–Antibody Binding*, in *eLS*2001, John Wiley & Sons, Ltd.
29. Vidal, J.C., et al., *Electrochemical affinity biosensors for detection of mycotoxins: A review.* Biosensors and Bioelectronics, 2013. **49**(0): p. 146-158.

30. Van Egmond, H.P., R.C. Schothorst, and M.A. Jonker, *Regulations relating to mycotoxins in food.* Analytical and bioanalytical chemistry, 2007. **389**(1): p. 147-157.
31. Langseth, W. and T. Rundberget, *Instrumental methods for determination of nonmacrocyclic trichothecenes in cereals, foodstuffs and cultures.* Journal of Chromatography A, 1998. **815**(1): p. 103-121.
32. Meneely, J.P., et al., *Current methods of analysis for the determination of trichothecene mycotoxins in food.* TrAC Trends in Analytical Chemistry, 2011. **30**(2): p. 192-203.
33. Rosenstein, Y., et al., *Immunosuppressive activity of Fusarium toxins. Effects on antibody synthesis and skin grafts of crude extracts, T2-toxin and diacetoxyscirpenol.* Immunology, 1979. **36**(1): p. 111.
34. Lee, Y.W., K.H. Kim, and H.S. Chung, *Production of T-2 Toxin and its metabolites by Fusarium-Sporotrichioides isolates from the corn producing area in South Korea.* Korean Journal of Mycology, 1990. **18**(1): p. 13-19.
35. Edwards, S., et al., *Emerging issues of HT-2 and T-2 toxins in European cereal production.* World Mycotoxin Journal, 2009. **2**(2): p. 173-179.
36. Langseth, W. and T. Rundberget, *The occurrence of HT-2 toxin and other trichothecenes in Norwegian cereals.* Mycopathologia, 1999. **147**(3): p. 157-165.
37. Perkowski, J., et al., *Natural contamination of spring barley with group A trichothecene mycotoxins in south-eastern Poland.* Food Additives and Contaminants, 1997. **14**(4): p. 321-325.
38. Sokolovi, M. and B. Impraga, *Survey of trichothecene mycotoxins in grains and animal feed in Croatia by thin layer chromatography.* Food Control, 2006. **17**(9): p. 733-740.
39. Omurtag, G.Z. and D. Yazicioglu, *Occurrence of T-2 toxin in processed cereals and pulses in Turkey determined by HPLC and TLC.* Food Additives and Contaminants, 2001. **18**(9): p. 844-849.
40. Cantalejo, M.J., et al., *Detection of fusarin C and trichothecenes in Fusarium strains from Spain.* Journal of Basic Microbiology, 1999. **39**(3): p. 143-153.

41. Khatoon, S., et al., *NATURAL OCCURRENCE OF AFLATOXINS, ZEARALENONE AND TRICHOTHECENES IN MAIZE GROWN IN PAKISTAN.* Pakistan Journal of Botany, 2012. **44**(1): p. 231-236.
42. Makun, H.A., et al., *Natural multi-occurrence of mycotoxins in rice from Niger State, Nigeria.* Mycotoxin research, 2011. **27**(2): p. 97-104.
43. Ler, S.G., F.K. Lee, and P. Gopalakrishnakone, *Trends in detection of warfare agents: Detection methods for ricin, staphylococcal enterotoxin B and T-2 toxin.* Journal of Chromatography A, 2006. **1133**(1–2): p. 1-12.
44. Wannemacher, R.W., et al., *Trichothecene mycotoxins.* Medical aspects of chemical and biological warfare, 1997. **6**: p. 655-76.
45. Ingle, A., A. Varma, and M. Rai, *Trichothecenes as Toxin and Bioweapons: Prevention and Control*, in *Mycotoxins in Food, Feed and Bioweapons*, M. Rai and A. Varma, Editors. 2010, Springer Berlin Heidelberg. p. 291-305.
46. Paterson, R.R.M., *Fungi and fungal toxins as weapons.* Mycological Research, 2006. **110**(9): p. 1003-1010.
47. Edwards, S.G., *Fusarium mycotoxin content of UK organic and conventional oats.* Food Additives and Contaminants, 2009. **26**(7): p. 1063-1069.
48. Barnavetro, I., et al., *ELISA tests for determination of T-2 and F2 toxin contents in cereal samples.* Magyar Allatorvosok Lapja, 1995. **50**(8): p. 505-510.
49. Piermarini, S., et al., *Rapid Screening Electrochemical Methods for Aflatoxin B1 and Type-A Trichothecenes: A Preliminary Study.* Analytical Letters, 2007. **40**(7): p. 1333-1346.
50. Gilbert, J. and E. Anklam, *Validation of analytical methods for determining mycotoxins in foodstuffs.* TrAC Trends in Analytical Chemistry, 2002. **21**(6–7): p. 468-486.
51. Krska, R. and A. Molinelli, *Rapid test strips for analysis of mycotoxins in food and feed.* Analytical and bioanalytical chemistry, 2009. **393**(1): p. 67-71.
52. DeSaeger, S. and C. VanPeteghem, *Dipstick enzyme immunoassay to detect Fusarium T-2 toxin in wheat.* Applied and Environmental Microbiology, 1996. **62**(6): p. 1880-1884.

53. Molinelli, A., et al., *Development of qualitative and semiquantitative immunoassay-based rapid strip tests for the detection of T-2 toxin in wheat and oat.* Journal of agricultural and food chemistry, 2008. **56**(8): p. 2589-2594.
54. Sundaram, P.V., *Waveguide for T-2 toxin detection using quartz-immobilized anti-T-2 monoclonal antibodies*, in *Okada, H., A. Tanaka and H. W. Blanch* 1990. p. 444-447.
55. Nabok, A.V., et al., *Registration of T-2 mycotoxin with total internal reflection ellipsometry and QCM impedance methods.* Biosensors & Bioelectronics, 2007. **22**(6): p. 885-890.
56. Meneely, J.P., et al., *A rapid optical immunoassay for the screening of T-2 and HT-2 toxin in cereals and maize-based baby food.* Talanta, 2010. **81**(1-2): p. 630-636.
57. Gupta, G., et al., *Supersensitive detection of T-2 toxin by the in situ synthesized pi-conjugated molecularly imprinted nanopatterns. An in situ investigation by surface plasmon resonance combined with electrochemistry.* Biosensors & Bioelectronics, 2011. **26**(5): p. 2534-2540.
58. Abdul Rahman, M.S., et al., *Detection of bacterial endotoxin in food: New planar interdigital sensors based approach.* Journal of Food Engineering, 2013. **114**(3): p. 346-360.
59. Zia, A.I., et al., *Technique for rapid detection of phthalates in water and beverages.* Journal of Food Engineering, 2013. **116**(2): p. 515-523.
60. Kassanos, P., et al., *Towards the development of an electrochemical biosensor for hCG beta detection.* Physiological Measurement, 2008. **29**(6): p. S241-S254.
61. Primiceri, E., et al., *Real-time monitoring of copper ions-induced cytotoxicity by EIS cell chips.* Biosensors and Bioelectronics, 2010. **25**(12): p. 2711-2716.
62. Yu, X., et al., *An impedance array biosensor for detection of multiple antibody–antigen interactions.* Analyst, 2006. **131**(6): p. 745-750.
63. Hleli, S., et al., *Atrazine analysis using an impedimetric immunosensor based on mixed biotinylated self-assembled monolayer.* Sensors and Actuators B: Chemical, 2006. **113**(2): p. 711-717.

64. Jie, M., et al., *An electrochemical impedance immunoanalytical method for detecting immunological interaction of human mammary tumor associated glycoprotein and its monoclonal antibody.* Electrochemistry Communications, 1999. **1**(9): p. 425-428.
65. Herzog, G., J. Raj, and D.W. Arrigan, *Immobilisation of antibody on microporous silicon membranes.* Microchimica Acta, 2009. **166**(3-4): p. 349-353.
66. Lvovich, V.F., *Impedance spectroscopy: applications to electrochemical and dielectric phenomena*2012: John Wiley & Sons.
67. Lillis, B., et al., *Investigation into the effect that probe immobilisation method type has on the analytical signal of an EIS DNA biosensor.* Biosensors and Bioelectronics, 2007. **22**(7): p. 1289-1295.
68. Behzadnasab, M., et al., *Corrosion performance of epoxy coatings containing silane treated ZrO2 nanoparticles on mild steel in 3.5% NaCl solution.* Corrosion Science, 2011. **53**(1): p. 89-98.
69. Grygoryev, K., *Investigation of micro-devices for neurobiological applications*, 2013.
70. Wen, X., *Design, Fabrication, and Characterization of Field-Effect and Impedance Based Biosensors*, 2011, Ohio State University.
71. Yu, H., et al., *High spatial resolution impedance measurement of EIS sensors for light addressable cell adhesion monitoring.* Biosensors and Bioelectronics, 2011. **26**(6): p. 2822-2827.
72. Mills, D.J. and S. Mabbutt, *Investigation of defects in organic anti-corrosive coatings using electrochemical noise measurement.* Progress in Organic Coatings, 2000. **39**(1): p. 41-48.
73. Kwon, D., et al., *A Facile and Sensitive Method for Detecting Cardiac Markers Using Ubiquitous pH Meters.* Analytical Chemistry, 2013.
74. Vashist, S.K., et al., *Effect of antibody immobilization strategies on the analytical performance of a surface plasmon resonance-based immunoassay.* Analyst, 2011. **136**(21): p. 4431-4436.
75. Dixit, C.K., et al., *Multisubstrate-compatible ELISA procedures for rapid and high-sensitivity immunoassays.* Nat. Protocols, 2011. **6**(4): p. 439-445.

76. Vashist, S.K., *Comparison of 1-Ethyl-3-(3-Dimethylaminopropyl) Carbodiimide Based Strategies to Crosslink Antibodies on Amine-Functionalized Platforms for Immunodiagnostic Applications.* Diagnostics, 2012. **2**(3): p. 23-33.
77. Vashist, S.K., *A highly-sensitive and rapid Surface Plasmon Resonance immunoassay procedure based on the covalent-orientated immobilization of antibodies.* 2011.
78. Vashist, S.K., M. Saraswat, and H. Holthšfer, *Comparative Study of the Developed Chemiluminescent, ELISA and SPR Immunoassay Formats for the Highly Sensitive Detection of Human Albumin.* Procedia Chemistry, 2012. **6**(0): p. 184-193.
79. Zheng, D., et al., *Rapid and simple preparation of a reagentless glucose electrochemical biosensor.* Analyst, 2012. **137**(16): p. 3800-3805.
80. Anderson, G.P., et al., *Effectiveness of protein A for antibody immobilization for a fiber optic biosensor.* Biosensors and Bioelectronics, 1997. **12**(4): p. 329-336.
81. Carter-Franklin, J.N., et al., *Fragments of protein A eluted during protein A affinity chromatography.* Journal of Chromatography A, 2007. **1163**(1): p. 105-111.
82. Suri, C., P. Jain, and G. Mishra, *Development of piezoelectric crystal based microgravimetric immunoassay for determination of insulin concentration.* Journal of biotechnology, 1995. **39**(1): p. 27-34.
83. Kusnezow, W., et al., *Antibody microarrays: an evaluation of production parameters.* Proteomics, 2003. **3**(3): p. 254-264.
84. Creager, S.E., L.A. Hockett, and G.K. Rowe, *Consequences of microscopic surface roughness for molecular self-assembly.* Langmuir, 1992. **8**(3): p. 854-861.
85. Nisnevitch, M., et al., *Immobilization of antibodies onto glass wool.* Journal of Chromatography B: Biomedical Sciences and Applications, 2000. **738**(2): p. 217-223.
86. Pharmacia Biosensor, A., *BIAapplications Handbook.* Pharmacia Biosensor AB, Uppsala, Sweden, 1994.

CHAPTER 7
CONCLUSION AND SUGGESTION

7.1 Conclusion

Overall, this thesis study has described the fabrication, characterisation and application of the microfabricated microelectrode arrays for T-2 mycotoxin immunosensor. The thesis is divided into two sections where the first sections (Chapters 3-4) described the initial fabrication and characterisation of the microelectrode array of different geometries, dimensions, substrates and interspacing distance. The second part of the thesis (Chapters 5-6) emphasized on the surface functionalisation of the microfabricated gold surface area for biomolecule immobilisation in life sciences application. The surface functionalisation was first studied on a planar macroelectrode before venturing into microelectrode array dimensions.

7.1.1 Fabrication of Microelectrode Array

The micro- and nanoelectrode array were first fabricated on two different substrates (silicon and glass) via microfabrication techniques to produce a single working electrode chip. The summary of the fabricated microelectrode array are listed below:

i) Two different geometries (band and disc) with dimension ranging from 10 μm, 1 μm and 100 nm.
ii) Three silicon nitride layer passivation thicknesses (200, 300 and 500 nm). However for the glass microelectrode, only 200 nm recess depth was selected in the fabrication process.

Scanning electron microscopy (SEM) revealed that both UV and e-beam lithography were successful for the development of silicon-based micro- and nanoelectrode

arrays. CV studies shown that all of the silicon-based microdisc and microband array of both 10 and 1 μm critical dimensions exhibited good experimental limiting current in comparison with the theoretical ones. However, due to the aging and delamination factors, the 1 μm microelectrode array's performance were found sluggish over time hence their characterisation through EIS could not be repetitively conducted. The 100 nm nanoband array on the other hand gave bad experimental currents which were one hundred times lower that the theoretical limiting current. Such behaviour was indicative of having planar and heavily overlapping diffusion.

Based on the stability and reproducibility of the 10 μm microelectrode array, this dimension was selected for further chemical modification study and subsequent fabrication of the on-chip microelectrochemical cell. Although the glass-based microelectrode array also exhibited performance comparable with the silicon-based ones, nevertheless due to fragility and brittleness of the substrate, the glass substrate was omitted for the subsequent studies.

The second part of Chapter 3 investigated the feasibility of applying electrochemical deposition for the surface modification on the 10 μm microelectrode array. With this regard, silica film sol-gel and nanoporous gold electrodeposition (NPG) were chosen to be performed on the microband and microdisc array respectively. These electrodeposition applications on microelectrode array for surface modification have not been reported by other researchers to date. In this part, characterisation studies consisted of both electrochemical (CV and EIS) and electron microscopy and spectral studies (SEM and EDX analysis). The main objective of this study was to increase the surface roughness. The silica-film sol-gel electrodeposition was achieved via electro-assisted self-assembled (EASA) technique. By adding the MPTMS partial self-assembled monolayer step on the gold electrode array and constituting the MPTMS in the CTAB:TEOS precursor, better adhesion of sol-gel films was obtained. When moving from a planar macroelectrode to a smaller recessed array, there were found changes of optimal electrodeposition parameters that need to be taken into account. For instance for successful surface modification on microelectrode, the current density needs to be increased (from -0.74 mA cm^{-2} to -7.4 mA cm^{-2}) and ageing at room temperature instead of high temperature in oven is preferred. The next chemical modification, the NPG electrodeposition was

performed on the 10 μm microdisc array by electrodeposition of $Au_{0.18}Ag_{0.82}$ followed by dealloying steps. This direct and simple method provides a higher surface roughness with higher current density while maintaining the merit of microelectrode behaviour. It was found that film thickness formed via EASA and NPG on the gold surface could be tuned by controlling the electrodeposition parameters. However, due to limited resources and time-constrain, these optimisation studies were not conducted.

In the following chapter of the fabrication, the development of the on-chip microelectrochemical cell was studied. Additionally to microelectrode array representing working electrode (WE) the microelectrochemical cell consisted of integrated reference electrode (RE) and counter electrode (CE); both were also achieved by the means of microfabrication techniques. While the 10 μm critical dimension for WE was still retained in this chapter, the interspacing distance (*d*) was varied. It can be concluded that the design and fabrication of the on-cell microelectrochemical chip were successful. Both CV and EIS have shown that the all on-chip electrochemical cell's measurement reading was the same as when using an external commercial CE and RE. Out of the 12 designs fabricated, only 9 designs were found reproducible and stable. The other three electrodes had the recurrence of the dead electrodes as well as delamination due to the continuous use in the saline buffer. It also could be attributed to the non-uniformity current disctribution across the surface. Through this chapter, as agreed theoretically, the interspacing between electrodes in an array (*d*), indeed played a significant role in determining the type of diffusion on the electrode. The *d* of 100 μm was proven to be sufficed in allowing individual hemispherical diffusion to take place. The impedance study performed correlates well with the limiting current and cyclic voltammetry study, thus supporting the diffusion behaviour proposed for the different geometries and interspacing distance. At a fixed potential, both resistance and impedance were found to be inversely proportional to the electrode area, as given by the Ohm's law.

7.1.2 Surface Functionalisation on Microfabricated Silicon-Based Gold Electrode

The surface functionalisation study was first carried out on a planar macroelectrode surface. Electrochemical characterisations attained from this initial stage provided us insight on the electrochemical behaviour upon surface modification before embarking on the surface functionalisation at microelectrode array surface. The first chapter on surface functionalisation (Chapter 5) aimed to investigate the suitable surface functionalisation on gold surface for immobilising two biological elements, namely Histidine-tagged protein and antibody. The immobilisation of Histidine-tagged protein was achieved by self-assembled monolayer using 11-MUA followed by adaptation of the IMAC technique by using NTA-ligand-metal coordination. The success of the surface functionalisation was demonstrated by the fluorescent-tagged histidine-tagged protein in the fluorescent study. The application on real histidine-tagged protein by using PduA shell protein was investigated by both electrochemical techiques and AFM characterisation. CV and EIS have indicated the PduA shell protein has been successfully immobilised on the gold surface and this was supported by the AFM images. The AFM images of the immobilised protein correlates well with the adsorbed protein in terms of the diameter and height as analysed by particle analysis SPIP software. However poor resolution of the immobilised PduA images was obtained which indicated the artefact of the probe due to the continuous biological sample scanning.

The antibody immobilisation was next studied by employing anti-T-2 toxin monoclonal antibody model. Unlike the histidine-tagged protein immobilisation, the surface functionalisation for antibody immobilisation was mostly achieved by silanisation technique. Three surface functionalisation studies included CM-Dextran and silanisation using GOPTS-PEG and APTES-PDITC. These three techniques were selected due to their widely successful application reported in biosensor for antibody immobilisation. It was found that the APTES-PDITC technique showed the best immobilisation performance in terms of reproducibility and substantial impedance change on a macroelectrode surface. Hence, this particular method was selected for further application on the microelectrode array surface for the

development of labelless T-2 toxin immunosensor using the microelectrode array transducer chip.

It was found that the surface functionalisation on the recessed microelectrode array was indeed an intricate one and differed from the macro counterparts. While APTES-PDITC technique suited the macroelectrode, its application on microelectrode array has led to the non-uniformity of active layer which affected the amount of concentration of anti-T-2 toxin antibody that can be immobilised on the surface area. The major concern however was the scattering signal in impedance measurement encountered at high frequencies. It was deduced that such noise can be attributed to the organic solvent traces that left on the surface of array. Although these traces could be removed by vigorously washing the electrode surface, this will eventually impair the silanised surface. Considering these facts and revising the APTES-PDITC method, several points were revisited. The two major issues were to seek new linker instead of PDITC and minimising/eliminating the excessive use of organic solvent. With this regard, a direct APTES silanisation method followed by EDC-NHS coupling was selected. The pre-treatment of the surface include the etching by means of piranha solution.

By using the APTES-EDC-NHS coupling, better active layer was formed as reflected in the reproducibility of results on more than two microelectrode surfaces. An excellent calibration anti-T-2 toxin antibody curve was obtained for the 10 μm microband array and 0.75 mg mL^{-1} of anti-T-2 toxin antibody concentration, which was optimal for the microband. Based on the T-2/HT-2 toxin calibration curve, the analytical sensitivity (LOQ) achieved by 10 μm microband was 4.89 ppb.

The antibody calibration curve for the 10 μm microdisc exhibited a sigmoidal shape that indicated saturation of antibody concentration has happened when surpassing 0.5 mg mL^{-1} anti-T-2 antibody concentration. The optimised concentration for the 10 μm microband was hence determined at 0.5 mg mL^{-1} but the T-2/HT-2 toxin calibration curve was still unacceptable. Thus, a 40 μm microdisc array was used instead which exhibited better T-2/HT-2 toxin calibration curve with LOQ of 1.53 ppb. This indicated and proved that surface functionalisation indeed require a larger surface area for better biomolecule attachment and binding process.

Throughout Chapter 6 we have proved that labelless detection of T-2 toxin is viable through labelless impedimetric approach with simple surface functionalisation. This novelty has not yet studied or reported by any researcher to date.

Overall, from the two big sections, it can be can be concluded that the fabrication and application of the nanoelectrode array of 1 μm and 100 nm critical dimensions were not attainable in this study. Its reproducibility and continuous usage in saline buffer resulted in sluggish performance due to the aging factor and delamination/mechanical defects. In terms of surface functionalisation, larger surface area was still preferred for better biomolecule immobilisation. When undertaking the microelectrode array application, while 10 μm microband array showed an excellent result, bigger dimensions (>10 μm) will be needed on the microdisc array. The preliminary study of the T-2 toxin labelless immunosensor was found promising.

7.2 Suggestions for Future Work

In this thesis, we have carried out immense surface modification and functionalisation. It is of interest if we could carry out real application of biological elements immobilisation on the modified microelectrode array with silica film and nanoporous gold in biosensor application. Also, further application on the on-chip microelectrochemical cell could be interesting as well. With this regard, several post-fabrication steps treatment can be carried in order to ensure the stability of the Ag/AgCl layer on the on-cell electrochemical chip.

Regarding the T-2 toxin immunosensor, the study could be consolidated by performing spike sample analysis, recovery analysis and cross-reaction interference in future.

LIST OF CONFERENCES AND PUBLICATION

CONFERENCES (POSTER PRESENTATION):

1. Characterisation of gold macro- and micro-electrodes for biomedical applications. Claire O'Connell, **Azura Said,** Eileen Hurley, Vladimir Ogurtsov & Karen Twomey. *7th CASi 2013, Conference of Analytical Sciences in Ireland*, 1-2 July, 2013, Devere Hall, UCC (Best Poster Presentation- 2nd Runner up).
2. Electrochemical and Atomic Force Microscopy Studies of PduA Shell Protein Immobilisation on Gold Electrode Surface. *Bioelectrochemistry2013*, 17-21 March 2013, Bochum, Germany. **Nur Azura Mohd Said**, Mingzhi Liang, Michael B. Prentice, Grégoire Herzog & Vladimir I. Ogourtsov.
3. Electrochemical impedance spectroscopy at recessed microelectrode arrays. **Nur Azura Mohd Said**, Karen Twomey, Grégoire Herzog & Vladimir Ogourtsov. *Electrochem2012*, 2-4 September, Trinity College Dublin, Ireland.
4. Electrochemical impedance spectroscopy at recessed microelectrode arrays**.** **Nur Azura Mohd Said**, Karen Twomey, Grégoire Herzog & Vladimir Ogourtsov. *Chemistry Postgraduate Day*, Chemistry Department, University College Cork, 30 August 2012.
5. Gold Micro- and Nanoelectrodes on Glass Substrates for Biosensing Application. **Nur Azura Mohd Said**, Karen Twomey, Grégoire Herzog & Vladimir I. Ogourtsov. *Tyndall Postgraduate Student Poster Competition*, 20 July 2012, Tyndall National Institute, Cork.
6. Electrochemical Impedance Spectroscopy and Cyclic Voltammetry Studies at Micro- and Nano-electrode Arrays for Sensor Applications. **Nur Azura Mohd Said**, Karen Twomey, Grégoire Herzog & Vladimir I. Ogourtsov. *Analytical Research Forum 2012*. 2-4 July, Durham University UK.

7. Fabrication and Electrochemical Characterization of Micro- and Nanoelectrode Arrays for Sensor Applications. **Nur Azura Mohd Said**, Karen Twomey, Vladimir I Ogurtsov, Damien W M Arrigan & Grégoire Herzog. *Sensors and Their Applications XVI*, 12-14 September 2011, Clarion Hotel, Cork, Ireland.
8. Biosensing at nanopore and nanoelectrode arrays. Grégoire Herzog, Jonathan S. Ellis, **Azura Said**, Karen Twomey, Jorg Strutwolf, Vladimir I. Ogurtsov, Barry Glynn, Damien W.M. Arrigan. *NanoBioEurope*, Cork 2011, June 21-23, 2011, Cork, Ireland
9. Nanoelectrode and nanopore arrays for sensor applications. Grégoire Herzog, Jonathan S. Ellis, **Nur Azura Mohd Said**, Karen Twomey, Jorg Strutwolf, Vladimir I. Ogurtsov, Barry Glynn, Damien W.M. Arrigan. *Nanoweek Conference 2011*, 31st January – 1st February 2011, Carton House, Co. Kildare, Ireland.

ORAL PRESENTATION:

1. Electrochemical Biosensor Based On Microfabricated Electrode Array For Life Sciences Applications. **Nur Azura Mohd Said.** *Chemistry Postgraduate Research Day*, 29th August 2013, UCC, Cork, Ireland.

JOURNAL:

1. Fabrication and Electrochemical Characterization of Micro- and Nanoelectrode Arrays for Sensor Applications. **Nur Azura Mohd Said**, Karen Twomey, Vladimir I Ogurtsov, Damien W M Arrigan and Grégoire Herzog. *J. Phys.: Conf. Ser. 307 012052* doi:10.1088/1742-6596/307/1/012052